2010-05-12

Simulating Flood Propagation in Urban Areas using a Two-Dimensional Numerical Model

Noemi Gonzalez-Ramirez
University of Miami, n.gonzalezramirez@umiami.edu

UNIVERSITY OF MIAMI

SIMULATING FLOOD PROPAGATION IN URBAN AREAS USING A TWO-DIMENSIONAL NUMERICAL MODEL

By

Noemi Gonzalez-Ramirez

A DISSERTATION

Submitted to the Faculty
of the University of Miami
in partial fulfillment of the requirements for
the degree of Doctor of Philosophy

Coral Gables, Florida

May 2010

UNIVERSITY OF MIAMI

A dissertation submitted in partial fulfillment of
the requirements for the degree of
Doctor of Philosophy

SIMULATING FLOOD PROPAGATION IN URBAN AREAS USING A TWO-DIMENSIONAL NUMERICAL MODEL

Noemi Gonzalez-Ramirez

Approved:

_____ Antonio Nanni, Ph.D. Chair and Professor of Civil Architectural and Environmental Engineering	_____ Terri A. Scandura, Ph.D. Dean of the Graduate School
_____ David Chin, Ph.D. Professor of Civil Architectural and Environmental Engineering	_____ Fernando Miralles-Wilhelm, Ph.D. Associate Professor of Civil and Environmental Engineering, FIU
_____ Reinaldo Garcia-Martinez, Ph.D. Senior Research Scientist Applied Research Center, FIU	_____ James Englehardt, Ph.D. Professor of Civil Architectural and Environmental Engineering
_____ Chandra S. Pathak, Ph.D. Principal Engineer South Florida Water Management District	

GONZALEZ-RAMIREZ, NOEMI (Ph.D., Civil Engineering)
Simulating Flood Propagation (May 2010)
in Urban Areas using a Two-Dimensional
Numerical Model

Abstract of a dissertation at the University of Miami.

Dissertation supervised by Fernando Miralles-Wilhelm, Ph.D. and Reinaldo Garcia-Martinez, Ph.D.

No. of pages in text. (192)

A two-dimensional numerical model (RiverFLO-2D) has been enhanced to simulate flooding of urban areas by developing an innovative wet and dry surface algorithm, accounting for variable rainfall, and recoding the model computer program for parallel computing. The model formulation is based on the shallow water equations solved with an explicit time-stepping element-by-element finite element method. The dry-wet surface algorithm is based on a local approximation of the continuity and momentum equations for elements that are completely dry. This algorithm achieves global volume conservation in the finite element, even for flows over complex topographic surfaces. A new module was implemented to account for variable rainfall in space and time using NEXRAD precipitation estimates. The resulting computer code was parallelized using OpenMP Application Program Interface, which allows the model to run up to 5 times faster on multiple core computers. The model was verified with analytical solutions and validated with laboratory and field data. Model application to the Malpasset dam break and Sumacarcel flooding event show that the model accurately predicts flood wave travel times and water depths for these numerically demanding real cases.

To illustrate the predictive capability of the enhanced model, an application was made of the city of Sweetwater flooding in Miami-Dade County, FL caused by the Hurricane Irene. The simulation starts with dry bed and rainfall is provided by NEXRAD estimates. Integrating NEXRAD rainfall estimates, developing a novel dry-wet area algorithm and parallelizing RiverFLO-2D code, this dissertation presents a proof of concept to accurately and efficiently predict floods in urban areas, identifying future improvements along this line of research.

This thesis is dedicated to my mother, her belief in me and her support through my entire life has made this possible.

ACKNOWLEDGMENTS

I would like to thank Dr. Fernando Miralles-Wilhelm and Dr. Reinaldo Garcia-Martinez for their encouragement, as well as technical, financial and emotional support. They provided me with the necessary guidance throughout the completion of these studies. Their knowledge and high technical level have helped build my research experience and made me a better scientist.

I would like to thank Mrs. Marcia Steelman from the Department of Environmental Resources Management (DERM) of Miami Dade County for her collaboration in collecting the data used in this research.

I also wish to thank Dr. Chandra Pathak who facilitates the NEXRAD estimates used in this research and my committee members: Thanks to you all for your critical comments and suggestions which have been very helpful to the completion of this work.

I am indebted to the rest of my doctoral committee, Dr. David Chin, Dr. James Englehardt and Dr. Antonio Nanni, for their useful input and comments that contributed to and improved this doctoral thesis.

I would like to thank my family, especially my husband Bernardo, for their trust in my ability to reach a successful end to this long commitment.

TABLE OF CONTENTS

LIST OF FIGURES

LIST OF TABLES

LIST OF SYMBOLS

c	Characteristic water wave propagation velocity
CFL	Courant–Friedrichs–Lewy Number
Δt	Computational timestep
Δx	Length of the interval in x direction
$\in$	Selective lumping parameter
F	Depth of rainfall infiltrated into the soil since the beginning of rainfall
f	Infiltration rate
Fr	Froude Number
g	Gravitational acceleration
η	Water surface elevation
H	Water depth
H_{eff}	Effective water depth for storativity technique
Hmin	Minimum depth or tolerance value
i	Rainfall intensity
K_s	Saturated hydraulic conductivity
$\overline{M}$	Lumped mass matrix
$\widetilde{M}$	Selective lumping mass matrix
n	Manning's roughness coefficient
N_α	Standard linear interpolation functions for the triangle
θ	Soil moisture deficit

θ_i	Initial moisture content
θ_s	Saturated moisture content
q	Flux at the surface
ρ	Water density
S	Computational Speedup
t	Time
T_{sp}	Time required for a single processor
T_{pp}	Time required for p processors in multiprocessor systems
U	Vertically averaged velocities in x direction
V	Vertically averaged velocities in y direction
x	Horizontal Coordinate
y	Horizontal Coordinate
ψ_f	Average capillary suction in the wetted zone
Zw	Water elevation for storativity technique
Zb	Bed elevation for storativity technique

LIST OF ABBREVIATIONS

API	Application programming interface
ASCE	American Society of Civil Engineers
ASCII	American Standard Code for Information Interchange
Argus ONE	Argus Open Numerical Environments
CEDEX	Centre for Studies and Experimentation of PublicWorks, Spain
CFL	Courant–Friedrichs–Lewy condition
CHJ	Jucan River Basin Authority
CPU	Central processing unit
DERM	Department of Environmental Resources Management
DTM	Digital Terrain Model
EDF-LNH	National Hydraulic and Environment Laboratory
ERDC	Engineer Research and Development Center
F	Froude number
FESWMS	Finite-element surface-water modeling system
FFG	Flash Flood Guidance
HEC-HMS	Hydrologic Modeling System
HEC-RAS	Hydrologic Engineering Centers River Analysis System
IDW	Inverse distance weighting
IHRC	International Hurricane Research Center
LIDAR	Light Detection and Ranging

MODFLOW	. Modular three-dimensional finite-difference ground-water flow
MSQPE	Multiple Sensor Quantitative Precipitation Estimation
NEXRAD	Next Generation Radar
NMQ	National Mosaic and Quantitative Precipitation Estimate
NOAA	National Oceanic and Atmospheric Administration
NSSL	National Severe Storms Laboratory
NWSRFS	National Weather Service River Forecasting System
OpenMP	Open Multi-Processing
QPI	Quantitative Precipitation Information
RMA	Resource Management Associates
RMSE	Root mean square error
SFWMD	South Florida Water Management District
SMS	Surface water Modeling System
TMC	Texas Medical Center
VSTQPF	Very Short Term Quantitative Precipitation Forecasts
WES	Waterways Experiment Station
WFO	Weather Forecast Office
1D	One dimensional
2D	Two-dimensional

CHAPTER 1. INTRODUCTION

1.1 OVERVIEW

Flash floods are rapid inundations of geomorphic low-lying areas caused by intense rainfalls associated with storms, dam failure or hydraulic structure failure. They are rapidly varying catastrophic events that often involve discontinuities (hydraulic jump, traveling positive wave) and mixed flow regimes over complex topography requiring for their prediction in the use of special numerical techniques. Flash floods are distinguished from regular floods, in that they occur in short timescales. Most flash floods are caused by slow-moving thunderstorms that repeatedly move over normally dry areas, heavy rains from hurricanes and tropical storms or the sudden release of large volume of water due to the failure of water retention structures.

In the last century, world population has increased vertiginously, with the resulting occupation of vulnerable areas. As a consequence, the human and structural cost of natural disasters has increased over time (Perry, 2000). According to the National Oceanic and Atmospheric Administration (NOAA), flooding is the primary weather-related loss of life event in the U.S. between 1980 and 2005. The U.S. has sustained 67 weather-related disasters in which overall damages and costs reached or exceeded $1 billion each (NOAA, 2009). Tropical Storm Allison in 2001 was responsible for $5 billion in total damages, and about 50,000 damaged structures, and is considered the costliest natural disaster in Houston's history (Bedient et al., 2000 and 2003).

Hurricane Irene in 1999 produced 10 to 20 inches (255 to 510 mm) of rainfall in the Miami metropolitan area, causing urban flooding unseen since Tropical Storm Dennis in 1981.

Despite being only a Category 1 hurricane, Irene caused 8 indirect deaths and $800 million in damage across Florida, most of the damage and deaths occurred due to the torrential rain the storm caused. Flooding in the US causes an average of 120 deaths per year based on data over the last 30 years (NOAA, 2009). The type of floods that cause the greatest damage and loss of life are flash floods because they combined an unpredictable occurrence with large water velocities and depths.

Since flooding is the most common natural hazard that affects humans and properties around the world, in recent years the phenomenon has attracted the attention of scientists and engineers. They are focused on improving techniques that allow providing warning advisories to society to help to reduce the loss of human lives and costly infrastructure.

Flood warning systems are of fundamental importance to manage and mitigate flood related damages. The National Weather Service (NWS) maintains a warning system that detects hazardous weather and alerts the public to avoid potential flood hazards. Forecasting flash floods in urban areas due to heavy rainfall events is a challenging problem because it requires predicting the occurrence of the event as well as forecasting complex precipitation patterns involving both temporal and spatial distribution of rainfall.

1.2 The Traditional Approach to Model Flash Floods

Flash flood modeling is a useful tool for effective flood mitigation. Mathematical models are an essential tool to support studies involving prediction of complex flow patterns with

irregular banks and bathymetry, and overbank flood. One dimensional (1D) numerical models have been used to simulate flash floods for more than 25 years, and until recently, they were the only feasible way for its numerical simulation (Fread, et al., 1995). Unfortunately, the intrinsic assumptions of 1D models of uniform water surface elevation and average velocity on each cross-section do not provide the needed detail to design and analyze flooding on valleys that are not confined or where the floodway area is relatively flat. Two-dimensional (2D) hydrodynamic depth-integrated models are now warranted because of their computational efficiency and relative accuracy in distributing the flood volume. They also provide spatially variable velocities and water surface elevations, which better capture the flood wave attenuation and overland storage.

Some 2D models use the finite-difference method (Garcia & Kahawita, 1986) while others use finite volumes (Murillo et al., 2006) or finite-element methods (Hervouet J., 2007; Heniche et al., 2000). Generally, the use of rectangular grids common to the finite difference methods limits representation of complex floodway geometries. Boundary fitted coordinates finite difference models, finite volume models on unstructured grids, and finite element models improve the spatial resolution for complex flood routing simulations.

The application of finite volume methods using triangular unstructured meshes is expanding (Murillo et al., 2006; Murillo et al., 2006). Although these models are able to resolve irregular geometries, they may require some explicit treatment for oscillations arising from the source terms in the shallow water equations (García-Navarro & Vázquez-Cendón, 2000; Murillo et al., 2006). The finite-element method is a natural

choice for problems with a complex geometry because it allows using numerical meshes that adapt to irregular bed and banks, and is supported by a solid mathematical foundation (Froehlich, 2003; Donnell et al., 2005; Garcia & Kahawita, 1986; Garcia et al., 2006).

1.2.1 Rainfall Estimates and Flood Warning Advisories

The traditional approach to flood forecasting has been to use rainfall estimates from a number of rain gauges in addition to lumped hydrological models. An example of this approach is the National Weather Service River Forecasting System (NWSRFS) for using short and long range precipitation forecasts as input to ensemble stream flow prediction (Hudlow, 1988).

While rain gauges systems can provide valuable information, the distribution of rain gauges is usually limited and generally insufficient to provide enough resolution in a dense spatial and temporal coverage for accurate runoff prediction and flood warnings (Knebl et al., 2005; Ahrens & Maidment, 1999; Bedient et al., 2003).

It is well known that rain gauges have limited ability to detect rainfall with enough lead time needed for flood prediction and warning. Several authors have evaluated the accuracy of gage point rainfall values compared with radar precipitation (Vieux & Farajalla, 1996; Mimikou & Baltas, 1996; James et al., 1993) and it has been determined that the remote sensing is a useful tool in the determination of rainfall amounts, mapping flood extent (Horrit & Bates, 2002) and hence for validating flood models. A high-resolution radar station can monitor a total area of 200,000 km^2 (Johnson & Dallman, 1987). A dense network of gauges is required to reach the accuracy level that can be

produced by radar technology. Presently, radar based quantitative precipitation estimation (QPE) has become a crucial element in timely and accurate flash flood identification and warnings (Xu et al., 2007). Recent work on high resolution of remotely sensed data has encouraged modeling at a higher spatial resolution and the integration of high resolution DEMs than were previously practical (Bates & De Roo, 2000; Bates, 2004).

Radar Technology, based on the Doppler Effect discovered by the Austrian physicist, Christian Doppler in 1842, can predict both precipitation and wind. The radar emits a short pulse of energy, and if the pulse strikes an object, the radar waves are scattered in all directions. A small portion of that scattered energy is directed back toward the radar and it is then received during the listener period of the radar. The reflectivity is the amount of transmitted power returned to the radar receiver after hitting precipitation.

The establishment of the Next Generation Radar (NEXRAD) network in the US, which obtains raw reflectivity, radial velocity and spectrum width, permits estimating weather information (precipitation and wind) based upon returned energy. It has provided a significant contribution to supporting the NWS to detect and predict precipitation (Gourley et al., 2002; Zhang et al., 2004 and 2006; Hyannis et al., 2005; Seo et al., 2005). On the NEXRAD network, radial reflectivity is collected at 1km intervals from each radar station and at one degree radial resolution (Crum & Alberty, 1993; Baeck & Smith, 1998). NEXRAD information has significantly contributed to improve flash flood warnings (Committee to Assess NEXRAD Flash Flood Forecasting Capabilities, 2004; Fread et al., 1995).

NOAA through their Weather Forecast Office (WFO) uses flash flood guidance as criteria established for issuing flash flood watches and warnings (Stallings & Wenzel, 1995; Larson, et al., 1995). Flash Flood Guidance (FFG) is a method that provides estimation of the amount of rainfall for given durations that is required to produce flash flooding. These estimates are affected by soil moisture state and threshold runoff. The WFO issue the flood warning comparing the flash flood guidance and rainfall estimates from the radars. Soil type and moisture are used to predict how much rain is needed in a time period to produce flash flooding. If the estimated radar rainfall exceeds flash flood guidance for a grid, the grid is switched to a red color and a flash flood warning is issued for the area represented for the grid. If the estimated radar rainfall is slightly less than flash flood guidance, the grid would be shown as yellow or orange and a flash flood watch would be issued by NOAA. If the radar rainfall is considerable less than flash flood guidance, the grid would be green and no advisory would be issued. Figures 1 to 3 show a 1 hour, 3 hours and 6 hours FFG in Florida.

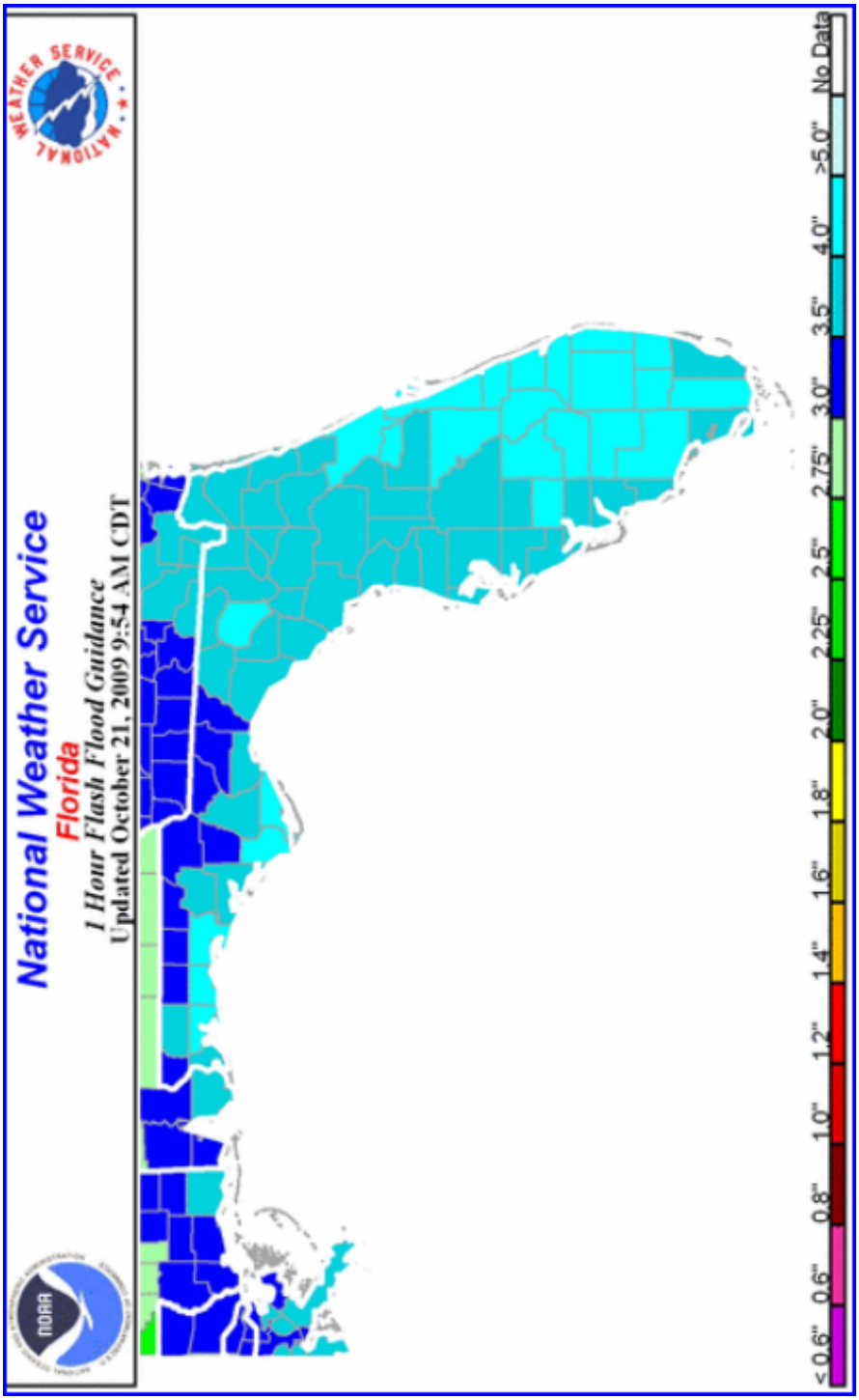

Figure 1. Flash Flood Guidance for 1 hour rainfall in Florida.

Source: www.srh.noaa.gov/rfcshare/ffg.php?duration=1&location=FL. October, 2009

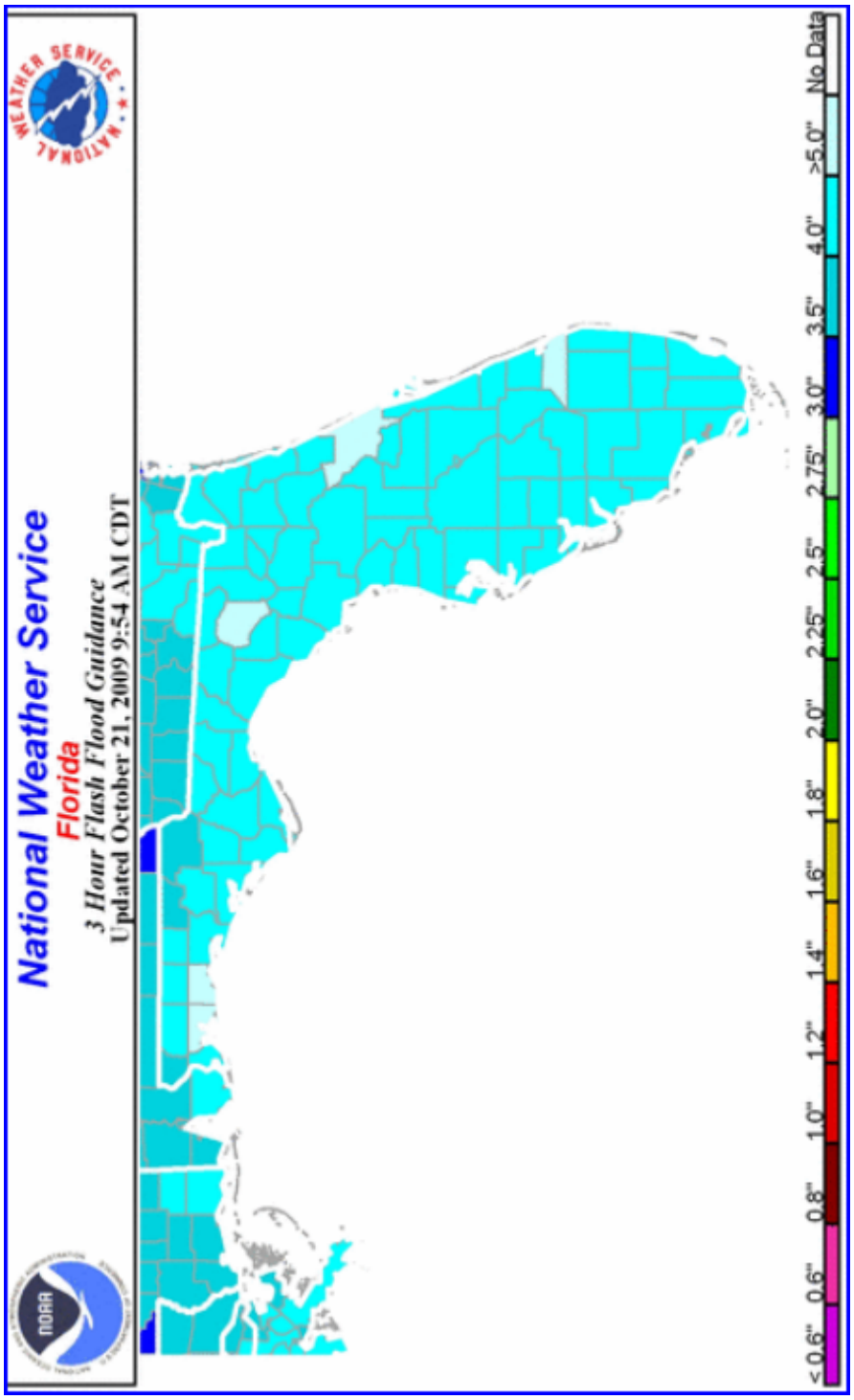

Figure 2. Flash Flood Guidance for 3 hours rainfall in Florida.

Source: www.srh.noaa.gov/rfcshare/ffg.php?duration=1&location=FL. October, 2009

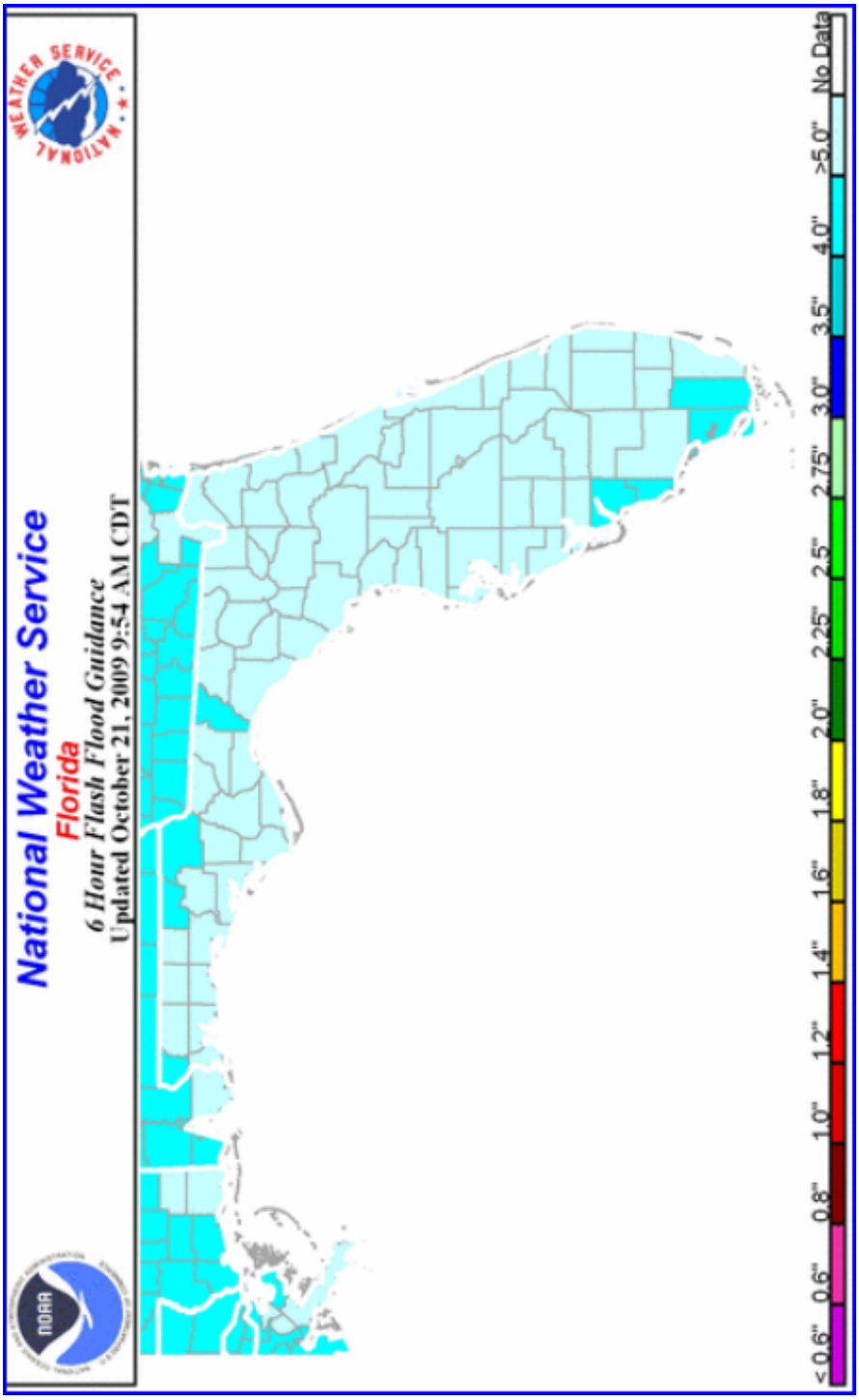

Figure 3. Flash Flood Guidance for 6 hours rainfall in Florida.

Source: www.srh.noaa.gov/rfcshare/ffg.php?duration=1&location=FL. October, 2009

Based on the analysis of the FFG, and NEXRAD estimated total rainfall, the National Weather Service issues urban flood advisories and flash flood warnings to the public. Figure 4 shows an example of the warning advisories issued by the NWS.

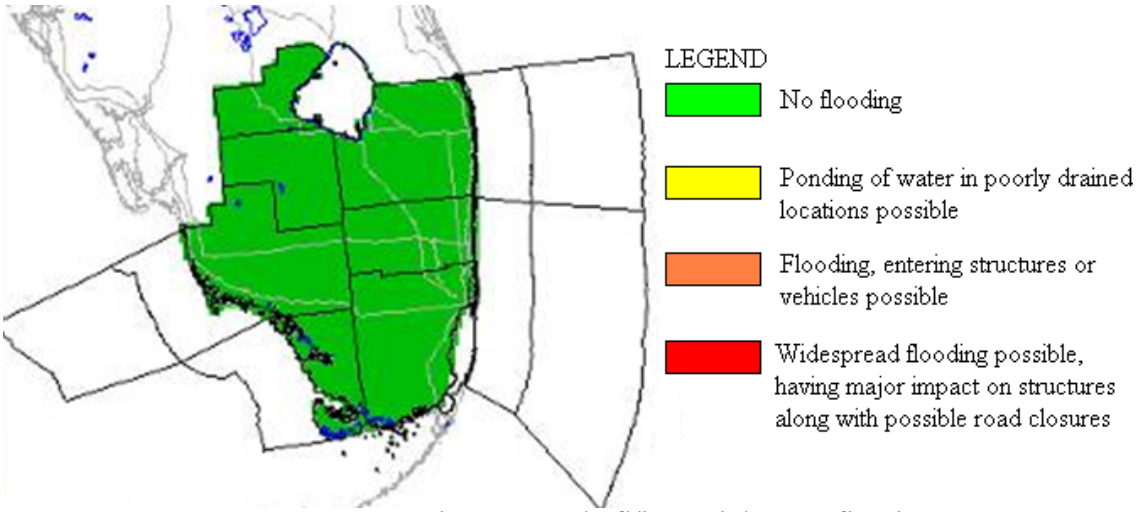

Source: www.srh.noaa.gov/mfl/hazards/?type=flood

Figure 4. Flood Impact Warning Advisory in South Florida.

NEXRAD also improved resolution (greater in detail and distance) of radar-based rainfall estimation and defined the three dimensional view of the weather. The National Mosaic and Quantitative Precipitation Estimate (NMQ) project (a joint initiative between the National Severe Storms Laboratory (NSSL), Federal Aviation Administration, National Weather Service/Office of Hydrologic Development, and other institutions) is evaluating operational use of high resolution 3D radar mosaics combined with satellite, model and surface observations to generate high resolution rain rates for use in hydrologic model assimilation and aviation applications. The objective of the NMQ is the generation of

Quantitative Precipitation Information (QPI) that includes Multiple Sensor Quantitative Precipitation Estimation (MSQPE) and Very Short Term Quantitative Precipitation Forecasts (VSTQPF) at high resolution for the monitoring and warnings of floods and flash floods and in support of comprehensive hydrology and ecosystem modeling.

1.2.2 Numerical Modeling Limitations

Although NWS releases urban flood advisories and warnings based on analysis of flash flood guidance and NEXRAD rainfall that provides detailed precipitation estimates, actual flooding also depends on the conveyance capacity of the urban drainage system, potential infiltration losses, impervious areas, topography, and flood mitigation works. To increase the accuracy and lead time of flood forecast and warnings, the NWS is very interested to implement techniques that would allow integrating radar rainfall estimates with hydraulic routing models that could simulate the complex flooding driven by the spatial characteristics of an urban watershed.

Runoff models are classified as either distributed-parameter models based on the resolution of partial differential equations or lumped-parameter models based on the resolution of ordinary differential equations. Lumped-parameter models consider entire sub-catchments on a watershed as single hydrologic elements, with the runoff characteristics described by one or more lumped parameters. This means that parameters in the mathematical model are a simplification of a physical system where variables that are spatially distributed fields are represented as single scalars instead. Distributed parameter models are applied for runoff processes on scales smaller than the size of the watershed. Distributed flood routing models can incorporate complex flow

parameterization that enhances flood volume distribution involving channel-floodplain exchange and urban features where different parameters to different elements can be assigned in the discretization, predicting the timing, spacing distribution and severity of the flood wave.

Most attempts recently made to link radar rainfall estimations to flood models to improve the accuracy of flood warnings have relied on lumped models. Neary et al., 2004 use radar-based precipitation to improve a spatially lumped continuous hydrologic model (HEC-HMS) in two sub basins of the Cumberland River basin in Middle Tennessee. Mimikou & Baltas, 1996 applied the HEC1F, an adaptation of the HEC-1 that employ the unit hydrograph theory and hydrologic routing to simulate flood-runoff in a basin using rainfall radar forecasting data. Townsend & Walsh, 1998 used NEXRAD rainfall estimates to generate potential inundation surfaces derived from regression models that related known flood elevations to river position and floodplain locations. Anderson, Chen, Kavvas, & Feldman, 2002 coupled the hydrologic model (Hydrologic Modeling System - HEC-HMS) with the MM5 mesoscale model to generate runoff forecasts. The HEC-HMS model does not account for the flooding details associated with flow distributed canals, streets and other urban features, and does not predict accurate flow depth and velocity in urban areas. The numerical prediction was not accurate in terms of matching the timing and magnitude of the peak inflow and total volume of runoff; it just provided more information to reservoir operators for flood control releases.

Bedient et al., 2003 developed a flood warning system for the Texas Medical Center (TMC) in Brays Bayou watershed in Houston, TX using NEXRAD rainfall estimates and

the HEC-HMS model to estimate flow rates and threshold runoff that are indicators of maximal sustainable surface runoff for a given watershed, and are essential component of the actual flash flooding warning systems in one-dimensional (1D) channels. Real-time rainfall basin averaging for lumped modeling over both space and time was accomplished by incorporating GIS technology. A HEC-1 hydrologic model was used to develop a nomograph of flows to convert these real-time rainfall intensities and durations to peak flows in the channel at the point of interest

Knebl et al., 2005 presented a regional scale flood model that integrates NEXRAD rainfall estimates with HEC-HMS hydrological model and Hydrologic Engineering Centers River Analysis System model (HEC-RAS, 1D model). The model, however, does not incorporate many urban flood conveyances, obstruction and storage features because the 1D approach ignores flooding components that are intrinsically two-dimensional, e.g. streets and buildings that affect flow patterns and flood depths. Whiteaker et al., 2006 extended Knebl et al., 2005 adding GIS capabilities but kept their 1D flood modeling method. Fulton & Seo, 2000, Smith, et al., 2003 and Reed, et al., 2007 have made significant contributions to increase the accuracy of weather warnings and evaluated the use of precipitation forecast using simplified distributed hydrological models at the basin scale.

Also, several authors have coupled novel technologies as Geographical Information Systems (GIS), remote sensing and real time information to improve the prediction of flooding results for hydrometeorological events usually in non-urban areas (Bates, 2004; Bedient et al., 2003; Vieux, 2005; Bedient et al., 2000; Anderson, et al., 2002).

Whiteaker et al., 2006 converts a map of rainfall data to a flood inundation map, using HEC-HMS and HEC-RAS by establishing information exchange points at which time series are passed between models and GIS. Other authors as Carpenter et al., 1999 use NEXRAD rainfall estimates, GIS and DEM to develop a methodology for determining threshold runoff during a given time period over a basin that is just enough to cause flooding at the outlet of the draining stream.

The progressive improvement of computing resources and the increasing availability of spatial data are rapidly overcoming the advantages of a lumped and are promoting the alternative approach to runoff prediction through distributed modeling.

The distributed modeling approach is often based on numerical integration of the shallow water flow equations (Zhang & Cundy, 1989; Vieux, 2005; Ogden & Julien, 1993). The use of distributed hydrologic model offers the potential to improve upon current Flash Flood Guidance (FFG) procedures which are based on lumped river (Reed et al., 2004, 2006 and 2007).

Consideration of the urban watershed's characteristics would permit predicting where flooding would occur with a spatial and temporal detail that is not provided in the warning advisories that are presently issued by Federal Agencies. Given that the response time of a flash flood event is usually short, the use of forecast precipitation radar rainfall estimates in conjunction with an efficient 2D flood model would improve warning lead-times and allow calculating more reliable flood warnings, and contribute to mitigate flooding damages.

1.3 Modeling Wetting and Drying Conditions

When solving the shallow water equations over terrain with positive and negative slopes, appearance of wet and dry areas may generate significant numerical error that affect the stability of the numerical solution.

Many 2D models do not allow starting the simulations with a dry bed (Froehlich, 2003; Donnell et al., 2005).

The lost or the gain of water in the mass balance is evident due to the presence of elements partially wet that are considered dry elements for the modeling process, and vice versa. Stability and mass balance problems may generate large errors that often produce negative water depths artificially high velocities and severe volume conservation errors (Brufau et al., 2002; Brufau et al., 2004).

Several techniques can be found in the literature to address the drying-wetting problem including adjustment of the boundary conditions (Akanbi & Katopodes, 1988), modifications of the governing equations in the very shallow areas (Meselhe & Holly, 1993), and using adapting boundary or deformable mesh (Lynch & Gray, 1980; Defina 2000; Defina et al., 1994; Tchamen & Kahawita, 1994 and 1998; Kramer et al., 2001).

The adapting boundary technique is a Lagrangian approach for the definition of the mesh in the domain, where it is continuously generated and calculated to adapt the wet domain in the simulation. This approach leads to very complicated mesh generation algorithms. It has not been extensively applied for real applications.

The two other techniques implies the use of a fixed Eulerian mesh, where the model equations have to be able to identify which areas are wet in the entire domain. The

issue can be handled by implementing novel techniques to deal with the hydrodynamics of the partially wet elements when a fixed computational grid along the total time of simulation is used (Kawahara & Umetsu, 1986; Umetsu & Matsumoto, 1998; Matsumoto et al., 2002; Nihoul & Djenidi S., 1995; Li & Zhan, 1988; Froehlich, 1989). All these techniques are based in a simplified numerical treatment of the wetting and drying boundaries that remove or improve many of the problems associated with wetting and drying problems (Defina, 2000; Bates & Hervouet, 1999; Hubbard & García-Navarro, 2000). A detailed review analyzing the numerical aspects of these concerns is given by Bates & Hervouet, 1999 and Tchamen & Kahawita, 1998.

The efforts are being recently concentrated in the improvement and evaluation of these techniques to control the loss of mass and the correct representation of the moving boundaries in the simulation process.

The necessity of a robust and mass conservative drying–wetting algorithm that permits modeling regions that start with a dry bed, and works adequately when large areas get dry and flood during the unsteady simulation, is imperative in this research.

1.4 Discussion of Hydrodynamics Models

A considerable number of models have been developed to simulate free-surface water flow. However, due to physical and mathematical difficulties (Zhang & Cundy, 1989), some numerical schemes are not reliable when applied to overland flow. The difficulties come from the following issues:

- The overland flow is very shallow and because of that, very small magnitude of numerical oscillations will result in a negative flow depth, thus causing instabilities in the numerical solution.
- Ground surface topography and variation of local slope have a large impact causing significant disturbance to the flow.
- The shear stress induced by bed roughness is large in relation to the other fluid forces for shallow water depths, causing numerical difficulties and instabilities.
- Rainfall and infiltration represent significant mathematical source and sink terms in the shallow water equations.
- Numerical simulation of overland flows over complex topography with large dry areas often leads to instabilities in the model. The presence of highly unsteady wet-dry fronts, the extremely small water depths and the high bed friction stresses may cause a lack of accuracy and instabilities if the numerical scheme used to solve the shallow water equations is not robust and accurate. Also water is lost or gained during the computation due to numerical instabilities.

A hydrodynamic modeling code that has been developed and is maintained by the Federal Highway Administration (Froehlich, 1989; Lee & Froehlich, 1989) is the FESWMS model. It is a two-dimensional vertically averaged flow model publicly available. Its current version is 3.22 (Froehlich, 2003). FESWMS is a computer model that simulates hydrodynamics supporting subcritical and supercritical flows. It is based on the time-dependent unsteady two-dimensional shallow water equations using an implicit numerical scheme to solve them. FESWMS applies the classical finite element

method based on triangular or quadrilateral element meshes that can be refined over regions of interest where higher resolution is needed.

The numerical model is not able to start the simulation with a dry mesh; an initial depth should be imposed to start the simulation, where all elements on the mesh are submerged. FESWMS provides an algorithm to dynamically handle drying beds based on the concept of element storativity, by which partially dry elements can be retained in calculations. The user needs to input 3 parameters that have to be tuned to each specific application. Users have reported program divergence and unstable results when parts of the mesh dry out on the receding phase of a hydrograph.

FESWMS model results have been compared with field measurements. However, there does not seem to have passed a code verification and validation process as recommended by ASCE Task Committee on Model Verification and Validation (Wang et al., 2008).

Another hydrodynamic model is the RMA2. RMA2 is two-dimensional depth averaged finite element model that computes water surface elevations and horizontal velocity components for subcritical, free-surface flow fields. The model was originally developed by Water Resources Engineers, for the Walla District, Corps of Engineers, in 1973 (Norton et al., 1973; Donnell et al., 2005) The current version is dated 2005 and is maintained by the U.S. Army Corps of Engineers. RMA2 applies the finite element method to solve the shallow water equations using an implicit numerical scheme based on triangular or quadrilateral element meshes that can be refined over regions of interest where higher resolution is needed. RMA2 computer simulation times can become considerably large when using a large number of elements due to the iterative method

used to solve the non-linear algebraic system of equations resulting from the finite element discretization.

RMA2 initial conditions require that all elements on the mesh are submerged. In RMA2 the "marsh porosity" concept allows elements to transition gradually between wet and dry states. However, the RMA2 Users Guide (Donnell et al., 2005) on page 112 indicates that the model is prone to instabilities when parts of the mesh dry or some wet elements are surrounded by dry elements. The model becomes unstable when large areas of the mesh are dry.

A Code verification process as recommended by ASCE Task Committee on Model Verification and Validation (Wang et al., 2008) does not seem to have been performed.

RiverFLO-2D is the model that has been selected for this research. RiverFLO-2D is a two-dimensional model based in the hydrodynamic shallow water equations that describe the free surface flow with a depth-averaged approximation.

The following characteristics were evaluated to select the RiverFLO-2D over FESWMS and RMA2:

1. RiverFLO-2D is capable of handling subcritical as well as supercritical flows.
2. RiverFLO-2D uses an explicit numerical scheme, so the numerical time step has a theoretical limitation (Courant–Friedrichs–Lewy condition, CFL). However, RiverFlO-2D uses a four-step time stepping scheme that permits longer time steps than other explicit finite element models, not requiring the assembly of the global matrices nor simultaneous solution of the global algebraic system (Garcia

et al., 2006). This is an important capability to take into the consideration for the simulation of flash floods that require short computational times.

3. RiverFLO-2D code was written in FORTRAN 95 following a strict structured programming method. Also, the solution method involves element by element matrix assembly and consequently, the mesh node numbering does not impact memory requirements or computer time, while facilitating code parallelization. RiverFLO-2D was programmed following a sequential structure that facilitates the implementation of OPENMP instructions without rewriting the original code.

1.5 Research Gaps

It is widely recognized that the hydrometeorological data analysis and the distributed hydraulic modeling are the fundamental components in the improvement of the prediction of flash floods and inundations. Despite of the considerable progress that has been achieved over the past few years with the computational and technology development in this topic, there are several gaps that need to be addressed to improve flash flood prediction.

The main gaps that have been identified include:

1. Lumped models (e.g. HEC-HMS, etc.) that commonly have been used for flash flood simulations are not able to capture the water flow behavior in complex terrain environments.

2. Most two-dimensional distributed numerical models are not capable to successfully handle the dry bed condition over the entire numerical domain that is the more frequent initial condition in the simulation of floods in urban areas.
3. Rainfall estimates from NEXRAD have not been commonly integrated with two dimensional distributed models to produce forecast flooding advisories and to simulate in detailed the rainfall-runoff process.
4. Two-dimensional distributed numerical models capable of accounting for urban features in the numerical simulation frequently require large runtimes for each simulation due to the need of large spatially distributed quantities of data and the resolution of the governing equations with a non efficient solution method.

1.6 Research Objectives and Specific Contributions

To address the gaps listed above, this research uses NEXRAD rainfall estimates with an enhanced version of a two dimensional physically-based hydrodynamic distributed numerical model (RiverFLO-2D) to simulate flood in urban areas.

This dissertation provides three novel contributions:

1. Development of numerical dry-wet bed surface algorithm that improves previous methods, providing significantly stable solutions even with large dry mesh areas and conserving volume. This capability is fundamental when modeling flooding where the bed is initially dry, then the bed gets flooded as the inundation advances over the terrain and it dries again as the wave recedes.

2. Implementation of the modified Green-Ampt infiltration method developed by Eggert, 1976 by including infiltration abstraction as a source term in the continuity equation.
3. Integration of NEXRAD rainfall estimates in a 2D free-surface hydraulic model to simulate flooding in nearly real time, and
4. Parallelization of the 2D code using OpenMP application interface, providing substantial computational performance improvements, which is a key factor for operational application of 2D flood models.

The enhanced RiverFLO-2D model includes the capacity to acquire the input data provided by NEXRAD rainfall estimates, and using this information it is able to generate depth and velocity detailed maps for flooding events accounting for the effects of the urban details on the inundation.

The resulting modeling tool has been verified and validated with analytical solutions, simplified test cases, laboratory experiments and comparisons against real cases where field data is available.

CHAPTER 2. MODEL DEVELOPMENT

This chapter contains the conceptual model, governing equations, numerical procedure and implemented techniques proposed in the dissertation.

2.1. RiverFLO-2D Model

The RiverFLO-2D is based on the Shallow Water Theory that describes a free surface flow where the vertical length scale (depth) is much smaller than the horizontal length scale. The equations are derived depth integrating the Navier-Stokes equations, where vertical velocities are assumed negligible and the velocities are uniform through the flow depth. Vertically integrated continuity and momentum flow equations are written as follows:

$$\frac{\partial \eta}{\partial t} + \frac{\partial UH}{\partial x} + \frac{\partial VH}{\partial y} = 0 \tag{1}$$

$$\frac{\partial U}{\partial t} + U\frac{\partial U}{\partial x} + V\frac{\partial U}{\partial y} + g\frac{\partial \eta}{\partial x} + \frac{\tau_{b_x}}{\rho H} = 0 \tag{2}$$

$$\frac{\partial V}{\partial t} + U\frac{\partial V}{\partial x} + V\frac{\partial V}{\partial y} + g\frac{\partial \eta}{\partial y} + \frac{\tau_{b_y}}{\rho H} = 0 \tag{3}$$

Where:

x and y are the horizontal coordinates,

t is the time,

η is the water surface elevation,

H is the water depth,

U and V are the depth averaged velocities in x and y directions respectively,

ρ is the water density,

n is the Manning's roughness coefficient, and

g is the gravitational acceleration.

$$\tau_{bx} = \frac{gn^2 U\sqrt{U^2+V^2}}{H^{4/3}} \tag{4}$$

$$\tau_{by} = \frac{gn^2 V\sqrt{U^2+V^2}}{H^{4/3}} \tag{5}$$

Applying the Galerkin Weighted Residual Method to the shallow water equations using three-node triangular elements with linear spatial interpolation; we obtain the following set of ordinary differential equations:

$$M^e_{\alpha\beta}\frac{d\eta_\beta}{dt} + X^e_{\alpha\beta\gamma}U_\beta H_\gamma + Y^e_{\alpha\beta\gamma}V_\beta H_\gamma = 0 \tag{6}$$

$$M^e_{\alpha\beta}\frac{dU_\beta}{dt} + X^e_{\alpha\beta\gamma}U_\beta U_\gamma + Y^e_{\alpha\beta\gamma}V_\beta U_\gamma + gR^e_{\alpha\beta}\eta_\beta + G^e_f M^e_{\alpha\beta}U_\beta = 0 \tag{7}$$

$$M^e_{\alpha\beta}\frac{dV_\beta}{dt} + X^e_{\alpha\beta\gamma}U_\beta V_\gamma + Y^e_{\alpha\beta\gamma}V_\beta V_\gamma + gS^e_{\alpha\beta}\eta_\beta + G^e_f M^e_{\alpha\beta}V_\beta = 0 \tag{8}$$

Where:

$$M^e_{\alpha\beta} = \int N_\alpha N_\beta d\Omega \tag{9}$$

$$X^e_{\alpha\beta\gamma} = \int N_\alpha N_\beta \frac{\partial N_\lambda}{\partial x} d\Omega \tag{10}$$

$$Y^e_{\alpha\beta\gamma} = \int N_\alpha N_\beta \frac{\partial N_\lambda}{\partial y} d\Omega \tag{11}$$

$$R^e_{\alpha\beta} = \int N_\alpha \frac{\partial N_\beta}{\partial x} d\Omega \tag{12}$$

$$S^e_{\alpha\beta} = \int N_\beta \frac{\partial N_\beta}{\partial y} d\Omega \tag{13}$$

$$G^e_f = \frac{gn^2\sqrt{\overline{U^2} + \overline{V^2}}}{\overline{H}^{4/3}} \tag{14}$$

$$\overline{H} = \frac{1}{3}\sum_{j=1}^{3} H_j \tag{15}$$

$$\overline{U} = \frac{1}{3}\sum_{j=1}^{3} U_j \tag{16}$$

$$\overline{V} = \frac{1}{3}\sum_{j=1}^{3} V_j \tag{17}$$

And N_α are the standard linear interpolation functions for the triangle.

The set of equations above can be rewritten as:

$$M^e_{\alpha\beta}\frac{dU_\beta}{dt} = -F(U_\beta) \tag{18}$$

Where:

U is the vector of unknowns,

F is a vector that includes the right hand terms in the equations.

RiverFLO-2D implements a four-step time stepping scheme that permits longer time steps than previous explicit finite element models, as the scheme presented by Topper & Kawahara, 1978 for a two-dimensional shallow water model based on a two-step scheme for wave propagation. The proposed time-stepping scheme does not require the assembly of the global matrices nor the simultaneous solution of the global algebraic system usually required in implicit finite element methods. The solution method is explicit and consequently, the mesh node numbering scheme does not impact memory requirements nor computer time, making the solution of large problems feasible in relatively small computers.

In order to solve equation 18, RiverFLO-2D uses a fourth-order fractional step decomposition of the Taylor series expansion for *U*.

First step

$$\overline{M}_{\alpha\beta} U_{\beta}^{n+1/4} = \widetilde{M}_{\alpha\beta} U_{\beta}^{n} - \frac{\Delta t}{4} F_{\alpha}(U^{n}) \tag{19}$$

Second step

$$\overline{M}_{\alpha\beta} U_{\beta}^{n+1/3} = \widetilde{M}_{\alpha\beta} U_{\beta}^{n} - \frac{\Delta t}{3} F_{\alpha}(U^{n+1/4}) \tag{20}$$

Third step

$$\overline{M}_{\alpha\beta} U_{\beta}^{n+1/2} = \widetilde{M}_{\alpha\beta} U_{\beta}^{n} - \frac{\Delta t}{2} F_{\alpha}(U^{n+1/3}) \tag{21}$$

Fourth step

$$\overline{M}_{\alpha\beta}U_{\beta}^{n+1} = \tilde{M}_{\alpha\beta}U_{\beta}^{n} - \Delta t F_{\alpha}(U^{n+1/2}) \tag{22}$$

Where:

$\overline{M}$ is the lumped mass matrix, that is defined as the one having zeros for all of the off-diagonal terms. It is a scheme to reduce the computer resources required for a solution.

$\tilde{M}$ is the selective lumping mass defined as follows:

$$\tilde{M}_{\alpha\beta} = \in \overline{M}_{\alpha\beta} + (1 - \in)M_{\alpha\beta} \tag{23}$$

Where:

$\in$ is the selective lumping parameter that may vary in the interval [0, 1].

It has been found (Kawahara et al., 1982) that the use of selective lumping reduces excessive numerical damping as compared with the use of pure lumped mass matrix (Kawahara et al., 1978).

According to Kawahara et al., 1982, in a practical computation, it is necessary to employ $0.95 > \in > 0.8$. From the Kawahara's numerical experiments, a selective lumping parameter $\in$ within these limits does not give rise to erroneous numerical damping.

To evaluate the stability of the numerical scheme, the CFL condition is used for the generation of the numerical solution. CFL is a necessary condition for the convergence of the solution of the hyperbolic shallow water partial differential equations when an explicit scheme is used. As a consequence, the time step must be less than a certain value; otherwise the simulation will become unstable.

The general CFL condition is usually calculated using the advection terms that is basically the hyperbolic part of the partial differential equation as follow:

$$CFL = \frac{u\Delta t}{\Delta x} \tag{24}$$

Where:

u is the horizontal velocity,

Δt is the time step,

Δx is the length of the interval.

However, when a stability analysis is performed to the selective lumping scheme, the resulting CFL indicates that the four-step scheme has a stability limit two times larger than the two-step scheme and 1.33 larger than the three-step scheme. The CFL condition for the four-step scheme after a stability analysis is (Garcia et al, 2006):

$$CFL = \frac{\Delta t}{\Delta x} \leq \frac{4}{3}\left(\frac{3}{gh}\right)^{1/2}\left(1-\in\right)^{1/2} \tag{25}$$

Where:

h is the water depth,

$\in$ is the selective lumping parameter that may vary in the interval ([0, 1]).

RiverFLO-2D uses triangular meshes that can be refined over regions of interest. The mesh is generated by a link with Argus ONE software (Argus Interware, 2009) that allows for selective and local high resolution refinement. Argus ONE is a GIS based pre- and post-processor software also used by other models like USGS's MODFLOW.

The numerical model generates ASCII output files for time-dependent velocity fields, water surface elevations, Froude number, etc.

The model has no intrinsic limitations on mesh size and can be refined along particular features to improve model accuracy. Since the FORTRAN 95 code has been made available through an agreement, and knowing that the formulation has been extensively reported in the literature (Garcia & Kahawita, 1986; Garcia et al., 2006), extension to add new features has been possible.

A limitation in the numerical modeling is represented for the structural error of the model. How the model represents the physical phenomena using mathematical equations and simplifications of the real life physical phenomena introduce a source of error that is very complex to evaluate.

2.2. RiverFLO-2D Model Enhancements

2.2.1 Implementation of NEXRAD Rainfall Estimates

Integrating high resolution weather data with new technologies into numerical models is fundamental to generate better flooding predictions to the general public, decision makers, and industry. To enable major prediction capabilities for floods, the gap between the collecting data systems in the understanding of hydrology processes and the use of them in the numerical models must be addressed.

The ability to enhance the numerical predictions will require higher-quality satellite observations, and one of the most important points, their effective assimilation into the current numerical models, and better communication between data producers and user communities.

The capability to include spatial and temporal distributions of rainfall and evapotranspiration estimates in the numerical simulation was added to the enhanced RiverFLO-2D.

NEXRAD rainfall estimates are interpolated from their original coordinate grid system (e.g. square cells 2km x 2km) to the coordinate systems of the finite element mesh by using Inverse Distance Weighting (IDW) interpolation method. One rainfall interpolated estimate is set for each element on the numerical mesh (Bedient et al., 2008).

The following RiverFLO-2D subroutines were modified to enhance model capability:

1. SUBROUTINE INPUT, this subroutine uses the interpolated NEXRAD rainfall estimates for each element in the numerical mesh. This subroutine was modified to include two different kind of files in the simulation. A file with rainfall data variable in time, where the input parameters are the number of data sets, and for each dataset the time at wich rainfall occurs, and the rainfall and evapotranspiration for each time. The other type of file is the one that corresponds with rainfall estimates variable in space and time. The file reads the number of rainfall datasets, and for each dataset the time at which the rainfall occurs, and the number of elements in the numerical mesh that have rainfall data different than zero in each time. Later for each time a list containing the element, the rainfall data and evapotranspiration is read.
2. SUBROUTINE RAINEVAPSOURCE, this subroutine was modified to linearly interpolate the rainfall estimates read in the subroutine input for each simulation time. The subroutine identifies for each time of simulation the two dataset times that contains it, and then the rainfall and evapotranspiration data for those

adjacent datasets is interpolated in time for the simulation time. This procedure has been included for the case of rainfall estimates variable in time and/or space.

3. SUBROUTINE FEM_SWE, this subroutine was modified to include the rainfall for each element in the continuity equation, as a source term that contribute to the equation in each timestep of the numerical simulation.

It is important to highlight the existence of errors due to the sensitivity of the numerical results to the interpolation method used to calculate the NEXRAD estimates. The uncertainty in the numerical results for different interpolation methods of the NEXRAD estimates can affect the results of the urban flooding. A detailed post flooding data has to be collected as well as NEXRAD estimates in a smaller grid has to be used to be able to performance an adequate sensitivity and uncertainty analysis of the RiverFLO-2D numerical results for the NEXRAD rainfall estimates.

2.2.2 Numerical Treatment of Dry Bed Condition

An algorithm capable of preserving positive values of water depths under complex characteristics of the terrain and fast flooding events with high velocities that may include entire dry areas has been designed and implemented in the RiverFlo2D.

Before the final wet and dry method was designed and integrated with the model, several wet and dry techniques in the finite element context were analyzed. Those techniques are enumerated as follows:

1. The first technique usually named *Storativity* is based on the wetting and drying approach developed by the Federal Highway Administration of the U.S.

Department of Transportation and used in the FESWMS two dimensional depth-averaged flow and sediment transport model.

The Storativity technique replaces the water depth $H = z_w - z_b$ for an effective water depth (H_{eff}) that depends of the bed storage coefficients λ_b in each timestep and for each node in the domain. Therefore, water depths are modified for the wet-dry technique. The changes in the water depths for each node are evaluated by using the concept of the element storativity (λ_b), where some coefficients are calculated as ratios of changes in stored water per unit element area with respect to changes in water elevation (Froehlich, 2003).

2. The second wetting-drying technique is the algorithm implemented by Umetsu & Matsumoto, 1998 that defines the location of the water boundaries in the mesh by applying a series of modifications to the partially wet elements. The modification that this technique carries out basically can be summarized as a new transient velocity that is imposed on dry nodes inside partially wet elements. The imposed transient velocity is the average velocity of wet nodes present in the element for each time step**.**

3. Kawahara & Umetsu, 1986 wet and dry approach include the modification of velocities and depths for partially wet elements. Velocities are specified equal to zero and the depths remained equal to the value that comes from shallow water theory for wet nodes of the element. Velocities as well as the depths are set equal to zero for dry nodes in the element.

Although the Kawahara & Umetsu, 1986 and Umetsu & Matsumoto, 1998 techniques conserve the water mass in the numerical problem, spurious velocities are present when large areas of the domain are completely dry. Therefore, a novel wet and dry technique was designed and implemented in the numerical model.

RiverFLO-2D drying and wetting algorithm is based in an improved version from the one originally proposed by Kawahara & Umetsu, 1986 and later by Umetsu & Matsumoto, 1998 in the finite element context. In this new approach the finite element mesh is generated so that it will cover the entire region that is expected to be flooded. The wetting-drying algorithm is as follows:

- At the beginning of each time-step all elements are evaluated to see if they are wet or dry. A completely dry element is defined when all nodal depths are less than a user defined minimum depth or tolerance value H_{min}, that can be zero. A partially dry element has at least one node, where depth is less than or equal to H_{min}.
- If the element is completely dry instead of the governing equations (continuity and momentum, see equations 1 to 3), the following equations are solved:

$$\frac{\partial \eta}{\partial t} = 0 \tag{26}$$

$$\frac{\partial U}{\partial t} = 0 \tag{27}$$

$$\frac{\partial V}{\partial t} = 0 \tag{28}$$

Equations 26 to 28 are discretized and solved using the finite element procedure described above, where the terms that contain the spatial derivatives and the temporal derivative in the governing equations are set equal to zero for the current element and time step. In this way, the collaboration of the dry element to the finite element mass matrix is null for the time step. The dry elements make no contribution to the momentum equation. Also, for dry elements, velocity components are set to zero for all nodes on the element.

- If an element is partially dry, the full equations are solved and velocity components are set to zero for all nodes on the element.
- Water surface elevations are not modified for dry elements.

The implementation of the wet and dry technique allows the RiverFLO-2D to initiate calculations assuming a dry bed everywhere in the model domain and the flow can enter from the upstream condition or from rainfall and advance over the dry bottom, maintaining volume conservation.

2.2.3 Green-Ampt Simplified Approach

Infiltration begins when precipitation reaches the land surface, and the runoff over the land begins when the precipitation rate exceeds the infiltration rate. A Green-Ampt approximation has been applied to estimate the amount of water loss because of infiltration into the soil matrix (Eggert, 1976; Li et al., 1976; Sabol et al., 1991).

Green & Ampt, 1911 proposed the simplified sketch of infiltration show in Figure 5. The basic assumption behind the Green & Ampt equation is that water infiltrates into (relatively) dry soil as a sharp wetting front.

The wetting front is a sharp boundary dividing soil with moisture content θ_i below from saturated soil with moisture content η above. The wetting front has penetrated to a depth H in time t since infiltration began. Water is ponded to a small depth on the soil surface.

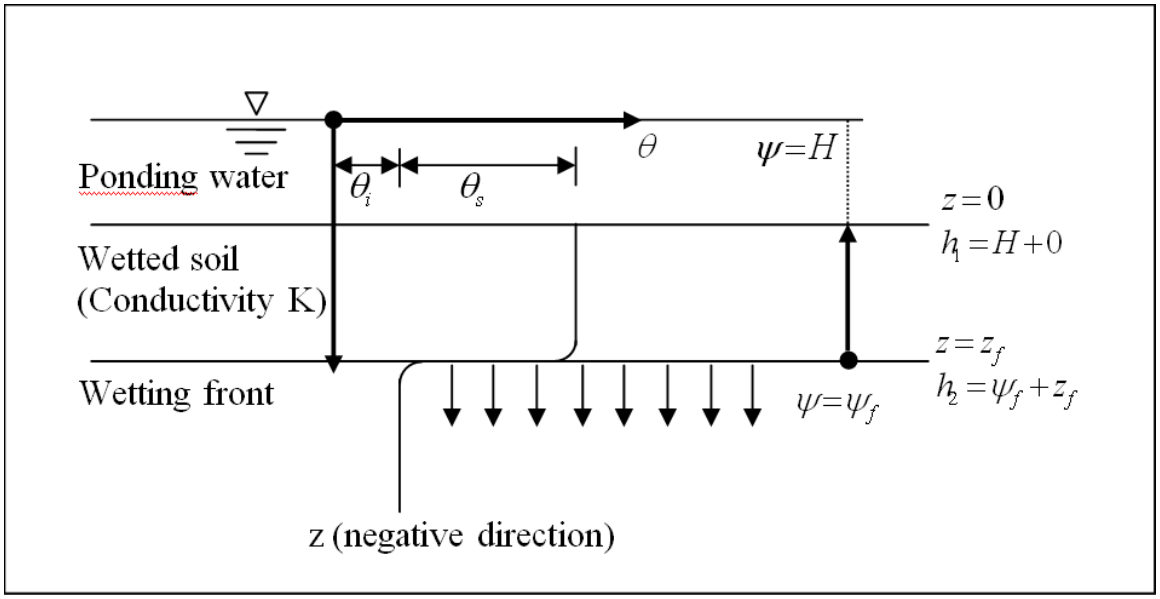

Figure 5. Variables in the Green-Ampt Infiltration Model where the vertical axis is the distance from the soil surface and the horizontal axis is the moisture content of the soil in the negative direction.

The derivation of the physical Green-Ampt approach starts from Darcy's equation as can be seen in the following expression.

$$q = -K_s \frac{dh}{dz} = -K_s \frac{h_2 - h_1}{z_2 - z_1} = -K_s \frac{(\psi_f + z_f) - (H + 0)}{z_f - 0} = -K_s \frac{\psi_f + z_f - H}{z_f}$$

(29)

Where,

H = the depth of ponding (L),

K_s = saturated hydraulic conductivity (L/T), that relates groundwater velocity to the hydraulic gradient and it is described as the volume of water that will flow through a unit soil column in a given time,

q = flux at the surface (L/T) and is negative,

ψ_f = suction at wetting front (negative pressure head), a measure of the combined forces that bind the water molecules to solid walls and the cohesive forces that attract water molecules to each other,

θ_i = initial moisture content (dimensionless), and

θ_s = saturated moisture content (dimensionless), the ratio of the volume of water to the total volume of a unit of porous media.

The following assumptions are made in the Green & Ampt formulation:

1. As rain continues to fall and water infiltrates, the wetting front advances at the same rate with depth, which produces a well defined wetting front.
2. The volumetric water contents remain constant above and below the wetting front as it advances.

3. The soil water suction immediately below the wetting front remains constant with both time and location as the wetting front advances.

Flux at the surface is equal to the infiltration rate f, at which water enters the soil surface (*L/T*). It is the first derivative of *F* with respect to time *t* in *hr*.

$$q = f = \frac{dF}{dt} \tag{30}$$

Substituting into Darcy's equation gives the following equation.

$$q = f = \frac{dF}{dt} = -K_s\left(\psi_f + \frac{F}{\theta_s - \theta_i} - H\right)\frac{\theta_s - \theta_i}{F} \tag{31}$$

Assume *H* is small relative to the other terms and the previous equation simplifies to the Green and Ampt infiltration rate equation.

$$\begin{aligned} f &= \frac{dF}{dt} = K_s\left(1 + \frac{\psi_f \theta}{F}\right), \quad for \quad f < i \\ f &= i, \quad for \quad f > i \end{aligned} \tag{32}$$

where,

f = infiltration rate (*L/T*), i = rainfall intensity (*L/T*),

θ = soil moisture deficit (dimensionless), equal to effective soil porosity times the difference in final and initial volumetric soil saturations, and

F = depth of rainfall that has been infiltrated into the soil since the beginning of rainfall (*L*).

The system of equations (32) is implicit with respect to f which impact the computational time of the solution. A simple method of solving the Green-Ampt one-dimensional

infiltration equation developed from Darcy's law has been used and tested for practical applications in this research.

The explicit solution is an approximation obtained by employing a power series expansion of the system of equations (32) and truncating all but the first two terms of the expansion (Eggert , 1976; Sabol et al., 1991). The simplified solution (Li et al., 1976) is presented below:

$$F = -0.5\left(2F - K_s\Delta t\right) + 0.5\left[\left(2F - K_s\Delta t\right)^2 - 8K_s\Delta t\left(\theta\psi + F\right)\right]^{1/2} \tag{33}$$

The average infiltration rate is:

$$f = \frac{\Delta F}{\Delta t} \tag{34}$$

The three infiltration parameters present in equation (33) are functions of soil characteristics, ground surface characteristics, and land management practices. The maximum error resulting from applying this simple explicit solution was reported as 8% by Li, Stevens, & Simmons, 1976 and a maximum error of 20% was reported by Eggert , 1976.

2.2.4 Parallel Programming with OpenMP

The two-dimensional finite element hydrodynamic model (RiverFLO-2D) is ported over to parallel platform using OpenMP paradigms and its performance had been tested on a multiprocessor computer. The parallel implemented instructions in the RiverFLO-2D rely in the modification of the existing serial code by maintaining the RiverFLO-2D structure. The user of the parallel RiverFLO-2D model will not require any extra effort to use the parallel code because OpenMP techniques have enable us to perform the parallel

computations in a hidden way (Chandra et al., 2001), the same code can be used to generate serial and parallel versions, being very adaptable to any user. The parallel RiverFLO-2D model is portable across all the machines and no modifications need to be done in it when a single processor machine is used. OpenMP could make use of widely available Intel's Duo and Quad processors and unlike others parallel platforms would not necessarily require a computer cluster.

The structure of the parallel implementation had been done to take into account the continued hardware improvement that can be expected regarding the multiprocessor development technology in the future. The RiverFLO-2D subroutines will be parallelized by distributing the workload of each loop between as many processors or cores as are available. In this way the model will optimize its computations to the particular architecture of each computer.

The parallel formulation is based on the implementation of OpenMP instructions. OpenMP is an Application Program Interface (API) that provides a portable, scalable model for developers of shared memory parallel applications. The API supports multi-platform shared-memory parallel programming in C/C++ and FORTRAN on architectures, including MAC OS, Unix and Windows platforms. The created OpenMP instructions include constructs and directives for specifying parallel regions, work sharing, synchronization and data environment (OpenMP, 2009).

OpenMP provides instructions to parallelize existing serial codes to run in shared-memory platforms ranging from affordable and widely available multiple-core computers to supercomputers. It also includes a set of runtime library routines and environment variables, which are called or examined to control the parallel statements in different

areas of the program. The directive-based language extensions, the runtime library routines and the environment variables taken together what is call the OpenMP application programming interface (OpenMP API).

RiverFLO-2D serial code has been enhanced by implementing OpenMP directives available in the Intel Visual Fortran compiler version 11.1. The source code of the numerical model has been written in FORTRAN 95 with over 80 subroutines.

The Intel® VTune™ Performance Analyzer with Intel® Thread Profiler for Windows is the software that was used to make a profile of the model performance identifying the computationally intensive subroutines in the numerical model. Intel® VTune™ Performance Analyzer evaluates applications on all sizes of systems based on Intel® processors, helping the user to improve the application performance. VTune Performance Analyzer makes application performance tuning easier and is an excellent tool that allow you to know where the computational bottlenecks are located in the numerical model.

The verification and validation tests (see chapter 3) were used to tune the performance of the model developing a sampling analysis (sampling configuration wizard) with the Intel® VTune™ Performance Analyzer with Intel® Thread Profiler for Windows Software (VTune Software). The Vtunes software runs the numerical model several times collecting samples of the computational performance. The Vtune Software is able to automatically generate tuning advice running the same sample one time, 10-30 times or more than 30 times, averaging the results for the number of runs performance.

Figure 6 shows the central processing unit (CPU) time (%) versus the name of the subroutine. It can be seen that from the total CPU time, the highest percentage corresponding to 94.8% is spent in two subroutines, the subroutine that perform all the

calculations in the mesh for the shallow water theory equations and the subroutine that modifies partially dry and wet nodes each timestep for the entire mesh.

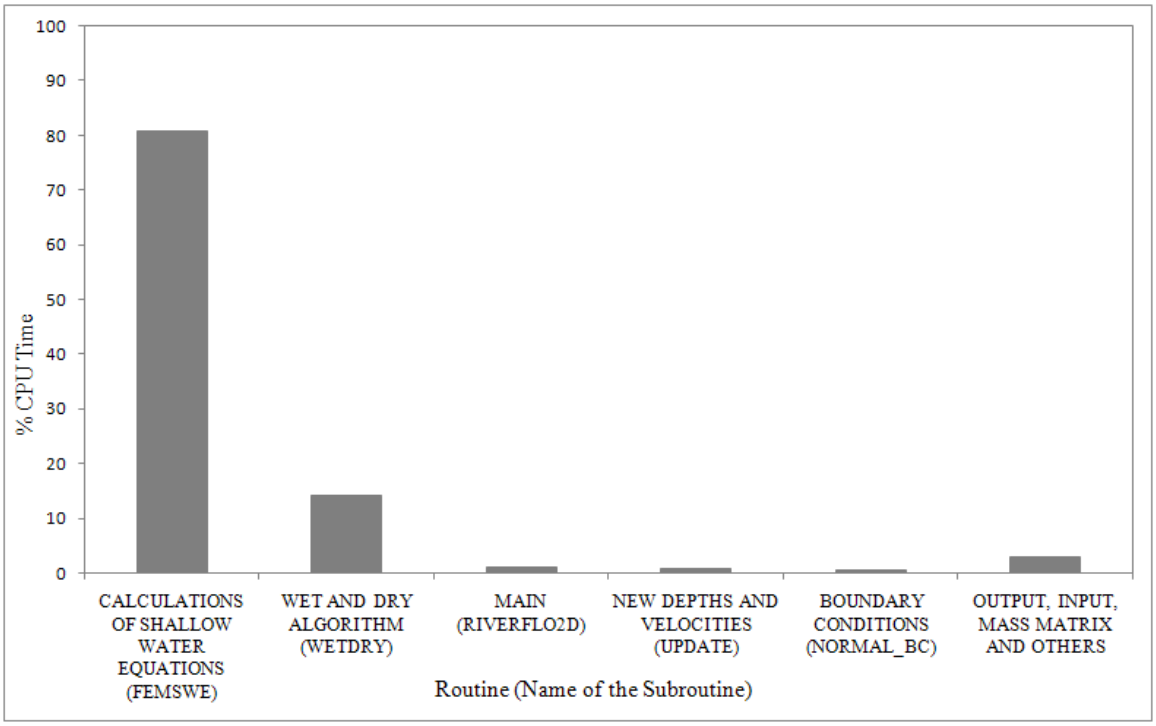

Figure 6. CPU Time for the computationally intensive subroutines in the RiverFLO-2D using Intel® VTune™ Performance Analyzer with Intel® Thread Profiler for Windows.

Using these results, the most time consuming subroutines of the RiverFLO-2D can be modified to reduce the numerical time of a simulation. Subsequently, the intensive loops of the subroutines that perform the numerical calculations are examined to be parallelized, dividing their loads between the numbers of processors available. Figure 6 shows the results of the sampling analysis performance with the Vtunes Software on the RiverFLO-2D model.

Additionally, there is a well known law in parallel processing called Amdahl's Law that can be used to find the maximum expected improvement to an overall system when only

part of the system is improved. It is often used in parallel computing to predict the theoretical maximum speedup using multiple processors.

The parameter that is usually used to measure the benefits to parallelize a code is the speedup (S) (Rao, 2004), a measure that captures the benefit to solve the problem in parallel, defined as the ratio of the serial run time of the best sequential algorithm for solving a problem to the time taken by the parallel algorithm to solve the same problem on p processors, where the processors are assumed to be identical to the one used by the sequential algorithm. The expression of speedup is given by:

$$S = \frac{T_{sp}}{T_{pp}} \tag{35}$$

Where:

T_{sp}, time required for a single processor, and

T_{pp}, time required for p processors in multiprocessor systems.

The speedup of a program using multiple processors in parallel computing is limited by the time needed for the sequential fraction of the program. According to Figure 6, the OpenMP parallelization was performance for three subroutines that sum up approximately between 90-95 % of the CPU time, the rest of the subroutines that have not been parallelized consume approximately 5-10 % of the CPU time in the numerical simulation. Also, it can be estimated that the loops that have been modified in the enhanced subroutines cover between 80-90% of the mathematical instructions present in the numerical routine. According to Amdahl's Law (see Figure 7) if we follow the 90-95% Parallel Portion lines, we would see a speedup between 4.5 and 6 after 8 processors,

the speed up slows down dramatically after an n number of processors that depends of the parallel portion (see Figure 7).

It is important to highlight that a program is really only as fast as its weakest portion in the serial code. It can be concluded that the parallelization task could be useless without an exhaustive sampling analysis to identify the weakest areas of the serial code, as the one that it was performed with the Vtunes Software in this research.

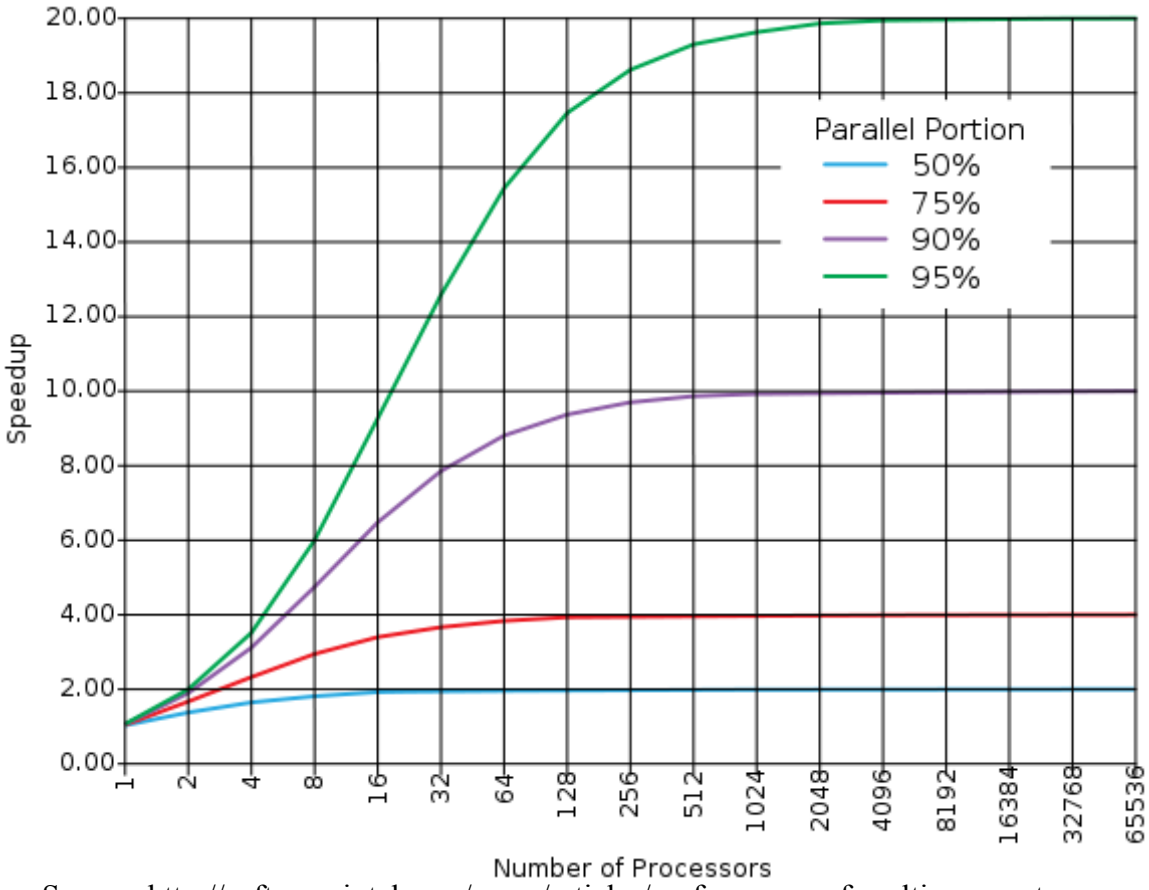

Source: http://software.intel.com/en-us/articles/performance-of-multicore-systems

Figure 7. Speedup for Amdahl's Law theory varying the degrees of parallelism.

Table 1. INTEL VTUNE detailed sampling analysis using the verification tests.

ANALYSIS	INTEL VTUNE Detailed Sampling Analysis Using the Verification Tests		
RESULTING INTENSIVE SUBROUTINES	FEMSWE	WET-DRY	MASS-MATRIX
NUMBER OF NUMERICAL LOOPS MODIFIED	2 loops	1 loop	1 loop
DESCRIPTION OF THE MODIFIED LOOPS	Loop 1 is the main loop of the numerical model that calculates for all elements in the mesh the Shallow Water Governing Equations including all their terms. A modification of the shallow water equations is included in this loop for all dry and partially dry nodes in the numerical mesh.	Loop that modifies the velocities that come from the shallow water equations for all dry and partially dry nodes in the numerical mesh.	Loop that calculates the lumped mass-matrix for all elements in the numerical mesh.
	Loop 2 updates velocities and depths recently calculate for timestep $n+1$ for all global nodes in the numerical mesh		

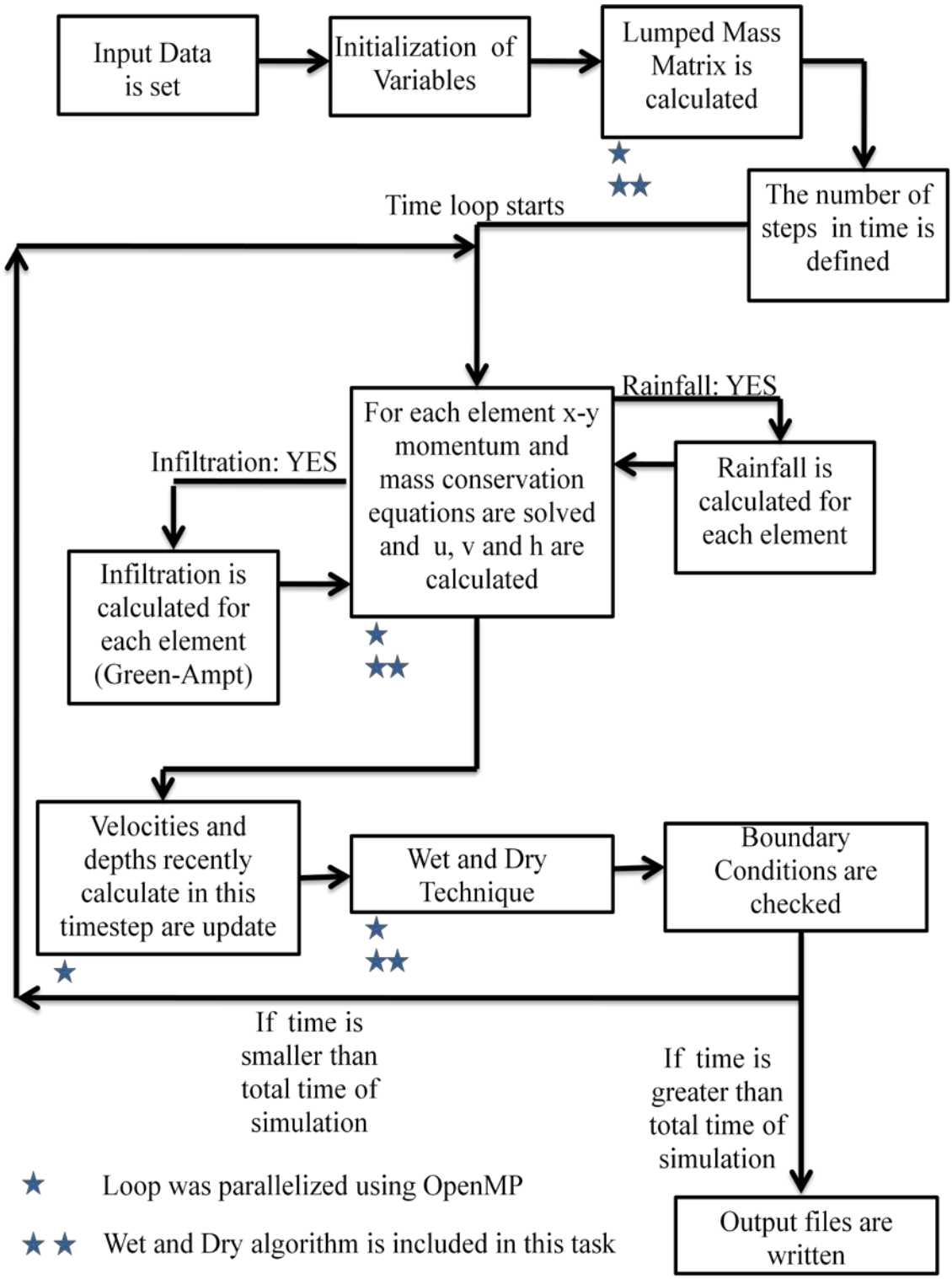

Figure 8. Flow graph showing the processes of enhanced RiverFLO-2D.

CHAPTER 3. VERIFICATION AND VALIDATION OF RIVERFLO-2D

Verification is intended to ensure that the model does what it is intended to do. According to the verification process recommended by ASCE Task Committee on Model Verification and Validation (Wang et al., 2008), the concept of verification is to solve the equations right and validation is to solve the right equations.

Model verification and validation are essential parts of the development process of a numerical model. The verification is done to ensure that the model is programmed correctly and non mistakes have been made in the implementation of the governing equations, methodologies and algorithms. Model verification proceeds as more tests are performed, errors are identified, and corrections are made to the model, often resulting in retesting requirements to ensure code integrity.

The validation ensures that the model meets its intended requirements in terms of the theory employed and the results obtained, reflecting correctly the physical phenomena being modeled by addressing the right equations.

The outcome for an extensive verification and validation process is a better understanding of the model's capabilities, limitations, and appropriateness for addressing a range of applications.

A model is usually developed to replicate physical phenomena, given us close predictions about the particular problem that has been studied. A numerical model is a representation of different parts of a system at different levels of abstraction. As a result, the model may

have different levels of validity for different applications across the full spectrum of the physical phenomena. Most model results depend mainly of three main aspects: the agreement between the natural phenomena and the mathematical equations that describe it, the assumptions of the numerical model to represent the physical problem, the uncertainty in the input parameters.

There are several approaches to validate that the model governing equations are predicting effectively the reality under particular idealizations of the physical problem. One of them is the expert intuition; the examination of the model should ideally be led by an expert with respect to the physical phenomena and capable to understand the dynamics of the model and how it works.

The most recommended approach is the comparison with laboratory experiments and real measurements, which is the most reliable and preferred way to validate that the numerical model is predicting properly the physical phenomena. Assumptions, input variables, output results and the general behavior of the model should all be compared with those observed in the real world. In the case of simulation models, when full measurement data is available it may be possible to apply the model and observe it under exactly the same conditions as the real case. The approach to verify a model is to use analytical solutions making sure that the model results agree for those cases by solving correctly the governing equations of the model.

Verification and validation of a numerical model against the results or behavior of other numerical models is a technique which should be used with care as both may be invalid in the sense that they both may not predict the behavior of the real system accurately. According to the verification process recommended by ASCE Task Committee on Model

Verification and Validation (Wang et al, 2008), the errors or mistakes could have happened in the long process of mathematical derivations or manipulations, implementations of numerical solution schemes, applications of special features for speeding-up/stabilizing, calculation algorithms, coding, etc. Some of these errors are hard to find, even by spending hours and days. Frequently, It has been found years later that the models passed verification and validation approaches having errors and/or bugs, which have been concealed by the parametric tuning.

In order to minimize the parametric tuning effect in the numerical model results, model developers have to identify the tuned parameters and make sure that they are physically reasonable.

In this research, new numerical routines has been implemented and used in the numerical model RiverFlo-2D, therefore an extended verification and validation process has to be made.

To verify and validate the enhanced RiverFLO-2D model results, the approaches and recommendations explained above were followed (Wang et al., 2008; Hervouet, 1993). The numerical model was tested with analytical solutions, simplified cases, laboratory experiments and comparisons with documented real cases, where field data is available checking every modification of the numerical model. A considerable wide number of verification cases were collected on this research, being this part of the research one of the most time-consuming tasks that was developed but it is necessary to meet requirements. Different geometries and types of flows have been included in the RiverFlo-2D verification and validation process, reaching a wide variety of flood cases

with complex dynamics. In order to evaluate the accuracy and application of the model, twelve verification cases have been included in this chapter.

3.1 Simple Test Cases

3.1.1 Static Cone

Case Description

The goal of this test is to evaluate the model performance of the enhanced RiverFLO-2D under hydrostatic conditions, where one part of the finite element mesh is dry and has irregular bed elevations and relatively steep slopes. Dry steep slope elements may pose a severe numerical problem because if handled incorrectly, the 2D gravity term in the equations can generate erratic flow. Starting with a static initial water depth that leaves part of bed dry, a properly working dry bed algorithm should preserve the initial static conditions, minimize mass conservation errors and be free from spurious velocities.

It appears that this numerical experiment was first proposed by Brufau, García-Navarro, & Vázquez-Cendón, 2004. The problem consists of a square pool 1 m × 1 m with a central bump on the bottom defined by the following formula:

$$z(x,y) = \max\left\{0, 0.025 - 5\left[\left(x-\frac{1}{2}\right)^2 + \left(y-\frac{1}{2}\right)^2\right]\right\} \tag{36}$$

The maximum bed elevation is 0.25 m. The initial condition is a water surface elevation of 0.1 m, and zero velocities everywhere. The finite element mesh has 3052 nodes and 5899 elements and frictionless bed (see Figure 10).

The total simulation time is 180 s. and the time step is 0.01 s. A wet and dry minimum water depth threshold of 0.005 m. is assigned for the entire grid. The output data is reported every 36 s. Figure 9 shows the bed elevation contour lines. Figure 10 shows the bed elevations in the numerical mesh.

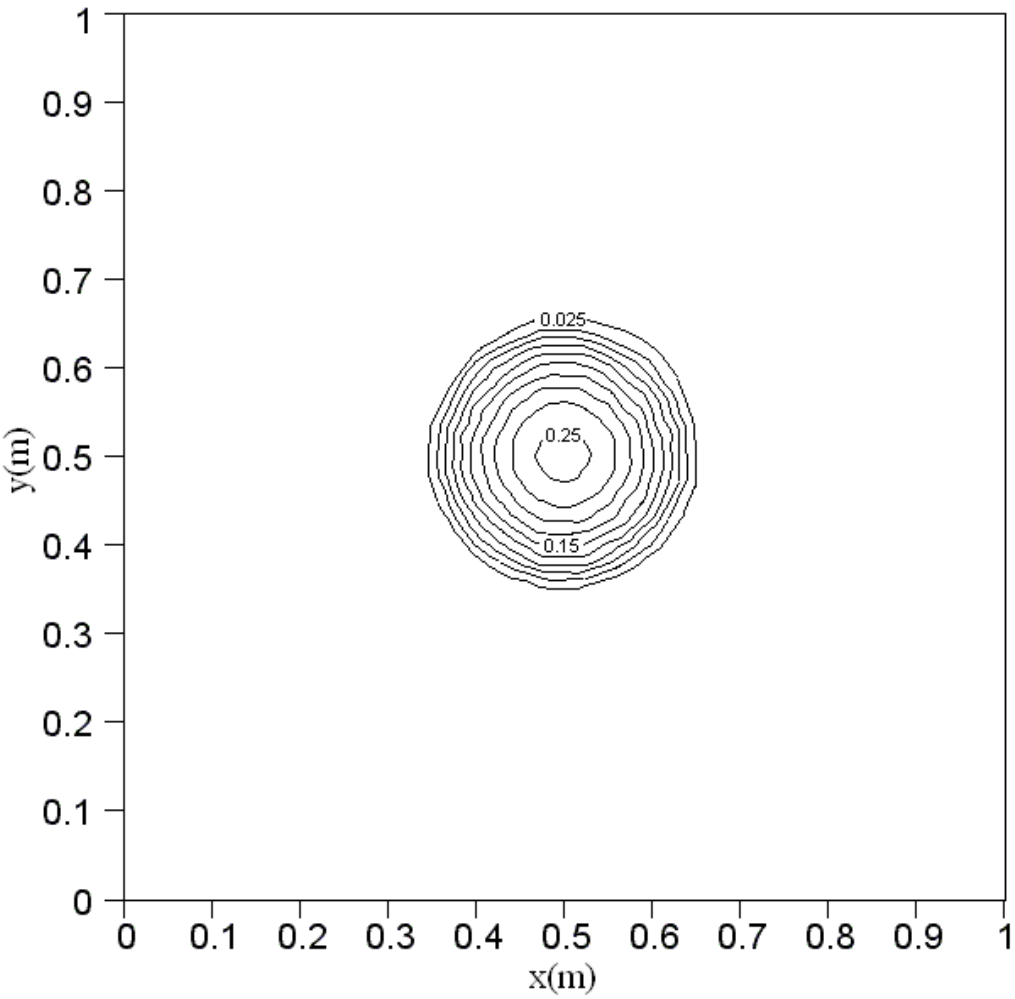

Figure 9. Static Cone Test. Bed contour lines for static dry-wet test.

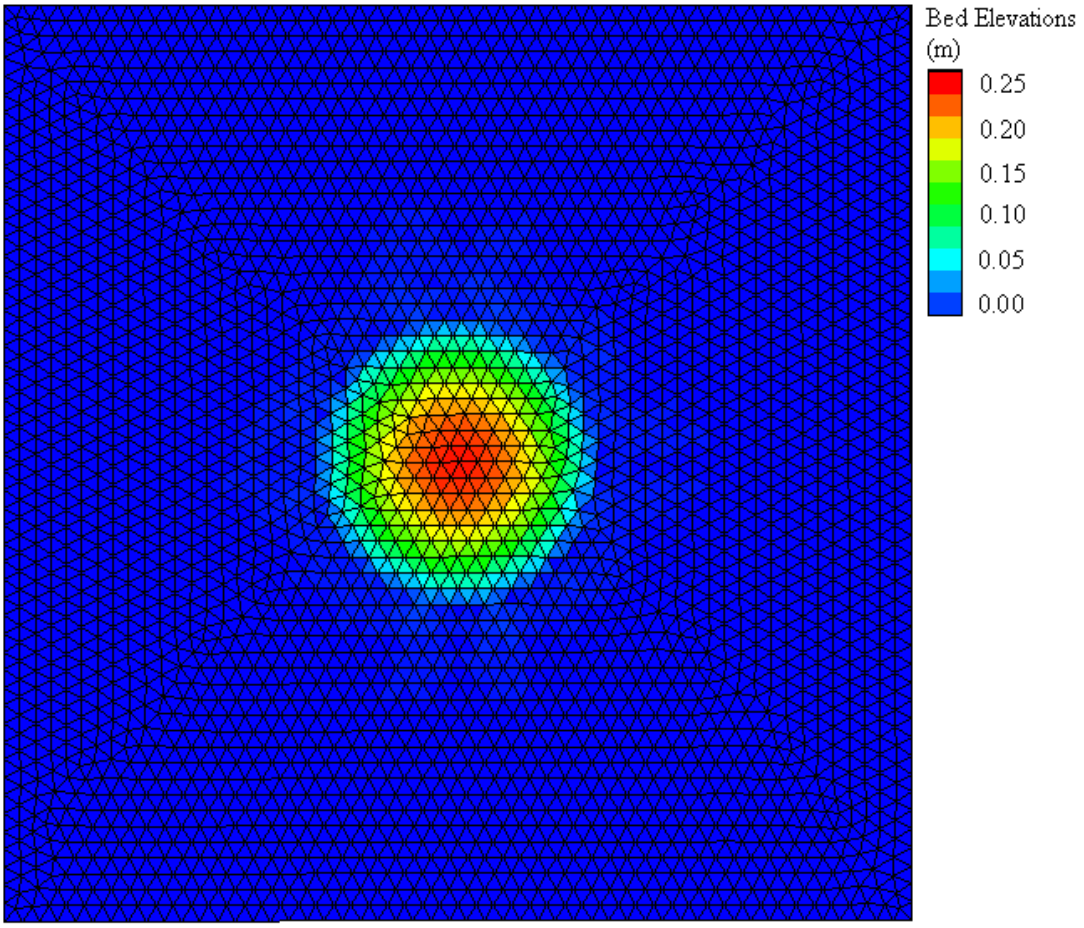

Figure 10. Static Cone Test. Bed Elevations in the numerical mesh.

Numerical Model Results

Figure 11 shows the numerical water surface elevations on a profile across the tank mid section and Figure 12 present the velocity field.

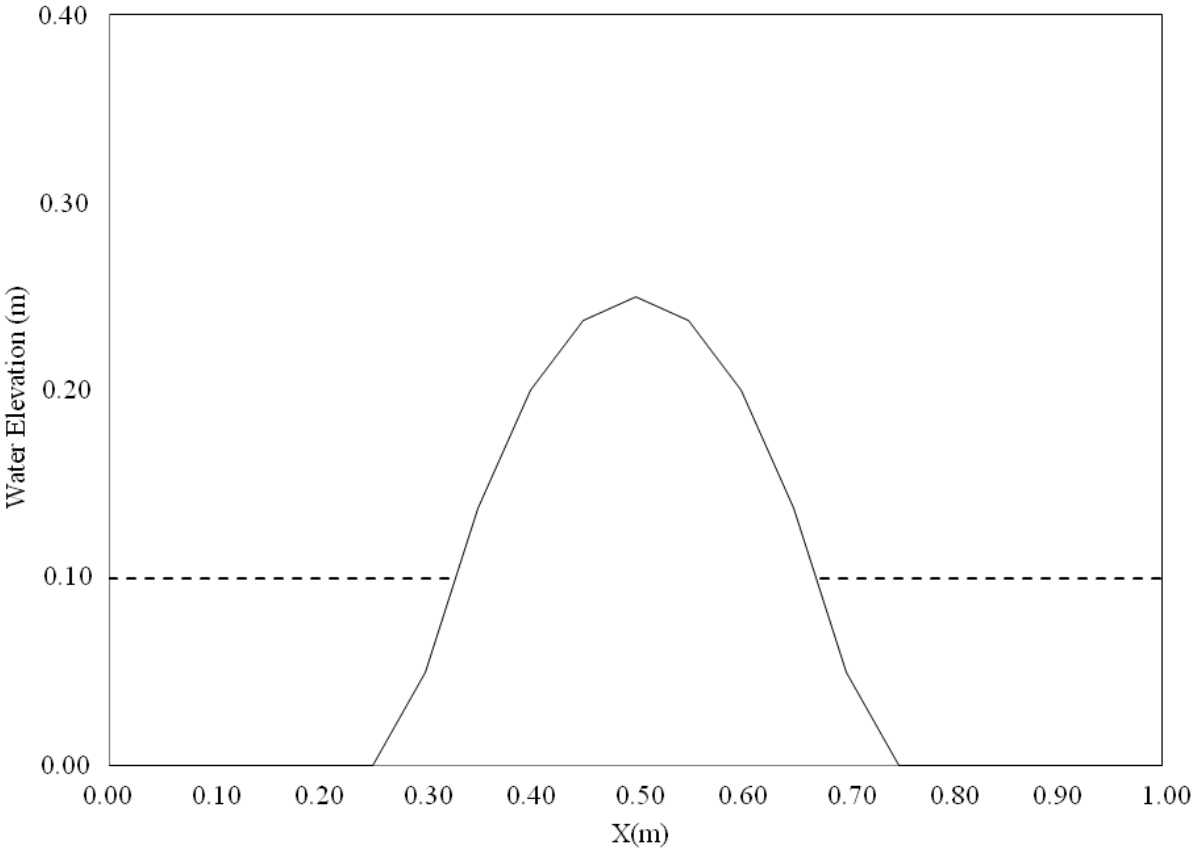

Figure 11. Static Cone Test. Profile across mid section for static dry-wet test.

Figure 11 and Figure 12 present the predicted water surface elevations and the velocity field for the static cone test. The numerical model preserves the initial conditions of the static water level on the tank, where the water surface is horizontal and without oscillations. During the simulation the model is able to handle completely dry elements as well as partial dry elements without the presence of unrealistic velocities. The implemented wet and dry methodology proved to be efficient in this respect even when the simulation presents irregular bed elevations, large completely dry areas and steep slopes.

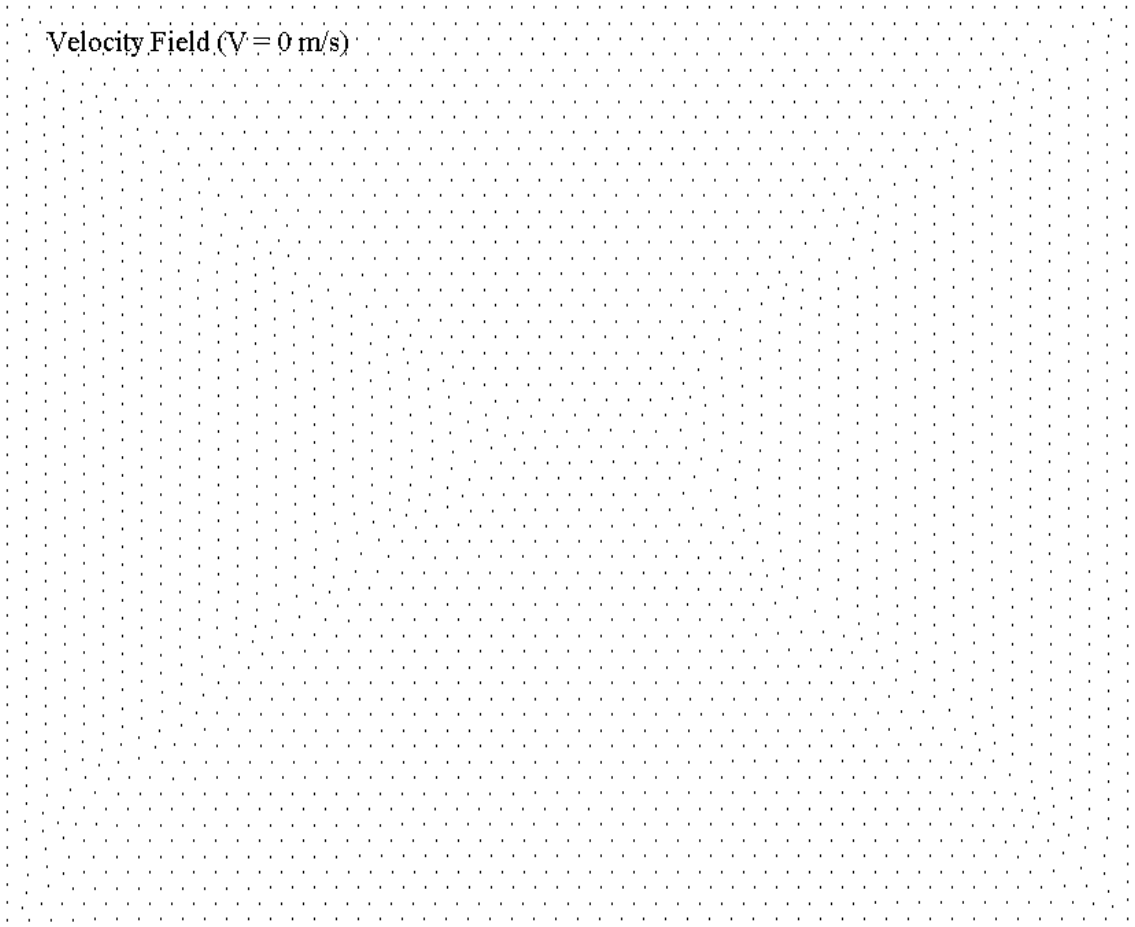

Figure 12. Static Cone Test. Velocity field for static dry-wet test, points represent zero velocity for all the vectors in the field.

3.1.2 Three Islands

Case Description

The purpose of this test is to verify the enhanced model performance of dynamic flooding under drying and wetting bed. The test was first proposed by Kawahara & Umetsu, 1986. It consists of a rectangular channel with three bumps on its bottom. Figure 13 shows the bed elevation contour lines. The channel length is 75 m and width is 30 m. Two symmetrical bumps at the left have maximum elevation of 1 m and the central bump elevation is 3 m. The finite element mesh has 1269 nodes and 2392 elements. The water flows from section AA–BB to section CC–DD. Boundary conditions include water elevation along boundary AA–BB as follows: h = 0.5 m for times 0 s to 300 s; h = 1.0 m, for times 300 s to 350 s; h = 2.5 m., for times greater than 350 s. Boundaries AA–DD and BB–CC are vertical walls, where a slip velocity condition is imposed. At boundary AA-BB velocity is 1 m/s. The downstream condition is an open outlet boundary and slip conditions are imposed on channel walls. Initial dry bed conditions (*Hmin* = 0.01) are imposed everywhere. The total simulation time is 900 s. and the time step is 0.01 s. A wet and dry minimum water depth threshold of 0.01 m is assigned for the entire grid. The output data is reported every 20 s.

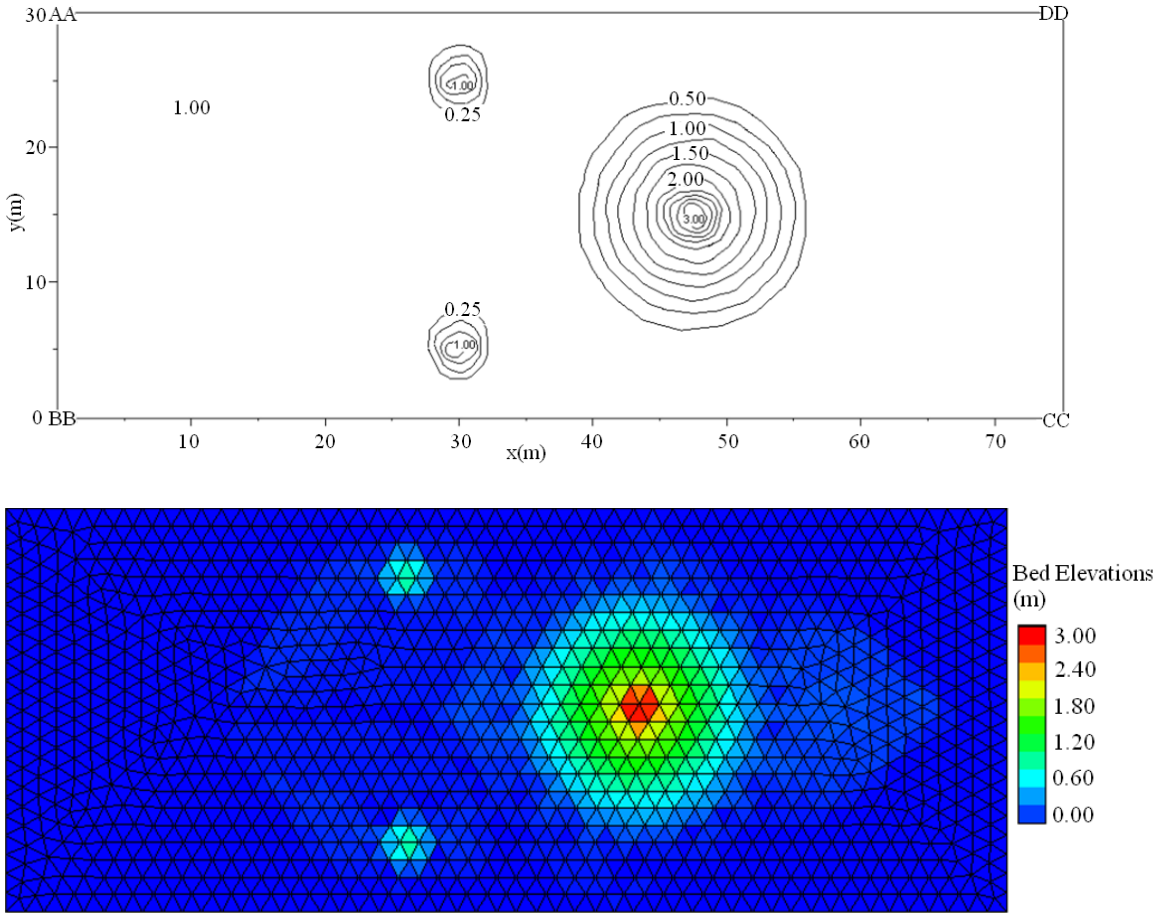

Figure 13. Three Islands Test. Bed contour lines for dynamic drying-wetting test and numerical mesh

Numerical Model Results

Figure 14 and Figure 15 present velocity fields and water surface profiles for times 20 s and 900 s respectively.

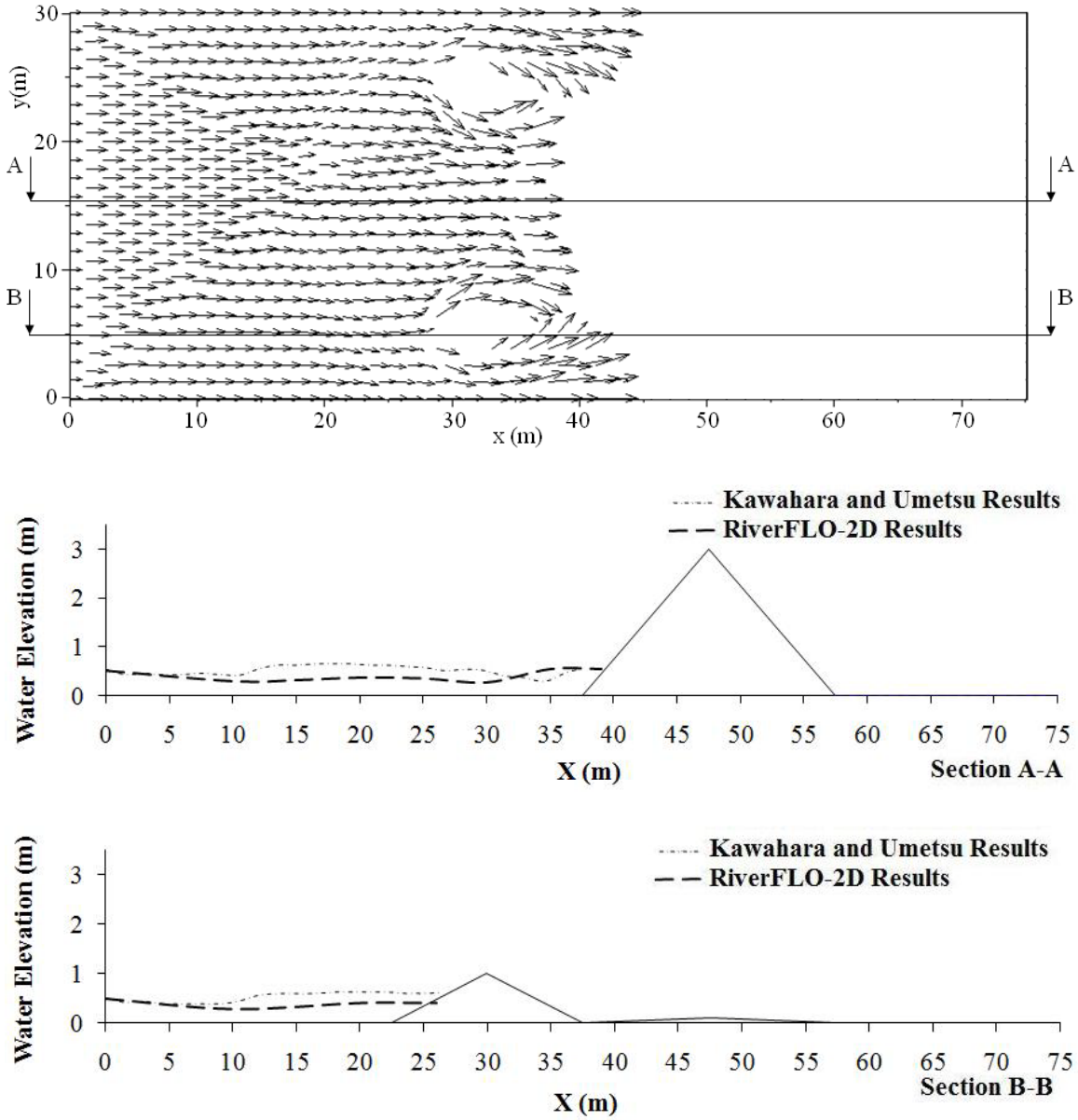

Figure 14. Three Islands Test. Dynamic drying-wetting test with results at 20 s presenting the velocities and water elevations through indicated profiles.

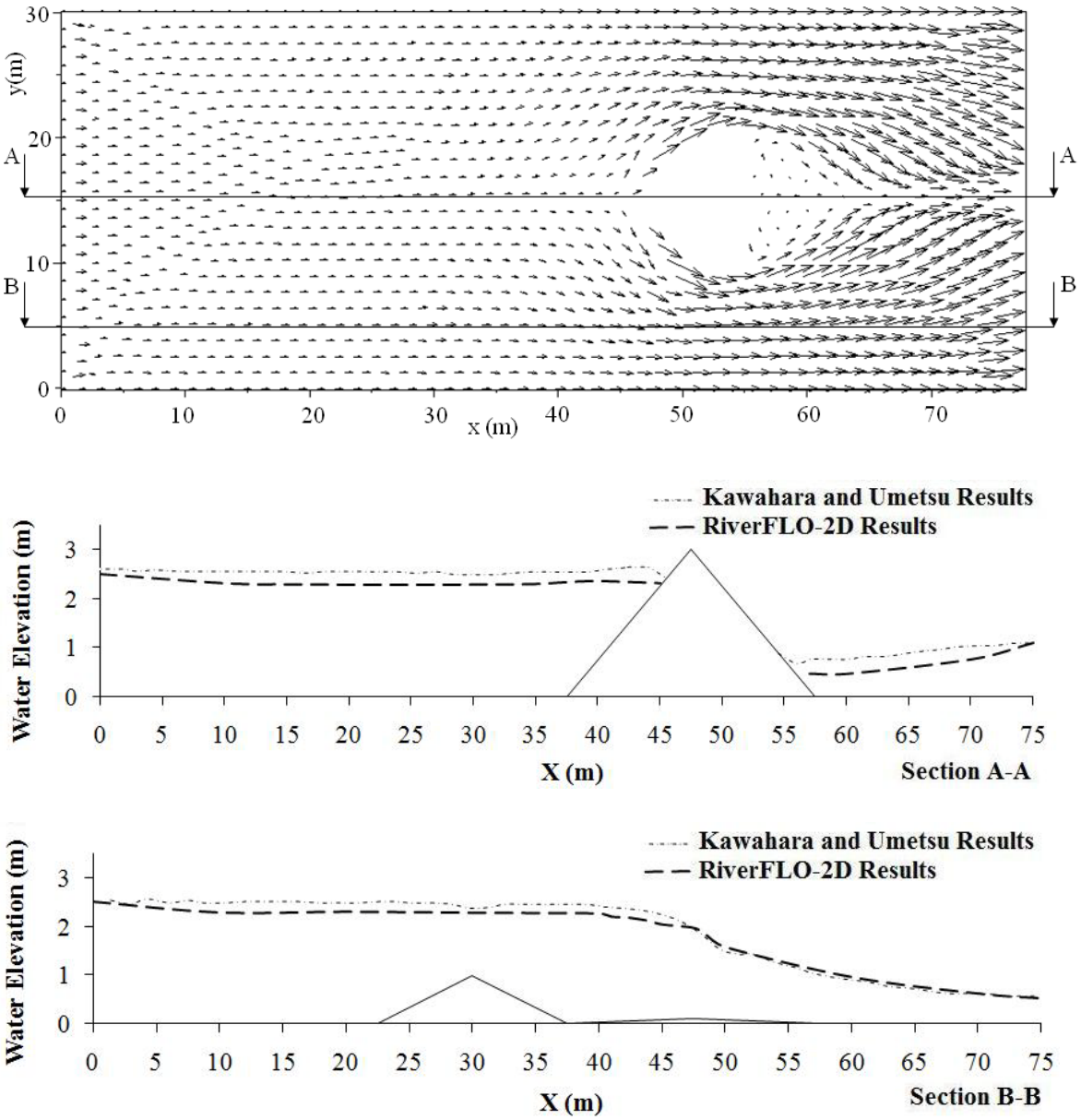

Figure 15. Three Islands Test. Dynamic drying-wetting test with results at 900 s presenting the velocities and water elevations through indicated profiles.

Figure 14 and Figure 15 present velocity fields and water surface profiles for times 20s and 900s, respectively. Velocity fields show stable results and no erratic velocities over the dry areas. Water surface profiles indicate correct treatment of the dynamic dry–wet interface.

3.1.3 Subcritical Uniform Flow

Case Description

The purpose of this test is to verify the model performance for a long channel that reaches the uniform flow condition, assuring that the two-dimensional depth averaged finite element hydrodynamic numerical model is capable of computing water surface elevations and horizontal velocity components for a subcritical free-surface flow. The flow in open channel is said to be subcritical is the Froude Number (F) is less than 1. The Froude Number is defined as a dimensionless number comparing inertia and gravitational forces:

$$F = \frac{v}{c} \tag{37}$$

Where:

v is the mean velocity, and

c is the characteristic water wave propagation velocity.

The depth average flow velocity and the area of flow cross-sections should be constant along the channel. Furthermore the uniform flow occurs when bed slope is equal to friction slope, and the other terms in the momentum equations are negligible, and so on relationship between velocities and water elevations is determined by Manning Equation. The Manning equation is:

$$V = \frac{R^{2/3} S_f^{1/2}}{n} \tag{38}$$

Where:

V is the average velocity,

R is the "hydraulic radius" defined by the expression $R = A/P$. Where, A is the cross-section area and P is the wetted perimeter,

S is the slope, and

n is the channel roughness referred to as Manning's n.

Table 2 shows the variable set for this test case.

Table 2. Subcritical uniform flow test. Theoretical values according Manning Equation.

Water Depth (m)	Manning's n	Hydraulic Radius	Velocity (m/s)	Froude Number
1	0.06	0.6	1.19	0.36

This case consists of a rectangular channel with a bed slope of 0.01. The channel length is 100 m and width is 3 m. The finite element mesh has 515 nodes and 818 elements as it is show in Figure 16.

The water flows from section A–B to section C–D. Boundary conditions include water flow rate along boundary A–B of 3.56 m^3/s and water flow elevation of 1 m along boundary C-D. Boundaries A–D and B–C are vertical walls, where a slip velocity condition is imposed.

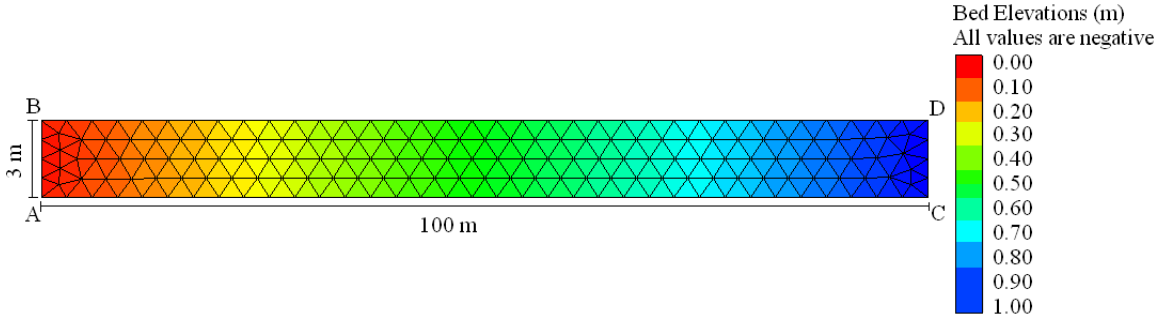

Figure 16. Subcritical uniform flow test. Bed Elevations in the numerical mesh

Numerical Model Results

Figure 17 shows velocity vectors for a simulation time of 3600 s respectively, where the uniform condition was developed in the channel with a F=0.36 that corresponds to subcritical flow. The water depth for $\in$ = 0.93 and Δt=0.1 is equal to 1m for the entire mesh.

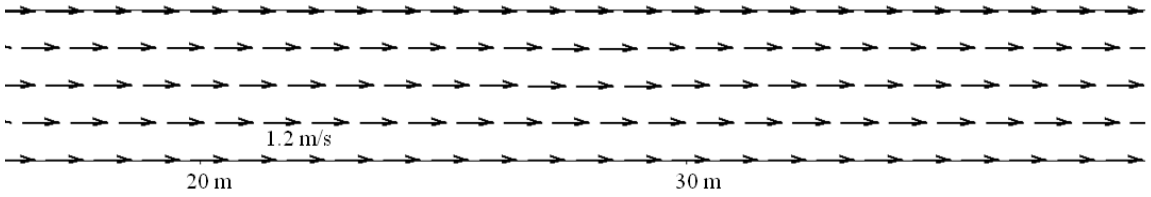

Figure 17. Subcritical uniform flow test. Velocities at 360s.

An analysis of sensibility was developed for the selective lumping parameter $(\in)$ that may vary in the interval [0, 1] and for the time step of the numerical simulation. According to Kawahara et al., 1982, it is seen that the lumping parameter $(\in)$ should be used larger than 0.8 and a refined finite element mesh should also be employed. It is also notable that according to Kawahara test results the time increment Δt is the shortest in the case when $\in$ = 0.9.

An average relative error was calculated as the absolute value of the difference between the theoretical result and the numerical result divided by the theoretical result. The average relative error was calculated for the velocity and water depth for the nodes located on the mid section in the numerical channel and for the velocity and water depth calculated using the Manning equation, with a constant time step and a variable selective lumping parameter. The average relative errors for different values of lumping parameter are shown on Figure 18.

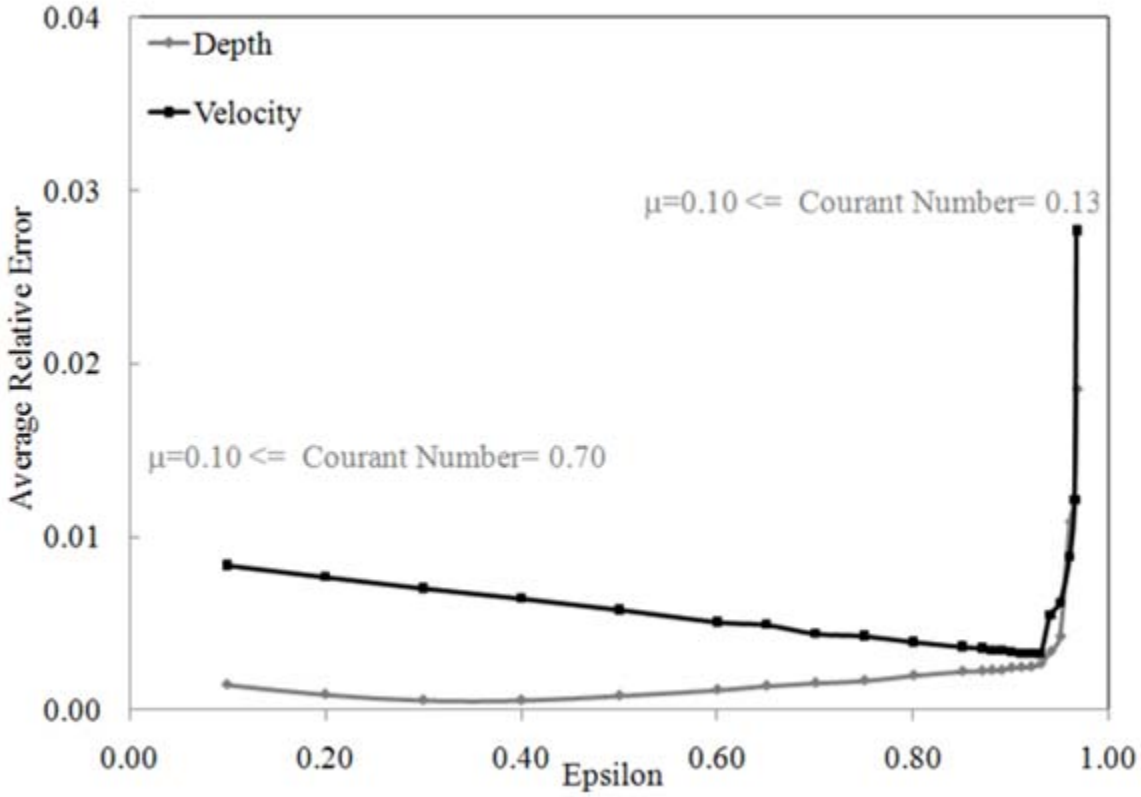

Figure 18. Subcritical uniform flow test. Average relative error for a fixed timestep of 0.1s.

In the same way, the relative error was calculated setting the lumping parameter as a constant and with a variable times step to run the simulation. The average relative error for different values of the time step is shown on Figure 19.

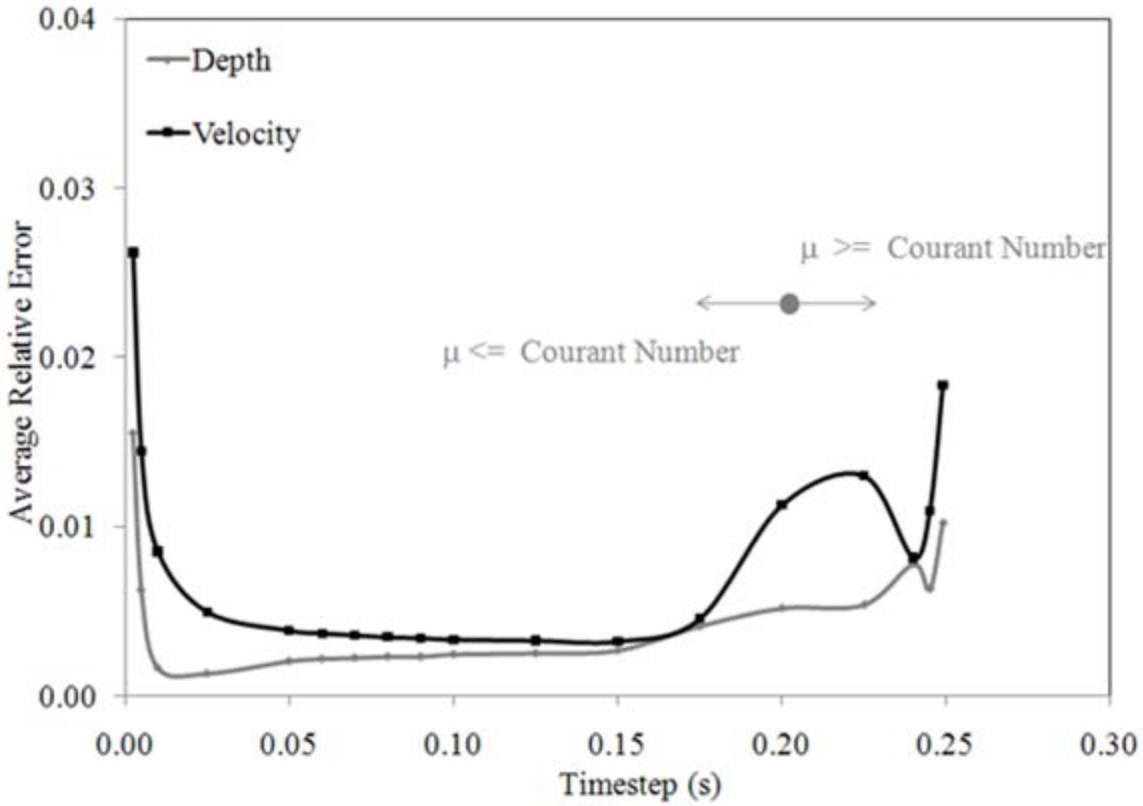

Figure 19. Subcritical uniform flow test. Average relative error for a fixed lumping parameter.

Figure 19 shows the average relative error for depths and velocities for different time steps, one is located left for time steps between 0s and 0.18s which corresponds with a stable condition for the Courant number, and the right side zone for time steps greater than 0.2s with Courant numbers that violate the stability condition. The average relative errors are small for time steps between 0.05 – 0.18. For time steps smaller than 0.05, the average relative error increases, this could happen because the accumulation of the numerical errors which are generated by the increment in the numerical calculations due to the reduction of the time step. For time steps greater than 0.18, where the stability Courant condition is violated, the average relative error goes up and numerical instabilities can be observed as oscillations in the numerical results.

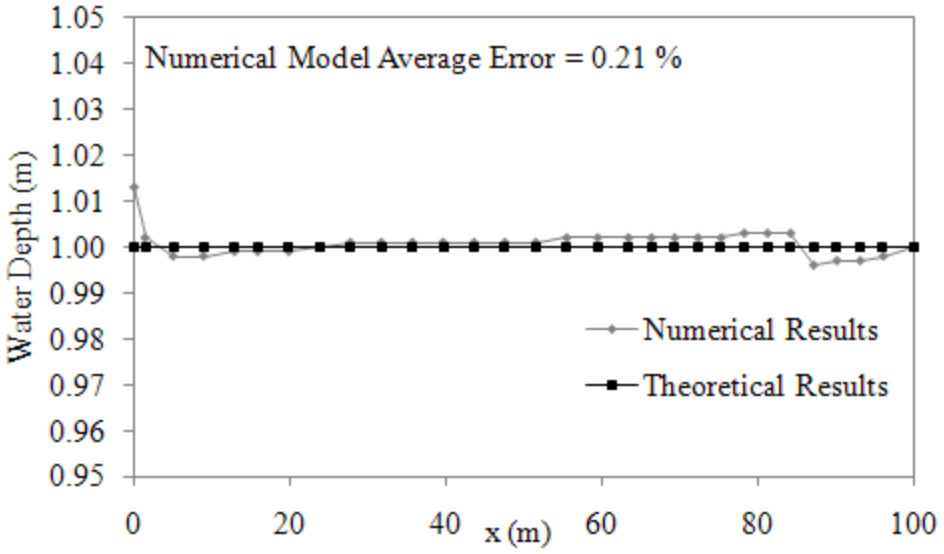

Figure 20. Subcritical uniform flow test. Comparison of the Numerical Results and Theoretical Results using Manning Equation with Δt=0.10s and $\in$ =0.93

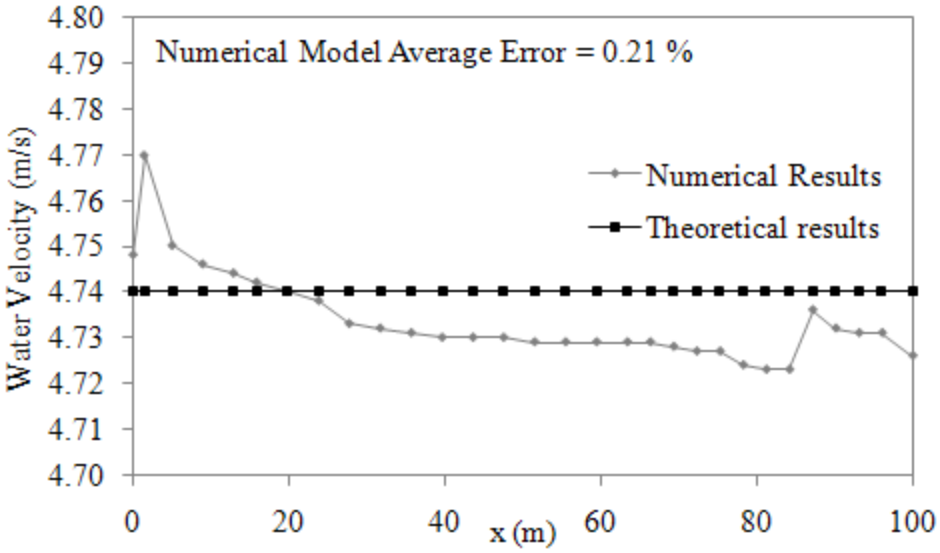

Figure 21. Subcritical uniform flow test. Comparison of the Numerical Results and Theoretical Results using Manning Equation with Δt=0.10s and $\in$ =0.93

The numerical water depths are close to 1 for the entire mesh when the simulation parameters $\in$ and Δt are set to 0.93 and 0.10, respectively. The results compare with an error of 0.21% between RiverFLO-2D and theoretical water depths and velocities obtained by Manning Equation for a subcritical uniform flow. The average relative errors

are small for lumping parameters between 0.8 – 0.95 which is consistent with the results presented by Kawahara et al, 1982.

3.1.4 Supercritical Uniform Flow

Case Description

The purpose of this test is to verify the model performance for a long channel that reaches the uniform flow condition for a supercritical free-surface.

The following table shows the set of parameters use for this test.

Table 3. Supercritical uniform flow test. Theoretical values according Manning equation.

Water Depth (m)	Manning's n	Hydraulic Radius	Velocity (m/s)	Froude Number
1	0.015	0.6	4.74	1.52

It consists of a rectangular channel with a bed slope of 0.01. The channel length is 100 m and width is 3 m.

The finite element mesh has 515 nodes and 818 elements as it is show in Figure 22. The water flows from section A–B to section C–D. Boundary conditions include water flow rate along boundary A–B of 14.23 m^3/s and water flow elevation of 1 m along boundary C-D. Boundaries A–D and B–C are vertical walls, where a slip velocity condition is imposed.

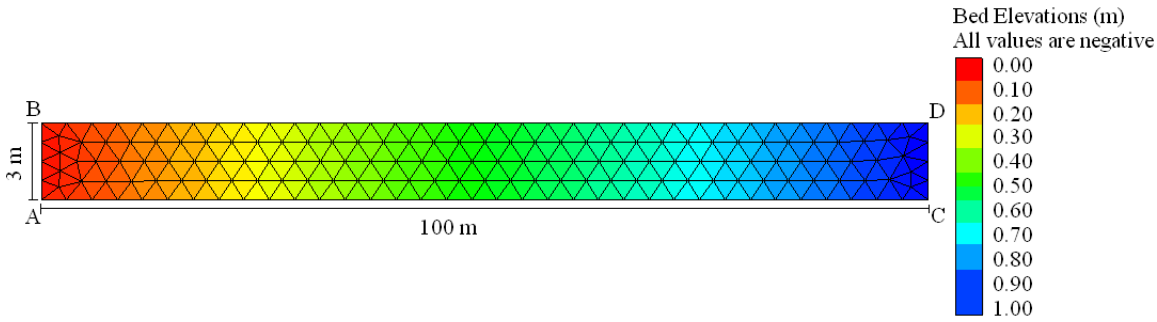

Figure 22. Supercritical uniform flow test. Bed Elevations in the numerical mesh.

Numerical Model Results

Figure 23 present velocity vectors for a simulation time of 3600 s respectively, where the uniform condition was developed in the channel with a Froude Number equal to 1.52 that corresponds to supercritical flow. The magnitude of velocity vectors is shown. The water depth is equal to 1 m for the all nodes in the numerical mesh.

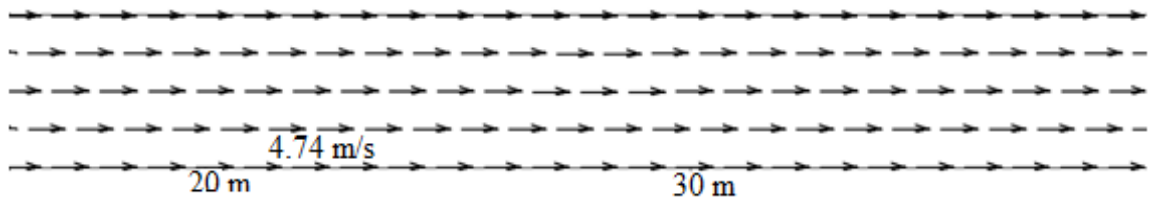

Figure 23. Supercritical uniform flow test. Velocities at 3600s.

An analysis of sensibility was developed for the selective lumping parameter ($\in$) that may vary in the interval [0, 1] and for the time step.

The time step was fixed allowing the selective lumping parameter varies, and the average relative error is shown in Figure 24.

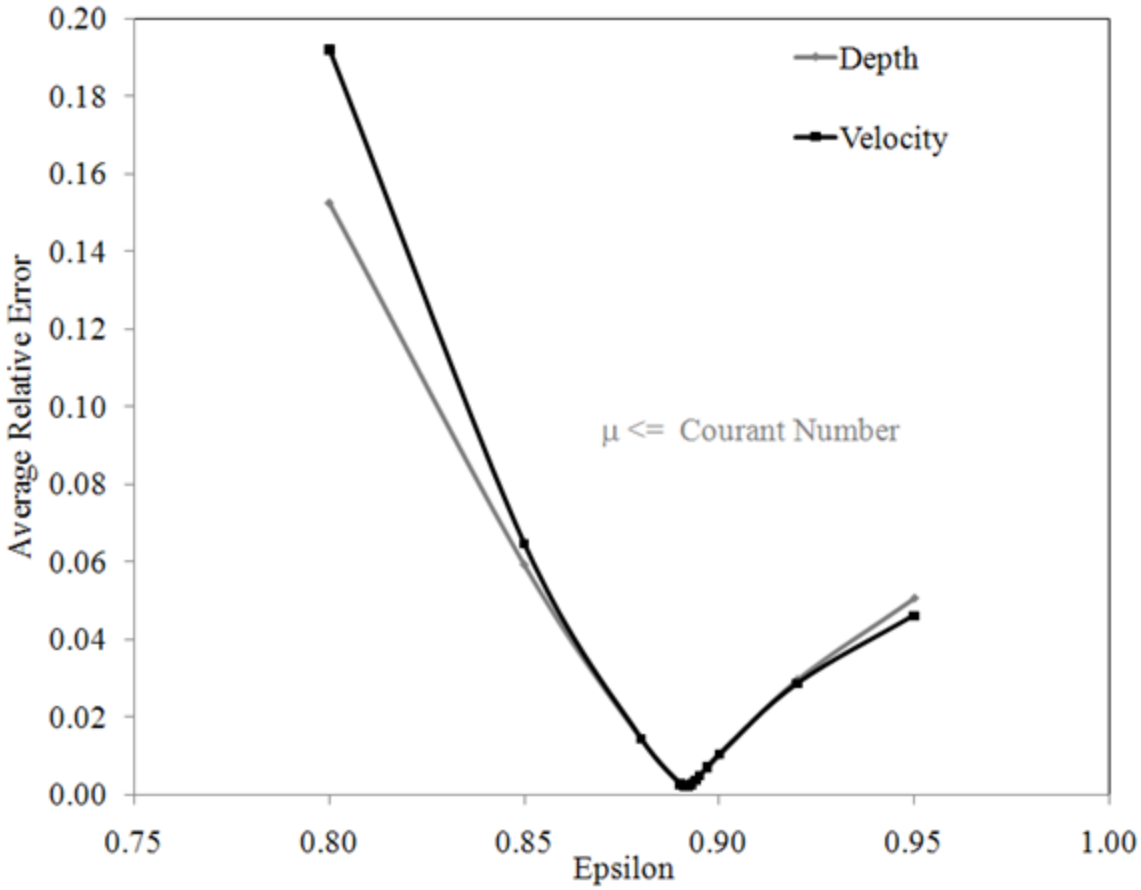

Figure 24. Supercritical uniform flow test. Average relative error for a fixed timestep of 0.02s.

The selective lumping parameter was fixed and several timestep were selected to run the simulation, and the results are shown in Figure 25.

Figure 24 shows the average relative error for depths and velocities. The average relative errors are small for lumping parameters between 0.88 – 0.92, as it can be seen in Figure 24.

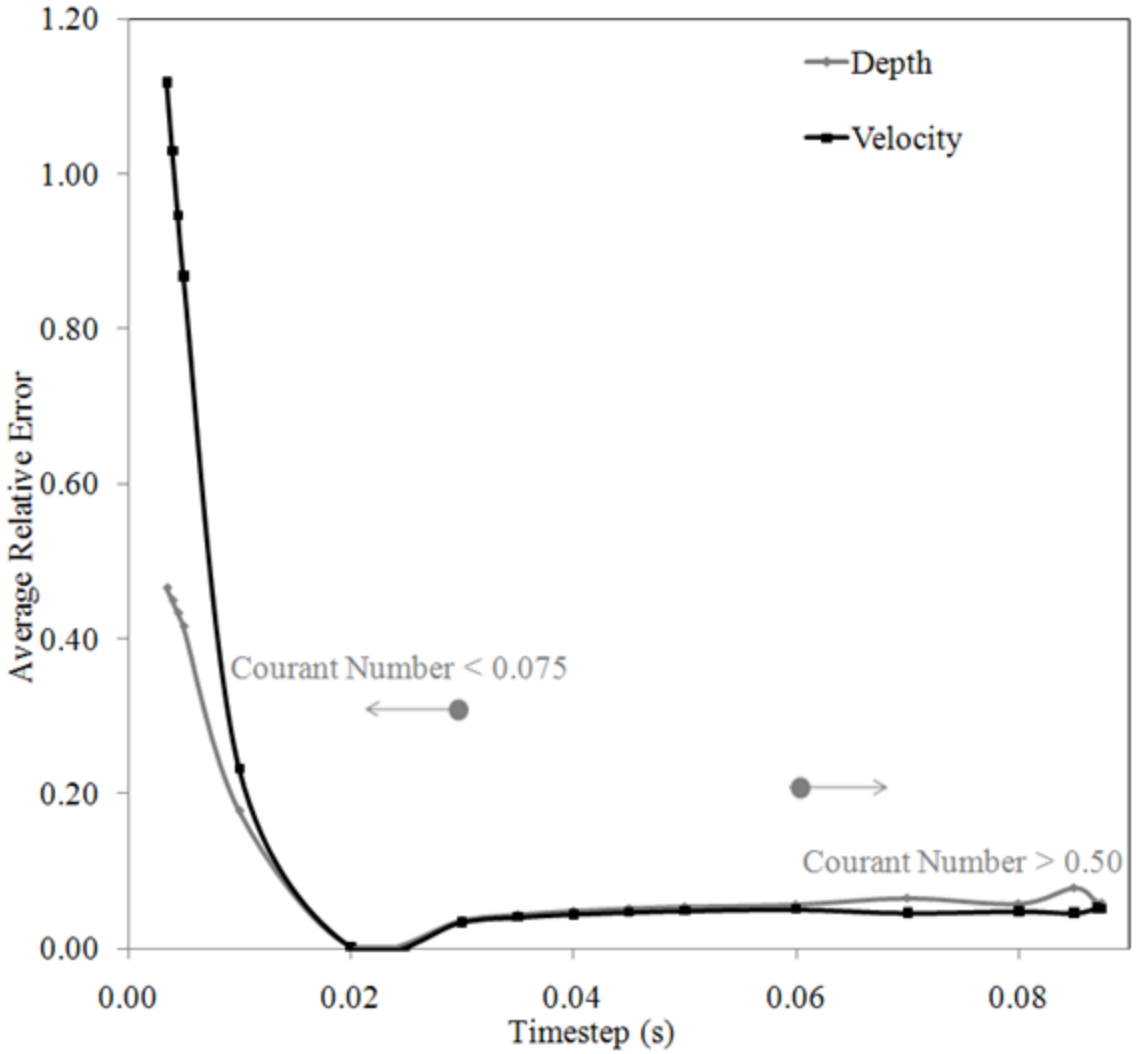

Figure 25. Supercritical uniform flow test. Average relative error for a fixed lumping parameter of 0.0892.

The numerical water depths are equal to 1 for the entire mesh when the simulation parameters $\in$ and Δt are set to 0.90 and 0.02s, respectively.

Figure 25 shows the average relative error for depths and velocities for different time steps, with similar results that the subcritical case (see Figure 19). The numerical instabilities are evident for Δt greater than 0.09s, and for Δt smaller than 0.01s the accumulation of numerical errors increases the average relative error for the calculations.

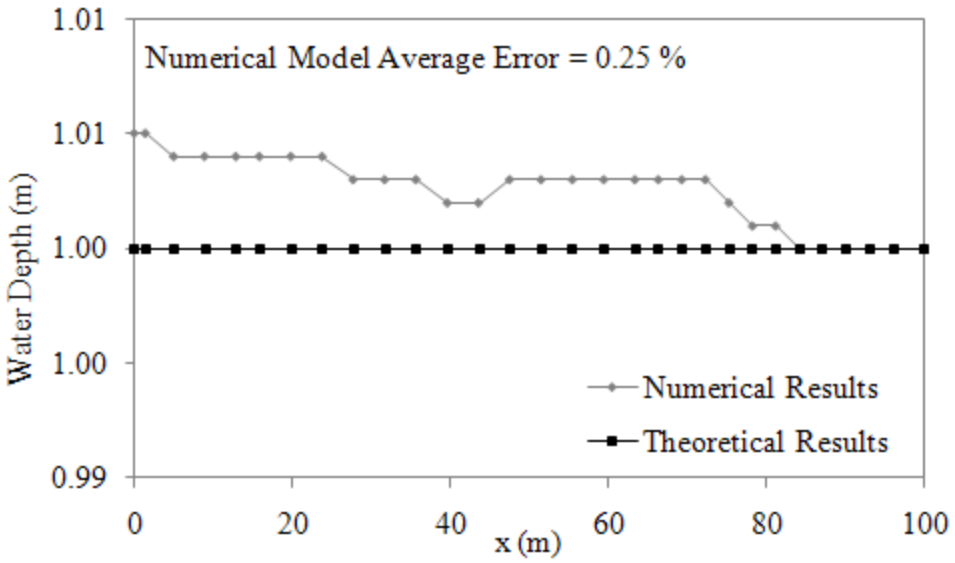

Figure 26. Supercritical uniform flow test. Comparison of the Numerical and Theoretical Water Depths using Manning Equation.

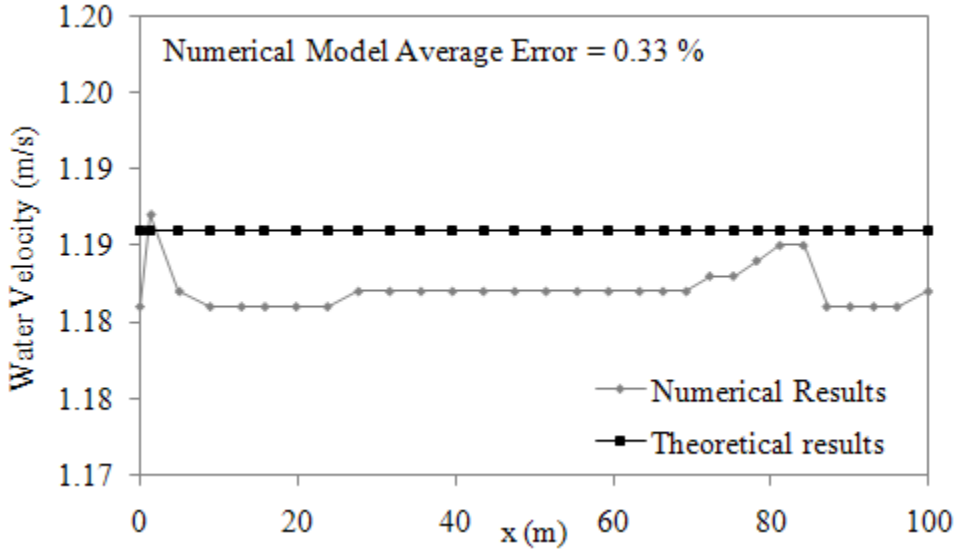

Figure 27. Supercritical uniform flow test. Comparison of the Numerical and Theoretical Water Velocities using Manning Equation.

Figure 26 and Figure 27 show a numerical model average error of 0.25% and 0.33% for the comparison between RiverFLO-2D and theoretical water depths and velocities, respectively.

3.1.5 Changes of Manning Roughness Coefficient for a Channel with Uniform Width.

Case Description

The purpose of this test is to understand the effects of changes in Manning's roughness coefficients on water surface elevations and to compare RiverFLO-2D with other FESWMS model. Understanding the effects of those changes helps to make reasonable and prudent adjustment of model parameters (Froehlich, 2003).

This test consists of a rectangular channel with a level bottom. The channel length is 800 m and width is 100 m. The finite element mesh has 542 nodes and 950 elements as it is show in Figure 28.

The water flows from section A–B to section C–D. Boundary conditions include water flow rate along boundary A–B of 100 m^3/s and water flow elevation of 1 m along boundary C-D. Boundaries A–D and B–C are vertical walls, where a slip velocity condition is imposed.

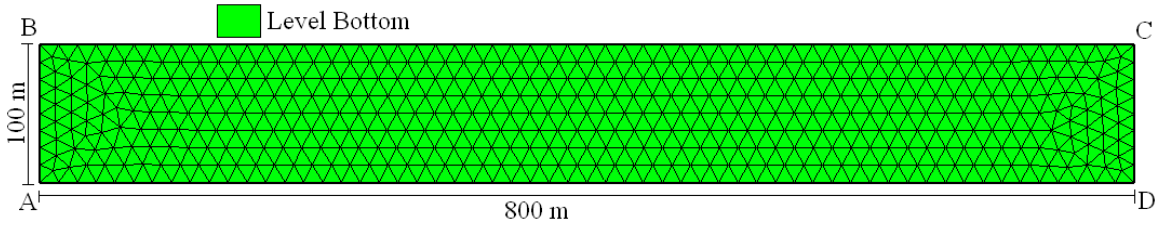

Figure 28. Channel with uniform width. Level Bottom in the numerical mesh.

Numerical Model Results

Figure 29 shows the effects of change Manning's roughness coefficient in the numerical water depths calculated for RiverFLO-2D and FESWMS along the channel.

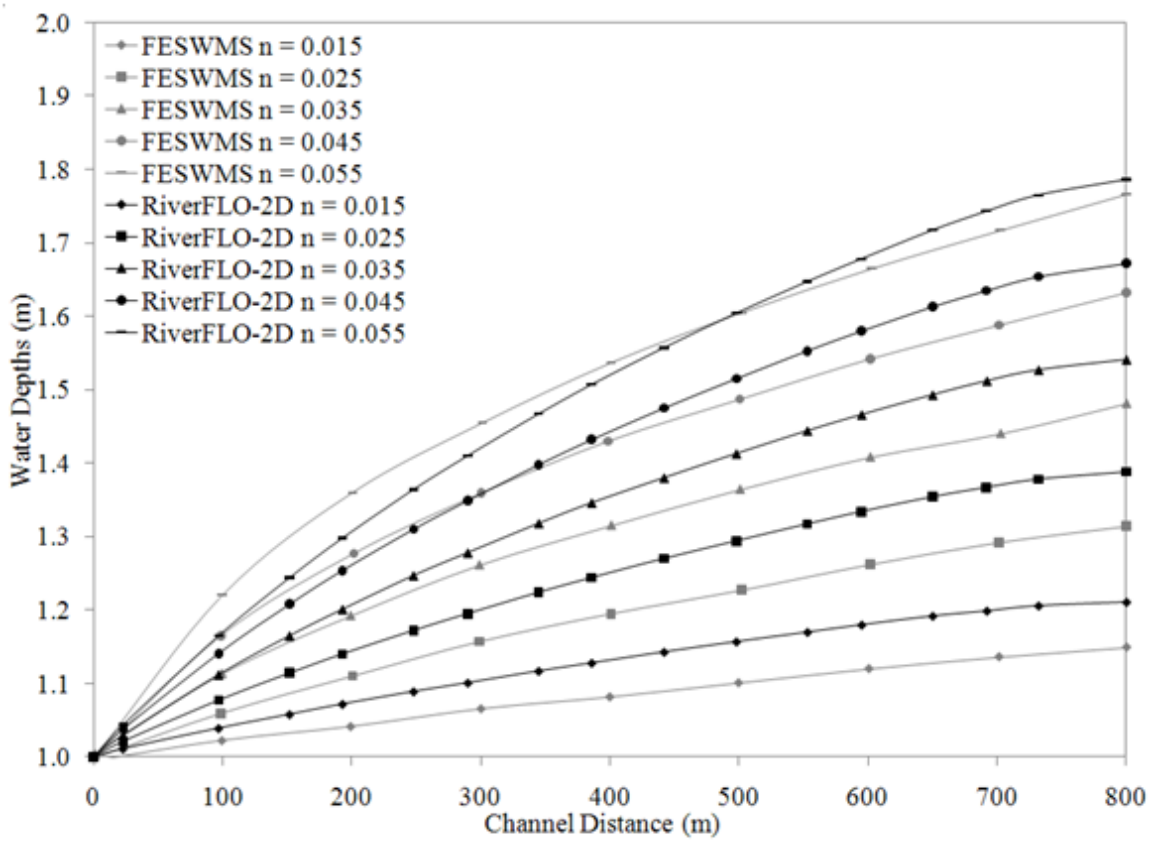

Figure 29. Channel with uniform width. RiverFLO-2D and FESWMS water depths along the center of channel for different bed roughness.

Figure 30 shows the comparison of RiverFLO-2D numerical results and FESWMS numerical results.

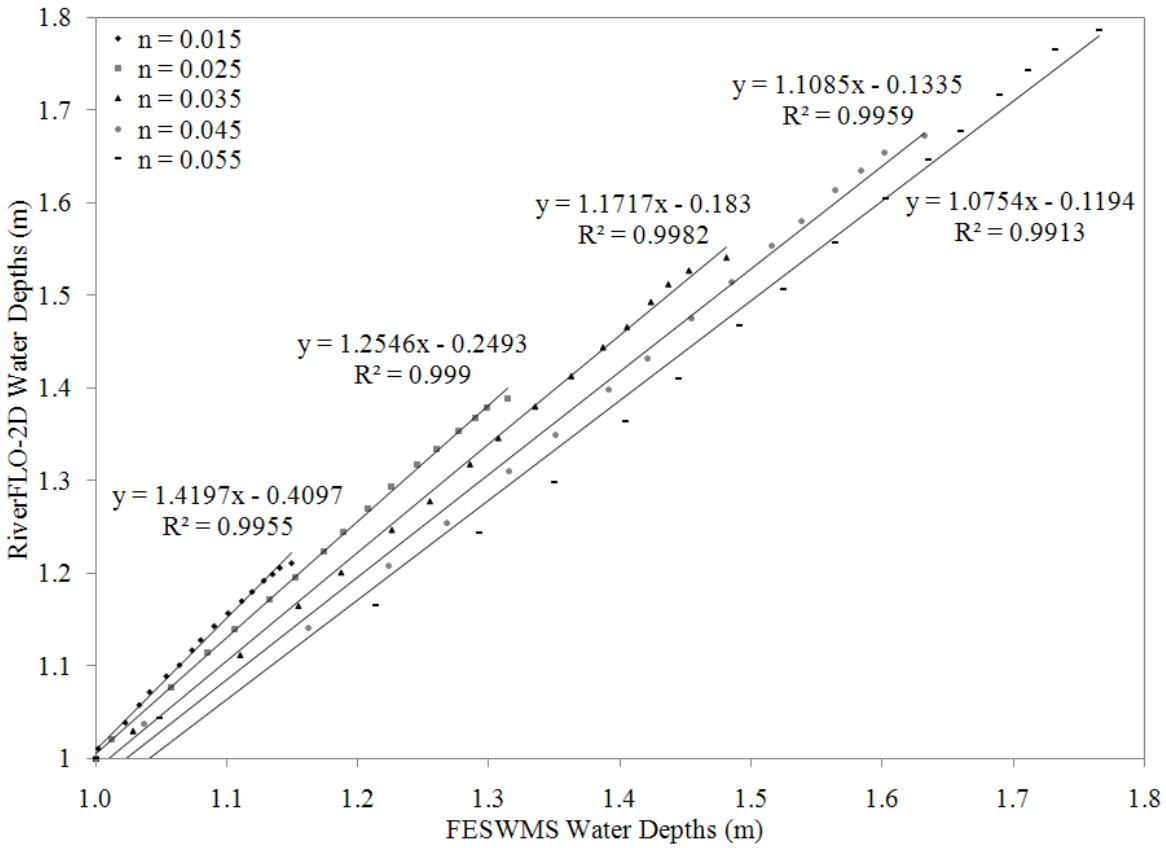

Figure 30. Channel with uniform width. Comparison of RiverFLO-2D and FESWMS Numerical Results along the center of channel.

It can be concluded that RiverFLO-2D numerical results are similar with FESWMS numerical results as it shows in Figure 30, with R^2 of 0.99 for five different scenarios. Figure 29 depicts the larger *n* of Manning coefficients predicting higher water depths. This test simulation starts with a completely dry bed, showing the RiverFLO-2D capacity to correctly handle the bed dry condition for flooding events. It is important to specify that FESWMS should start the simulation using a completely wet mesh that converges in time to the solution; this is a big disadvantage that was solved by using the adequate wet and dry technique.

3.1.6 Infiltration

Case Description

The purpose of this test is to verify the performance of the model when infiltration is taken into consideration in the simulation. The Green & Ampt approximation was used to calculate the amount of water that is loss by infiltration in this verification test (see subchapter 2.3). RiverFLO-2D results are compared with results presented by Chow et al., 1988.

The configuration of the basin consists of a rectangular simplified basin with dimensions L x L, where L is equal to 1 m with a flat horizontal bed, see figure below. The finite element mesh has 152 nodes and 259 elements as it is show in Figure 31.

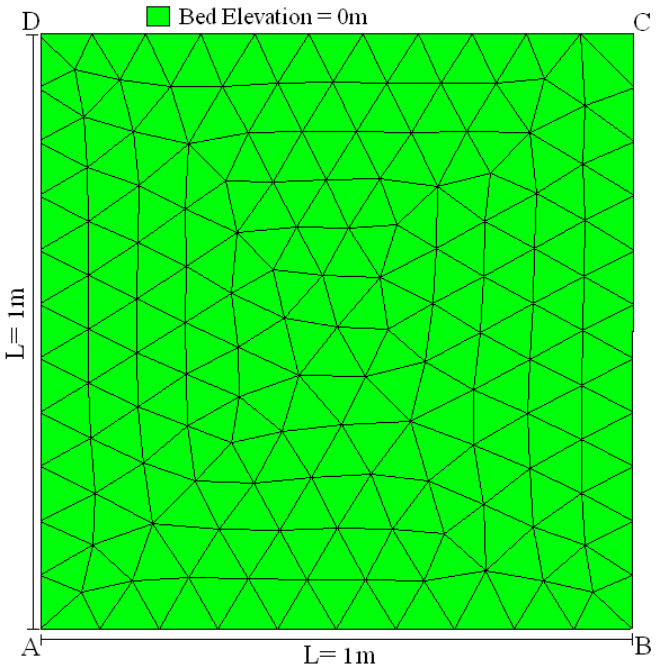

Figure 31. Infiltration test. Bed Elevations in the numerical mesh.

The water comes from rainfall over the entire basin. Boundaries A–B, B–C, C–D and D–A are open boundaries. The initial condition is a dry bed over the entire basin.

The infiltration parameters that are functions of soil characteristics are set uniform for the basin as follow:

1. The saturated hydraulic conductivity (K_s) is 1.09 cm/h
2. An average capillary suction in the wetted zone (ψ_f) is 11.01 cm
3. The soil moisture deficit (θ) is 0.247. Soil moisture deficit is equal to effective soil porosity times the difference in final and initial volumetric soil saturations.

The rainfall intensity (i) is variable in time and uniform in space and it can be seen in the following table. The storm has duration of 3 hrs (see Table 4).

Table 4. Infiltration test. Rainfall Distribution.

Time (min)	**Rainfall Intensity (cm/h)**
0 - 10	1.08
10 - 20	1.26
20 - 30	1.56
30 - 40	1.92
40 - 50	2.22
50 - 60	2.58
60 - 70	3.84
70 - 80	6.84
80 - 90	19.08
90 - 100	9.90
100 - 110	4.86
110 - 120	3.12
120 - 130	2.52
130 - 140	2.16
140 -150	1.68
150 - 160	1.44
160 - 170	1.14
170 -180	1.02

Numerical Model Results

Figure 32 presents the water depths versus time for RiverFLO-2D in one numerical cell of the domain and the solution reported by Chow et al., 1988. The results are the same for each cell of the numerical domain.

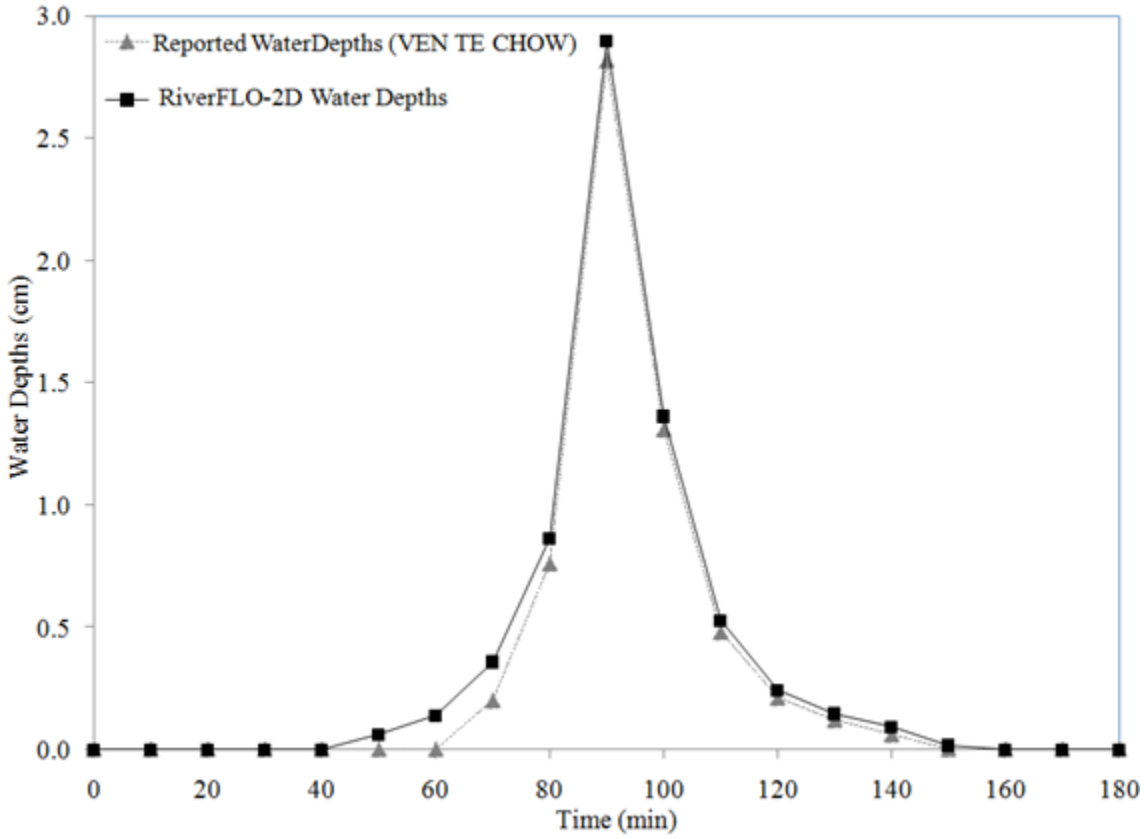

Figure 32. Infiltration test. Water Depths for Chow, et al., 1988 and RiverFLO-2D.

Table 5 presents the conservation of volume using the Green-Ampt formulation in RiverFLO-2D. The total rainfall depth is 11.37 cm and the total depth of water at the end of the simulation in the numerical mesh is 11.61 cm. The average numerical error for the Green- Ampt computation in the total volume of water is 2% which is below of the maximum error reported by Li et al., 1976 that is 8% and the maximum error reported

by Eggert, 1976 of 20% by using the Green & Ampt approximation. The numerical velocity field is equal to zero for the entire mesh.

Table 5. Infiltration test. Conservation of volume using the Green & Ampt formulation in RiverFLO-2D.

Total Volume (cm)		
Rainfall	**RiverFLO-2D Results Infiltration plus Runoff**	**Relative Average Error (%)**
11.37	11.61	2

Figure 33 shows the comparison of the results from RiverFLO-2D model with the theoretical reported results from Chow et al., 1988.

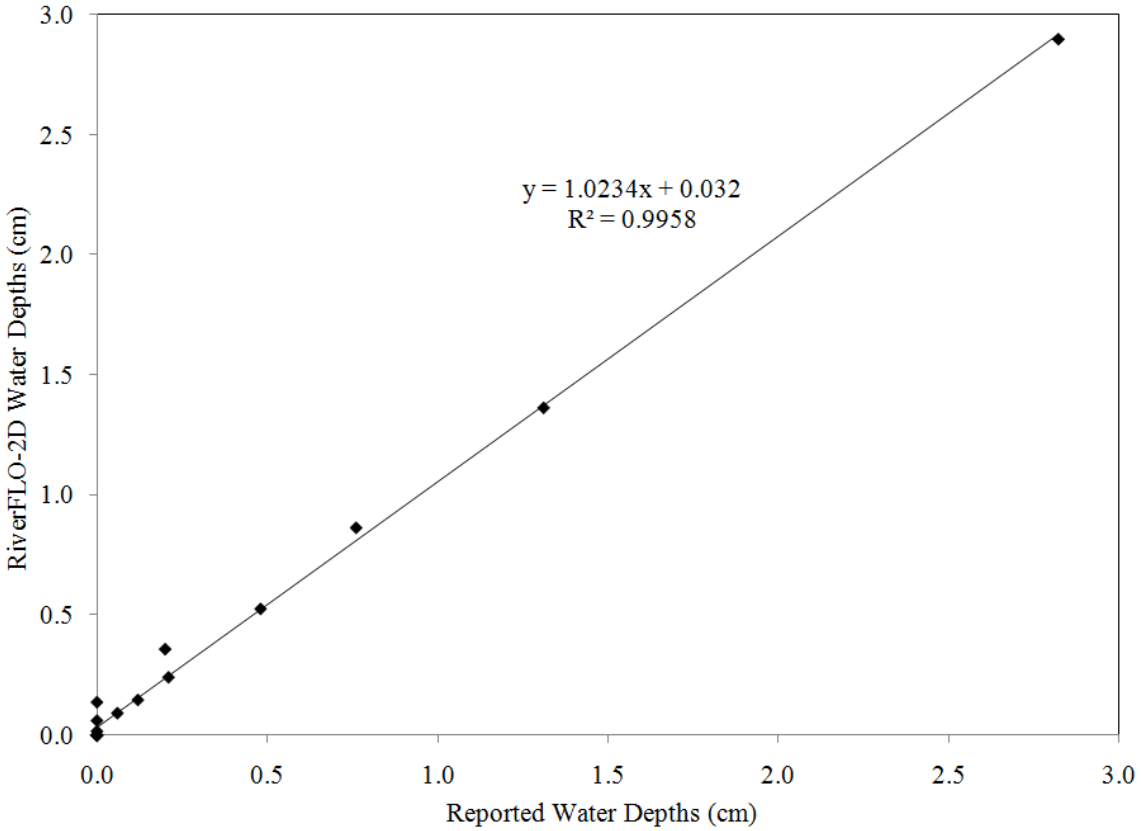

Figure 33. Infiltration test. Comparison of RiverFLO-2D and theoretical water depths using a simplified Green & Ampt Solution.

The results indicates that the RiverFLO-2D water depths computed on the modified Green-Ampt method compare with the theoretical results reported by Chow et al., 1988 (see Figure 32 and Figure 33), with an R^2 of 0.99.

3.1.7 Preservation of Rainfall Volume for a Simplified Pool

Case Description

The purpose of this test is to evaluate the rainfall calculations included in the enhanced RiverFLO-2D and the preservation of the rainfall volume that falls over a simplified pool. The numerical mesh and rainfall intensity were selected arbitrarily for this verification test. The rainfall volume was compared with the numerical water volume at the end of the simulation.

The configuration of the basin consists of a rectangular simplified pool with dimensions L x L, where L is equal to 1 m with a flat bed slope, see figure below. The finite element mesh has 19 nodes and 24 elements as it is show in Figure 34. Boundaries A-B, B-C, C-D and D-A are vertical walls. The duration of the rainfall is 1h with a numerical timestep of 0.1s. A 0.9 lumping parameter was used for this simplified rainfall test.

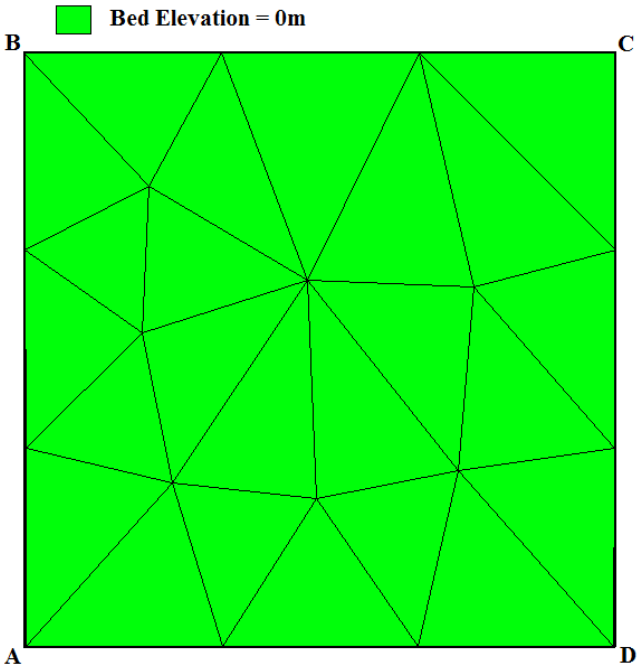

Figure 34. Rainfall on a simplified pool. Bed Elevations in the numerical mesh.

The rainfall occurs over the simplified pool with different intensities and durations that vary in space and time (Table 6).

Table 6. Rainfall on a simplified pool. Rainfall data for case 1, 2 and 3.

RAINFALL				
CASE	Sub Areas	Time (h)	Duration (h)	Intensity (mm/d)
1	1	0-1	1	1000
2	1	0 -0.5 0.5 -1	0.5 0.5	1000 2000
3	1	0 -0.5 0.5 -1	0.5 0.5	1000 2000
	2	0 -0.5 0.5 -1	0.5 0.5	2000 1000

Numerical Model Results

The following tables present the numerical results of water volume for case 1 to 3 and the average relative error calculated comparing the numerical water volume and the analytical rainfall volume at the end of the simulation.

Table 7. Rainfall on a simplified pool. Conservation of rainfall volume for Case 1.

Case 1					
Rainfall			Volume (m^3)		Average Relative Error (%)
Time (h)	Intensity (mm/d)	Duration (h)	Analytical	RiverFLO-2D	
0 - 1	1000	1	0.041667	0.041667	0.00

Table 8. Rainfall on a simplified pool. Conservation of rainfall volume for Case 2.

Case 2					
Rainfall			Volume (m^3)		Average Relative Error (%)
Time (h)	Intensity (mm/d)	Duration (h)	Analytical	RiverFLO-2D	
0 - 0.5	1000	0.5	0.020833	0.020833	0.00
0.5 - 1	2000	0.5	0.041667	0.041647	0.05

Table 9. Rainfall on a simplified pool. Conservation of rainfall volume for Case 3.

Case 3	RAINFALL			VOLUME (m^3)		Average Relative Error (%)
Subarea	Time (h)	Intensity (mm/d)	Duration (h)	Analytical	RiverFLO-2D	
1	0 - 0.5	1000	0.5	0.031250 0.062500	0.031293 0.062500	0.14
	0.5 - 1	2000	0.5			
2	0 - 0.5	1000	0.5	0.031250 0.062500	0.031250 0.062500	0.14
	0.5 - 1	2000	0.5			

Table 7, Table 8 and Table 9 present the conservation of rainfall volume by comparing the analytically calculated rainfall volume with the numerical water volume calculated from the water depth ponding on the pool bed at the end of the numerical time.

The results indicate that the RiverFLO-2D water depths computed on the modified rainfall features compare with the analytical results. The comparison between the numerical and the analytical water volumes (see Table 7 to Table 9), presents a low average relative error.

3.1.8 Surface Runoff in a Simplified Parking Lot

Case Description

The purpose of this test is to verify the performance of the model when runoff is taken into consideration in the simulation. The test involves the verification of the flood wave propagation over an idealized parking lot at Duke University, as it can be seen in Figure 35 (Kazezyilmaz-Alhan & Medina, 2007).

The configuration consists of a 182.88m long rectangular simplified parking lot with a bed slope of 0.0016. Rainfall last for 30 min with an intensity of 50.8mm/h. The finite element mesh has 2019 nodes and 3030 elements with an *n* of Manning of 0.025.

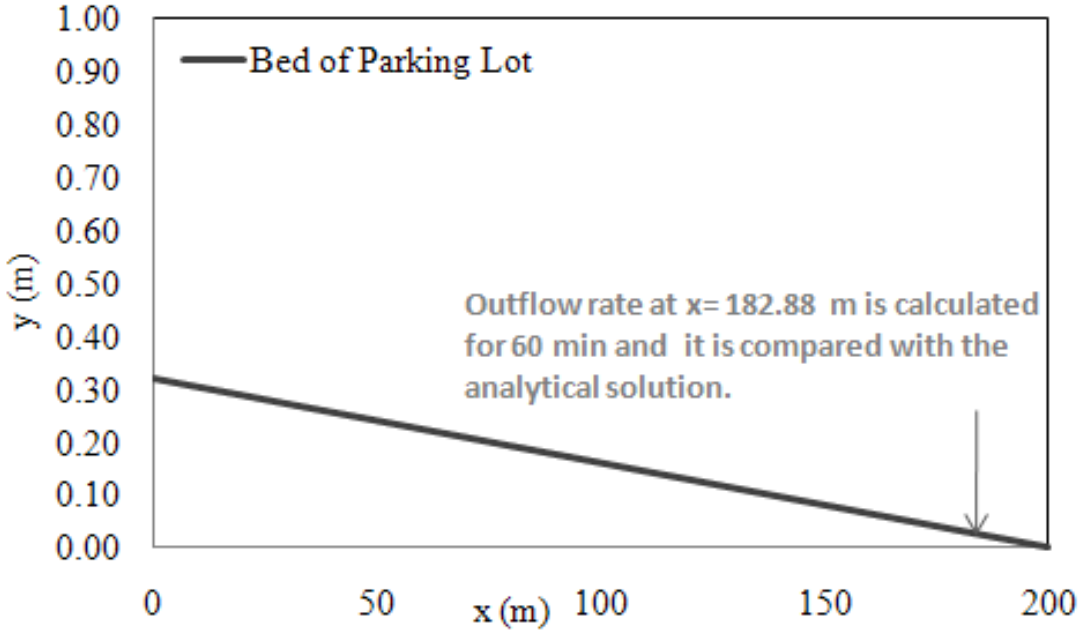

Figure 35. Surface runoff test in a simplified parking lot. Sketch of a simplified parking lot at Duke University.

Numerical Model Results

The numerical outflow rate at the end of the idealized parking lot is calculated for 60 min and it is compared with the analytical solution, see Figure 36.

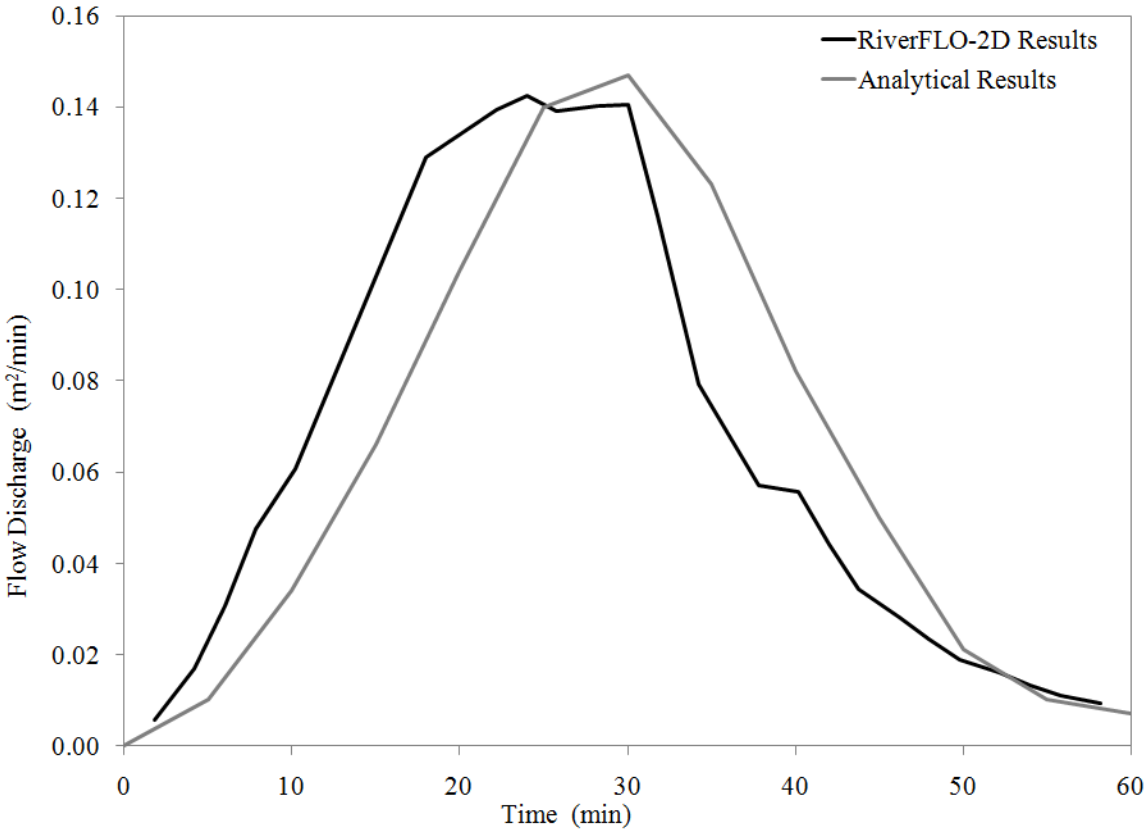

Figure 36. Surface runoff test in a simplified parking lot. Flow Discharge at x=182.88 Analytical Solution and RiverFLO-2D.

Figure 37 shows the results of the numerical discharge compares with the analytical discharge.

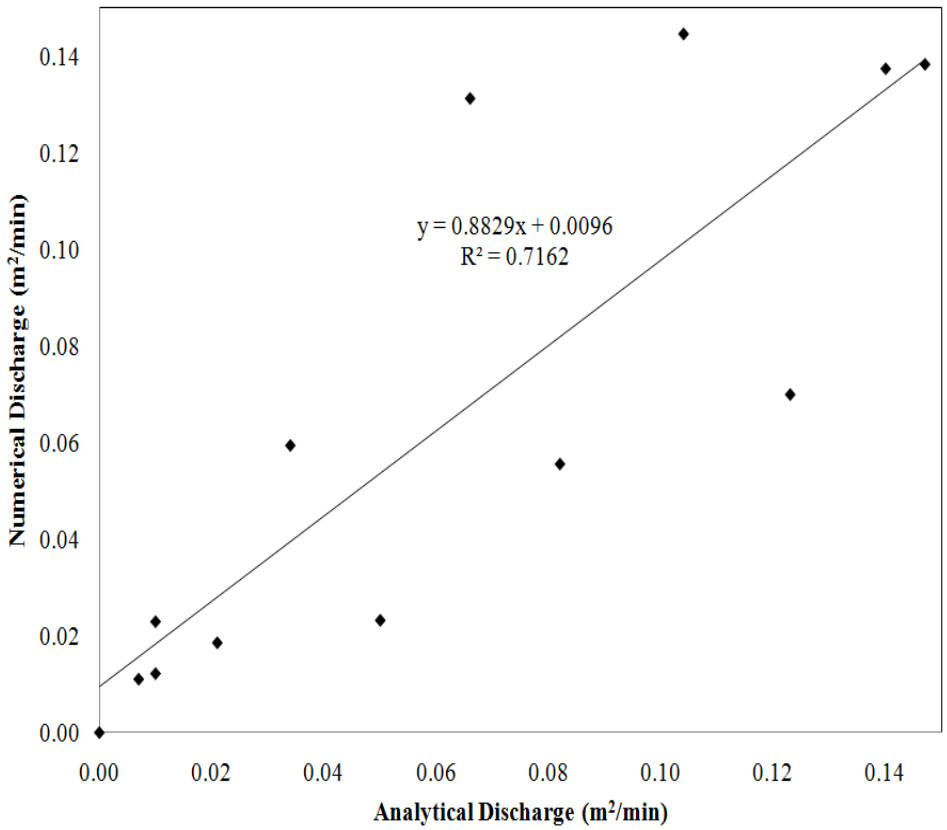

Figure 37. Surface runoff test in a simplified parking lot. Comparison of the flow discharge at x=182.88 for RiverFLO-2D results and the analytical solution.

Figure 37 illustrates the comparisons of flow discharge versus time for the numerical and the analytical solution of the kinematic wave, which assumes that the weight or gravity force of flowing water is simply balanced by the resistive forces of bed friction (Wooding, 1965; Henderson & Wooding, 1964). The analytical and computed flow discharges are shifted approximately 3min, and the peak is underestimated by the computed flow discharge, although the results are coincident. The difference between both results can be because the analytical solution is for the kinematic wave approximation and the numerical solution includes is for the full shallow water equations. Numerical and analytical results are in agreement with an R^2 of 0.71.

3.2 Laboratory Test Cases

3.2.1 Flood Wave over a Triangular Obstacle

Case Description

In this test, the enhanced RiverFLO-2D model results are compared with experimental flood measurements from a laboratory study performed by Recherches Hydrauliques Laboratory Chatelet and University of Bruxelles (Brufau et al., 2002). The test involves the advance of a flood wave over a triangular obstacle located on a horizontal concrete bed channel as indicated in Figure 38. Initial reservoir depth is 0.75 m. The test starts by instantaneously removing the dam-gate. Depth evolution is measured at gauging points G1, G2, G3 and G4 shown in Figure 38.

The finite element mesh used in the numerical computations has 6793 nodes and 12802 triangular elements (see Figure 39). Manning's *n* coefficient was set to 0.0125. The downstream condition is an open outlet boundary and slip conditions are imposed on channel walls.

The total simulation time is 40 s. and the time step is 0.005 s. The output data is reported every 1 s.

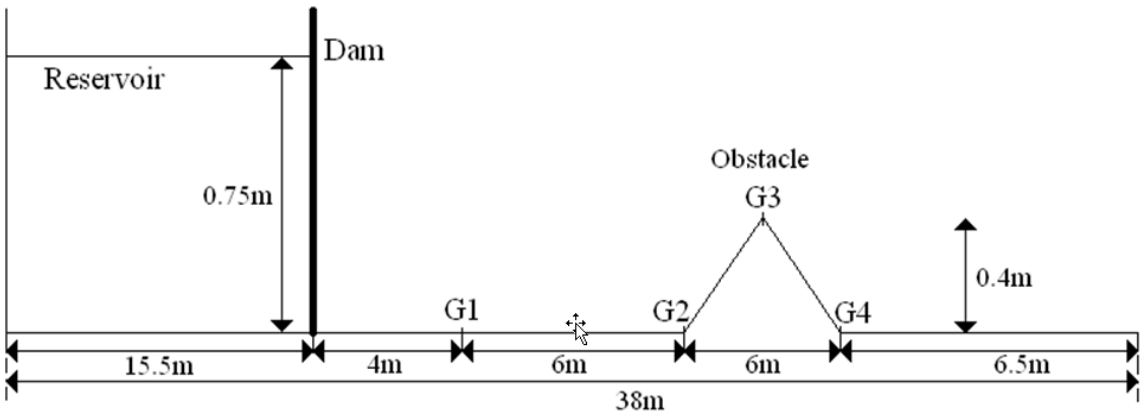

Figure 38. Flood wave test over a triangular obstacle. Experimental model for dam-break flood over a triangular obstacle. G1, G2, G3 and G4 indicate location of gauging points.

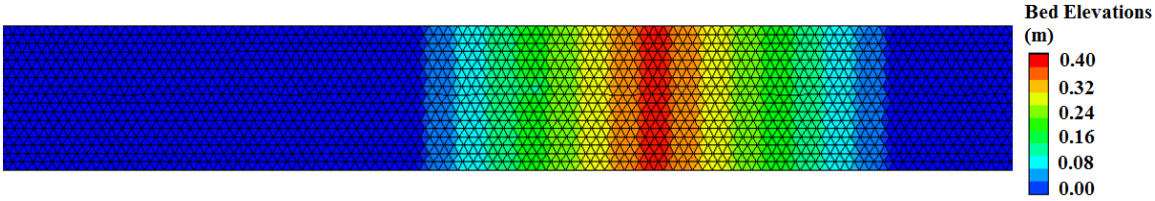

Figure 39. Flood wave test over a triangular obstacle. Bed Elevations in the numerical mesh.

Numerical Model Results

Numerical results were compared with the experimental measurements for the 4 gauging points or stations. Figure 40 to Figure 43 show the measured and predicted evolution of water depth at each station.

Figure 44 to Figure 47 show the water profiles for 3 s, 5 s, 10 s, and 20 s since dam removal. Note that the model predicts a steep front, which gives an indication that the model is not introducing excessive numerical diffusion.

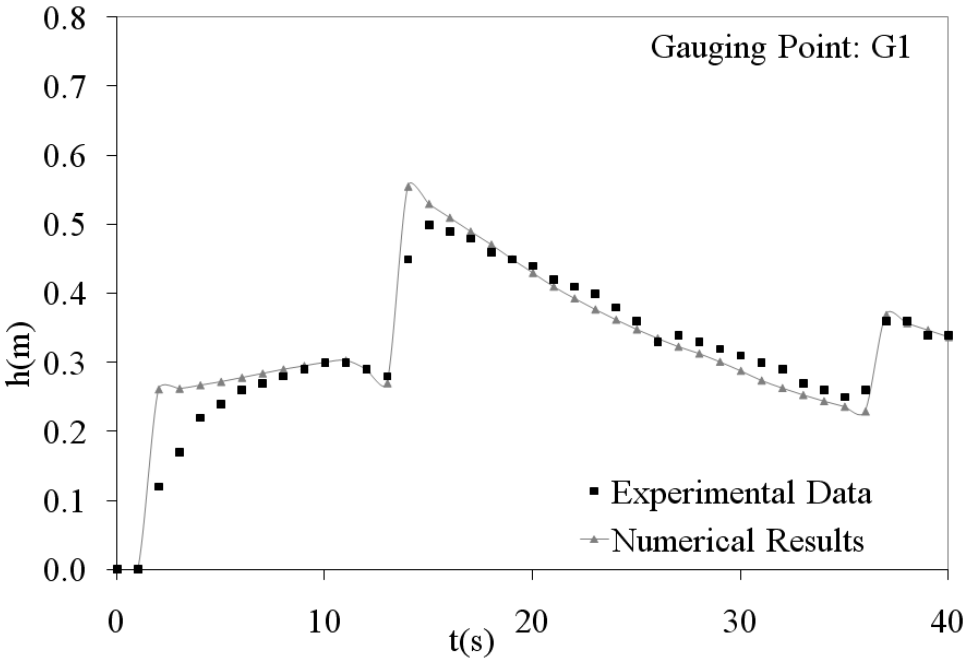

Figure 40. Flood wave test over a triangular obstacle. Free surface evolution of the dam-break wave at gauge points G1.

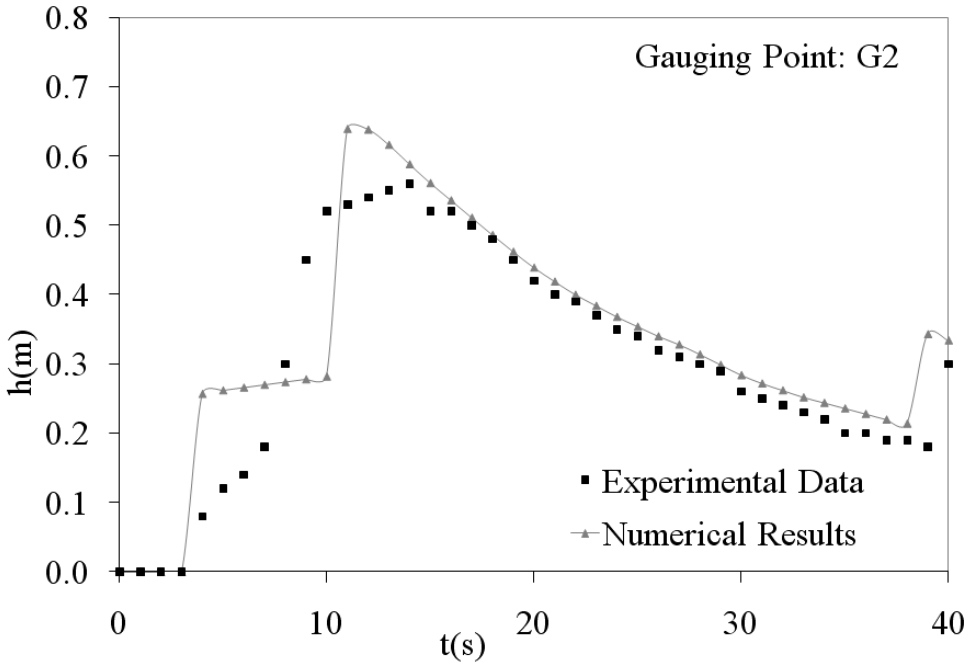

Figure 41. Flood wave test over a triangular obstacle. Free surface evolution of the dam-break wave at gauge points G2.

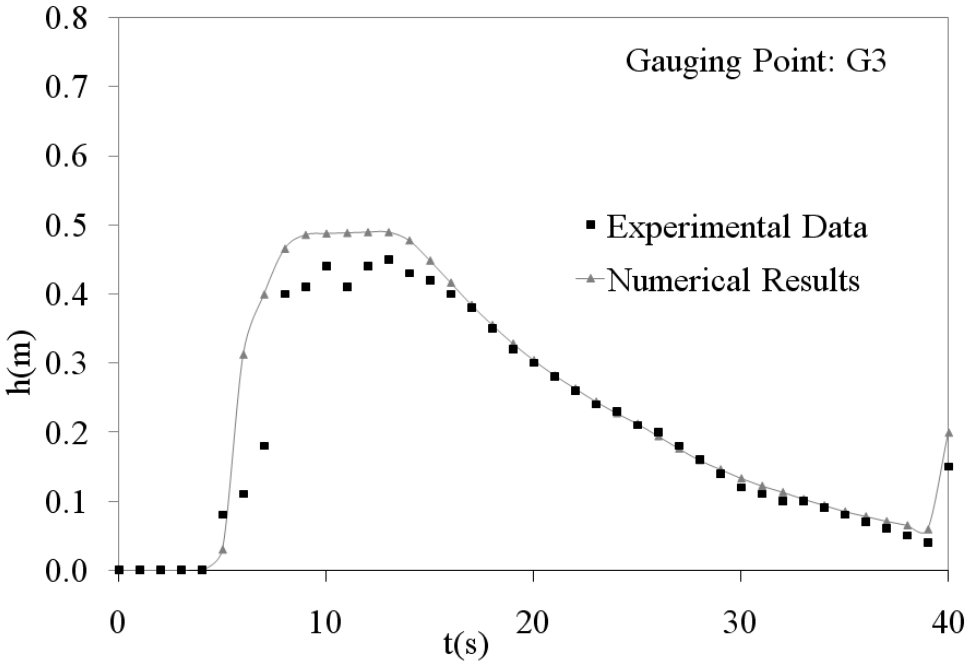

Figure 42. Flood wave test over a triangular obstacle. Free surface evolution of the dam-break wave at gauge points G3.

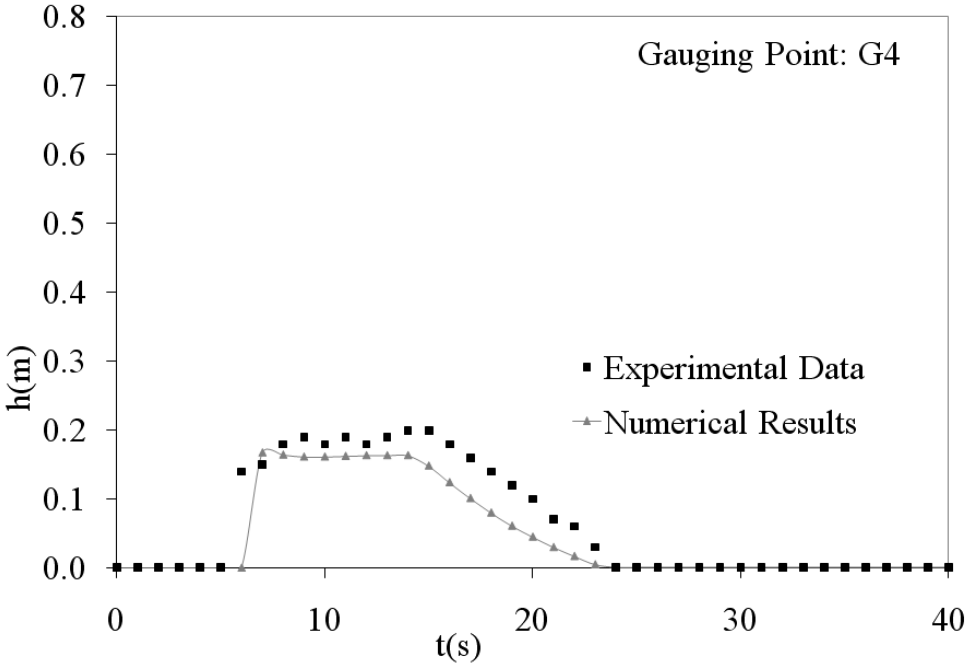

Figure 43. Flood wave test over a triangular obstacle. Free surface evolution of the dam-break wave at gauge points G4.

Some discrepancies may be observed (see Figure 40 to Figure 43) particularly at gauging point G2, where numerical results tend to predict a steeper depth increase than the experimental model. It is possible that this could be attributed to the instantaneous dam removal assumption in the numerical model. In the experimental setup the dam removal takes a finite time and this lapse of time may induce a more gradual increase in water depths.

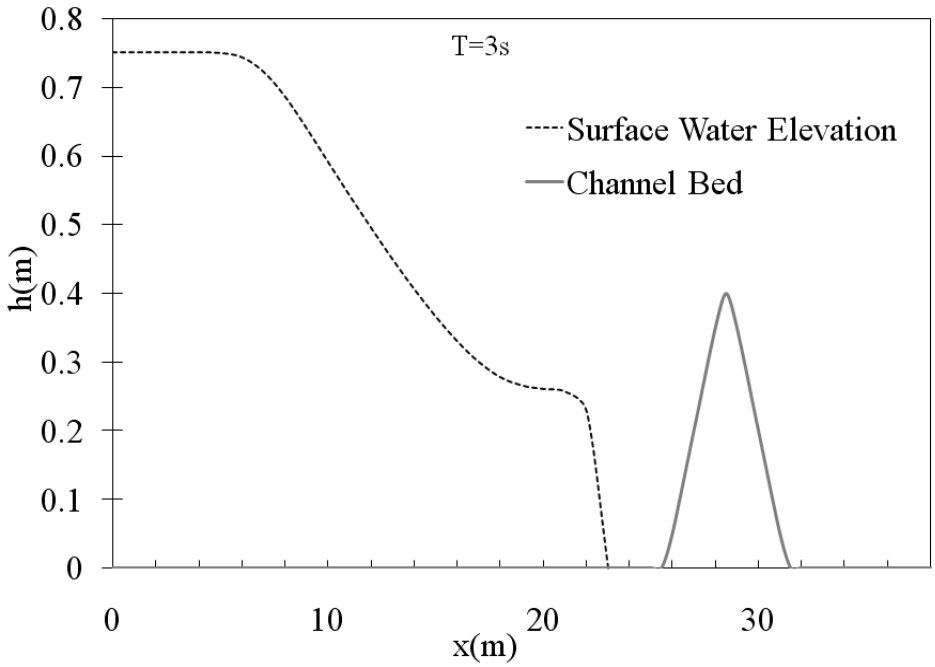

Figure 44. Flood wave test over a triangular obstacle. Numerical water surface profile for dam-break wave at 3 s.

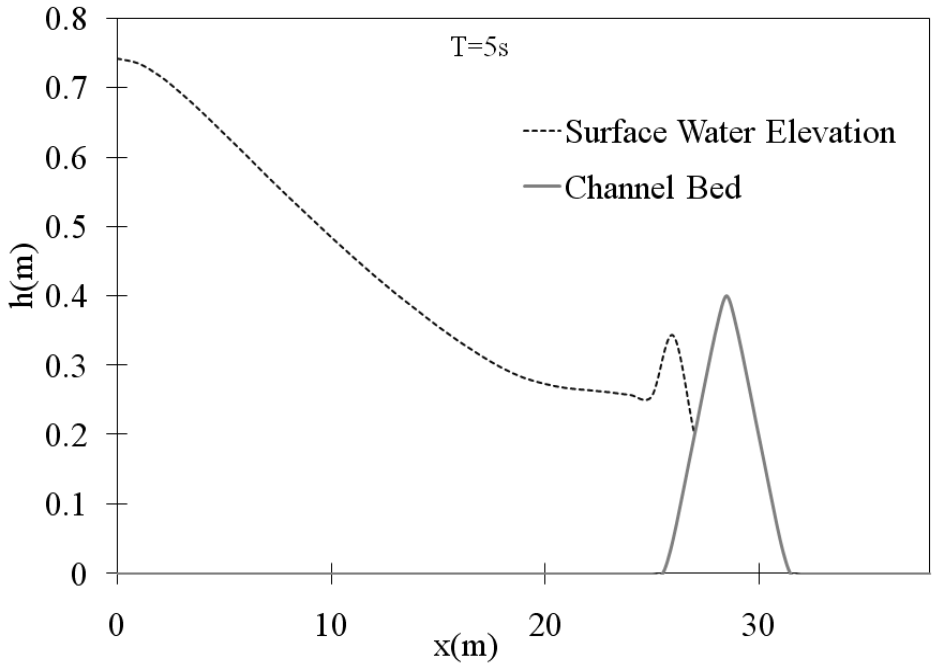

Figure 45. Flood wave test over a triangular obstacle. Numerical water surface profile for dam-break wave at 5 s.

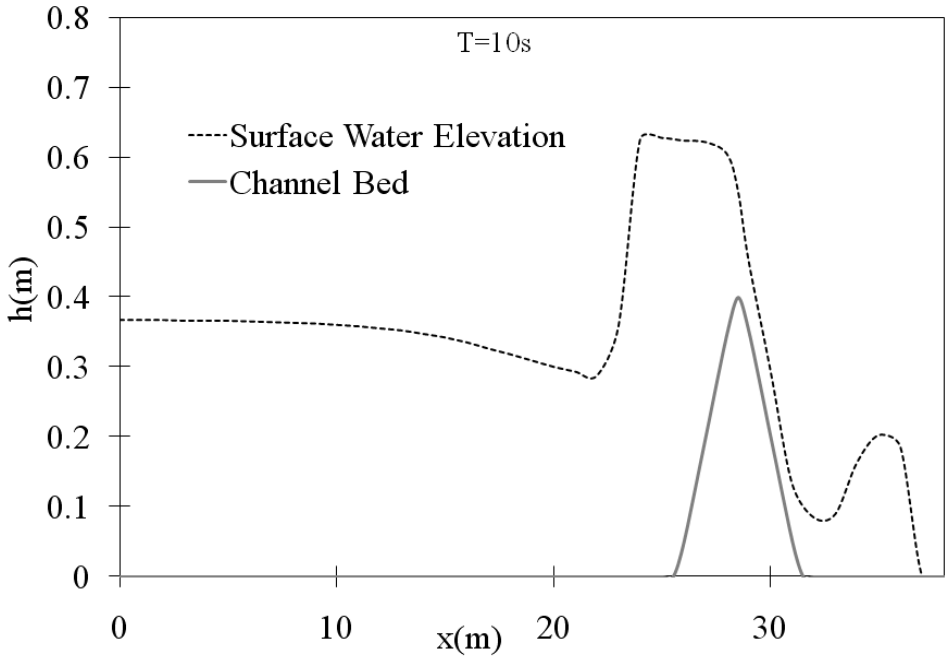

Figure 46. Flood wave test over a triangular obstacle. Numerical water surface profile for dam-break wave at 10 s.

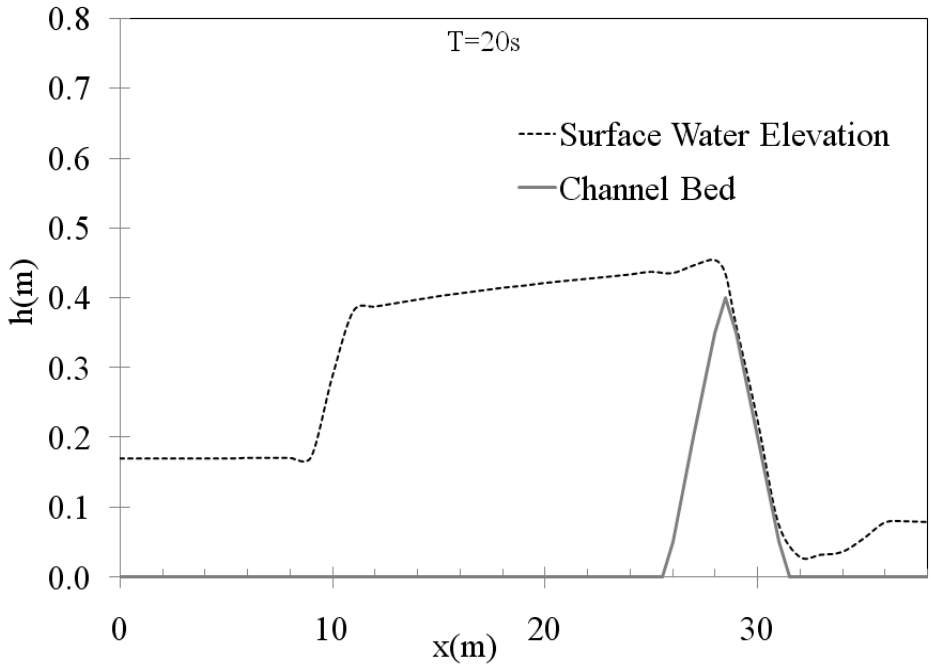

Figure 47. Flood wave test over a triangular obstacle. Numerical water surface profile for dam-break wave at 20 s.

Figure 48 compares the numerical water depths with the experimental data, since dam removal for a constant time step and for six different values of the lumping parameter (ϵ).

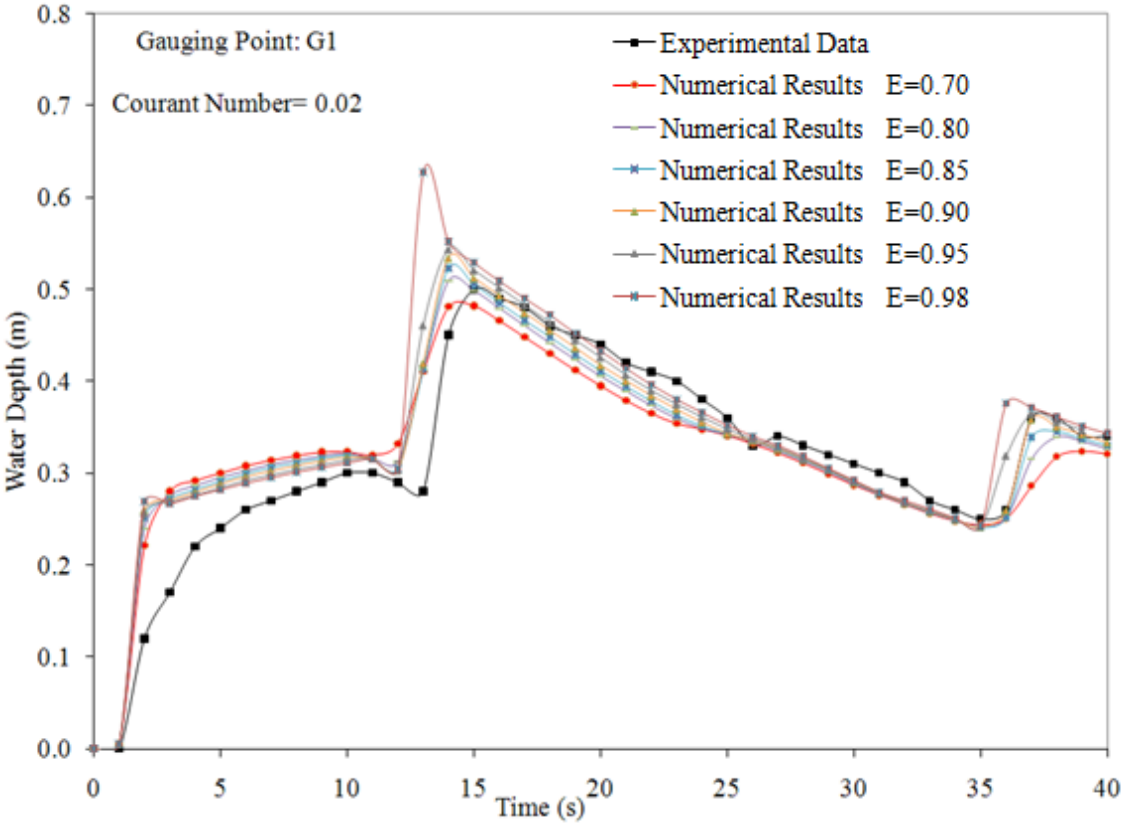

Figure 48. Flood wave test over a triangular obstacle. Numerical and experimental water depths for dam-break wave varying the lumping parameter and with a constant timestep of 0.001.

Figure 49 compares the numerical water depths with the experimental data, since dam removal for a lumping parameter equal to 0.95 and for six different values of the time step.

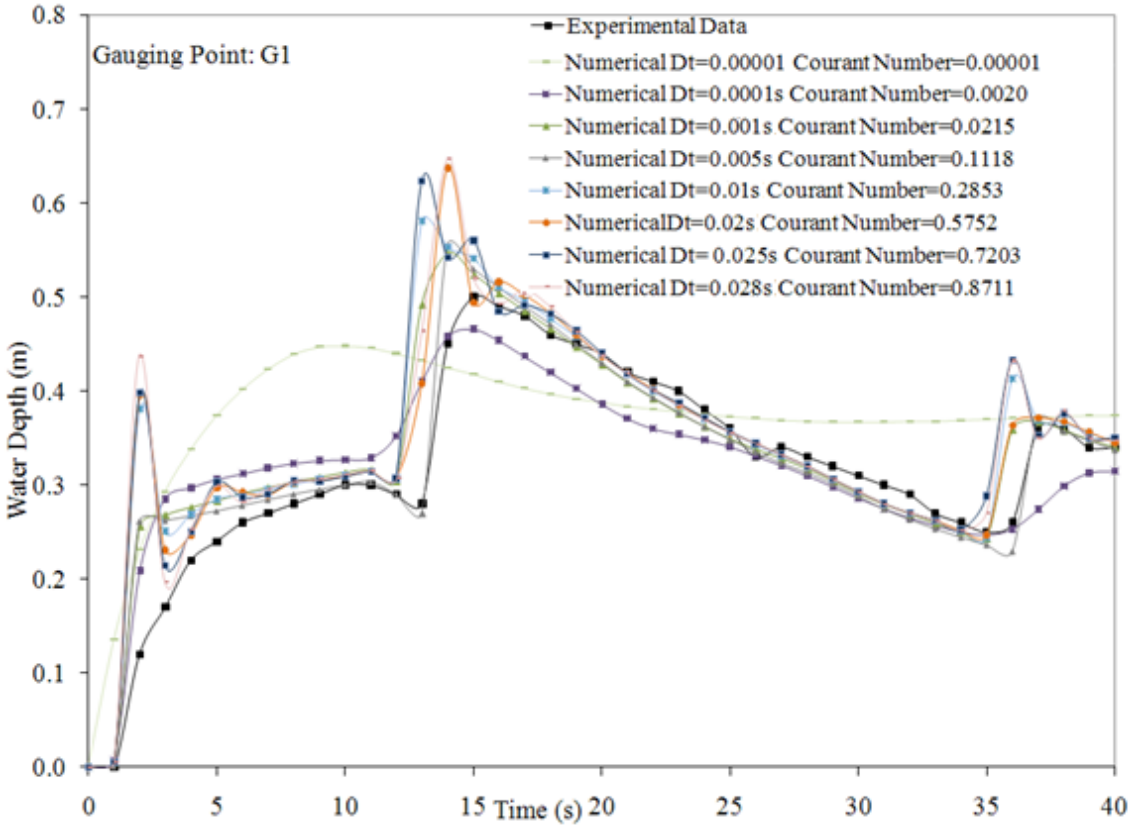

Figure 49. Flood wave test over a triangular obstacle. Numerical and experimental water depths for dam-break wave varying the time step and with a constant lumping parameter of 0.95.

Figure 49 shows that some numerical instability can be observed for the larger Courant Numbers in the analysis. Those instabilities are because the domain of dependence of the numerical method is not correctly catching the true physical domain of dependence. A time step between 0.001 and 0.005 generates a numerical solution with a better agreement with the experimental data.

Figure 50 shows the mass balance in percentage for the three wet and dry algorithms evaluated.

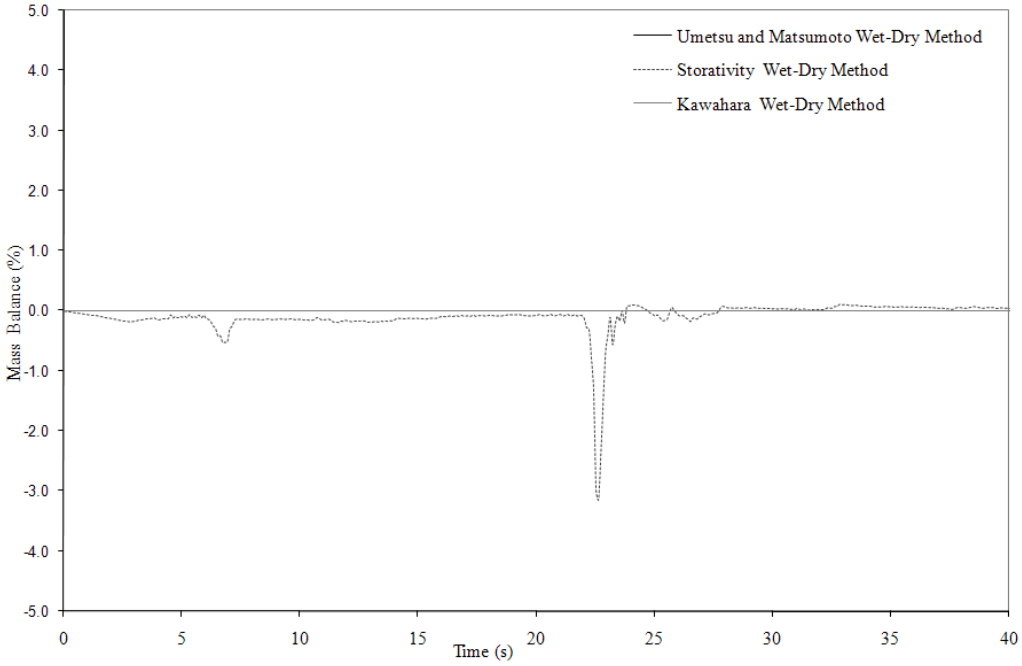

Figure 50. Flood wave test over a triangular obstacle. Mass Balance.

Figure 50 shows the mass balance in percentage for the three wet and dry algorithms evaluated, where both the Kawahara technique and Umetsu and Matsumoto technique present an acceptable conservation of volume. However, the presence of erroneous velocities for complex geometries or for domains with large dry areas was evident. The volume of mass has been computed as the difference between the initial volume of water and the differences between how much water is accumulate in the numerical elements and the outflow volume of water. The modification of the wet and dry technique excluding the totally dry elements from the mass matrix in Finite element method seems to be a very good approximation to correctly solve this problem.

Figure 51 to Figure 54 show the comparison between the numerical water depths and the experimental water depths for gauging point G1, G2, G3 and G4.

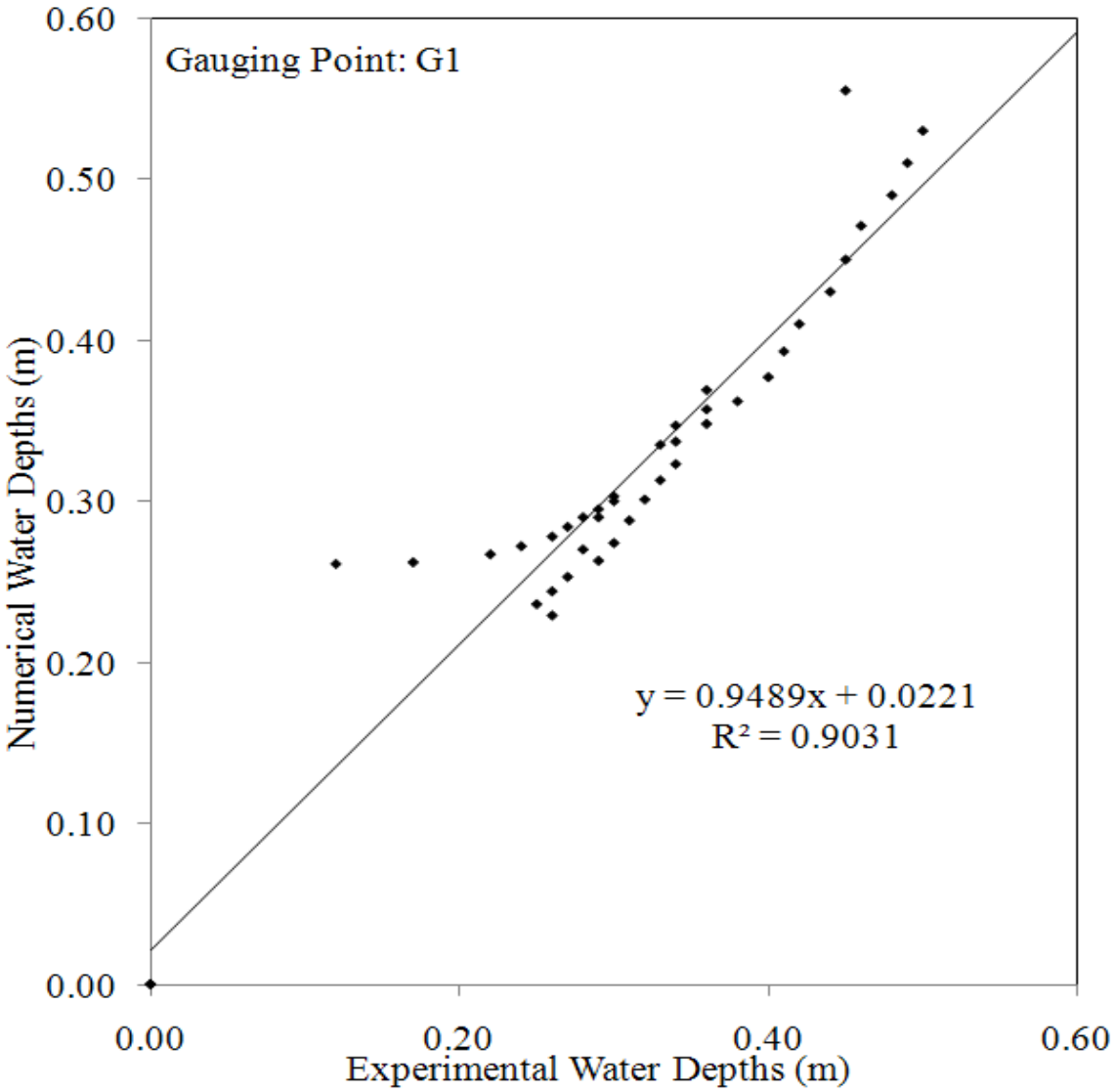

Figure 51. Flood wave test over a triangular obstacle. Comparison of RiverFLO-2D numerical and experimental water depths at gauge 1.

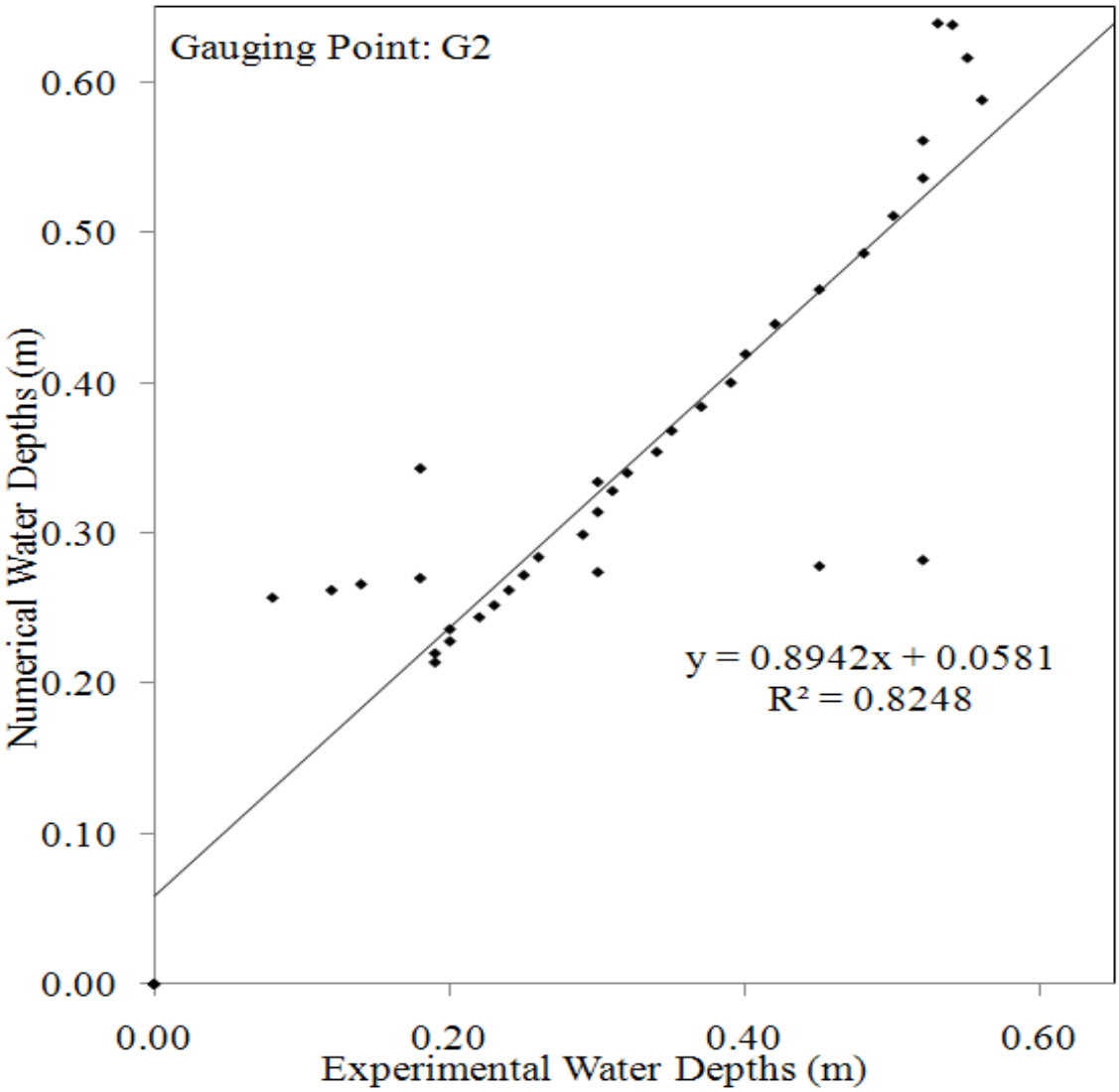

Figure 52. Flood wave test over a triangular obstacle. Comparison of RiverFLO-2D numerical and experimental water depths at gauge 2.

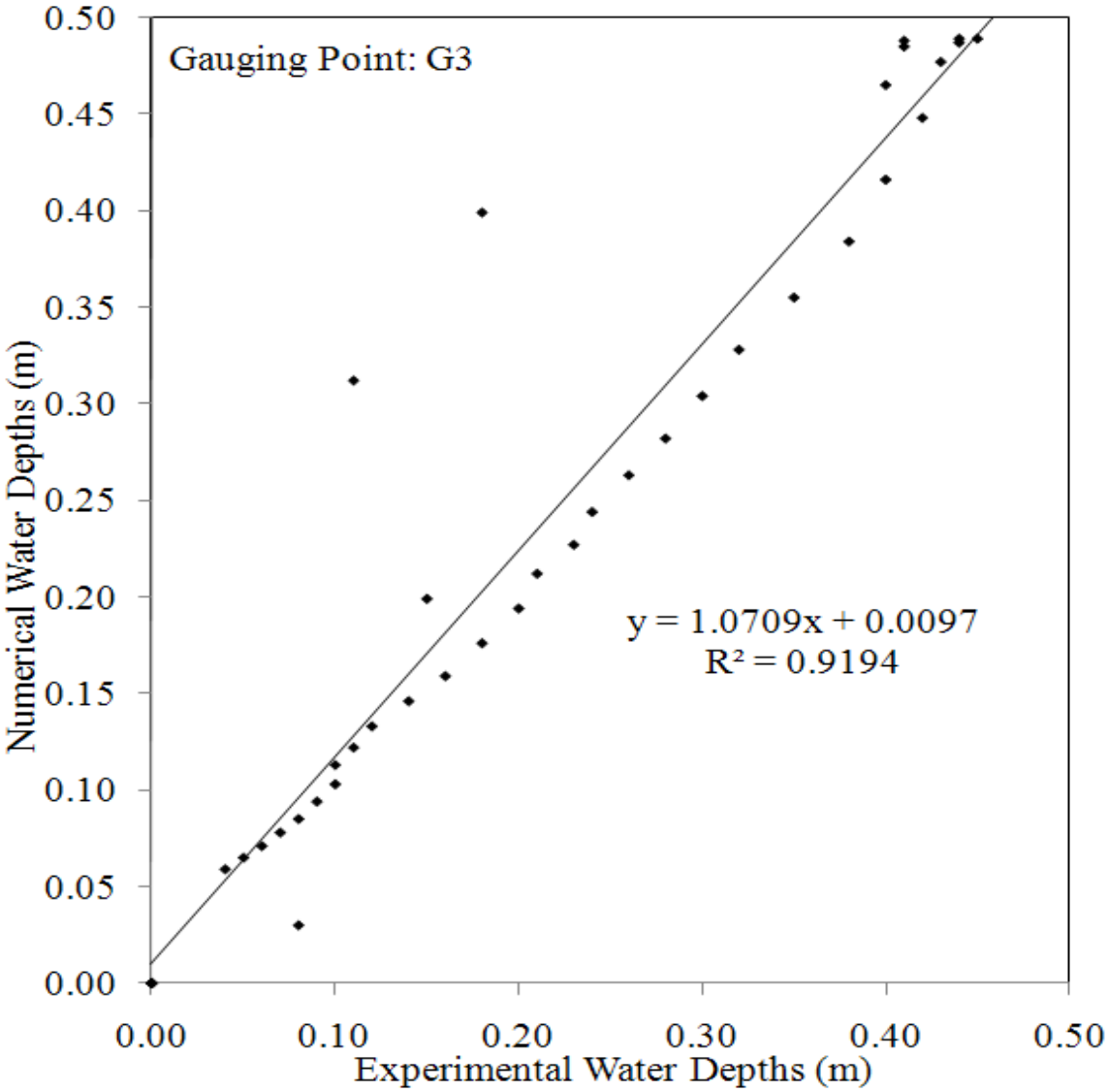

Figure 53. Flood wave test over a triangular obstacle. Comparison of RiverFLO-2D numerical and experimental water depths at gauge 3.

Figure 51 to Figure 54 shows the comparison between the numerical water depths and the experimental water depths for gauge G1, G2, G3 and G4 with a correlation factor between 0.82 and 0.91.

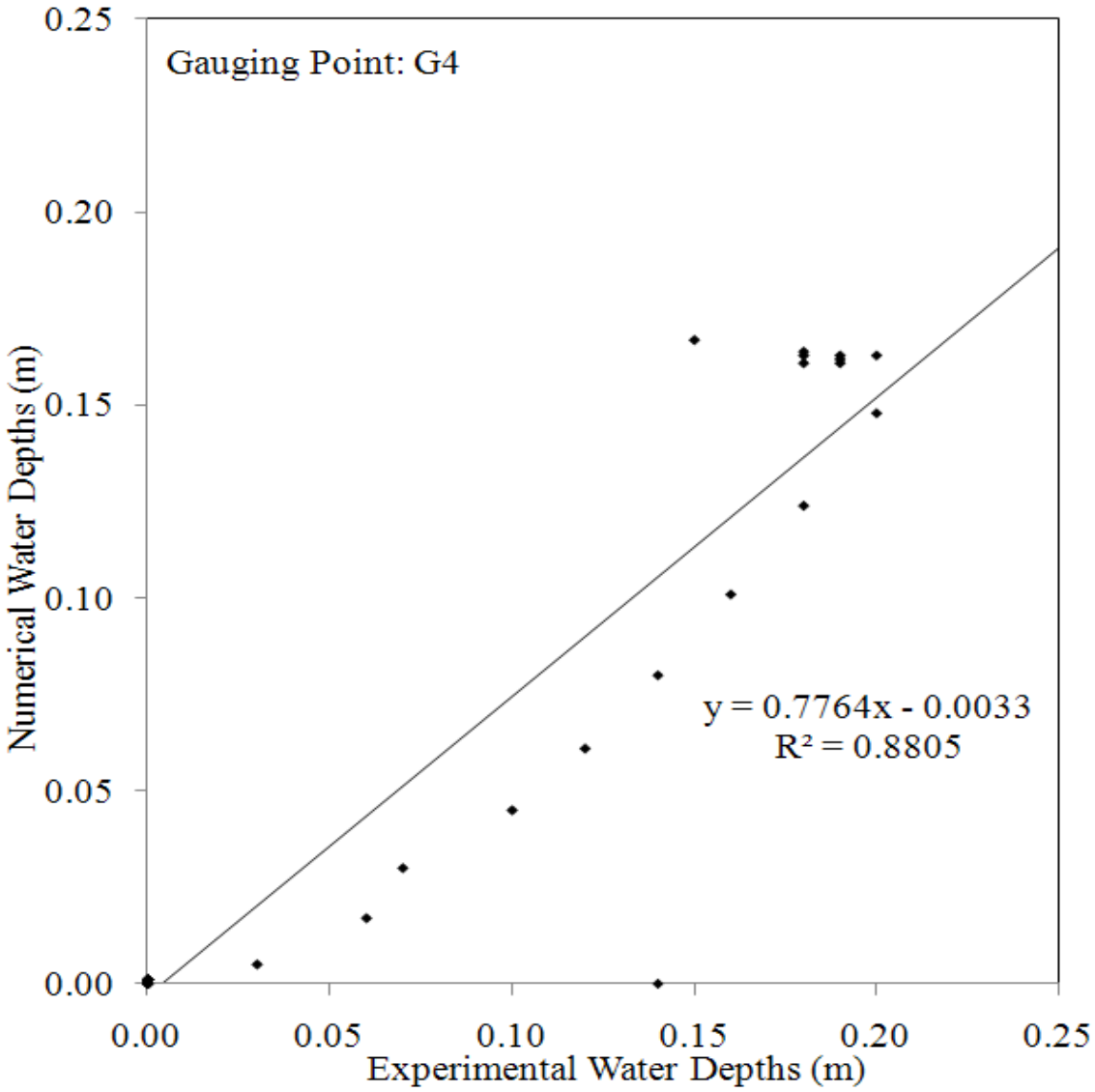

Figure 54. Flood wave test over a triangular obstacle. Comparison of RiverFLO-2D numerical and experimental water depths at gauge 4

Figure 55 to Figure 59 show the RiverFLO-2D water depths and velocity vectors. The figures present on top (a) of the following pages correspond with the RiverFLO-2D numerical simulation with Umetsu & Matsumoto, 1998 wet and dry technique. On bottom (b) the RiverFLO-2D numerical simulation including the dry and wet technique implemented in this research is shown.

Figure 55. Flood wave over a triangular obstacle. Numerical Water Depths and Velocity field for t=1s.
a) Umetsu & Matsumoto, 1998 dry and wet technique. b) With Wet and dry technique.

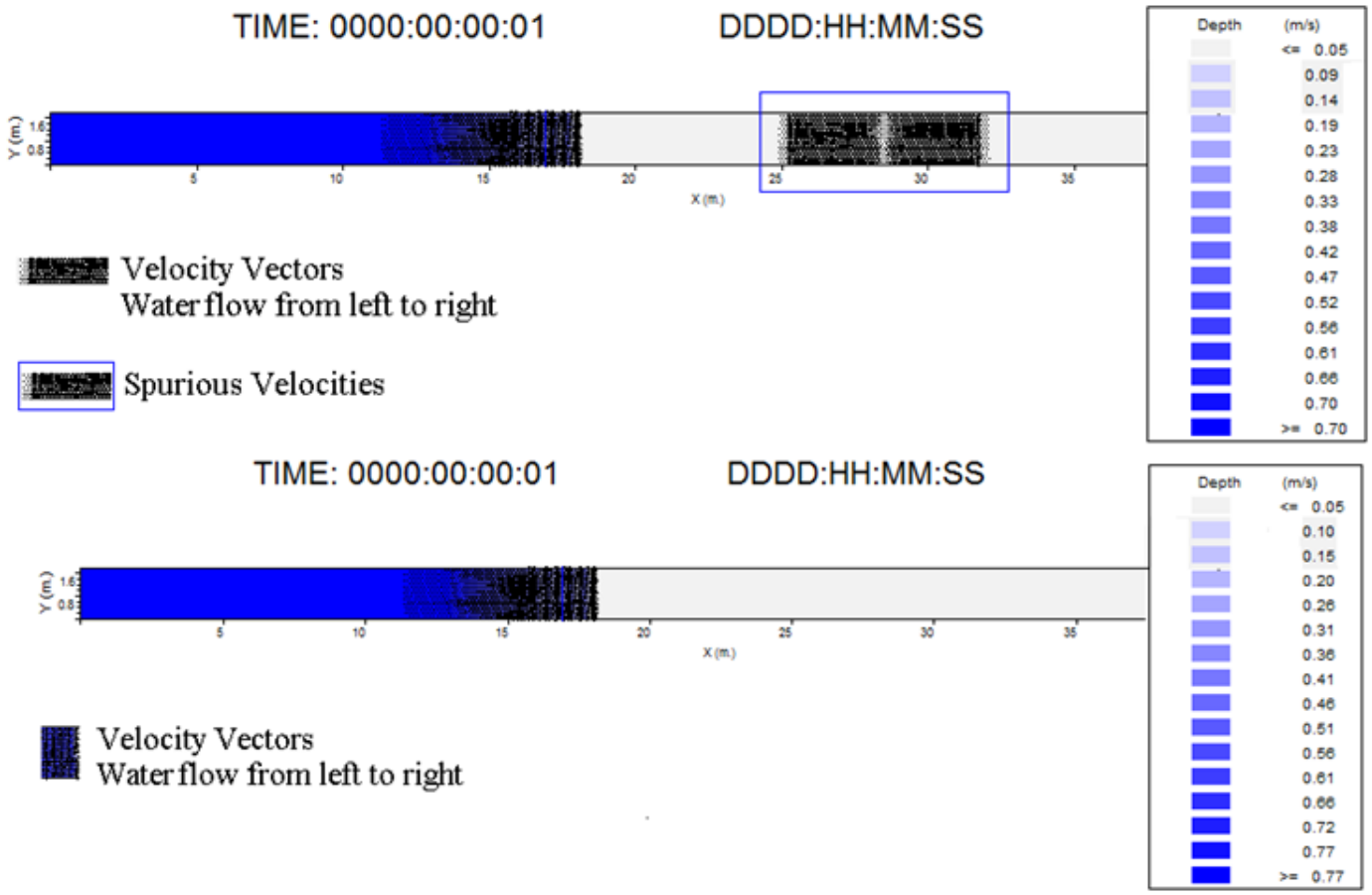

Figure 56. Flood wave over a triangular obstacle. Numerical Water Depths and Velocity field for t=2s.
a) Umetsu & Matsumoto, 1998 dry and wet technique. b) With Wet and dry technique.

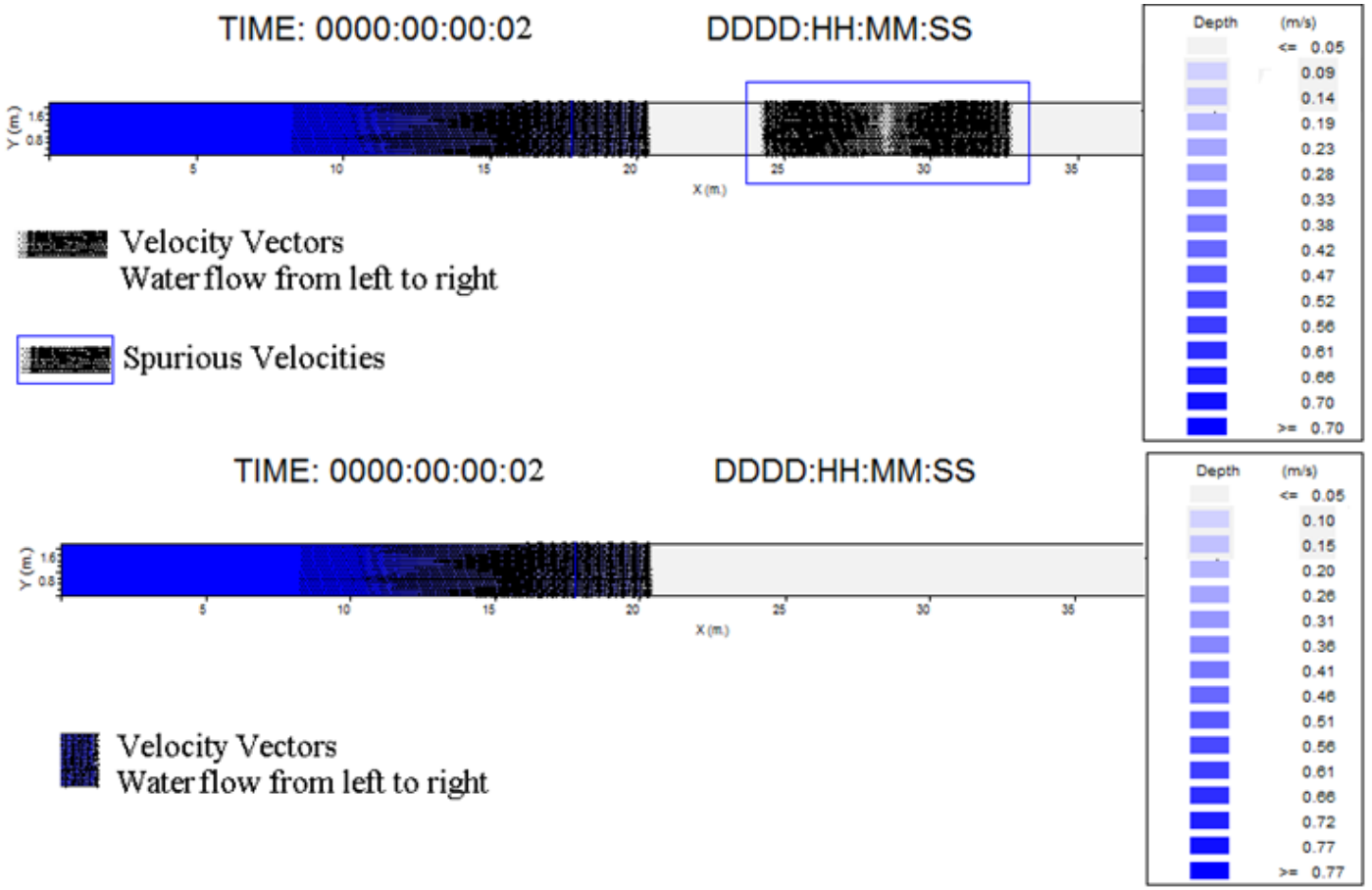

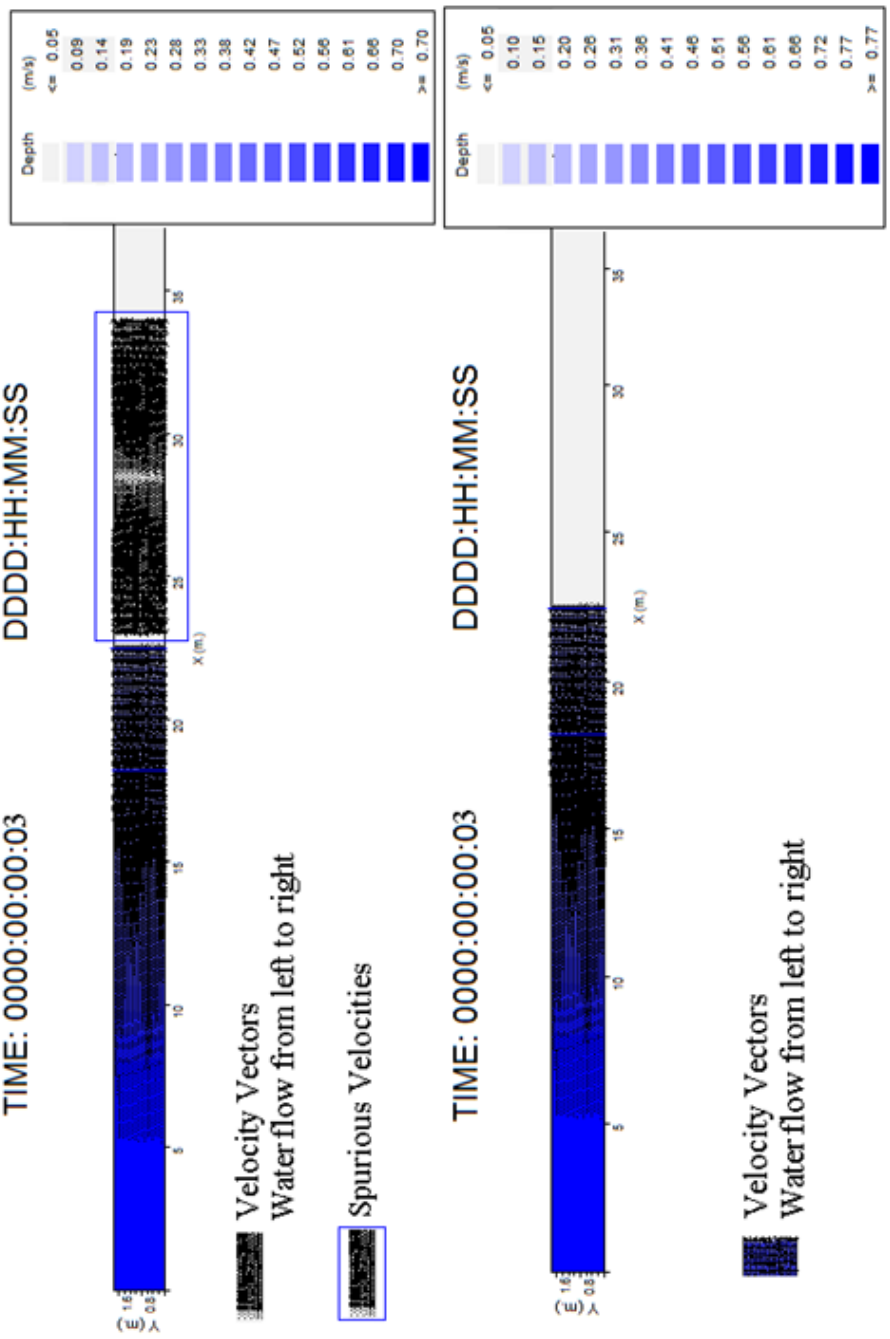

Figure 57. Flood wave over a triangular obstacle. Numerical Water Depths and Velocity field for t=3s. a) Umetsu & Matsumoto, 1998 dry and wet technique. b) With Wet and dry technique.

Figure 58. Flood wave over a triangular obstacle. Numerical Water Depths and Velocity field for t=4s. a) Umetsu & Matsumoto, 1998 dry and wet technique. b) With Wet and dry technique.

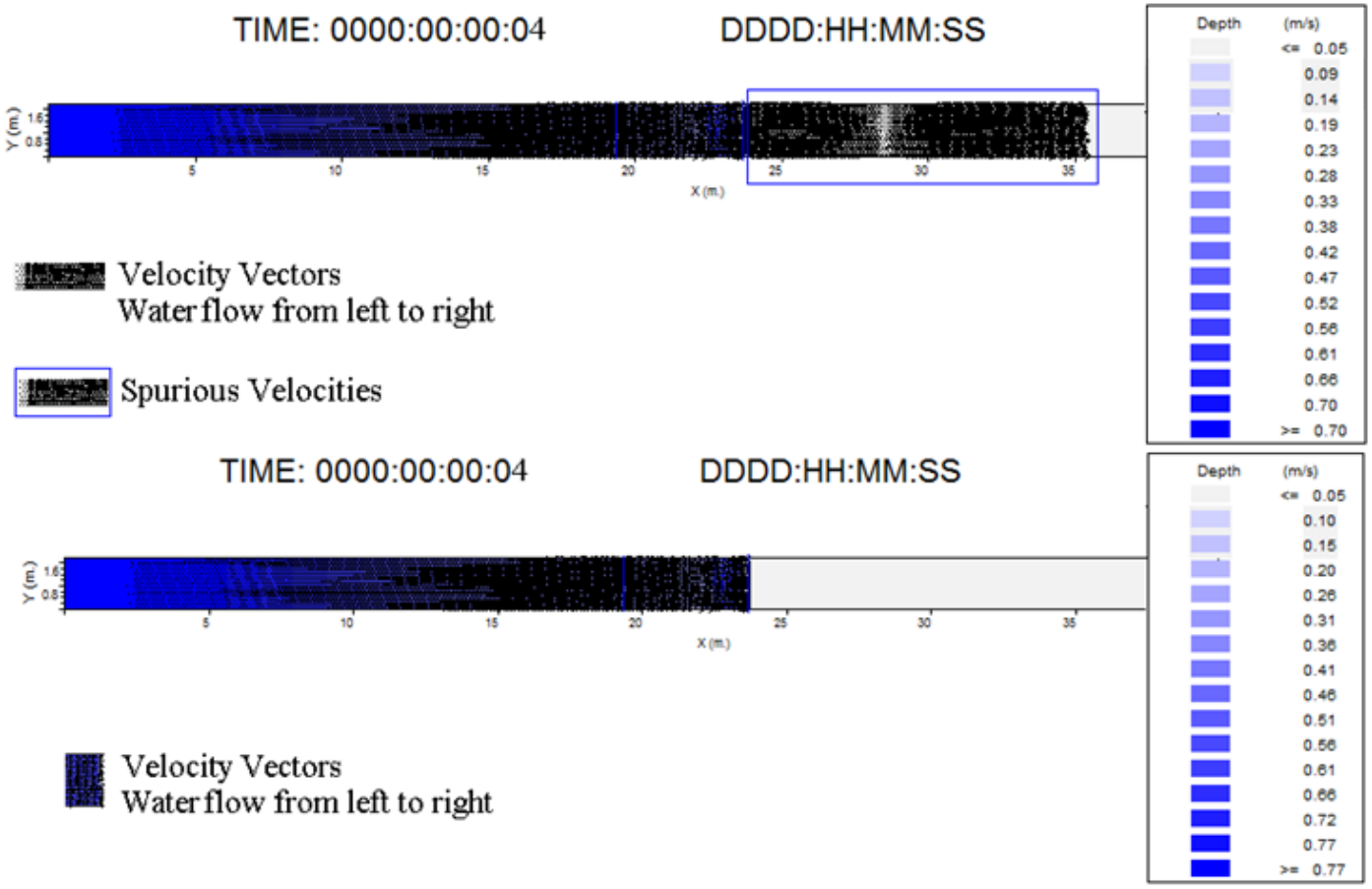

Figure 59. Flood wave over a triangular obstacle. Numerical Water Depths and Velocity field for t=5s.
a) Umetsu & Matsumoto, 1998 dry and wet technique. b) With Wet and dry technique.

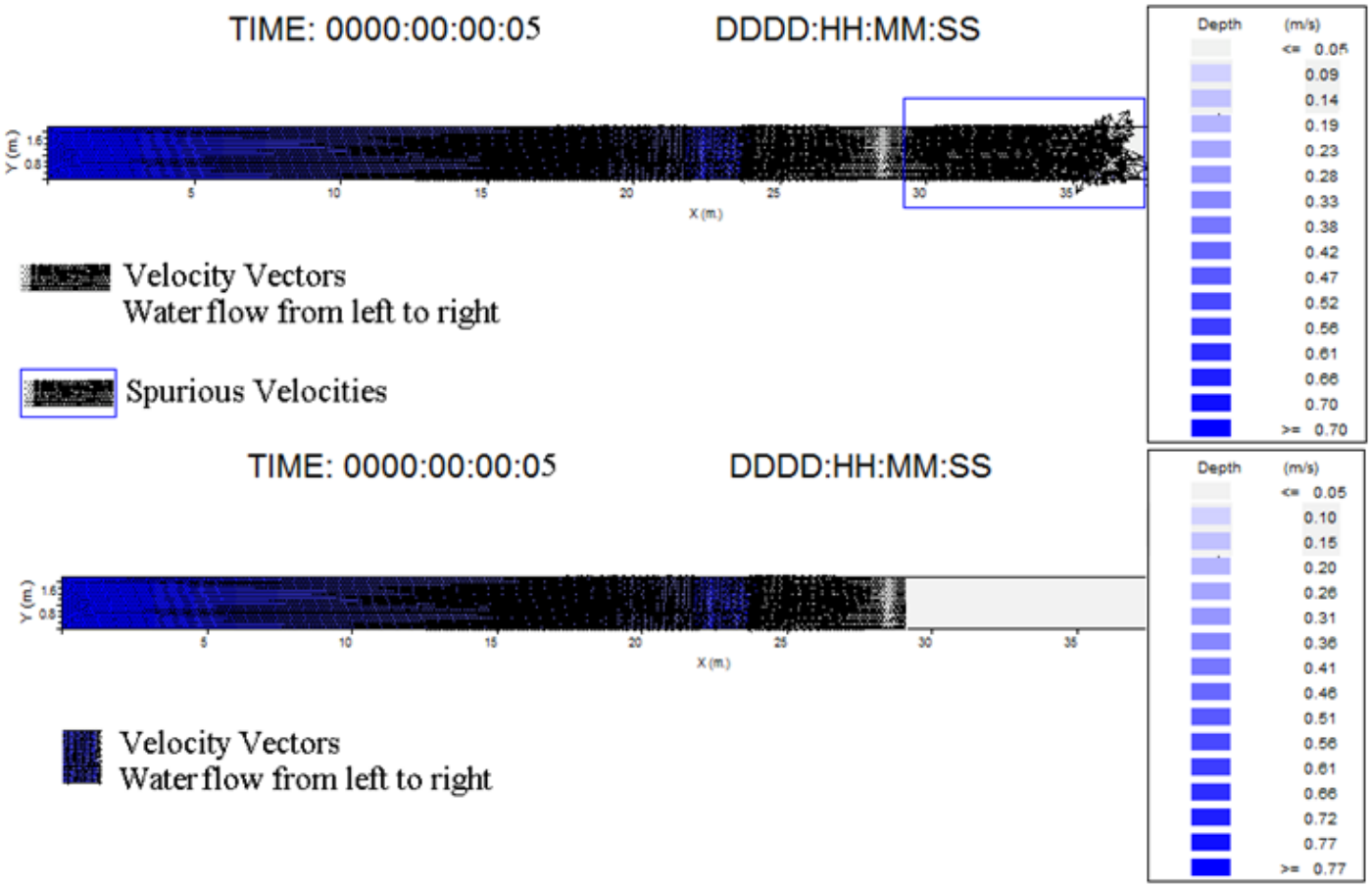

3.2.2 Runoff over a Cascade Surface

Case Description

The goal of this test is to evaluate the model performance of the enhanced RiverFLO-2D under variable rainfall in space. In this test, the enhanced RiverFLO-2D model was run on a channel with three slopes, which it was developed by Iwagaki in a laboratory flume of Kyoto University (Iwagaki, 1955). The results are compared with experimental overland flow measurements from the laboratory study performed by Iwagaki, 1955 as well as the numerical predictions reported by Zhang & Cundy, 1989.

The Iwagaki's Laboratory experiments were conducted in a 24 m long laboratory flume made of very smooth aluminum. Manning's *n* coefficient was set to 0.009 as it is recommended by Zhang & Cundy, 1989. The flume was divided into three reaches of equal length equal to 8m. The three slopes are 0.020, 0.015, 0.010 from upstream to downstream. Initial flume bed is completely dry. The test starts by an instantaneously increase in the rainfall intensity from upstream to downstream to 3890, 2300 and 2880 mm/h. The duration of the rainfall is 30 s and the runoff hydrograph is calculated at the end of the flume.

The finite element mesh used in the numerical computations has 5254 nodes and 8996 triangular elements. The downstream condition is an open outlet boundary and slip conditions are imposed on channel walls. The total simulation time is 60 s. and the time step is 0.0012 s.

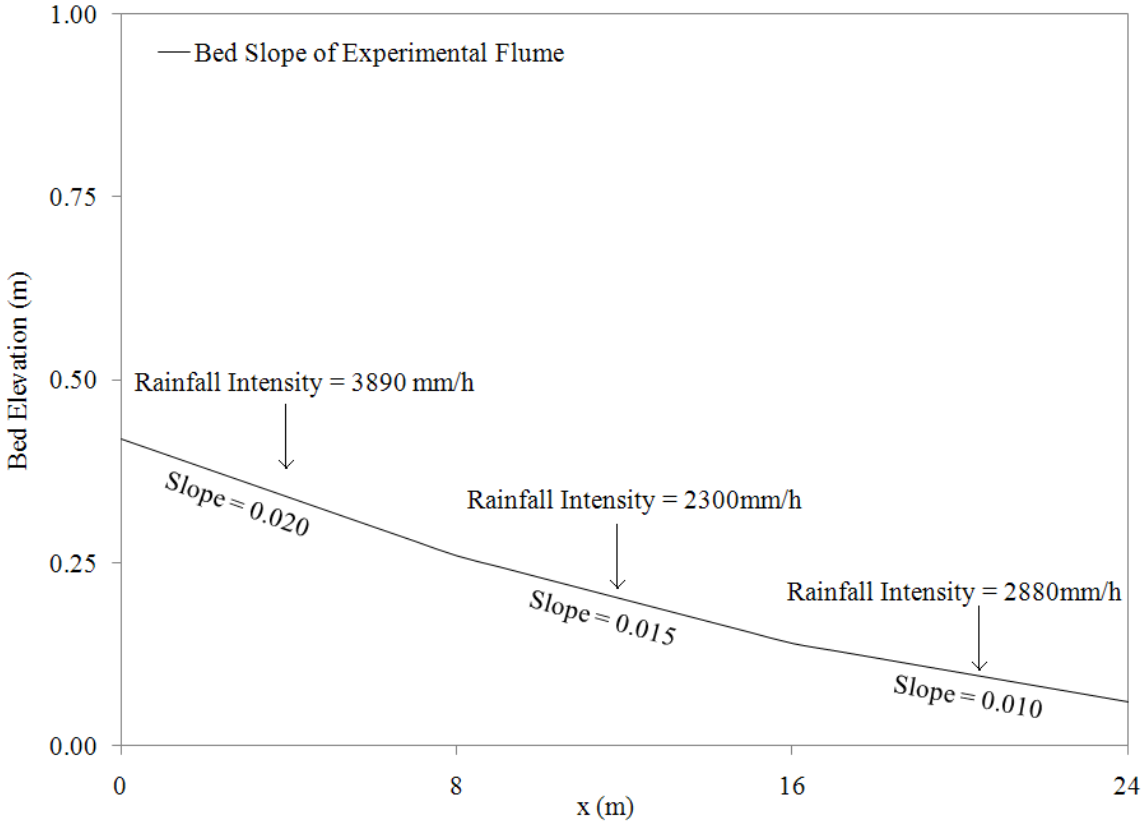

Figure 60. Runoff over a Cascade Surface. Bed Elevations in the numerical simulation.

Numerical Model Results

Numerical results of the runoff hydrograph were compared with the experimental measurements at the end of the flume (x=24m). Figure 61 show the measured and the predicted runoff hydrograph for RiverFLO-2D, Zhang's and Borah's numerical results (Zhang & Cundy, 1989).

Table 10 show the peak of the runoff hydrograph for experimental and numerical results. Figure 62 show the comparison between the experimental results of Iwagaki, 1955 and the RiverFLO-2D numerical results.

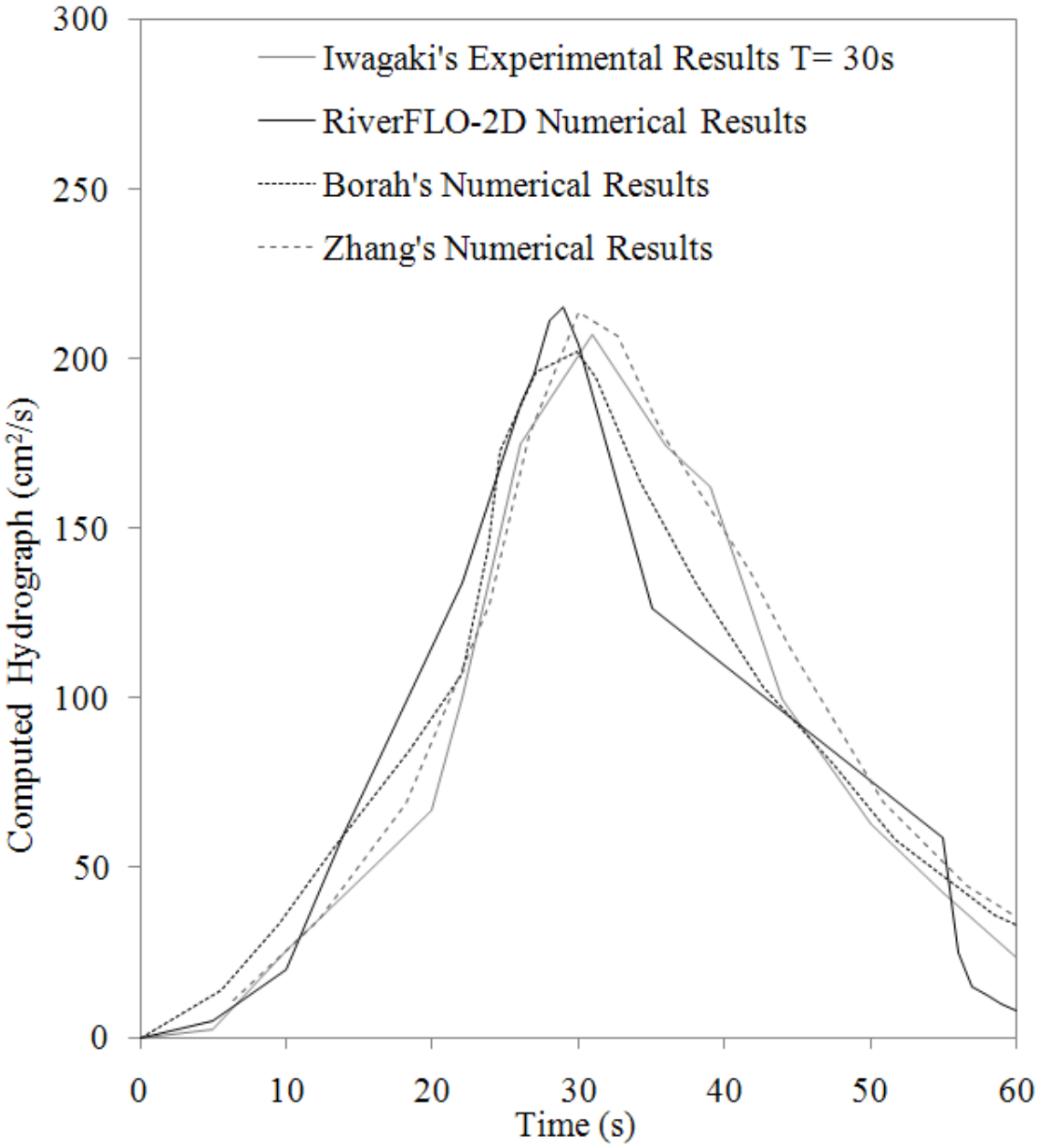

Figure 61. Runoff over a Cascade Surface. Comparison of the runoff hydrograph (t=30s) for RiverFLO-2D results, Borah's and Zhang's numerical results with Iwagaki's experimental laboratory results.

Table 10. Runoff over a Cascade Surface. Comparison of the runoff hydrograph peak (t=30s) by RiverFLO-2D results, Borah's and Zhang's numerical results with Iwagaki's experimental laboratory results.

	Results		Average Numerical Error (%)	
	Time to peak (s)	Peak Runoff (s)	Time to peak (s)	Peak Runoff (s)
Iwagaki Experimental Results	31	210	----	----
Zhang Numerical Results	30	215	3.23	2.38
Borah Numerical Results	29	201	6.45	4.29
RiverFlo-2D Numerical Results	29	215	6.45	2.38

Note that the rainfall condition for this case produces rapidly varying flow, since the highest rainfall intensity occurs in the upstream steepest reach representing a region of faster flow, while a low rainfall intensity and bed slope are those of the downstream reach resulting in a slower flow. The results show in Figure 61, Figure 62 and Table 10 show the comparison of the results computed by RiverFLO-2D with those reported by Iwagaki, 1955 with a correlation factor of 0.85.

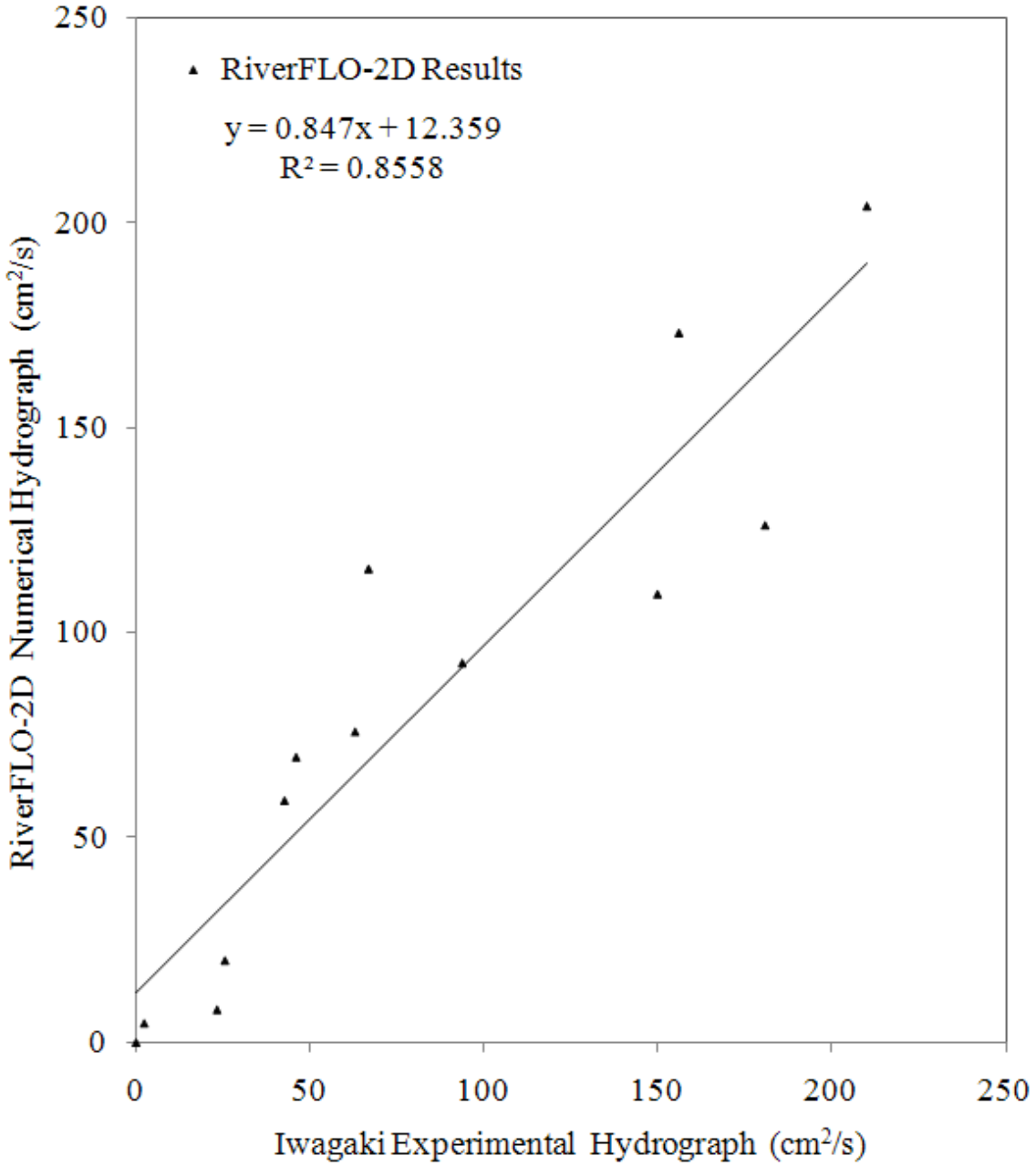

Figure 62. Runoff over a Cascade Surface. Comparison of RiverFLO-2D runoff hydrograph with Iwagaki's runoff hydrograph.

3.3 Field Tests Cases

3.3.1 Malpasset Dam-break Flooding

Case Description

An example of a flooding due to a Dam-break is provided for the Malpasset dam. The Malpasset dam was located in a narrow gorge of the Reyran River Valley, in France. Shortly after finalizing construction, the dam failed on December 2nd, 1959. The collected flooding field data and information include estimates of the frontal wave pass inferred from the shutdown times of three electrical transformers that were located along the river valley, and a post-event flooding survey that recorded 100 water elevation marks (see Figure 64 for location). Also in 1964, a non-distorted 1/400 scale model was constructed at National Hydraulic and Environment Laboratory (EDF-LNH, Chatou) and 14 gauges were located to record the physical water depths (see Figure 65 for location) (Hervouet, 2007; Brufau et al., 2004; Hervouet & Petitjean, 1999).

In order to test RiverFLO-2D for Malpasset dam-break event, a 16150 node/30935 element mesh was generated that extends for approximately 17.5 km (see Figure 63 and Figure 66). The total time of simulation was 0.7 hour with a time step of 0.5 s. Element sizes range from 20 m to 100 m approximately. The initial conditions were 100 m water surface elevation on the reservoir and dry bed downstream from the dam location. Manning's *n* was set to 0.033, constant for all elements.

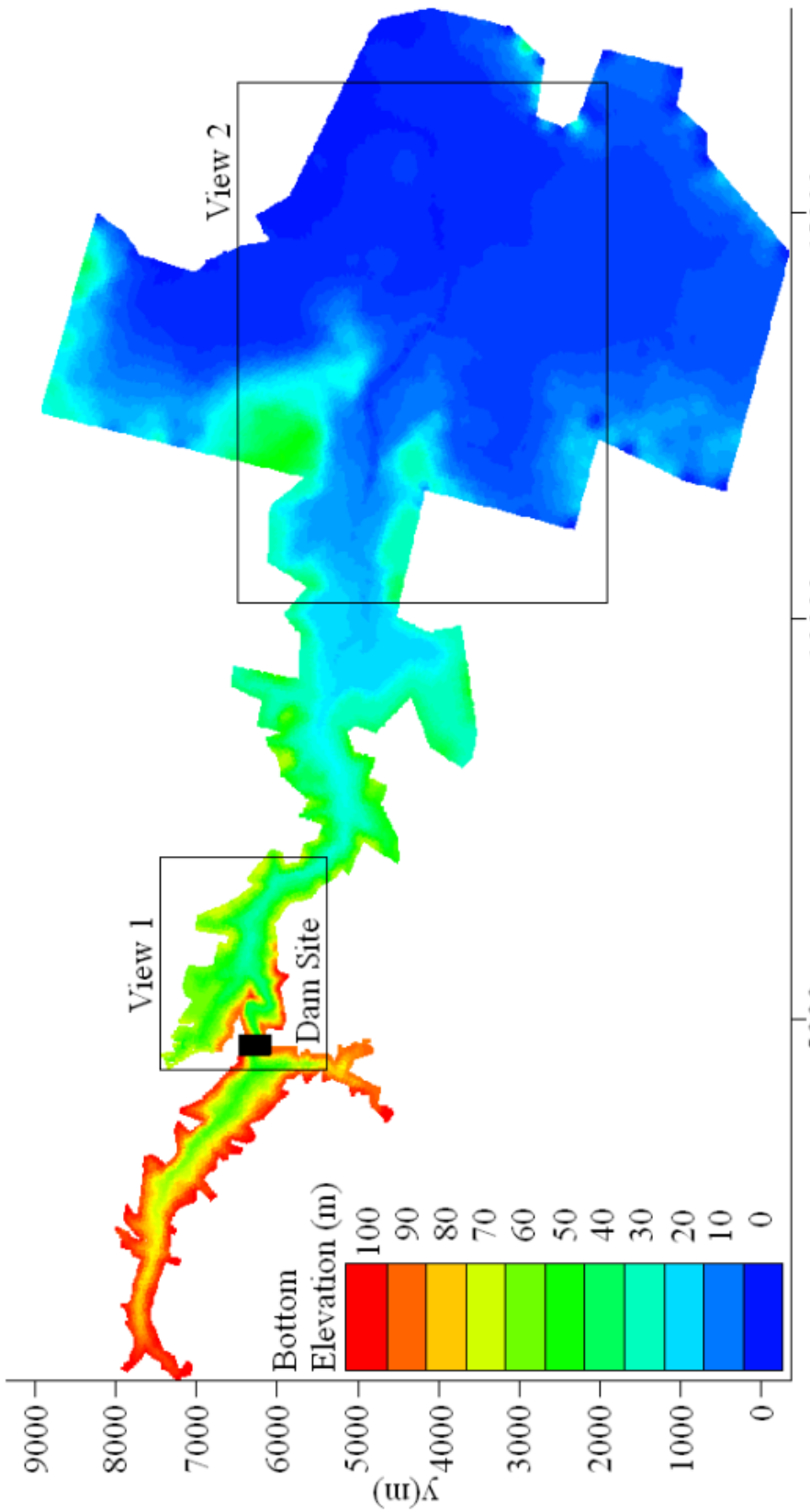

Figure 63. Malpasset flooding test. Bottom elevations and mesh extent.

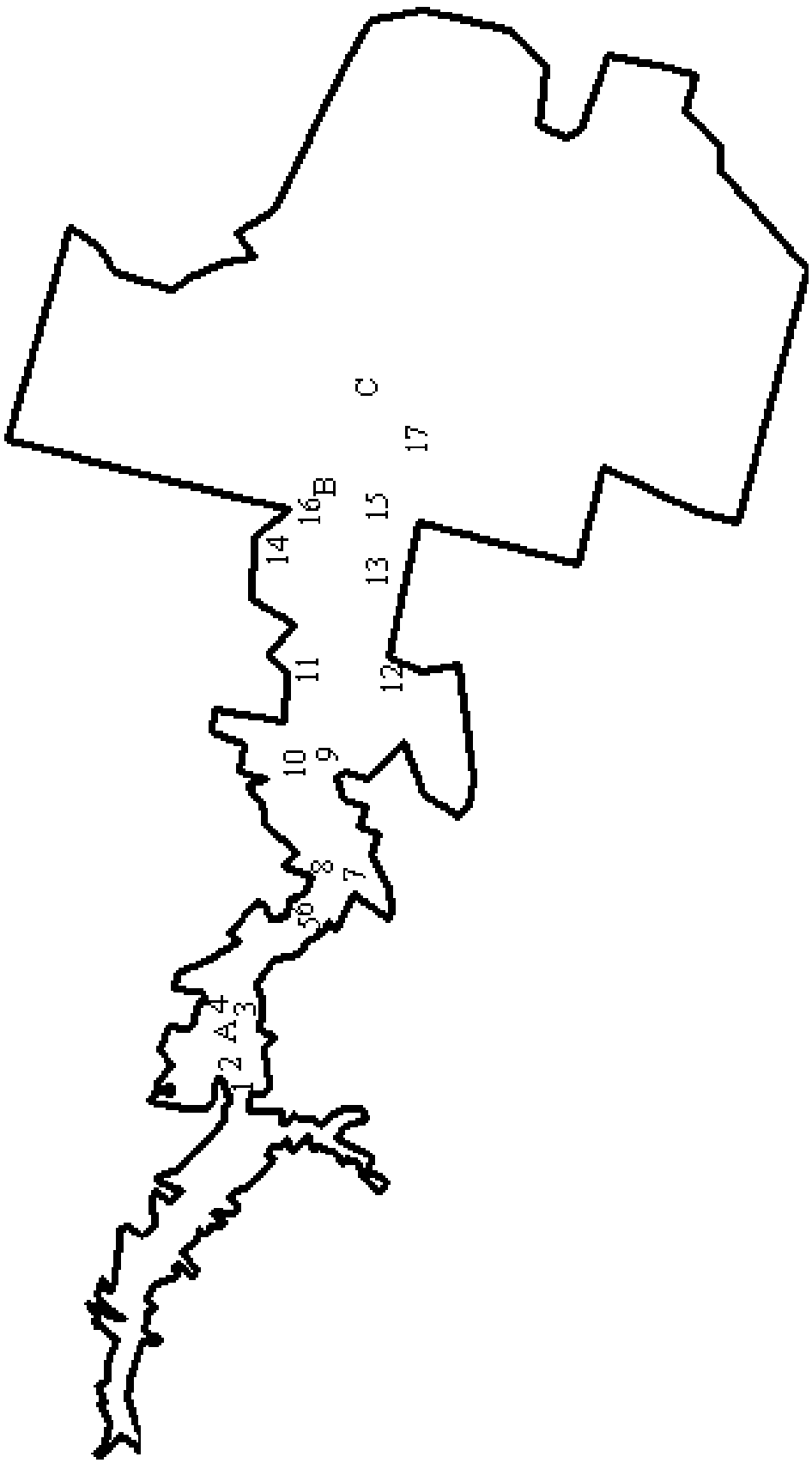

Figure 64. Malpasset flooding test. Electrical transformers and post-event surveyed police points location.

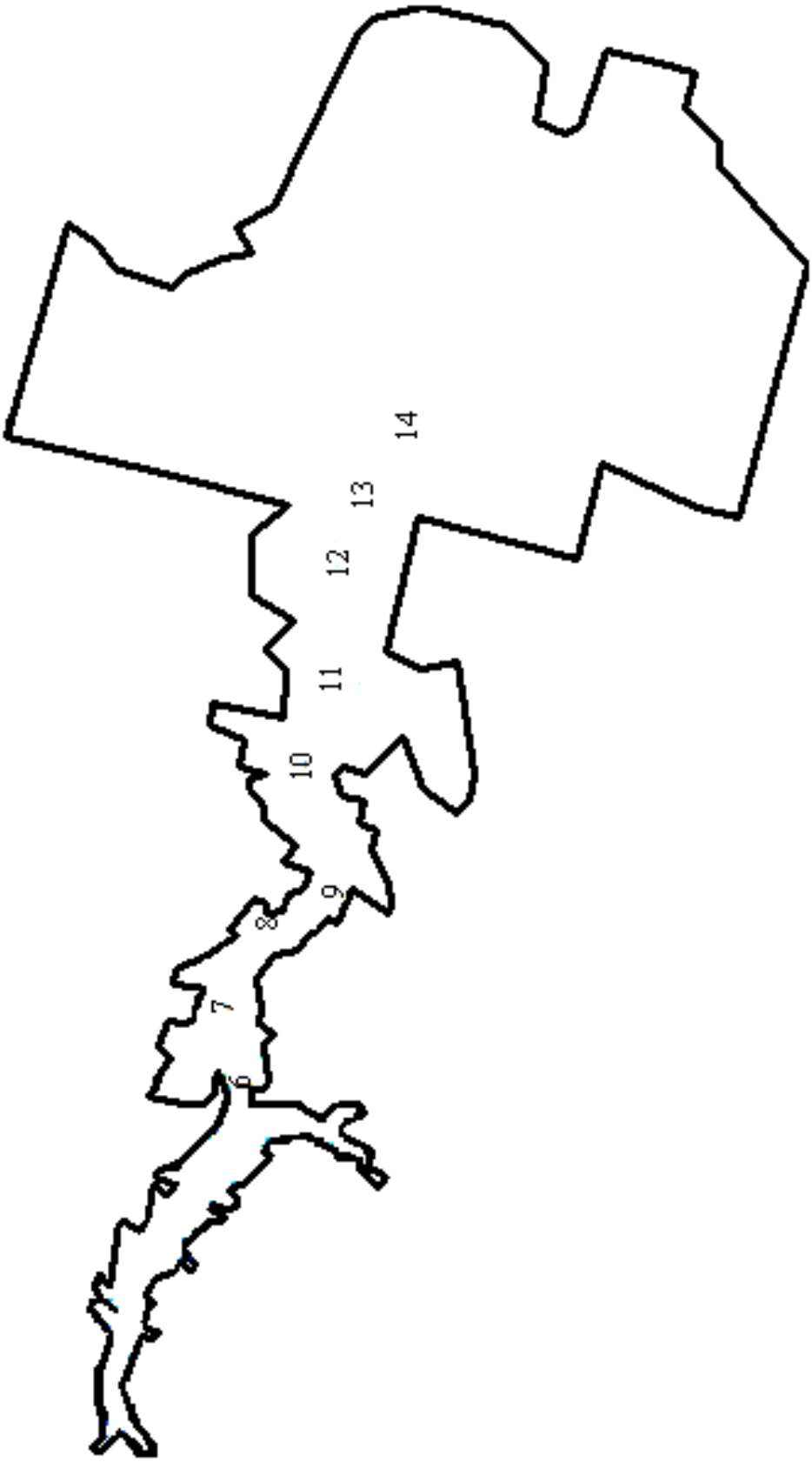

Figure 65. Malpasset flooding test. Physical model gauges location.

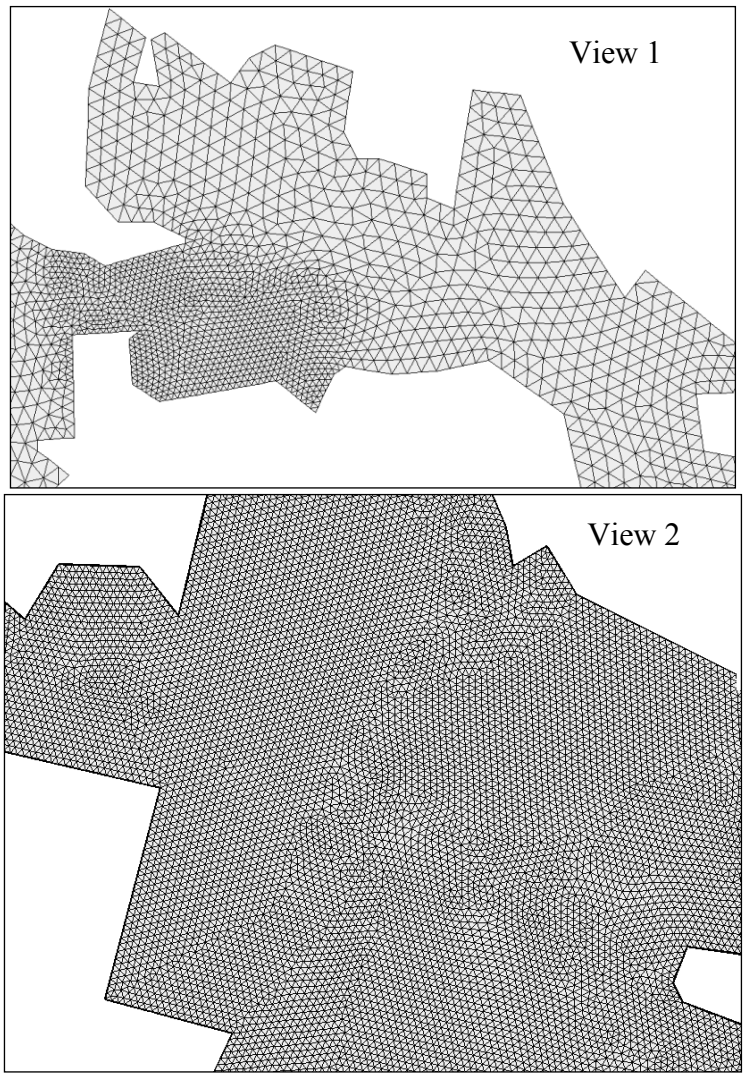

Figure 66. Malpasset flooding test. Mesh (View 1) and Mesh detail (View 2).

Numerical Model Results

Table 11 presents the electrical transformers shutdown times and the model frontal wave arrival times.

Table 11. Malpasset flooding test. Data of electric transformers shutdown and RiverFLO-2D frontal wave arrival times.

Transformer	**X (m)**	**Y (m)**	**Measured shutdown Time (s)**	**RiverFLO-2D Shutdown Time (s)**
A	5550	6400	100	108
B	11900	5250	1240	1260
C	13000	4700	1420	1300

The remarkable points surveyed for the local police showing nearly 100 points of the flooding water marks on the banks are enumerated in Table 12. Coordinates in x and y are in a relative coordinate system.

Table 12. Malpasset flooding test. Data of the surveyed police points.

			Data Surveyed	**RiverFLO-2D Results**
Points	**X (m)**	**Y (m)**	**Water Level (m)**	**Water Level (m)**
P1	4913.11	6244.01	79.15	84.69
P2	5159.75	6369.62	87.20	87.38
P3	5790.63	6177.76	54.90	57.18
P4	5886.54	6503.97	64.70	60.60
P5	6763.05	5429.6	51.10	50.47
P6	6929.97	5591.87	43.75	47.88
P7	7326.02	4948.78	44.35	38.81
P8	7441.01	5232.12	38.60	36.80
P9	8735.94	5264.61	31.90	31.91
P10	8628.60	5604.63	40.75	37.73
P11	9761.13	5480.36	24.15	25.41
P12	9800.00	4414.79	24.90	26.69
P13	10957.00	4651.94	17.25	25.55
P14	11156.99	5800.72	20.70	21.03
P15	11689.05	4592.36	18.60	18.94
P16	11626.05	5406.80	17.25	19.78
P17	12333.72	4269.74	14.00	16.44

The results for the gauges located in the physical model are shown in Table 13.

Table 13. Malpasset flooding test. Data of the gauges located in the physical model (EDF-LNH, Chatou)

			Data Surveyed		**RiverFLO-2D Results**	
Gauge	**X (m)**	**Y (m)**	**Water Level (m)**	**Time (s)**	**Water Level (m)**	**Time (s)**
S6	4947.46	6289.71	84.2	10.2	86.16	10
S7	5717.30	6407.61	49.1	102.0	56.65	108
S8	6775.14	5869.23	54.0	182.0	54.79	216
S9	7128.20	51620	40.2	263.0	48.20	252
S10	8585.30	5443.08	34.9	404.0	36.82	396
S11	9674.97	5085.89	27.4	600.0	26.49	612
S12	10939.15	5044.78	21.5	845.0	20.08	864
S13	11724.37	4810.41	16.1	972.0	18.15	936
S14	12723.70	4485.08	12.9	1139.0	13.48	1260

The Manning's *n* value recommended by Hervouet, 2007 and Brufau et al., 2004 was used in the simulation.

All tables from Table 11 to Table 13 present the comparison for the numerical results and the police post-event reported flooding data and the physical model for the electrical transformers shutdown times and the model frontal wave arrival times. Comparison for the first two transformers located at 5550 m and 11,900 m from the dam site indicates that the model is able to correctly capture the wave progression over the dry river valley.

Note that there are no erratic velocities on the wet–dry interface. A satisfactory transition between dry and wet zones without oscillations is observed.

Figure 67 presents the evolution of numerical water depths versus time of simulation in the location of the transformers A, B and C.

Figure 68 presents the evolution of numerical water depths versus time of simulation for the location of the 16 surveyed police points.

Figure 69 presents the evolution of numerical water depths versus time of simulation for the location of the 14 physical model gauge locations.

Figure 70 and Figure 71 show the velocity fields at two locations for times 350 s, and 2400 s respectively.

Figure 72 shows the contour lines for depths at 350s, 900s, 1850s and 2400s.

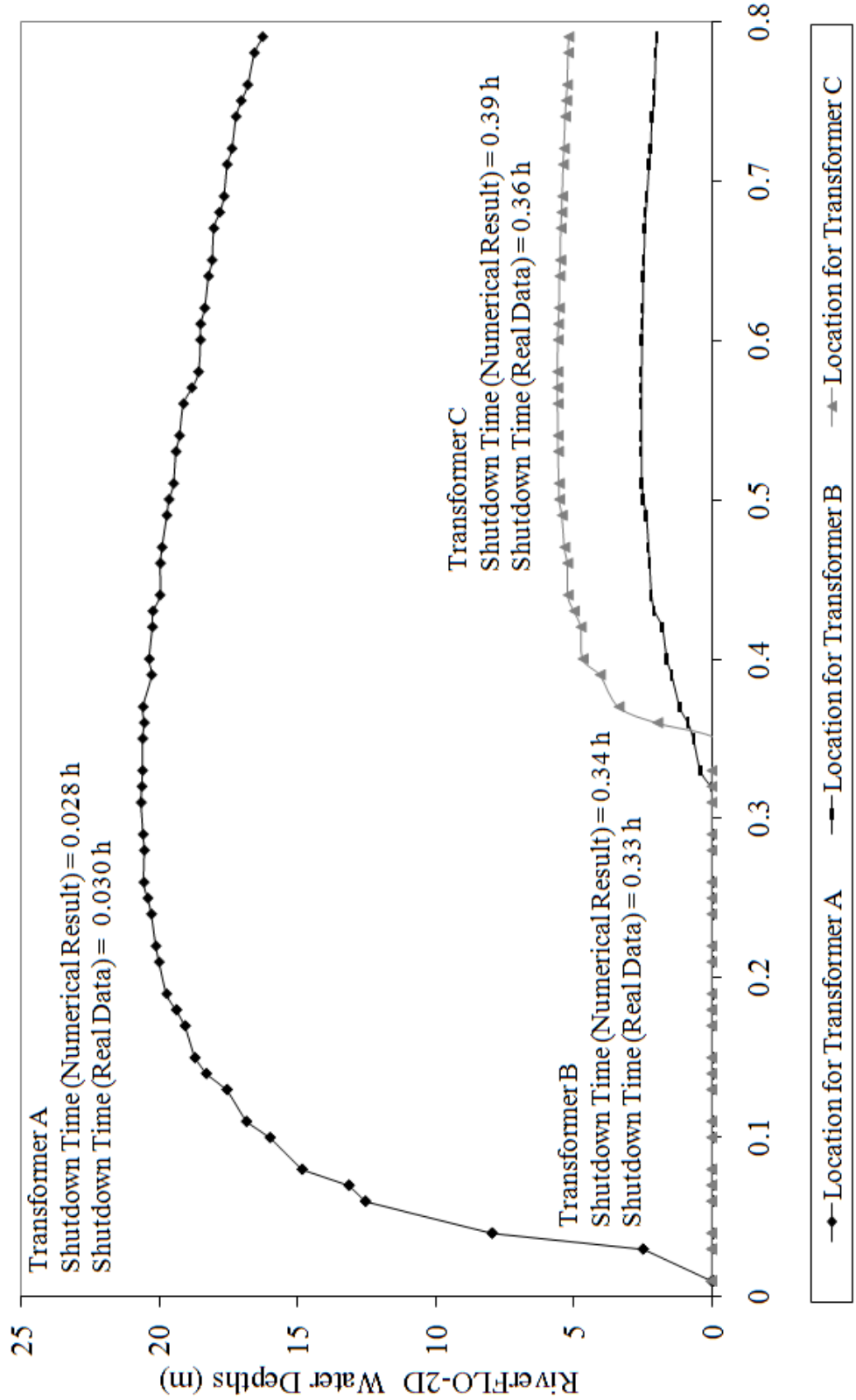

Figure 67. Malpasset flooding test. Numerical Water Elevation in the location of the transformers.

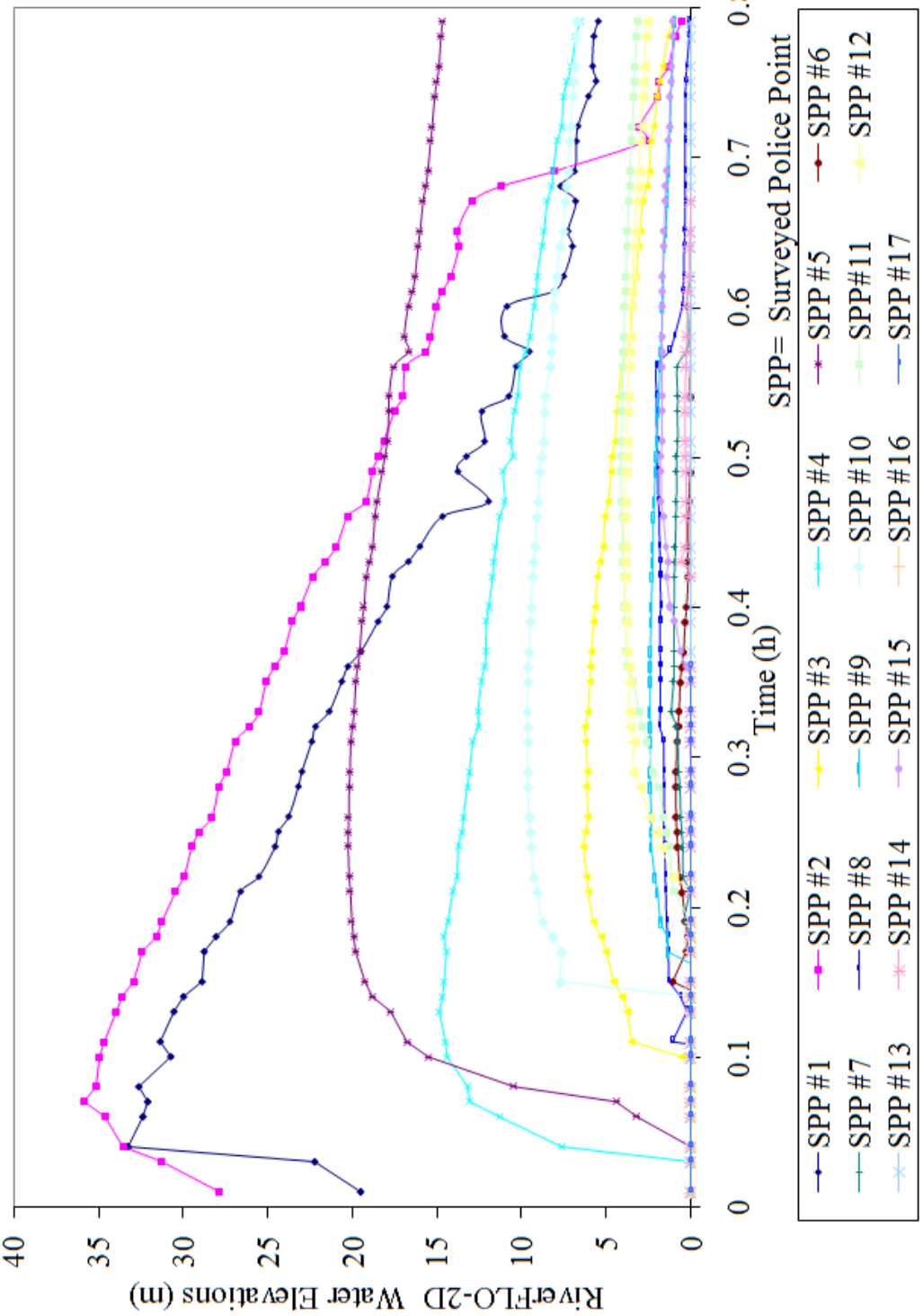

Figure 68. Malpasset flooding test. Numerical Water Elevation in the surveyed police point locations.

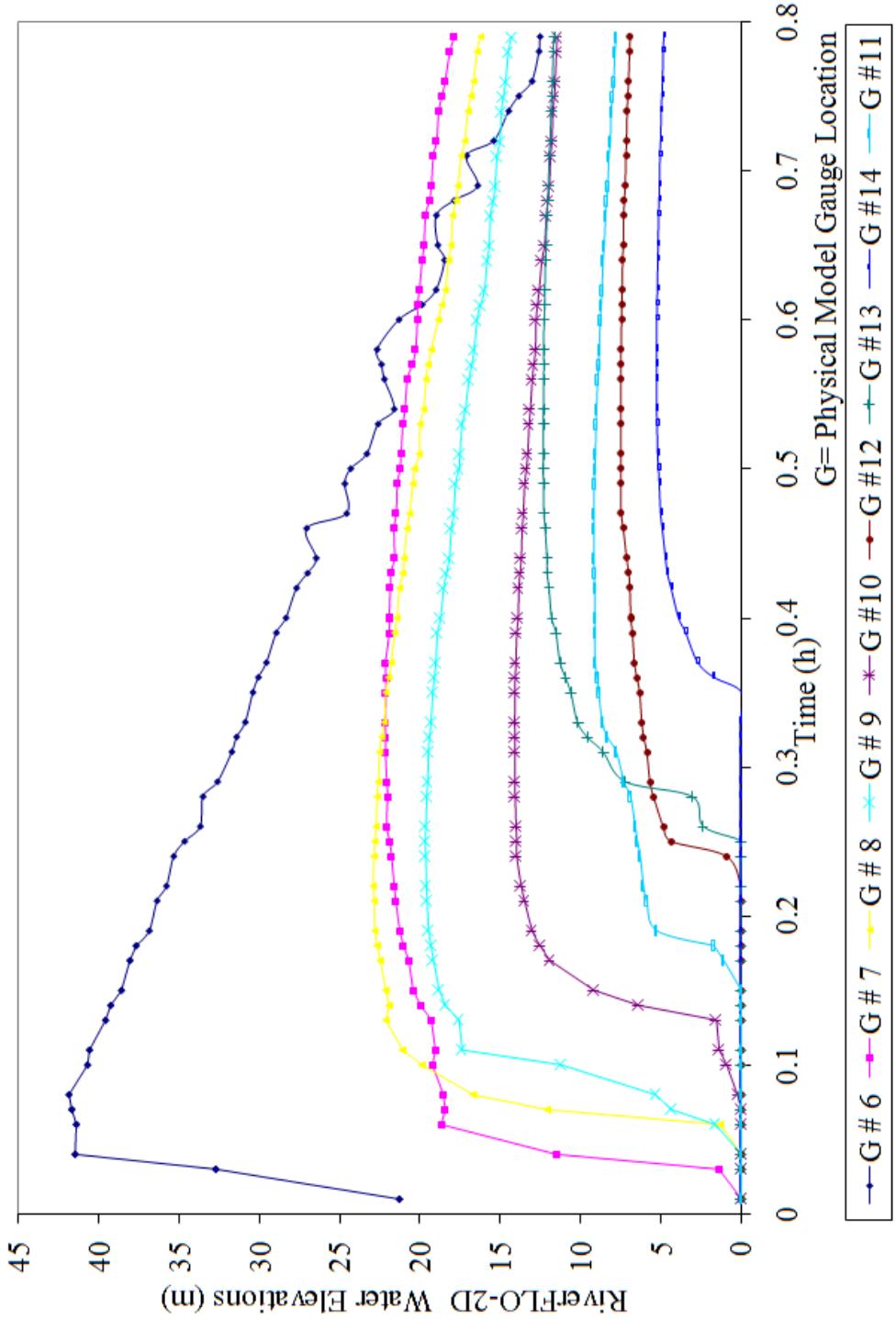

Figure 69. Malpasset flooding test. Numerical Water Elevation in the physical model gauge locations.

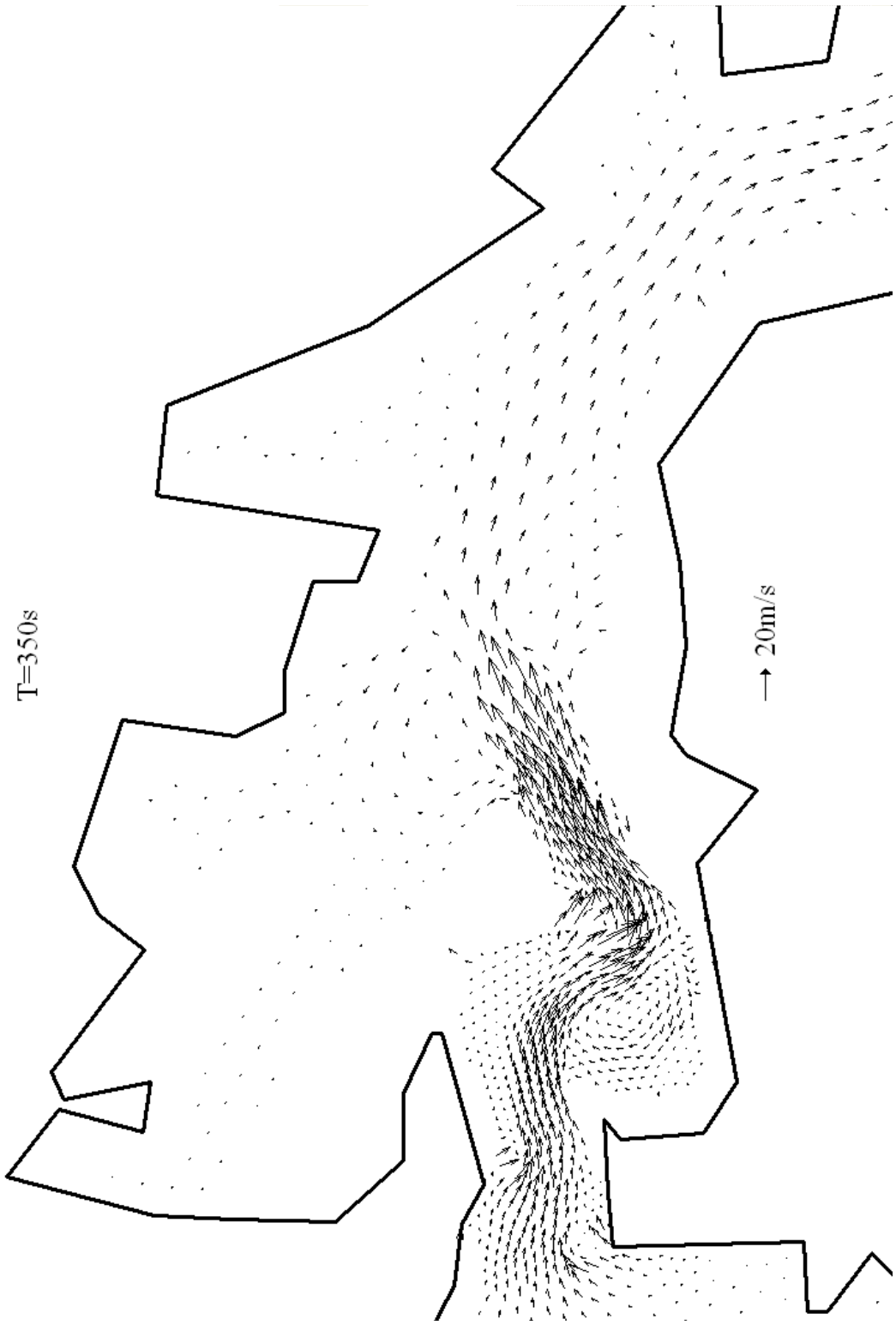

Figure 70. Malpasset flooding test. Velocity field detail for view 1 t=350 s. after dambreak (View 1).

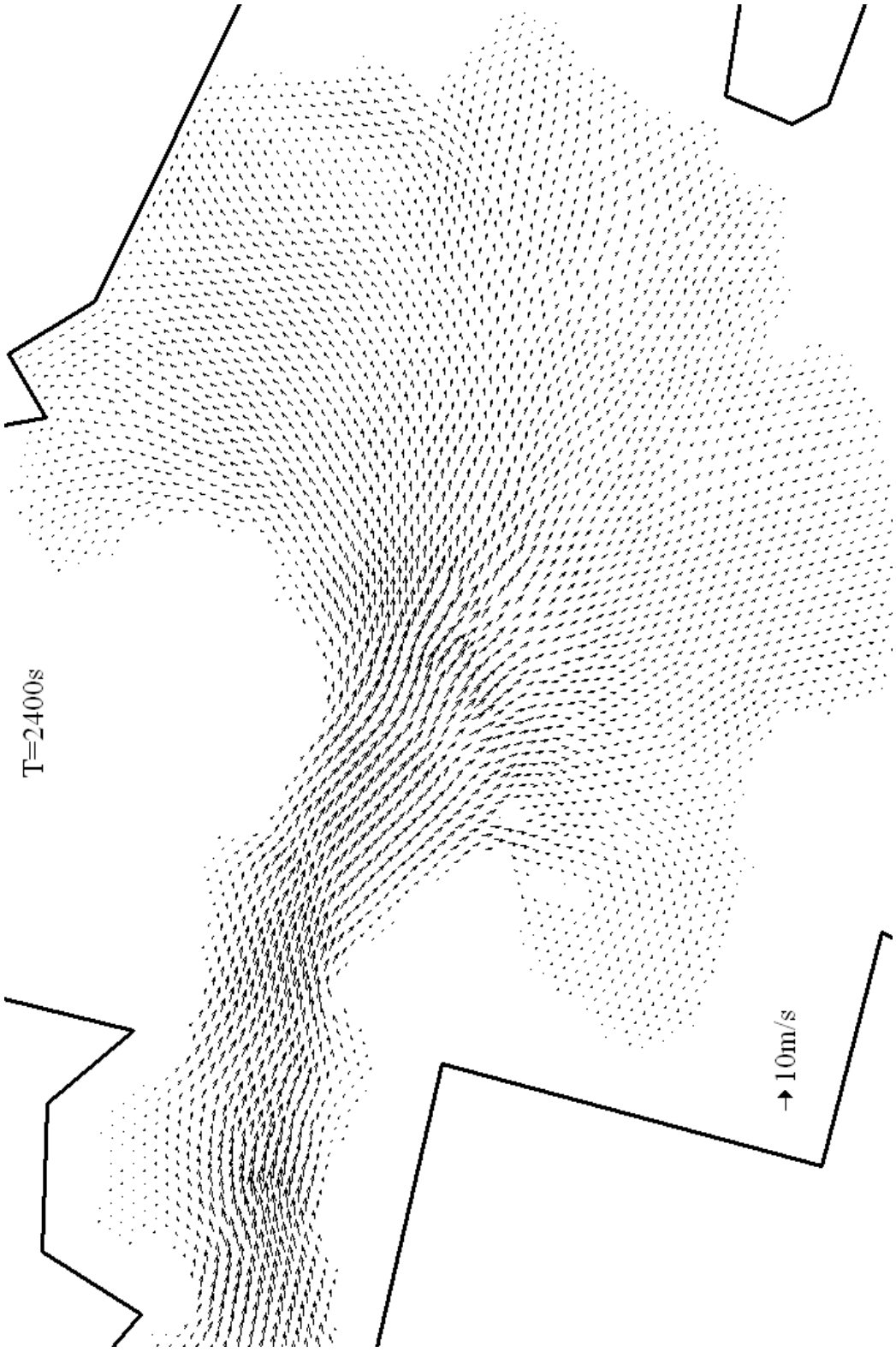

Figure 71. Malpasset flooding test. Velocity field detail for view 2 at t=2400 s after dam-break (View 2).

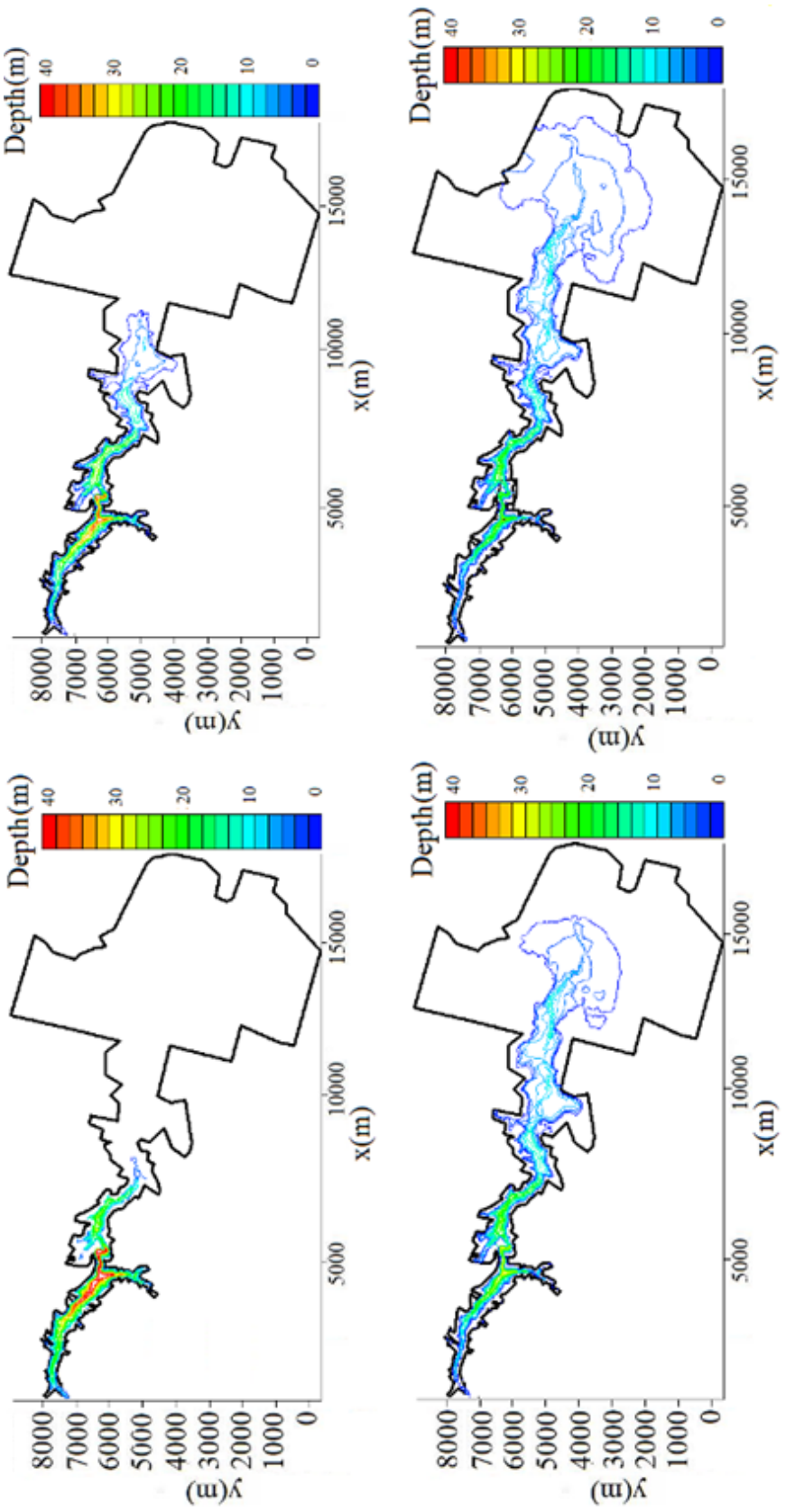

Figure 72. Malpasset flooding test. Contour lines for Depths of Malpasset Dambreak at t= 350s (a), 900s (b), 1850s (c) and 2400s (d)

Figure 73 to Figure 76 shows the results of RiverFLO-2D model compares with physical data and field data for Malpasset flooding event.

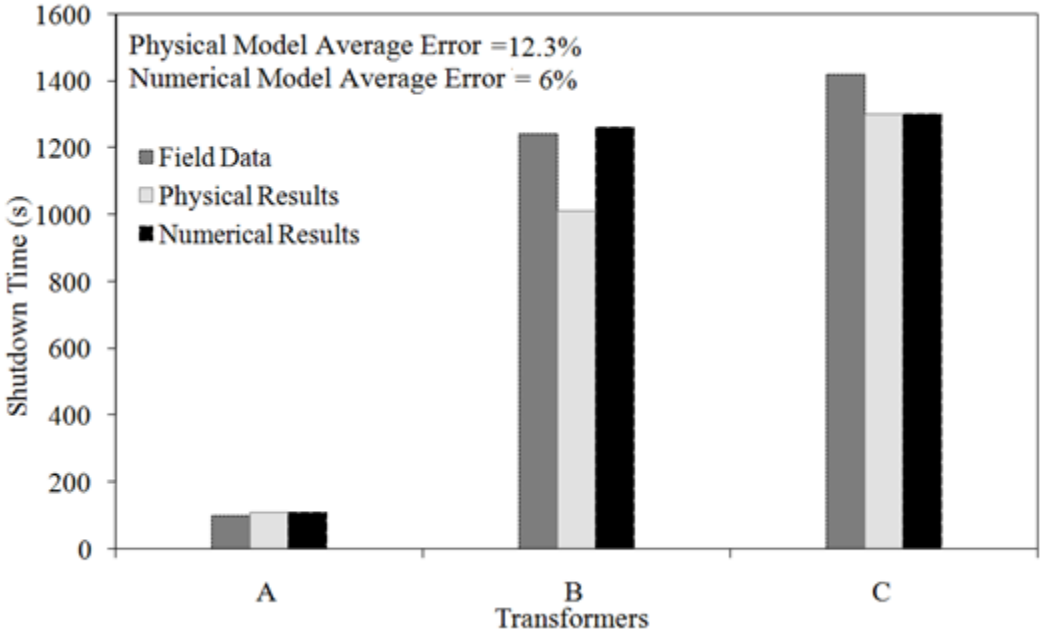

Figure 73. Comparison of the Numerical Results, Physical Model Data and Field Measures for the shutdown time of the Electrical Transformers along the river.

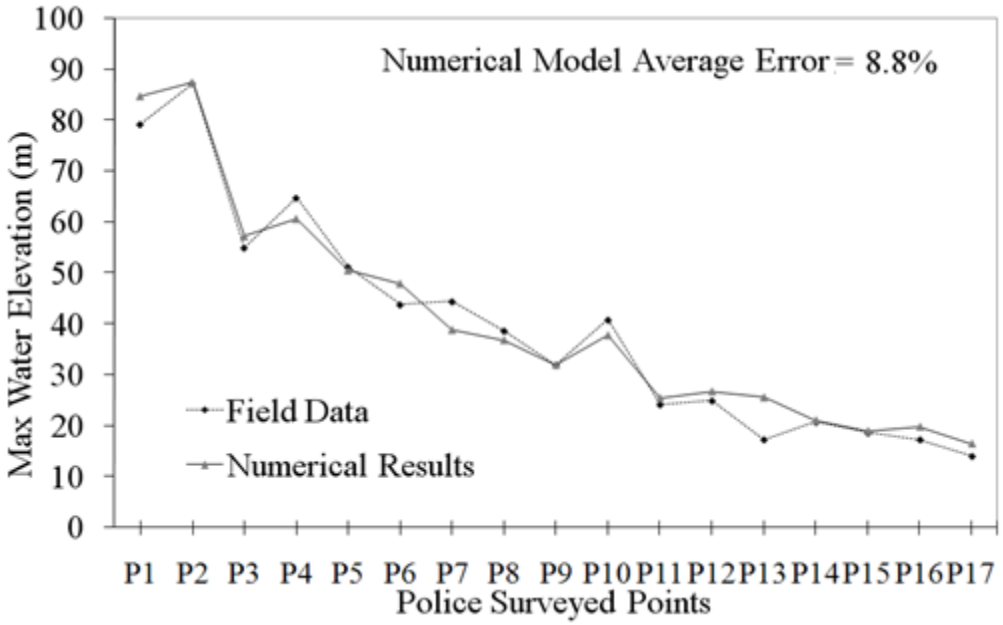

Figure 74. Comparison of the Numerical Results and Field Measures for the police surveyed points.

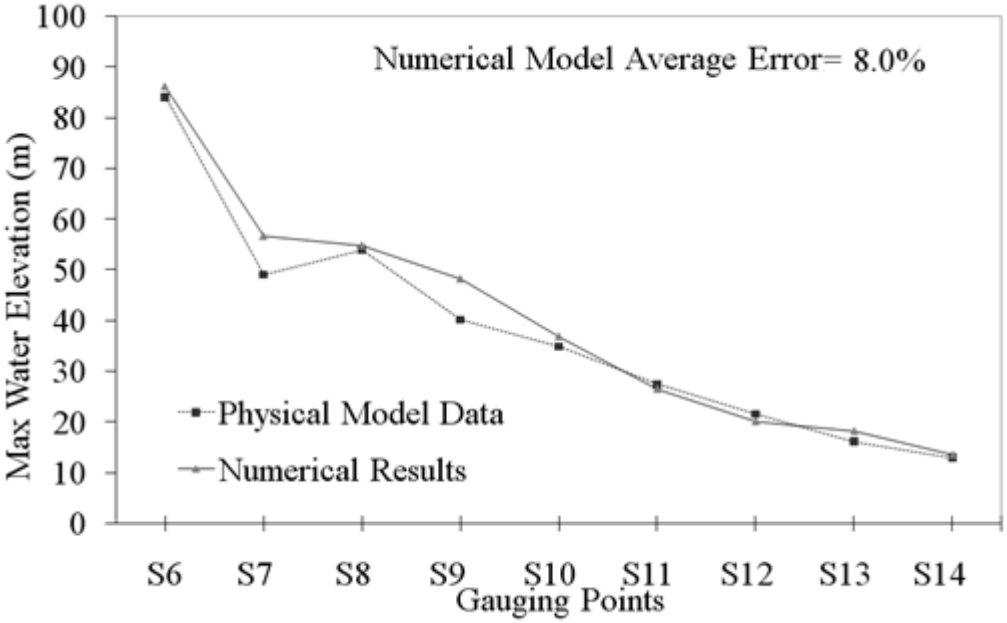

Figure 75. Malpasset flooding test. Comparison of the Numerical results and Physical water elevation Data for the gauging point.

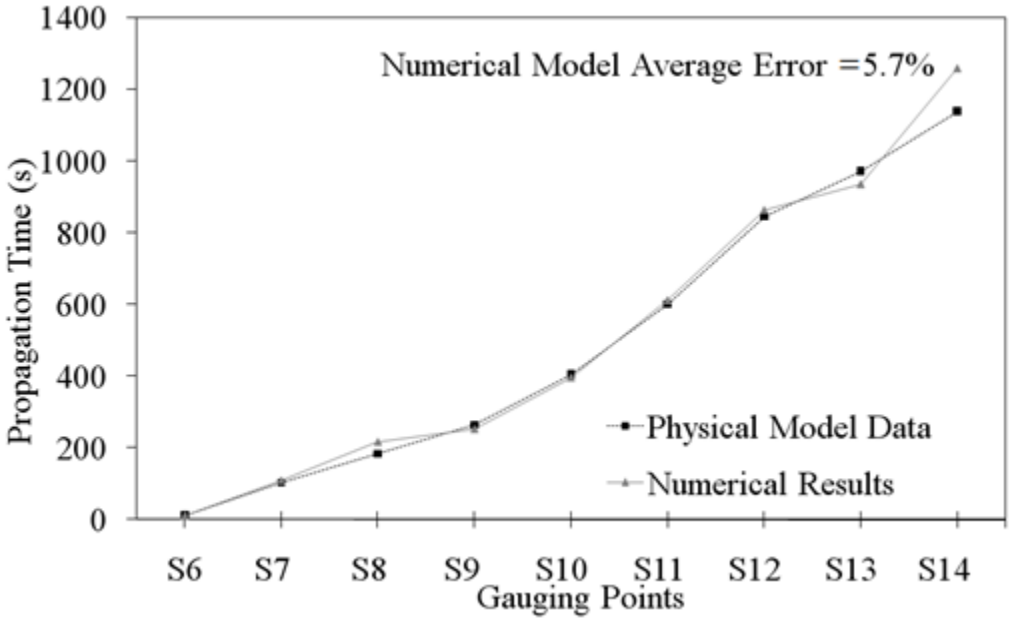

Figure 76. Malpasset flooding test. Comparison of the Numerical Results and Physical propagation time Data for the gauging point.

Figure 73 presents numerical results, physical model measurements and field data for the shutdown times of the electrical transformers. The model compares well with the field data for the first and second transformers, and is 8% off for the last transformer.

It can be concluded for this test that overall, the comparison for the water surface elevation between the model results and the field data presents an average error for the 17 surveyed points of 8.8%. Although the predicted model water surface elevations are somewhat higher for points S7 and S9 in Figure 75, the comparison for other points are acceptable. The average error including all points is 8%. The errors are low except for point S14 where the error is about 9%. The overall error is 5.7% approximately.

Figure 77 to Figure 80 show the results of RiverFLO-2D model compares with the physical data and field data for Malpasset flooding event.

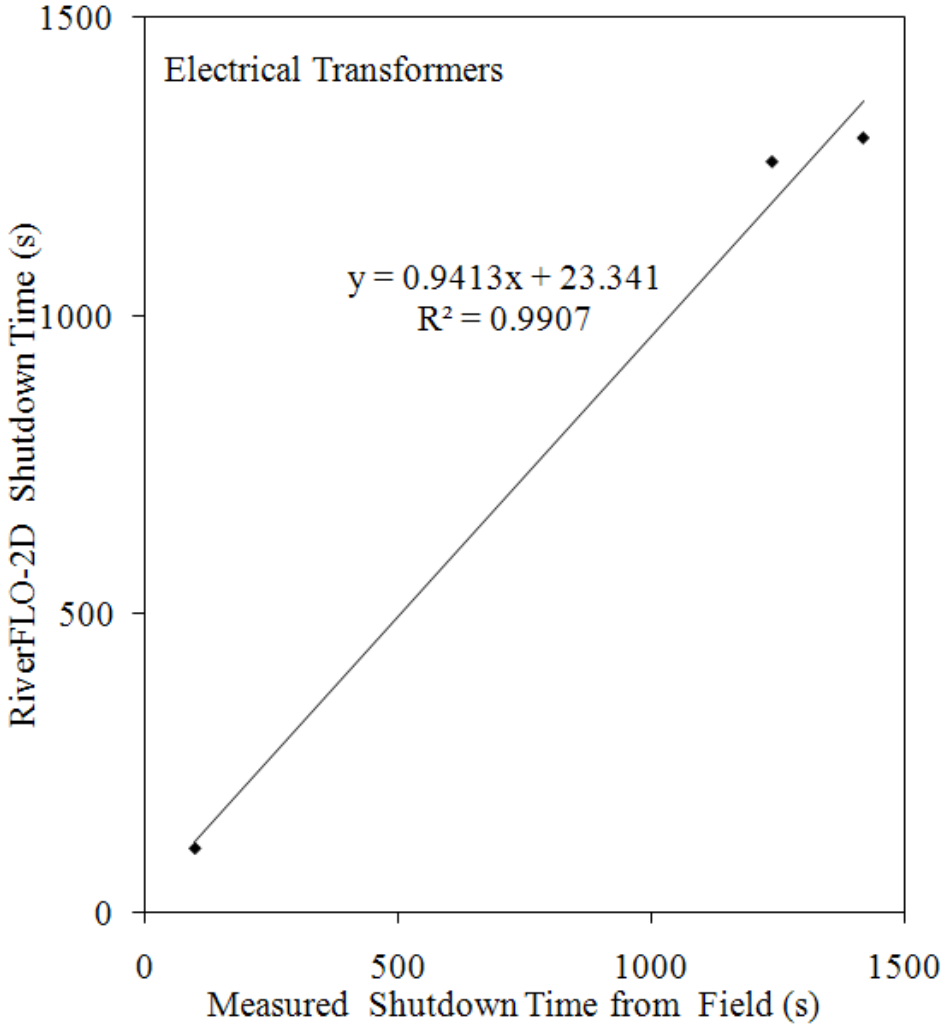

Figure 77. Malpasset flooding test. Comparison of water elevation marks with numerical water surface elevations for electrical transformers.

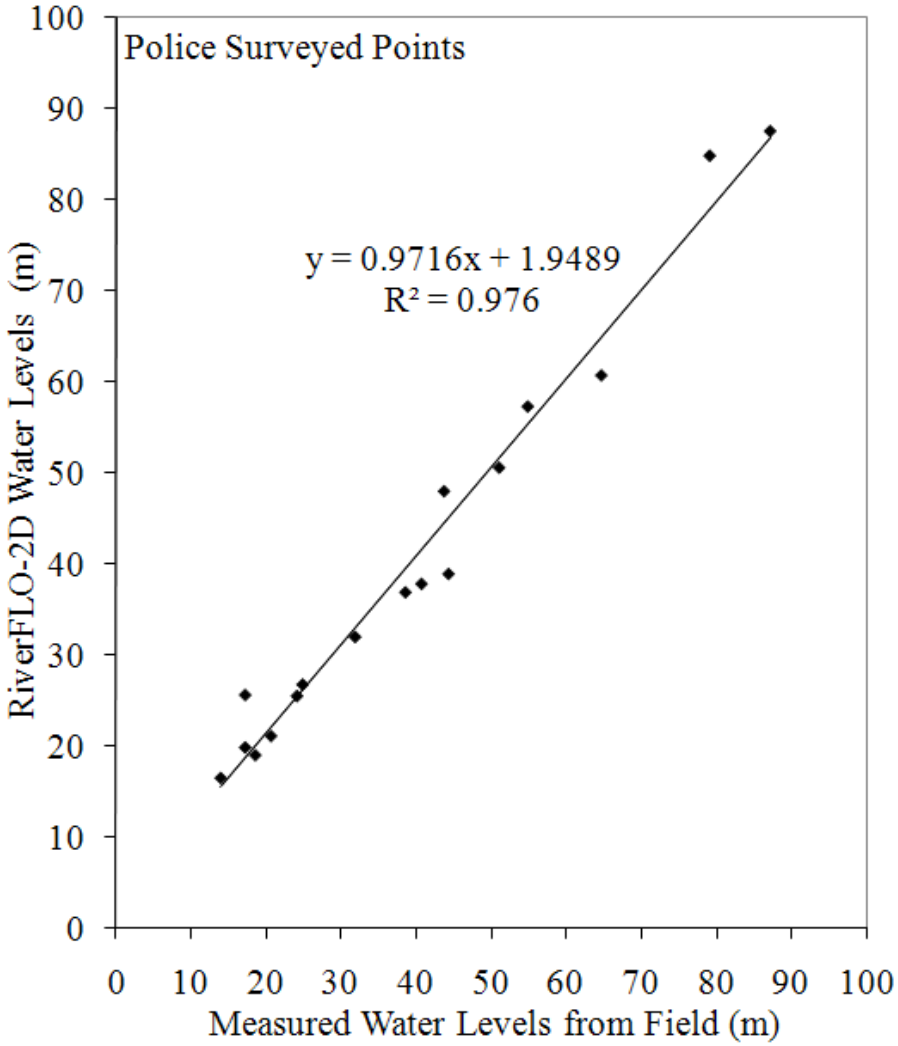

Figure 78. Malpasset flooding test. Comparison of water elevation marks with numerical water surface elevations for 17 locations surveyed by local police along the river valley.

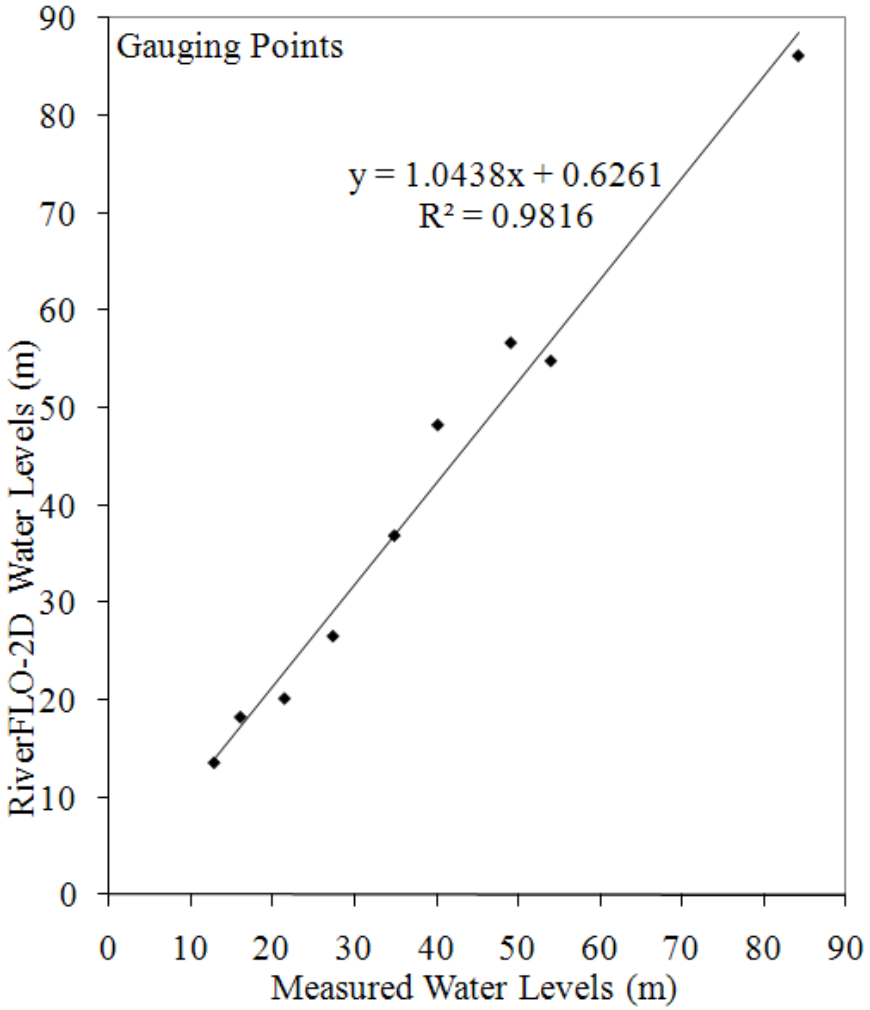

Figure 79. Malpasset flooding test. Comparison of water elevation marks for the physical model with numerical water surface elevations.

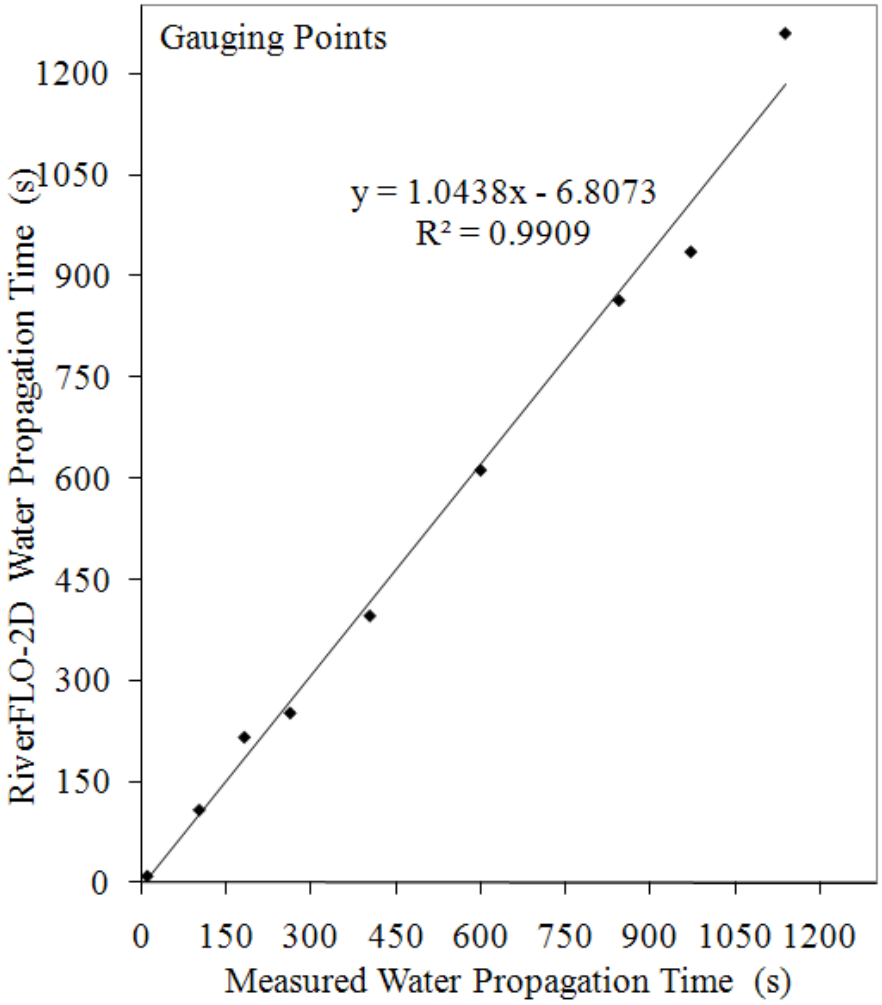

Figure 80. Malpasset flooding test. Comparison of water elevation marks for the physical model with numerical water surface elevations.

Figure 81 shows the mass balance in percentage for the three wet and dry algorithms analyzed. The modified wet and dry designed technique is a modification of the presented Kawahara technique and Umetsu and Matsumoto technique. The modified wet and dry technique was designed because the presences of erroneous velocities with the three subroutines show below for tests with complicated boundary conditions.

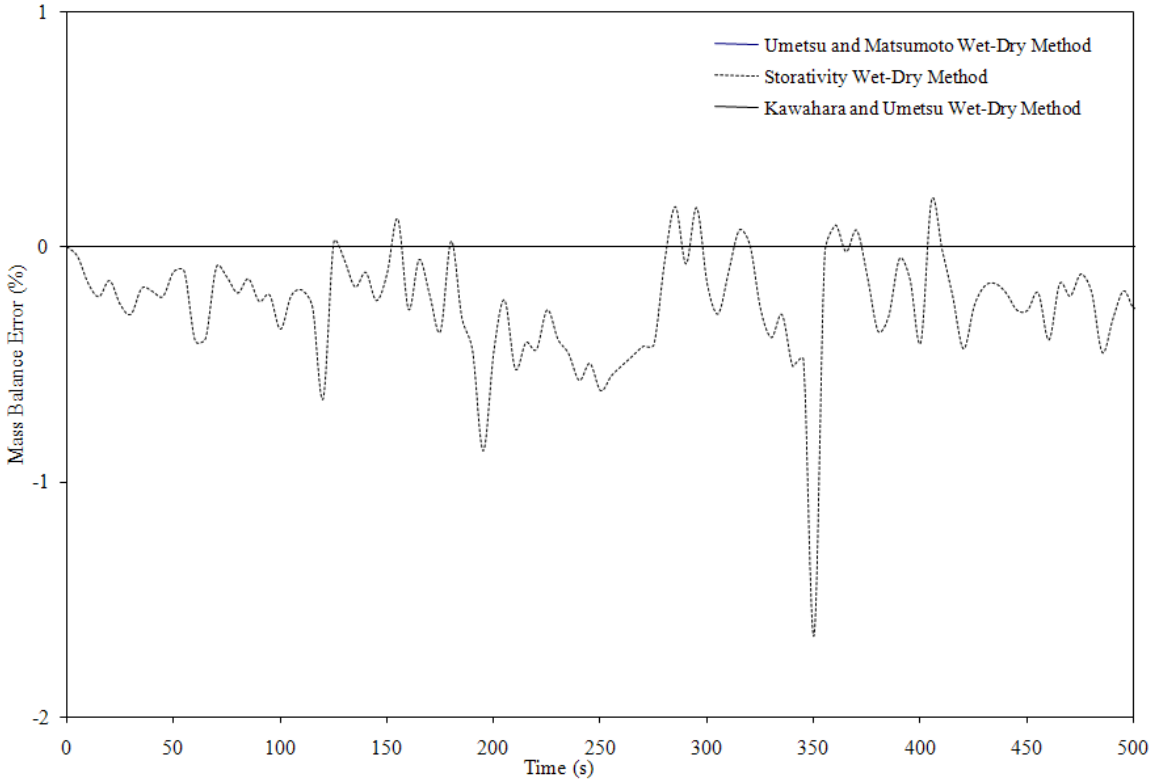

Figure 81. Malpasset flooding test. Mass Balance.

A comparison can be seen for all the numerical results show in Figure 77 to Figure 80 where R^2 varies from 0.976 to 0.990. All points lie very close on a straight line with a correlation of approximately 97.6% to 99%.

The maximum numerical velocities that can be seen in Figure 70 and Figure 71 are in the same order as the maximum velocities reported by other authors. Maximum velocities up to 23m/s were reported by other research. (Hervouet, 2007; Brufau et al., 2004; Hervouet & Petitjean, 1999).

OpenMP Results

Figure 82 shows the RiverFLO-2D speedup for up to 8 processors.

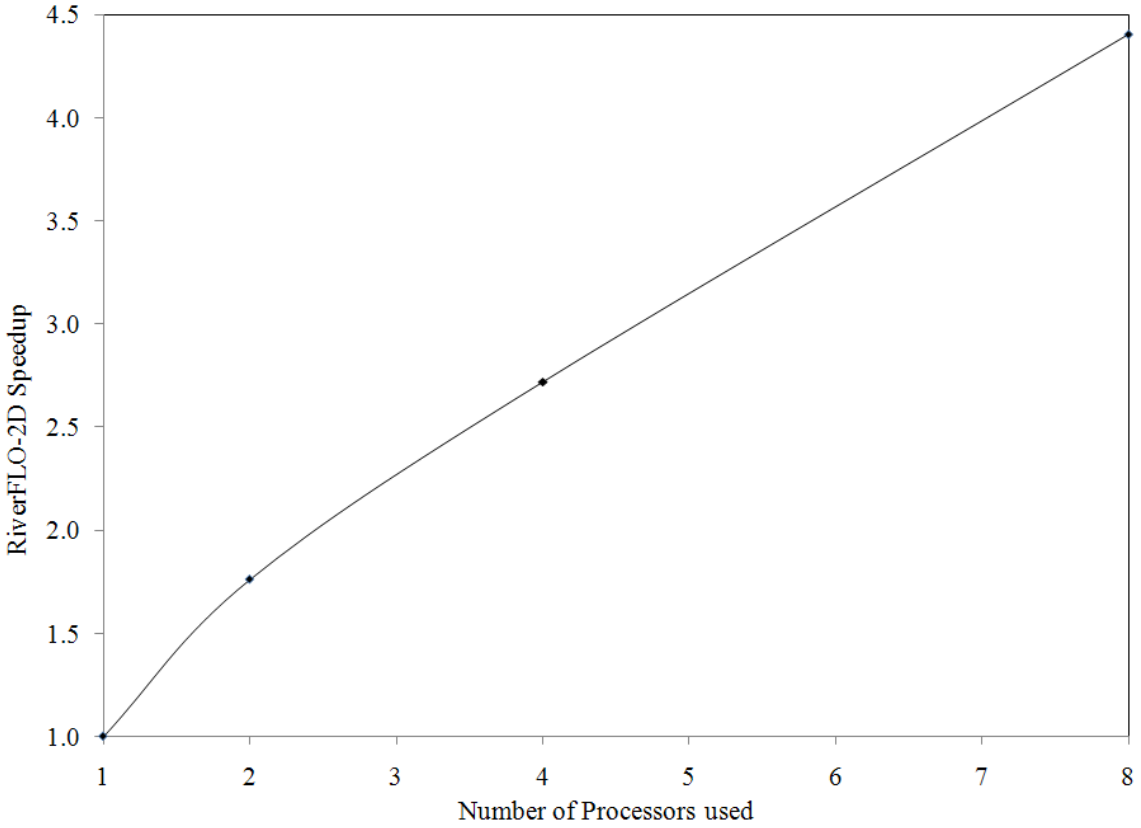

Figure 82. Malpasset flooding test. Speed up using RiverFLO-2D parallelized code.

The computer time for a 67min simulation is approximately 20min on a dual-core AMD Opteron processor 2220SE 2.80 GHz without parallelization improvements. For a 40min simulation was approximately 4min on 2 quad-core DELL PRECISION T7400 Intel Xeon CPU X5472 @3.00GHz 16GB of RAM without parallelization improvements.

The speedup in the computer time can be seen in Figure 83 with an improvement of approximately 4.5 times faster for 8 processors. This result can be compared with the speedup (4.5-5) predicted by Amdahl's Law Theory (see Figure 7).

3.3.2 Flooding of Sumacarcel

Case Description

The failure of Tous Dam in Spain and the flooding of Sumacarcel, a small town located 5km downstream, is considered as a test case in this dissertation (see Figure 83). The Tous Dam overtopping failure occurred on October 20, 1982 due to extremely heavy rainfall in the area. The complete set of data used in this case of study was put together during a European project named Investigation of Extreme Flood Processes and Uncertainty (Frazao, 2003; Alcrudo & Mulet, 2007). The collected field data and information include estimates of the flooding water depth marks that were located along the town of Sumacarcel. The pictures used in this case of study as well as the set of data have been collected by different modeling teams within IMPACT Project, especially by Alcrudo & Mulet, 2003 & 2007.

Figure 83. Sumacarcel Flooding Test. Aerial View of the Jucar River with the Tous Dam upstream and the town of Sumacarcel downstream.

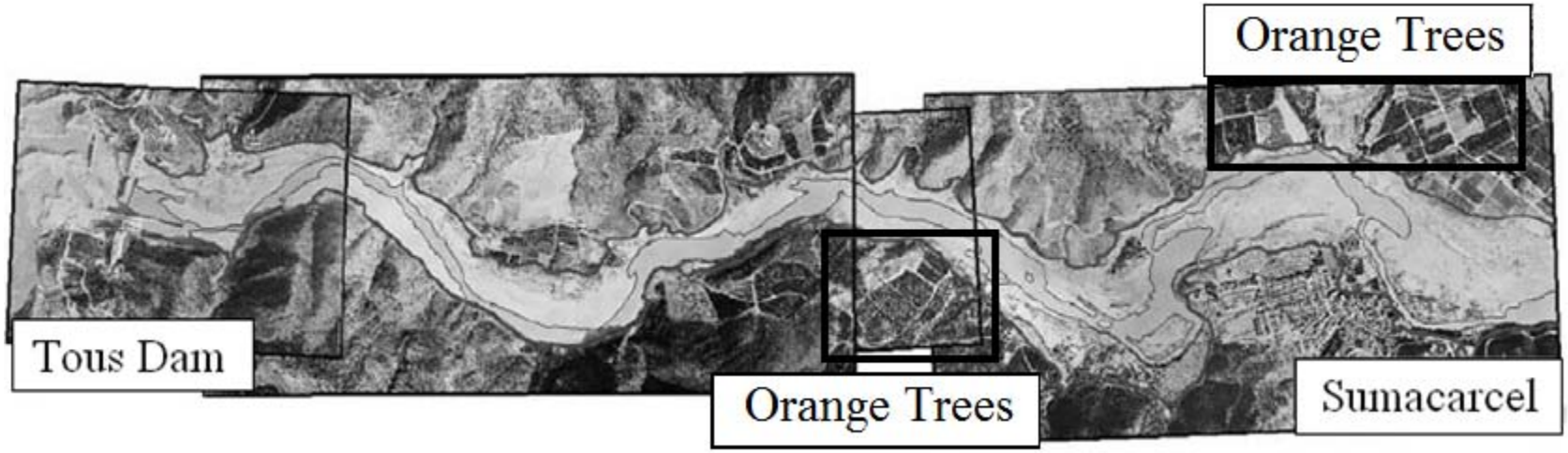

From the aerial pictures an analysis of the Manning's *n* was conducted by the Centro de Estudios y Experimentación de Obras Públicas, CEDEX (Centre for Studies and Experimentation of the Ministry of Public Works, Spain). They suggested a base Manning's *n* of 0.030 for the whole mesh and then increased it in the orange trees orchids' zone (see Figure 83). Finally, the Manning's *n* is set to 0.03, constant for all elements and two large areas are set with a Manning's *n* of 0.075, which corresponds with two dense orange tree orchards polygons adjacent to Sumacarcel (see Table 14 and Figure 83). According to these cited studies the areas where the trees where located produce a strong impact on the flood characteristics, particularly in steering the flood into the town by means of the increased flow resistance that dammed water up, by slowing down significantly the water velocity. After witnesses, the flood was directed towards the river bank opposite to the one where Sumacarcel lies due to the topography (see aerial pictures). However, that bank was covered with very tall orange trees (5–6m high) that dammed up water leading to a lateral flooding of Sumacárcel (Jucan River Basin Authority, CHJ) (Alcrudo & Mulet, 2003; Alcrudo & Mulet, 2007; CEDEX, 1998; CEDEX, 1984; CHJ, 1985 and 1999).

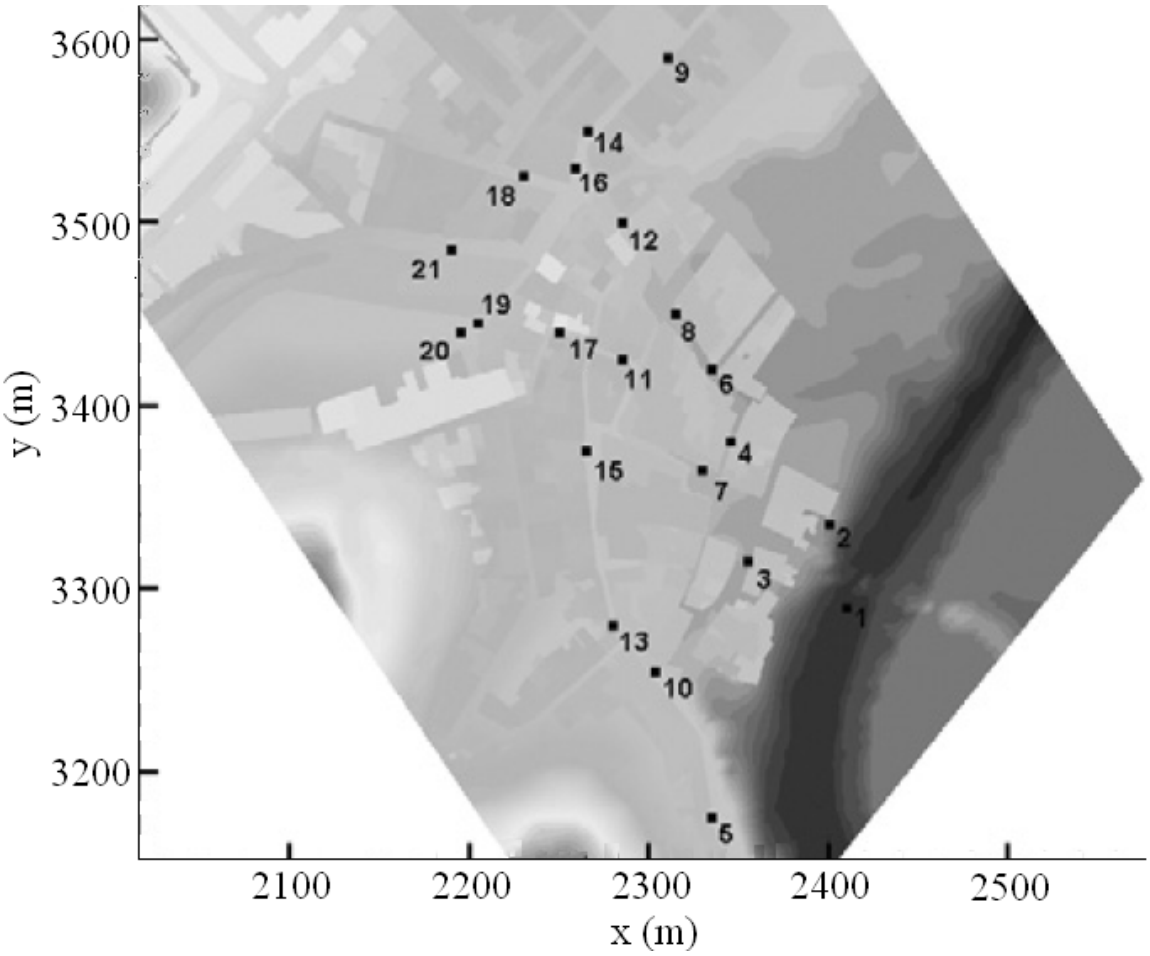

Figure 84. Sumacarcel Flooding Test. Sumacarcel recorded locations (IMPACT Project).

A 7347 node/13869 element mesh was generated for the Jucar River Basin (see Figure 88 and Figure 89). The total time of simulation is 30 hour. The initial conditions are dry bed downstream from the dam location.

Listings of the buildings present in the area (the town of Sumacarcel and some dispersed buildings in the valley) with their shape and co-ordinates of the vertices including rooftop elevation were provided by CEDEX (Alcrudo & Mulet, 2007). Additional documentation was drawn from the Catastro Provincial de Valencia (Land Registry of Valencia) (Alcrudo & Mulet, 2007). The data were corrected to the time of the flood with the aid of

local paper maps and discussions with citizens of Sumacarcel. A precise description of the buildings shape and position was included in the topography information that was used to create the numerical mesh (see Figure 88 and Figure 89).

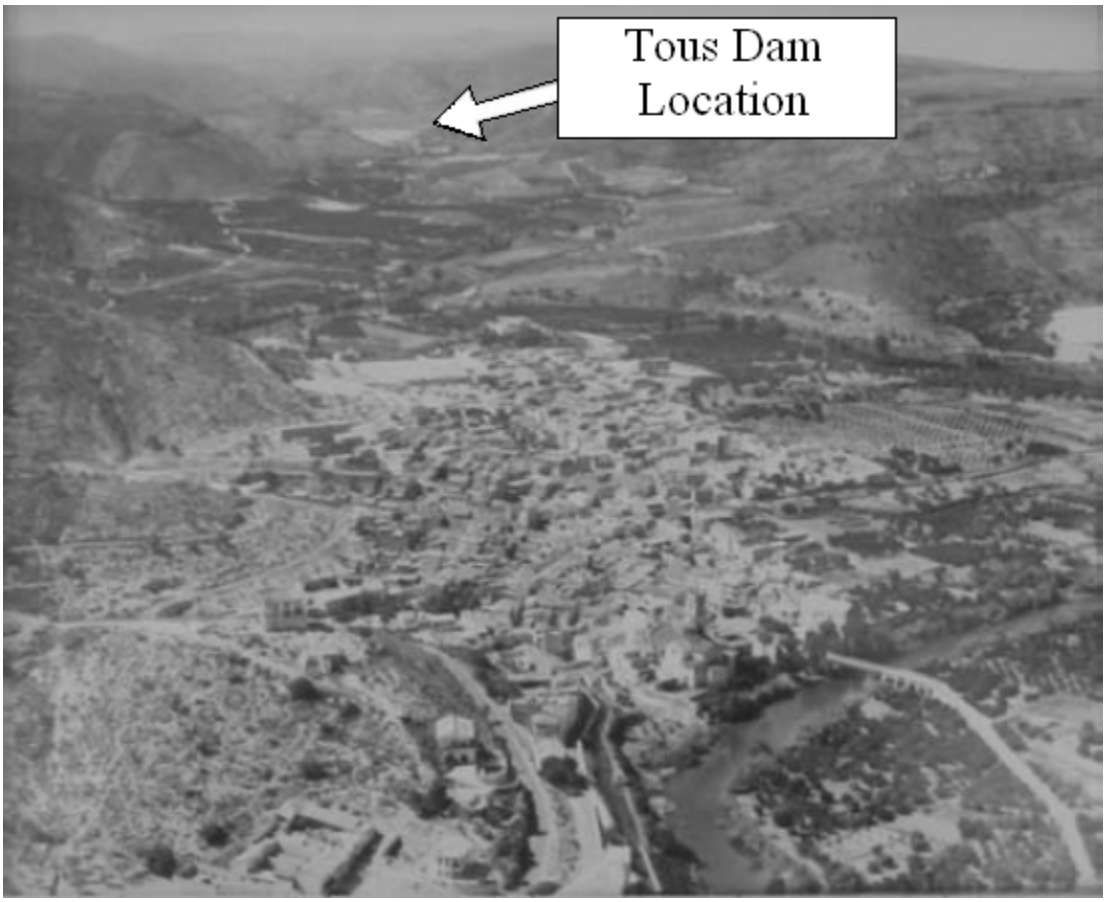

Figure 85. Sumacarcel Flooding Test. Sumacarcel before the flooding.

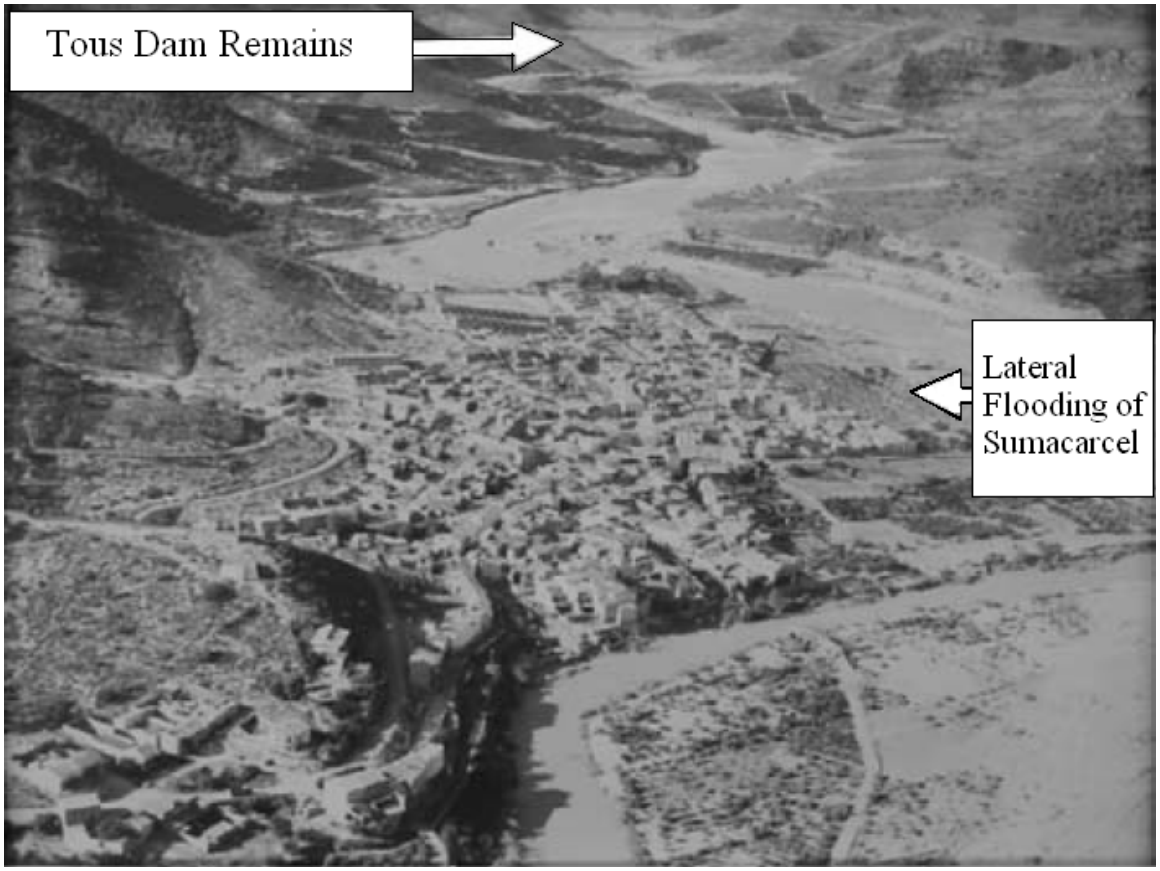

Figure 86. Sumacarcel Flooding Test. Sumacarcel after the flooding with the remaining hydraulic structure of Tous Dam upstream, lateral effect of flooding is highlighted.

The input hydrograph was obtained by using mathematical formulation by CEDEX, being the time of the hydrograph corrected based on the recorded inundation times for Sumacarcel (Alcrudo & Mulet, 2003; Alcrudo & Mulet, 2007; CEDEX, 1984, 1988, 1989 and 1998; CHJ, 1985 and 1999). The hydrograph was imposed on the downstream section of failure Tous Dam (see View 1 on Figure 89). The base flow of Júcar River is approximately 50 m^3/s, which is negligible in comparison with the scale of the hydrograph. The Tous outflow hydrograph was imposed as an inflow boundary condition at the downstream section of the dam.

Given the good performance of the implemented dry and wet technique that allow us to simulate both the rising limb and the recession limb and also the big volume of water (see Tous hydrograph Figure 87), the numerical calculations were started with a dry bed.

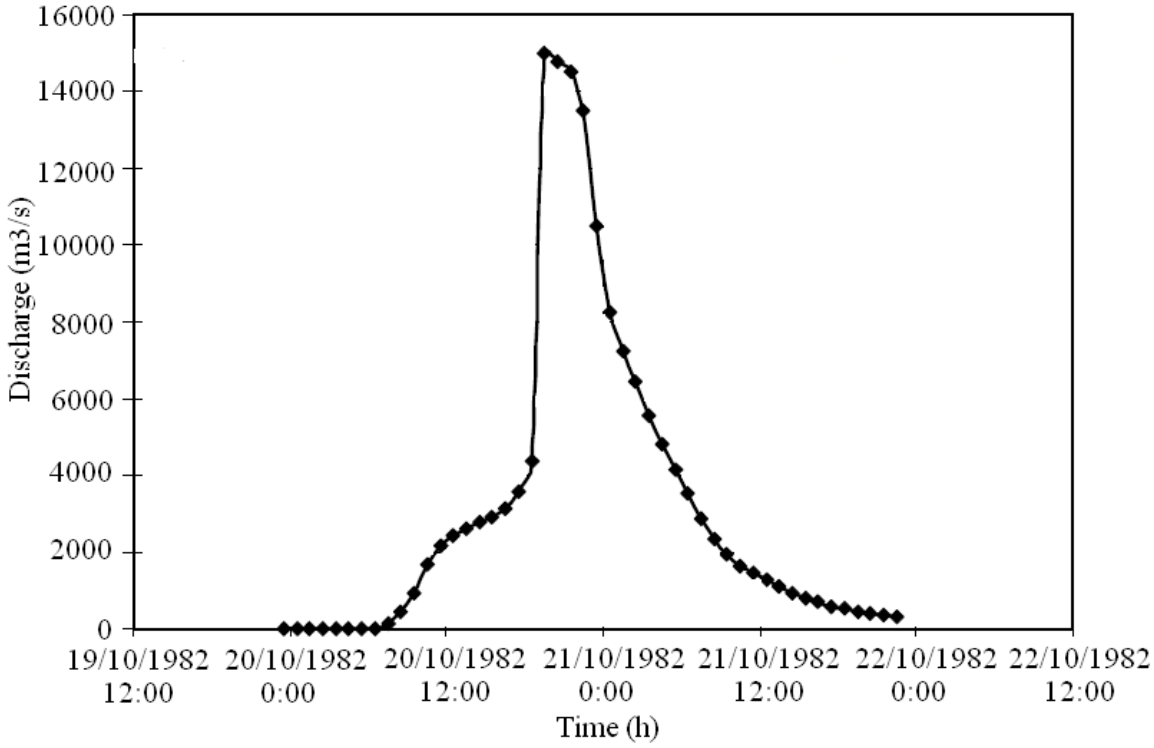

Figure 87. Sumacarcel Flooding Test. Outflow Hydrograph.

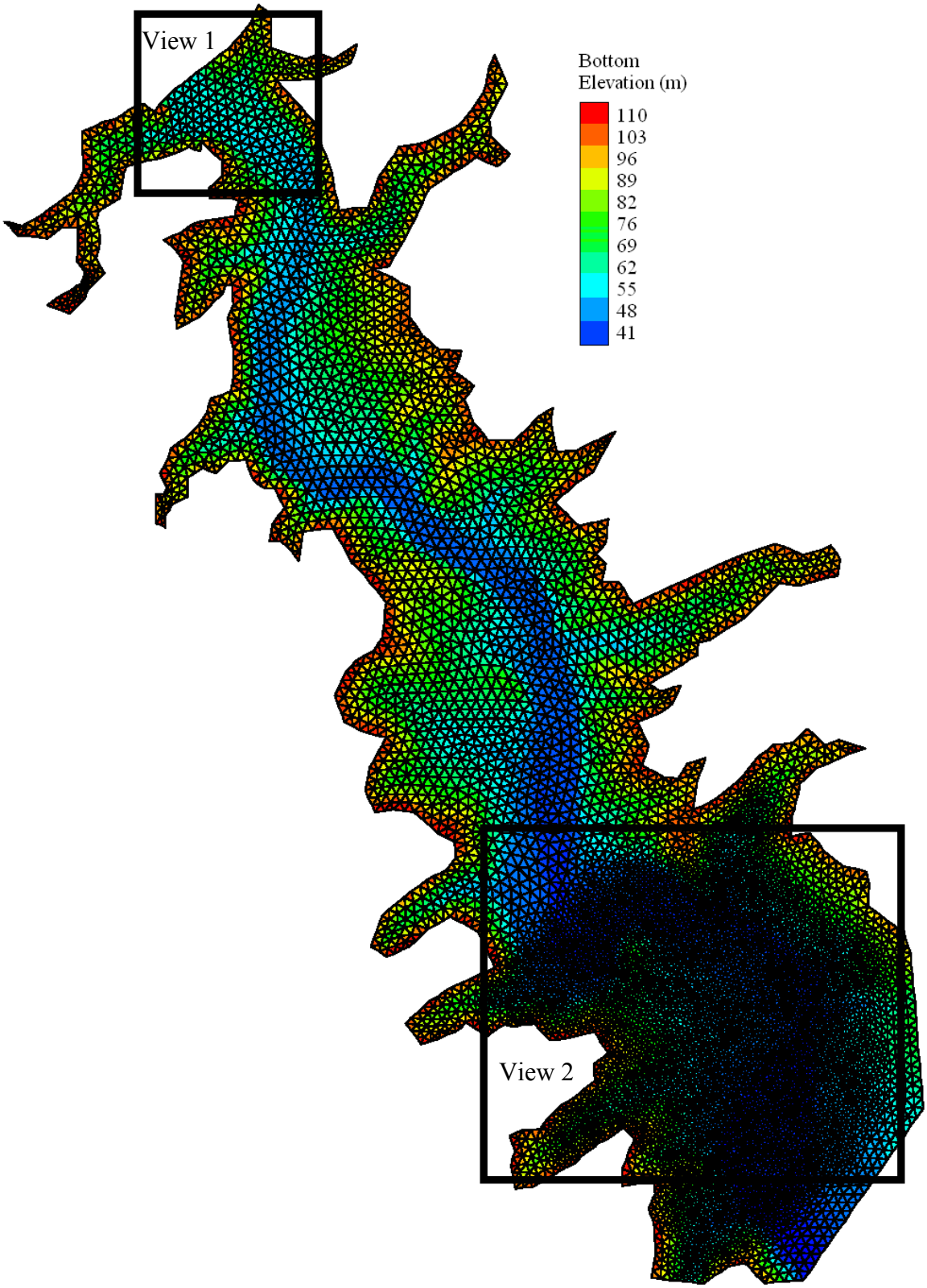

Figure 88. Sumacarcel Flooding Test. Bottom elevations and mesh extent.

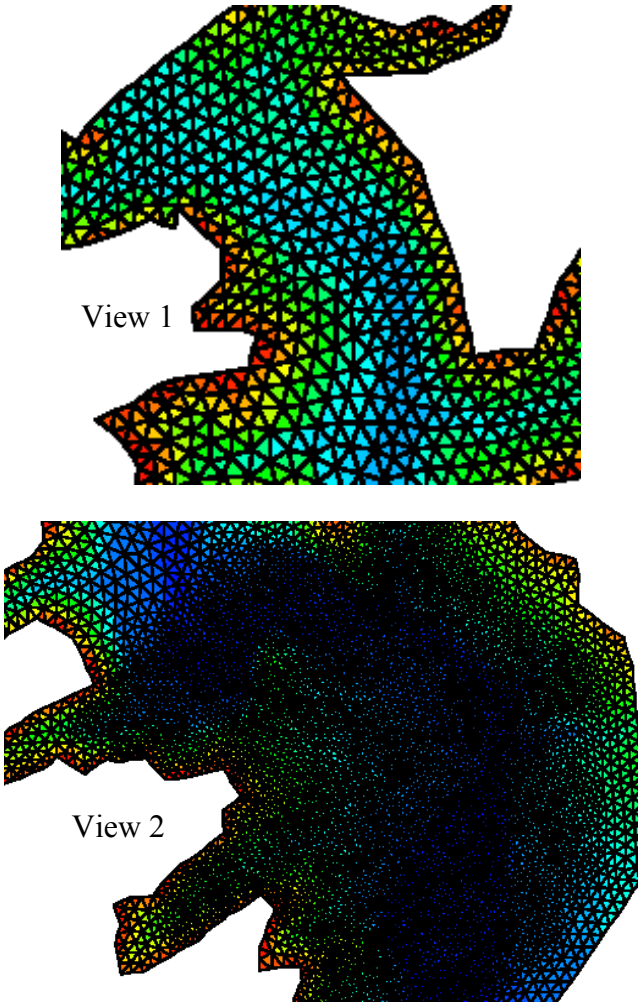

Figure 89. Sumacarcel Flooding Test. Two views of the numerical mesh.

Numerical Model Results

Based on the interview of several eye witnesses of the flood, including a local police member, 21 maximum water elevation marks were collected. The 21 gauge estimates are compared with RiverFLO-2D results. The information collected is enumerated in Table 14 along with RiverFLO-2D results.

Table 14. Sumacarcel Flooding Test. Data of the surveyed research points.

			Estimated Data	**RiverFLO-2D Results**
Gauge	**X (m)**	**Y (m)**	**Water Depth (m)**	**Water Depth (m)**
1	2410	3290	18.25	17.81
2	2400	3335	8.50	10.96
3	2355	3315	7.50	9.42
4	2345	3380	7.00	8.63
5	2335	3175	0.20	0.04
6	2335	3420	5.50	5.59
7	2330	3365	6.00	5.47
8	2315	3450	5.00	5.96
9	2310	3590	0.00	0.00
10	2303	3255	4.00	3.44
11	2285	3425	2.00	2.11
12	2285	3500	5.50	6.07
13	2280	3280	2.75	3.28
14	2266	3550	2.00	1.93
15	2265	3400	0.00	0.00
16	2259	3530	3.50	3.46
17	2250	3440	0.00	0.00
18	2230	3525	0.00	0.00
19	2205	3445	2.50	3.12
20	2195	3440	2.00	3.12
21	2190	3485	0.00	0.37

Figure 90 compares surveyed water elevation marks and model results.

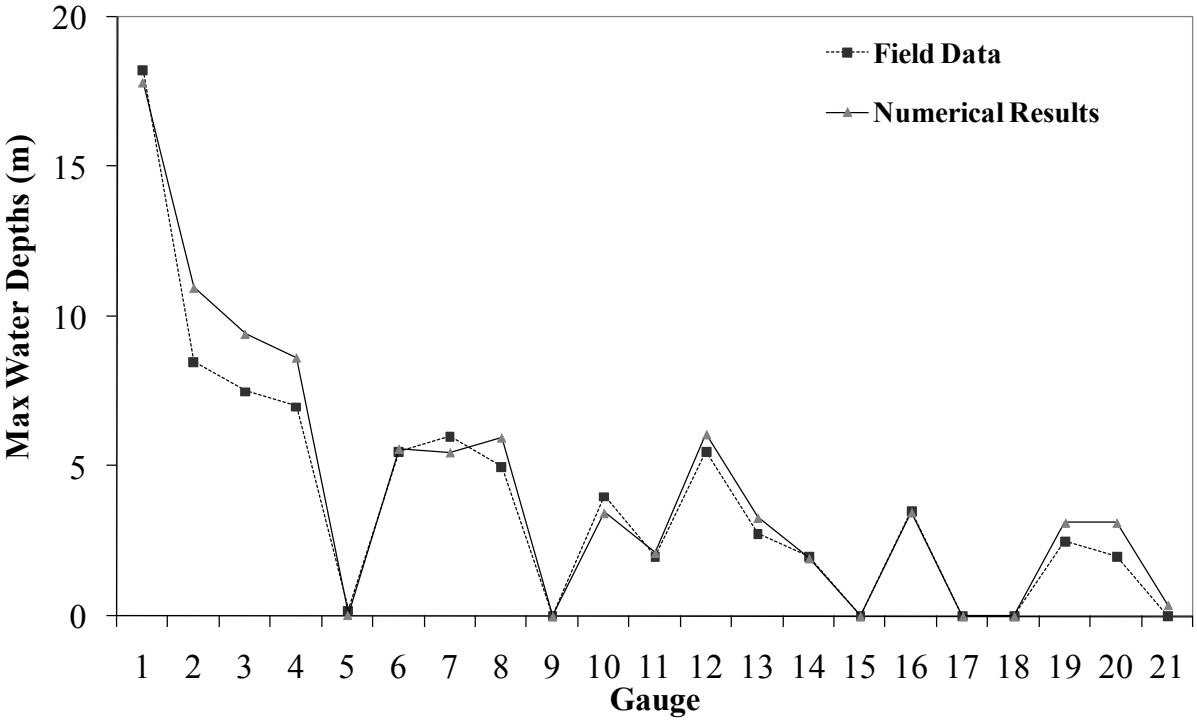

Figure 90. Sumacarcel Flooding Test. Comparison of water elevation marks with numerical water surface depths for 21 locations along Sumacarcel.

Figure 90 shows the comparison of recorded flood levels with numerical water surface depths for 21 locations along the river banks and the town of Sumacarcel. Details of the comparisons between estimated flood data and numerical results can be seen from Figure 90 to Figure 95, where flooding water depths were estimated on some Sumacarcel streets. According to collected testimonials of Sumacarcel flooding, the flood did not travel as a wave front, but rather as a quick lateral rise of water level as can be seen in the numerical simulation.

It can be concluded for this test that overall, the numerical results in the urban area seem to compare with the numerical data in terms of peak values for the gauges 1, 6, 9, 11, 14, 15, 16, 17, 18 and 21 (see Figure 84 for location of gauging points).

Figure 91 to Figure 95 present five different locations were flooding water depths were estimated and the comparison with RiverFLO-2D numerical water depths.

Figure 91. Sumacarcel Flooding Test. Water elevation mark and numerical water surface depth for gauge 3 in the Church Street of Sumacarcel.

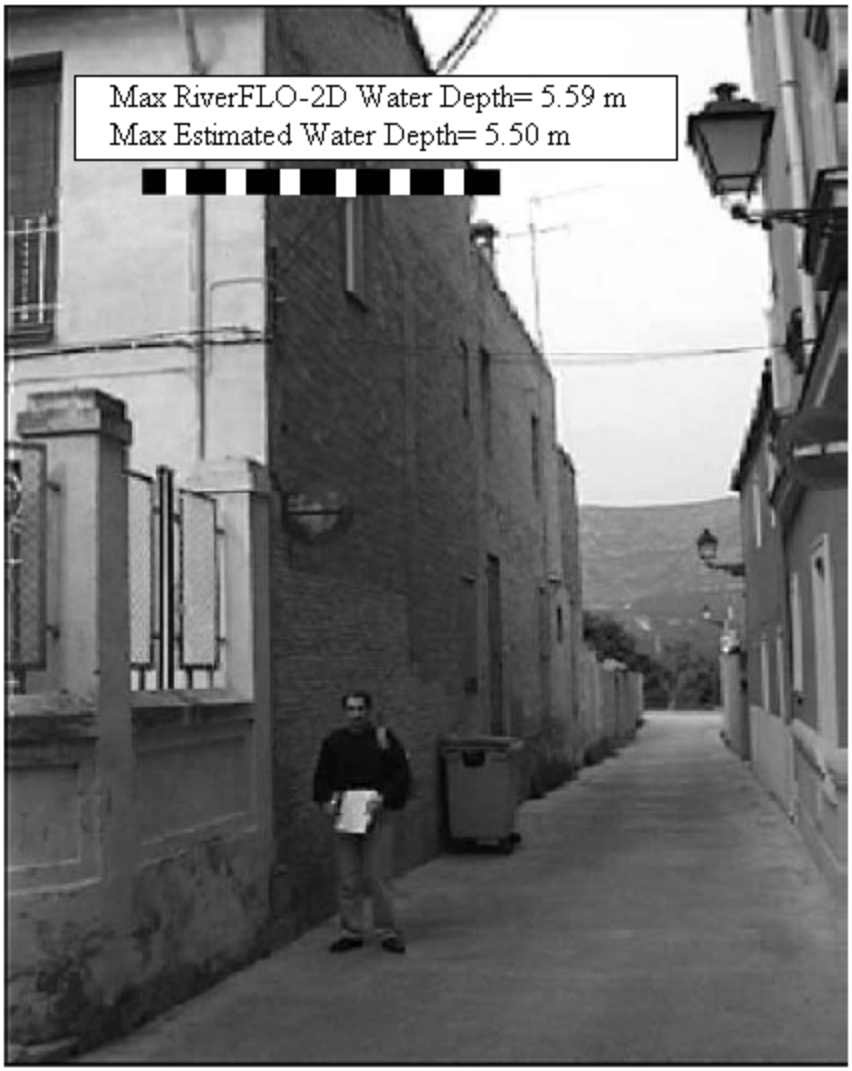

Figure 92. Sumacarcel Flooding Test. Water elevation mark and numerical water surface depth for gauge 6 in the Proyecto C Street of Sumacarcel.

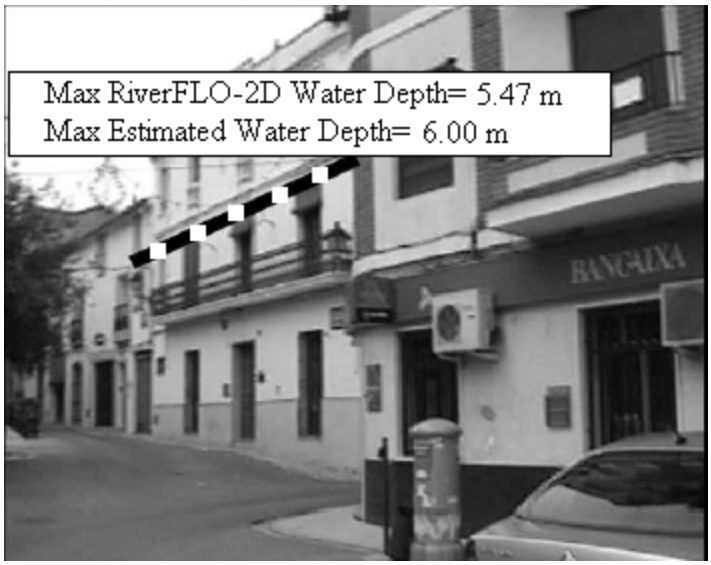

Figure 93. Sumacarcel Flooding Test. Water elevation mark and numerical water surface depth for gauge 7 in the Old City Hall of Sumacarcel.

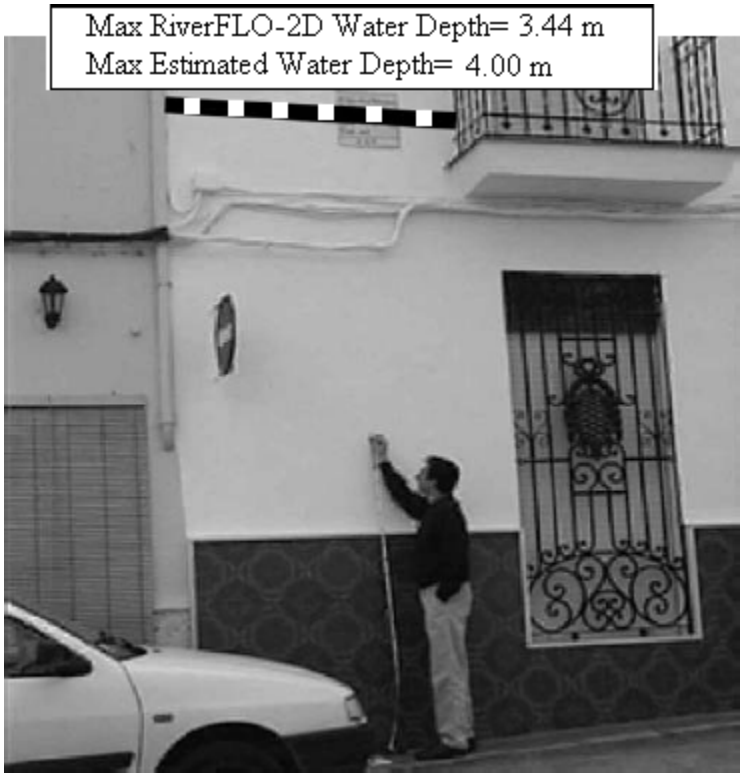

Figure 94. Sumacarcel Flooding Test. Water elevation mark and numerical water surface depth for gauge 10 in Jucar Street of Sumacarcel.

Figure 95. Sumacarcel Flooding Test. Water elevation mark and numerical water surface depth for gauge 16 in Pintor Sorolla Street of Sumacarcel.

Figure 96 and Figure 97 show the velocity fields at two locations for time 11 h.

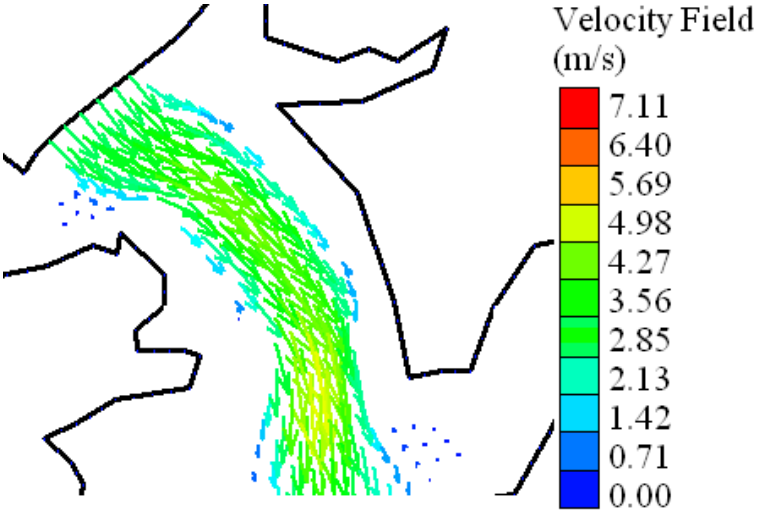

Figure 96. Sumacarcel Flooding Test. Velocity field detail for view 1 T=11 h. (View 1).

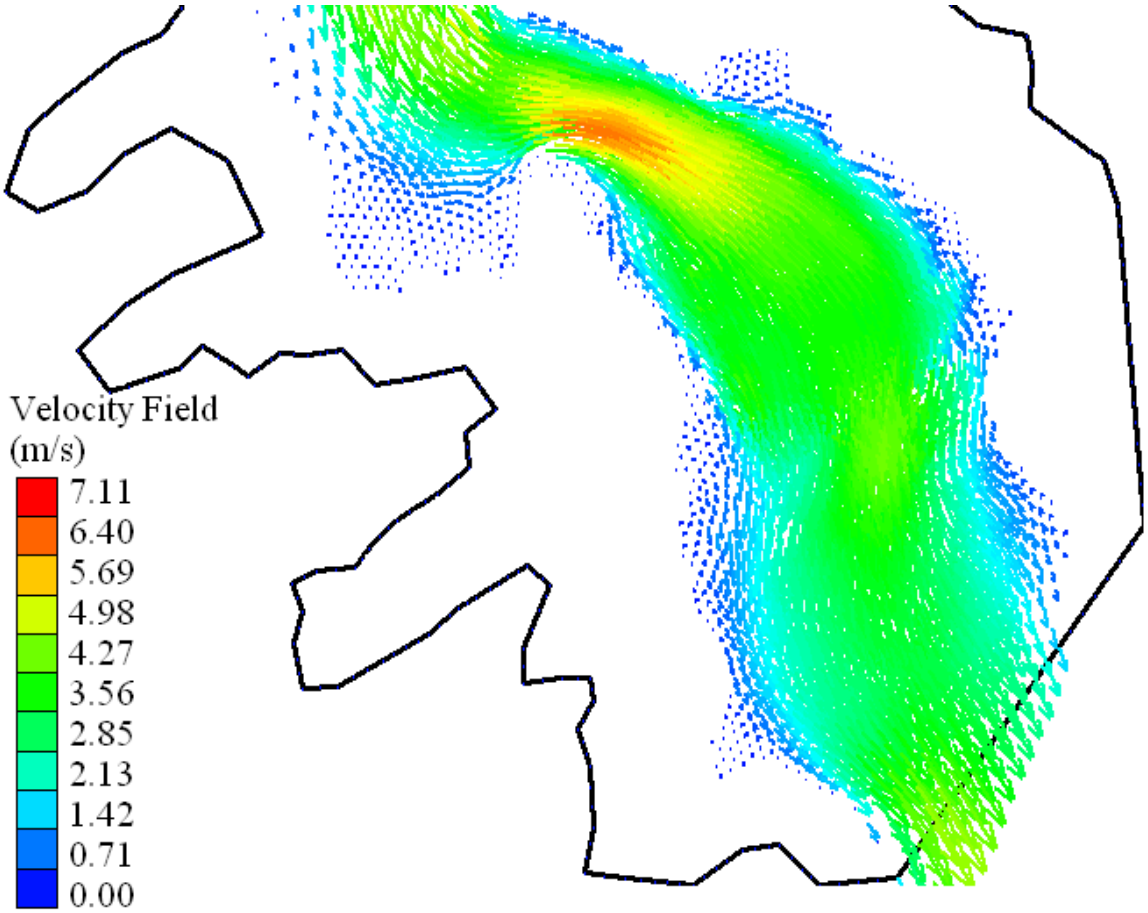

Figure 97. Sumacarcel Flooding Test. Velocity field detail for view 2 at T=11 h (View 2).

The results obtained from the enhanced model indicate that the proposed method generates stable numerical solutions predicting correctly the flooding of Sumacarcel. No spurious velocities over dry areas are presented in the simulation as can be seen in Figure 96 and Figure 97.

Figure 98 shows the results of RiverFLO-2D model compares with field data for Tous Dam-Break.

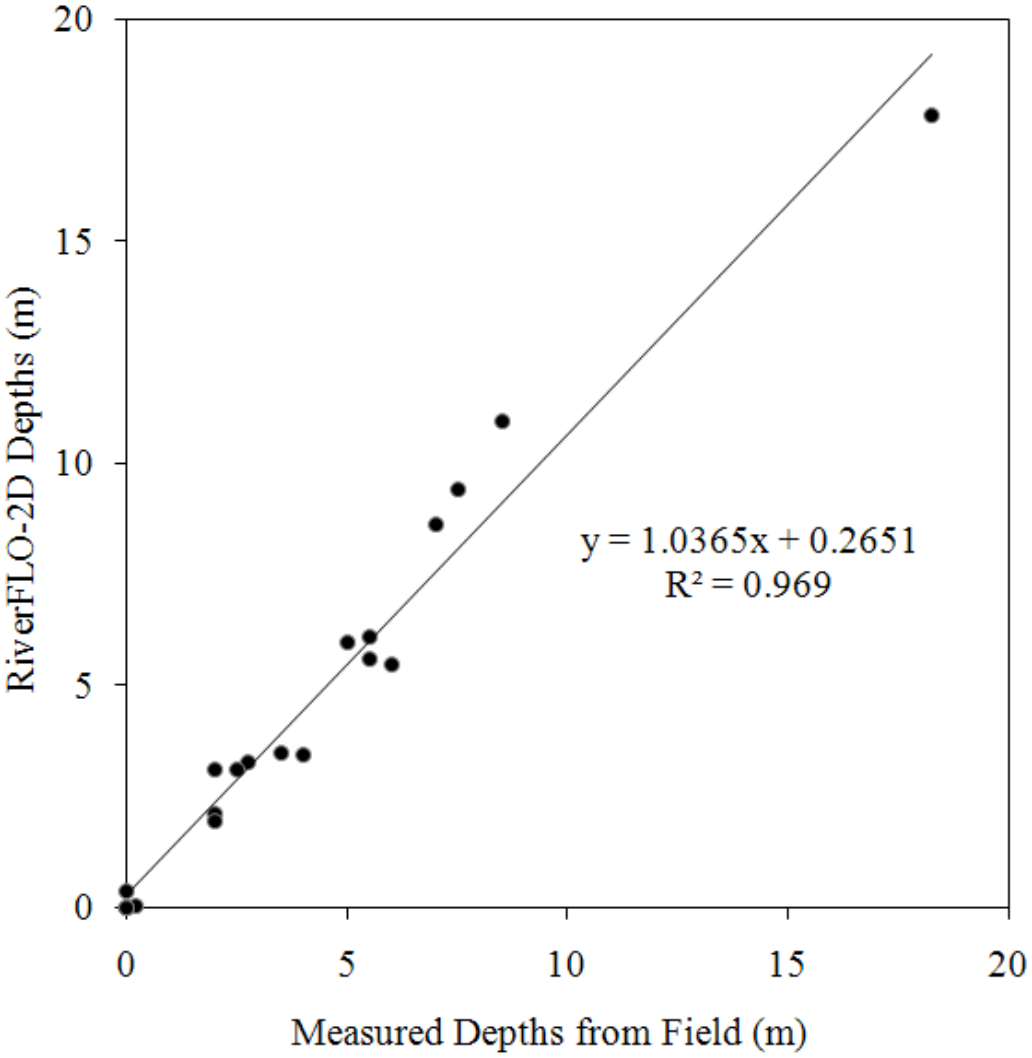

Figure 98. Sumacarcel Flooding Test. Comparison of the Numerical Results and Field Data for the gauging points.

The numerical model compares well with the recorded flood mark for all the numerical results as it shows in Figure 98, where an R^2 of approximately 0.97 is calculated. All points lie very close on a straight line with a correlation of approximately 97%. The enhanced numerical model shows that is capable to predict flooding events in complex geometries handling refined completely dry mesh and producing very accurate results without the presence of instabilities or erroneous velocities and depths in the simulation.

OpenMP Results

The sequential and parallel code was run for Sumacarcel Flooding Test. The comparison of RiverFLO-2D velocity and depth results for both runs can be seen in Figure 99 and Figure 100.

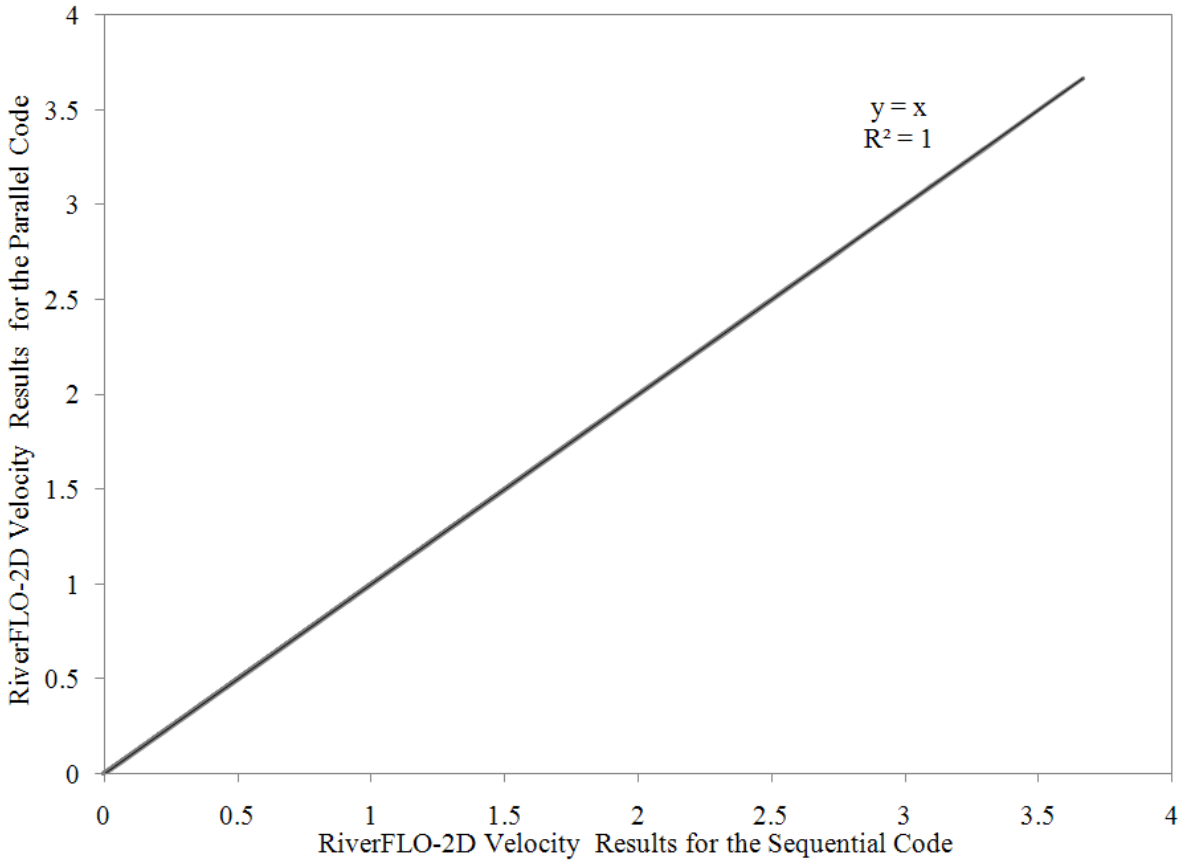

Figure 99. Sumacarcel Flooding Test. Comparison of the RiverFLO-2D velocity results for the parallel and the sequential code.

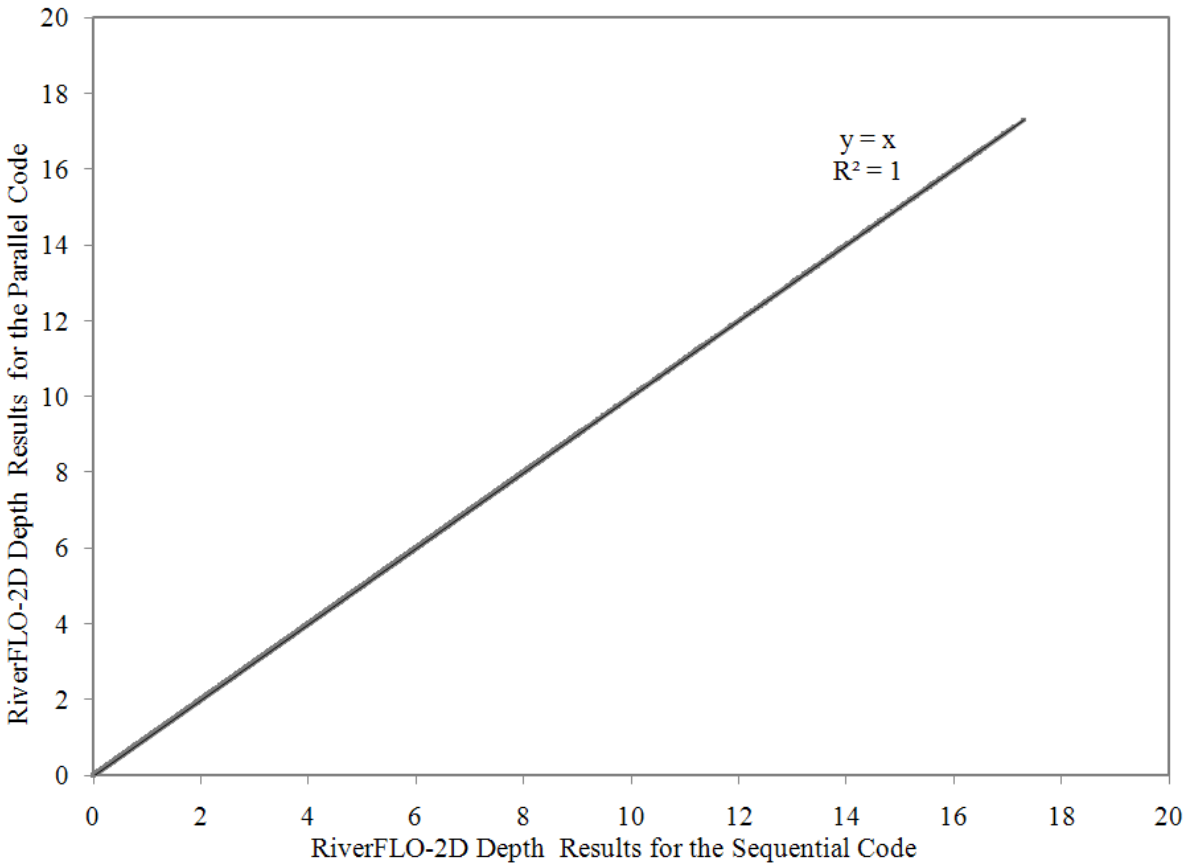

Figure 100. Sumacarcel Flooding Test. Comparison of the RiverFLO-2D depth results for the parallel and the sequential code.

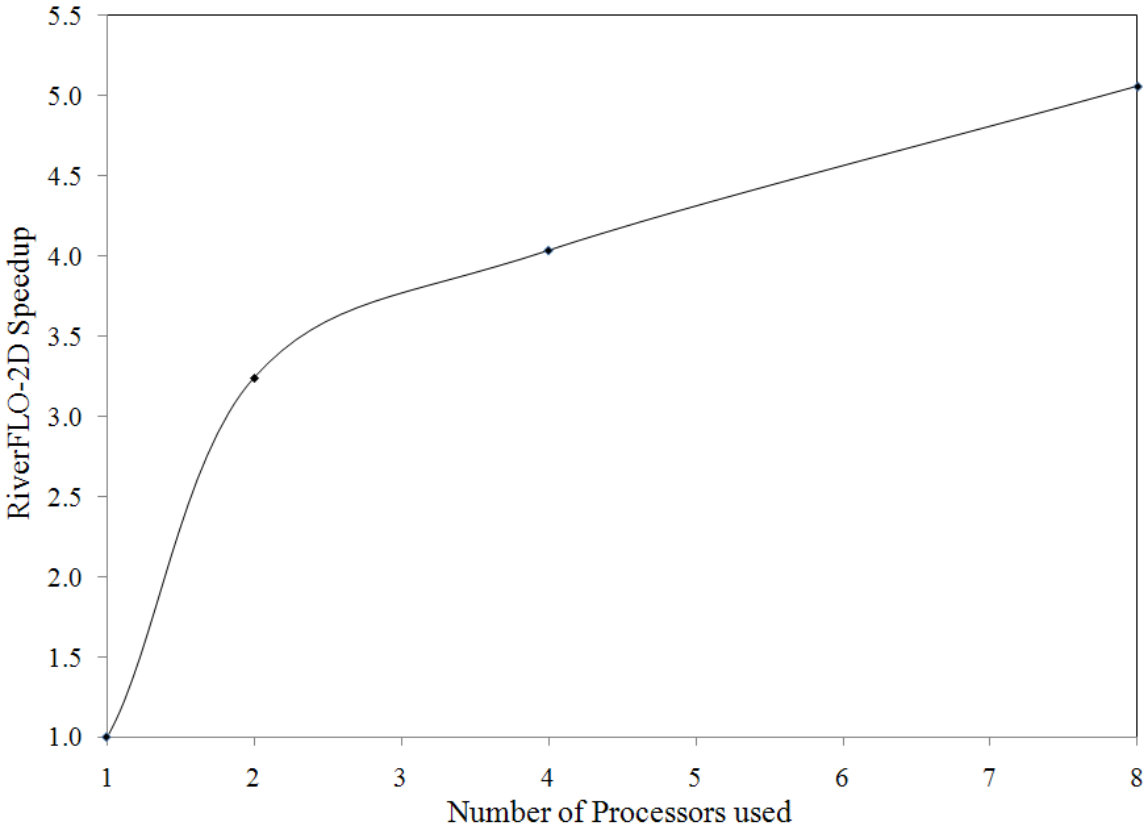

Figure 101. Sumacarcel Flooding Test. Speed up using RiverFLO-2D parallelized code.

No differences can be found between the comparison of numerical results for the parallel code and for the sequential code. OpenMP parallelization was programmed without any alteration of the original numerical calculations of RiverFLO-2D as it can be seen in Figure 99 and Figure 100.

The computer time for a 30hr simulation was approximately 6.5hr on 2 quad-core DELL PRECISION T7400 Intel Xeon CPU X5472 @3.00GHz 16GB of RAM without parallelization improvements. The speedup in the computer time can be seen in Figure 101 with an improvement of approximately 5 times faster for 8 processors. This result is consistent with the speedup (4.5-6) predicted by Amdahl's Law Theory (see Figure 7).

CHAPTER 4. FLASH FLOOD ILLUSTRATIVE APPLICATION

Case Description

Two recent flooding events changed the way water resources engineers, water managers and residents approached disasters in South Florida. Prior to Hurricane Irene, the focus had been on hurricanes as potential wind hazards, and no particularly flood events. In October 1999, Hurricane Irene developed and started a path towards South Florida. Irene traveled through the state and, on October 15, passed just to the west of Miami-Dade County.

Tropical Storm Irene strengthened as it moved northward, and reached maximum sustained winds of 70mph (115km/h) early on October 14. Irene continued to move towards the north-northeast, crossed over the western portion of the Isla de la Juventud as a strong tropical storm, and hours later, it struck mainland Cuba. The storm was able to strengthen further over the Florida Straits, and Irene attained hurricane status on October 15 dumping from 10 to 20 inches of rain. It passed over Key West, turned more to the north-northeast, and struck mainland Florida at Cape Sable as an 80mph (130km/h) hurricane. Irene entered the Atlantic Ocean near Jupiter, Florida early on October 16, still as a Category 1 hurricane.

Wet tropical cyclones were a common phenomena in the 1930s and 1940s with similar effects over Florida although somewhat more widespread. Another similar case of a wet hurricane was Tropical Storm Gordon in November 1994.

Figure 102 shows an aerial view of the Irene Hurricane and the track of Irene over Cuba and Florida.

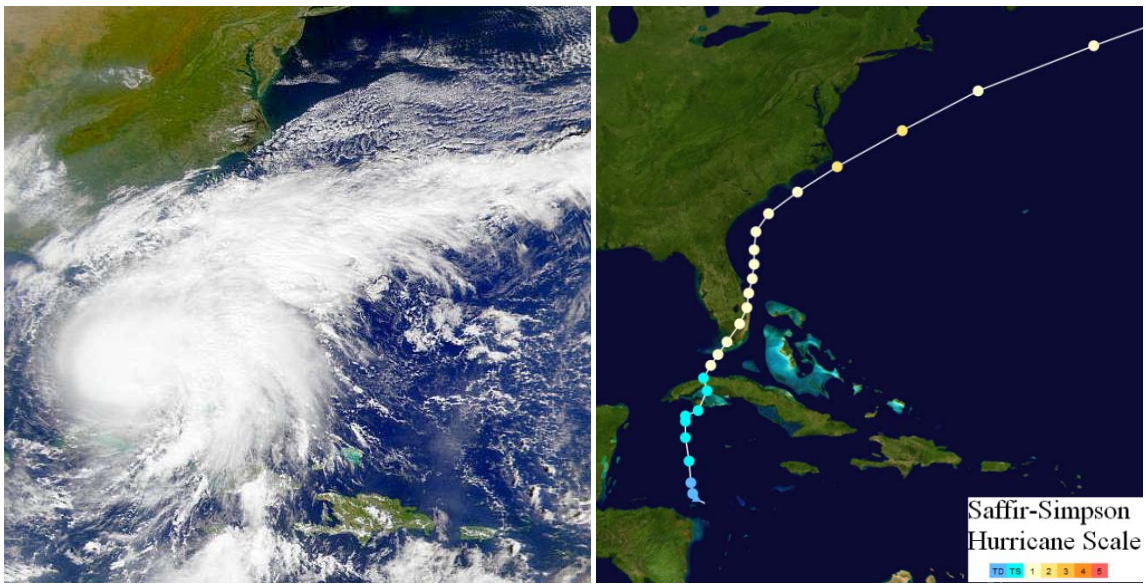

Source: NOAA

Figure 102. Flash Flood Illustration. Aerial view of the Irene Hurricane and the track of the storm over Cuba and Florida.

Irene caused considerable damage due to the big amount of rainfall (approximately 15 inches) that carried with it, flooding extended areas of South Florida. In Miami-Dade County the following residential areas were severely affected (Flood Management Task Force, 2000)

1. City of Sweetwater
2. City Of West Miami
3. City of Miami Springs
4. Village of Virginia Gardens
5. City of Hialeah
6. City of North Miami

7. City of Opa-Locka
8. City of Homestead

According to Miami-Dade County reports, Hurricane Irene flooded 100% of the City of Sweetwater in Miami-Dade County, affecting homes, vehicles, streets and producing several economical losses. Residential streets were impassable for almost one week.

Figure 103 shows the reported troubled areas in northern areas of Miami-Dade County collected by the Flood Management Task Force 2000. Flooding was reported through the entire City of Sweetwater for Public Works offices as well as for neighbords.

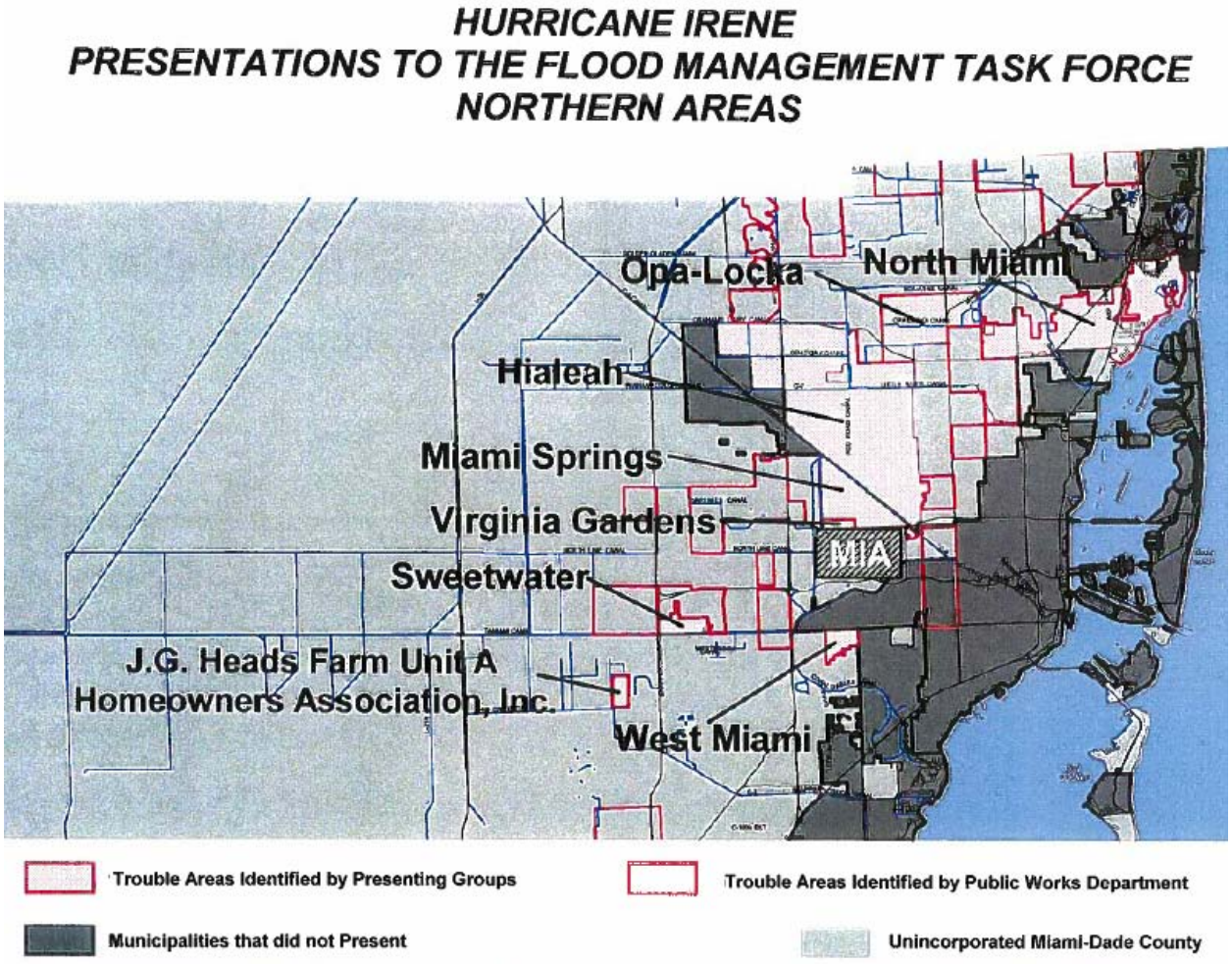

Source: Hurricane Irene - Task Management Force Report.

Figure 103. Flash Flood Illustration. Troubled areas in northern areas of Miami-Dade County because Hurricane Irene flooding.

Figure 104 shows the total precipitation for Hurricane Irene, as measured by various rain gages and observers, the source of this map is the National Weather Service Weather Forecast Office at Miami, South Florida. A total rainfall volume of approximately 15 inches was reported over the City of Sweetwater.

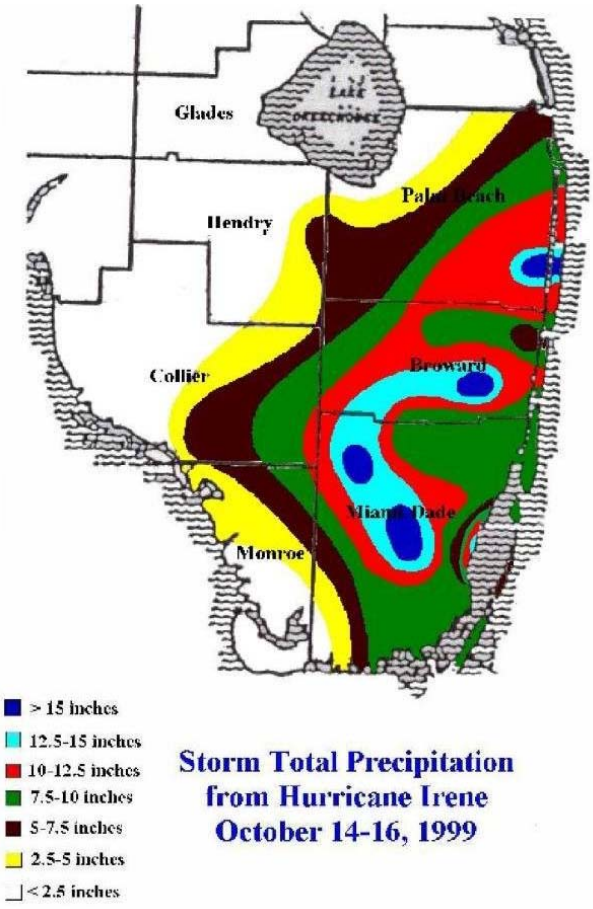

Source: Hurricane Irene - Task Management Force Report.

Figure 104. Flash Flood Illustration. Total Precipitation from Hurricane Irene, as measured by various rain gages and observers.

Figure 105 shows the total precipitation as depicted by the Miami WSR-88D doppler weather radar. The rainfall maximum, and overall shape of the precipitation pattern, compare well with the rain gauge measurements, the source of this map is the National Weather Service Weather Forecast Office at Miami, South Florida.

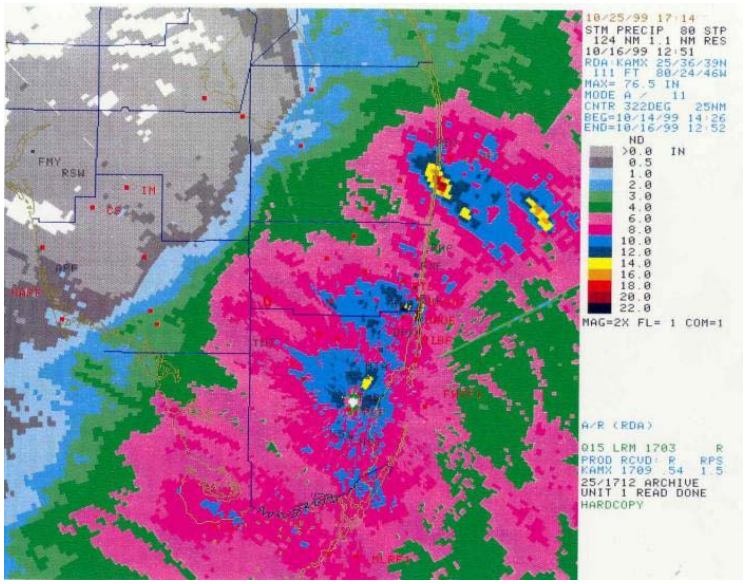

Source: NOAA

Figure 105. Flash Flood Illustration. Total precipitation as depicted by the Miami WSR-88D Doppler Weather Radar.

The following pictures present the flooding damages of the Hurricane Irene in some neighborhoods of South Florida.

Source: FEMA News Photo / G. Mathieson

Figure 106. Flash Flood Illustration. Davie, Florida, October 23, 1999. Rural side streets remain flooded days after Hurricane Irene hit the area.

Source: FEMA News Photos / G. Mathieson

Figure 107. Flash Flood Illustration. Davie, FL, October 23, 1999. Local residential roads remain flooded, days after Hurricane Irene dropped up to 15 inches of rain on some areas in Florida.

Source: FEMA News Photo/G. Mathieson

Figure 108. Flash Flood Illustration. Broward County, Florida, 10/20/1999. Local drivers negotiate the back roads in the aftermath of Hurricane Irene.

Figure 109 and Figure 110 show two pictures with the effects of Hurricane Irene in some neighborhoods of Sweetwater. It can be notice an inundation approximately in the order of 80 cm of water.

Source: Hurricane Irene - Task Management Force Report.

Figure 109. Flash Flood Illustration. Flooded neighborhoods in the City of Sweetwater.

Source: Hurricane Irene - Task Management Force Report.

Figure 110. Flash Flood Illustration. Flooded neighborhoods in the City of Sweetwater.

Local residential roads remain flooded, days after Hurricane Irene dropped up to 15 inches of rain on some areas of Miami Dade County.

The purpose of the present application is to assess the predictive capability of a physically based rainfall-runoff model capable to include NEXRAD rainfall estimates in the analysis. The Sweetwater City is part of the C-4 basin located in the west area of Miami-Dade County (See Figure 111).

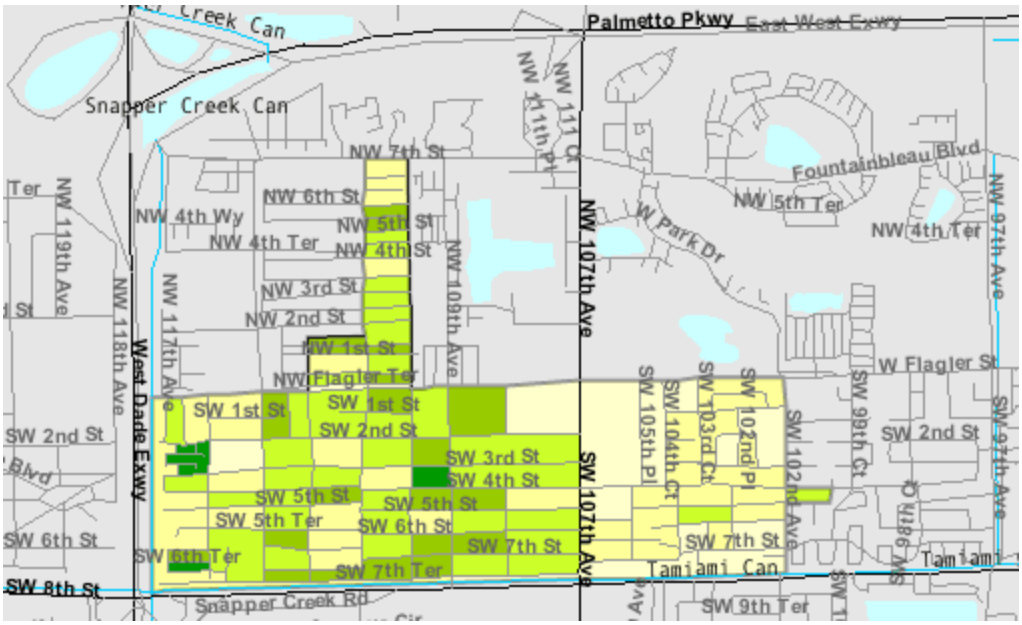

Figure 111. Flash Flood Illustration. Limits for the City of Sweetwater.

The scarcity of data for the flooding event of Hurricane Irene represents an obstacle for the calibration process; no calibration was attempted for this illustration case due to the inexistence of field measurements of water depths or flooding marks. Only general observations of the event were found in several Miami-Dade County reports, consequently a simplified sensitivity analysis was conducted. The sensitivity analysis of the modeling results will be provided in terms of the Manning's *n* parameter and the mesh size of the grid, under the assumption that RiverFLO-2D model predictions depend on the uncertainty of the hydraulic parameters. The influence of those parameters will be tested by altering just one of them in each calculation and by checking the induced modifications in the numerical results and explaining the origin of the changes. The extension of the inundation and maximum depths will be calculated but no detailed comparison can be done for the lack of flooding real data. Those analyses will be conducted to measure the goodness of the results that will allow us to judge when the

performance is acceptable and basically show us the capabilities of the enhanced RiverFLO-2D model. It is important to highlight that the few available estimations of the flooding effect in the City of Sweetwater were used only for an evaluation of the capabilities of the enhanced RiverFLO-2D model.

The Digital Terrain Model (DTM) used in this illustration case was the Light Detection and Ranging (LIDAR) elevation data. LIDAR elevation data was provided by the Department of Environmental Resources Management (DERM) at Miami Dade-County (see Figure 112). The used DTM data was collected as part of the Windstorm Simulation & Modeling Project per the contract agreement established October 8, 2002 between, Florida International University International Hurricane Research Center (IHRC) and Miami-Dade County. The DTM resolution is 5m and the vertical datum is NAVD 88. Error analysis of the Miami-Dade County LIDAR data indicates a root mean square error (RMSE) of 12 cm. This corresponds to a vertical accuracy of +/- 24 cm at the 95% confidence level.

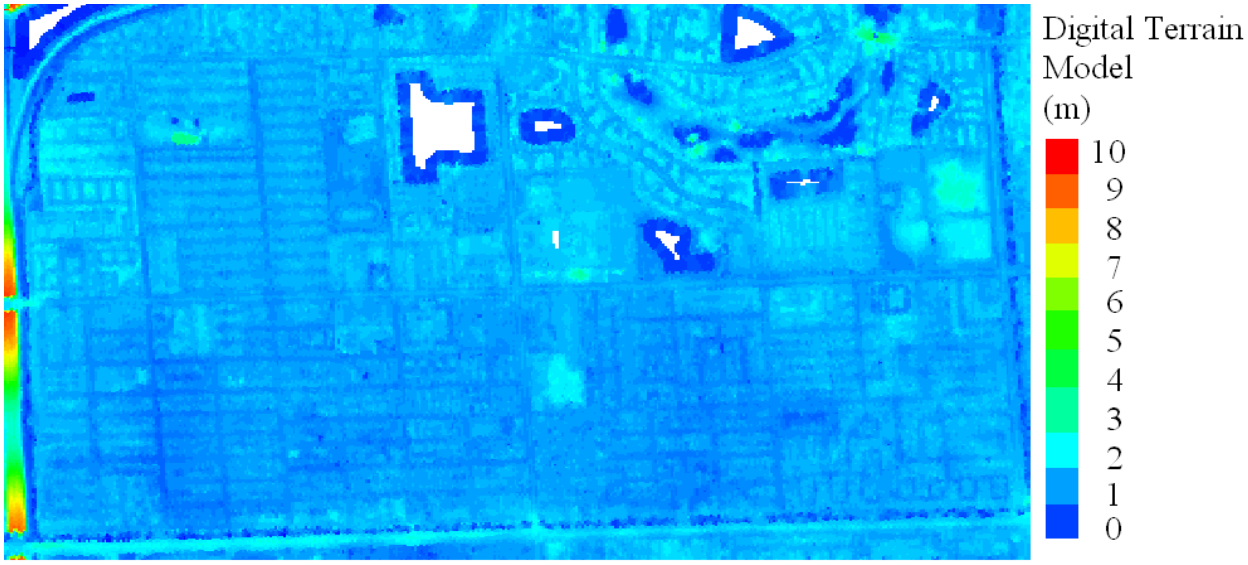

Figure 112. Flash Flood Illustration. Digital Terrain model for City of Sweetwater

A NEXRAD rainfall estimates in each element were an input for this illustration case. The NEXRAD estimates were interpolated from the rainfall estimates received from South Florida Water Management District (SFWMD). The reflected signal measured by the radar is proportional to the sum of the sixth power of the diameter of the raindrops in a given volume of atmosphere; small changes in the size of raindrops can have a dramatic effect on the radar's estimate of the rainfall. For this reason the radar is scaled to match the volume measured at the rain gauges. The best of both measurement techniques is realized by using rain-gauge data to adjust NEXRAD values (Pathak, 2008). The NEXRAD rainfall estimates included in this research are hourly gauge-adjusted at 1 hour time interval and with a resolution of 2km x 2km. The numerical time of simulation was 52 hr using the NEXRAD rainfall estimates for October 14, October 15 and the two first hours of October 16 when the rainfall recedes to lower amounts as it can be seen in the rain gauge data from Station S26 and Miami Field Station (See Figure 113).

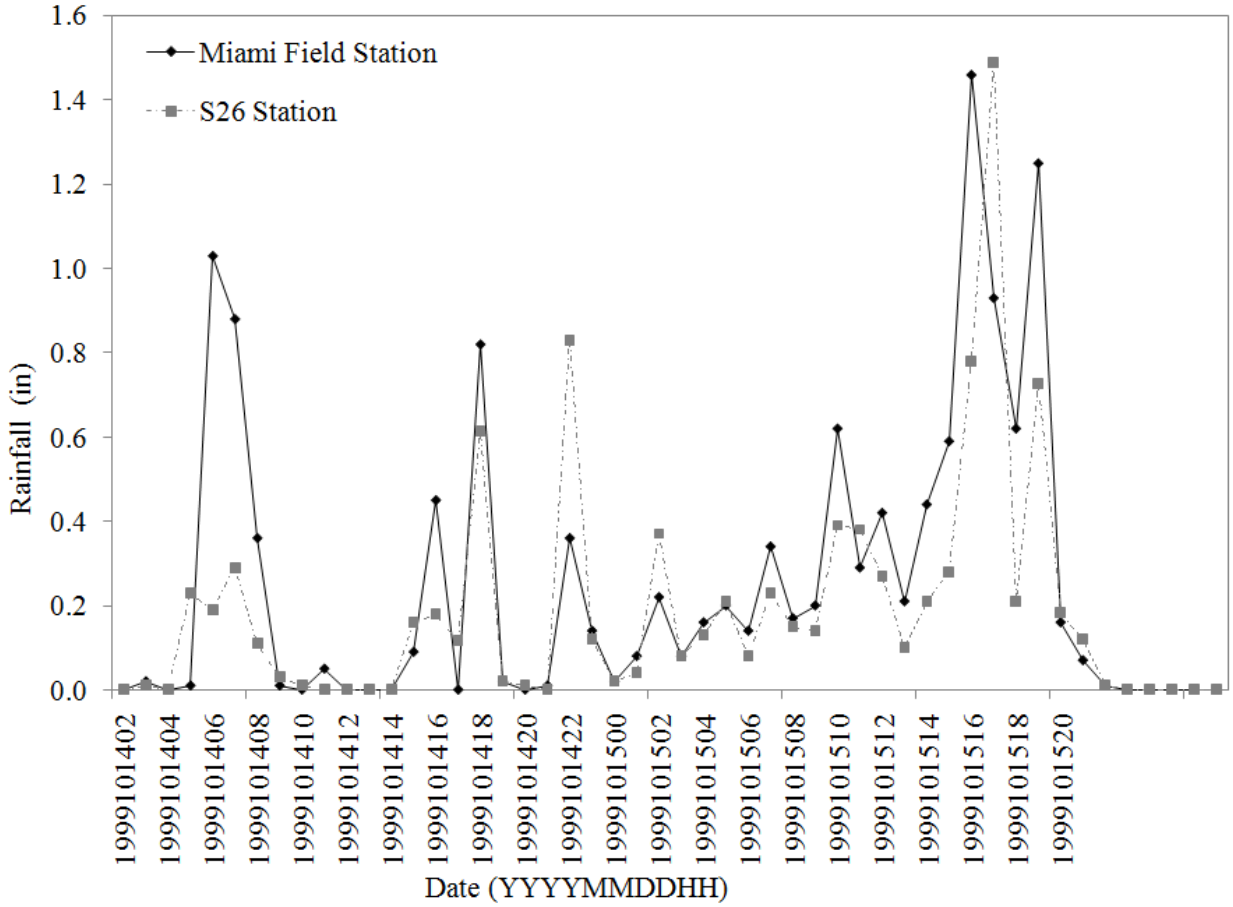

Figure 113. Flash Flood Illustration. Rain gauge data from Station S26 and Miami Field Station.

The following cases were conducted:

1. Five simulations were completed (see Table 15). Mesh was refined until the grid cell size interpolation of the DTM points was acceptable in the mesh. The purpose of this scenario was to get a mesh that satisfactorily balance accuracy and computing resources using the mesh convergence analysis and to estimate the sensitivity of the results to the numerical mesh size. A mesh was created using the fewest, reasonable number of elements and the model was analyzed. After that, the mesh was recreated with a denser element distribution, and reanalyzed to compare the results to those of the previous mesh. The mesh size density was

increasing and the model was reanalyzed until the results converge satisfactorily. This type of mesh convergence study allows the user to obtain an accurate solution with a mesh that is sufficiently dense and not overly demanding of computing resources.

2. A simulation was conducted including the main streets in the basin of the City of Sweetwater (see Table 16). The purpose of this scenario is to evaluate the influence of streets in the flooding. The inundation depths and flooding extension were compared with the reported post-flooding observations (Flood Management Task Force, 2000).

3. The influence of the Manning's *n* parameter was evaluated in the flooding event of Sweetwater. A simulation was conducted with a value of *n* of 0.020 for streets, 0.040 for undeveloped areas, and 0.07-0.08 for medium and high developed areas, respectively (see Figure 114). Second and third simulations were conducted with an increment of 100% and a decrease of 100% respect to the original set of the *n* values.

Table 15. Flash Flood Illustration. Scenarios used in the analysis of the mesh convergence.

Scenario	Δx (m)	Elements	Water Depth Differences
RUN0	70	2696	---
RUN1	50	4872	YES
RUN2	32	10930	YES
RUN3	31	12001	YES
RUN4	27	14658	NO

Table 16. Flash Flood Illustration. Names of the streets included in the simulation.

Street N^0	Name of street
1	NW 114^{th} Av
2	SW 114^{th} Av
3	SW 113^{th} Av
4	NW 112^{th} Av
5	SW 112^{th} Av
6	SW 110^{th} Av
7	NW 109^{th} Av
8	SW 109^{th} Av
9	NW 107^{th} Av
10	SW 107^{th} Av
11	NW 102^{nd} Av
12	SW 102^{nd} Av
13	NW 3^{rd} St
14	W Flagler St

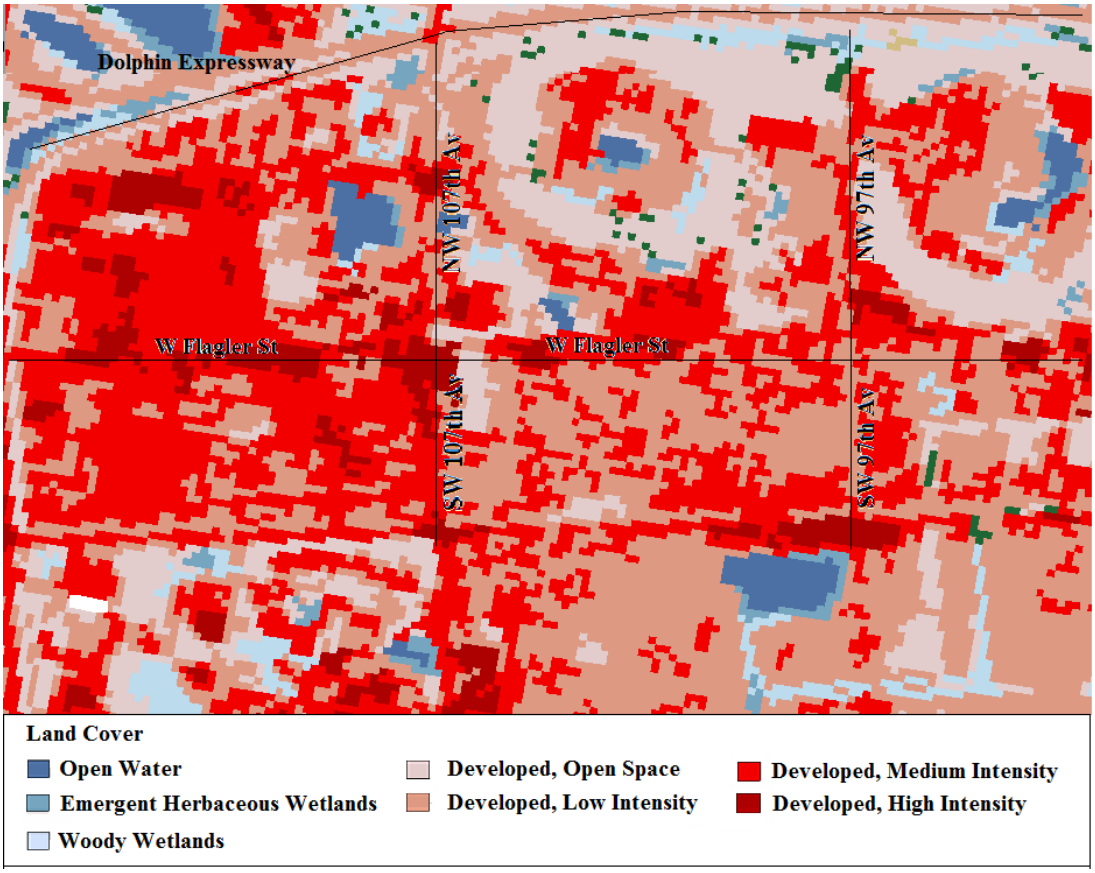

Source: The National Map Seamless Server U.S. Geological Survey (USGS).

Figure 114. Flash Flood Illustration. Land Cover for the City of Sweetwater, 2001.

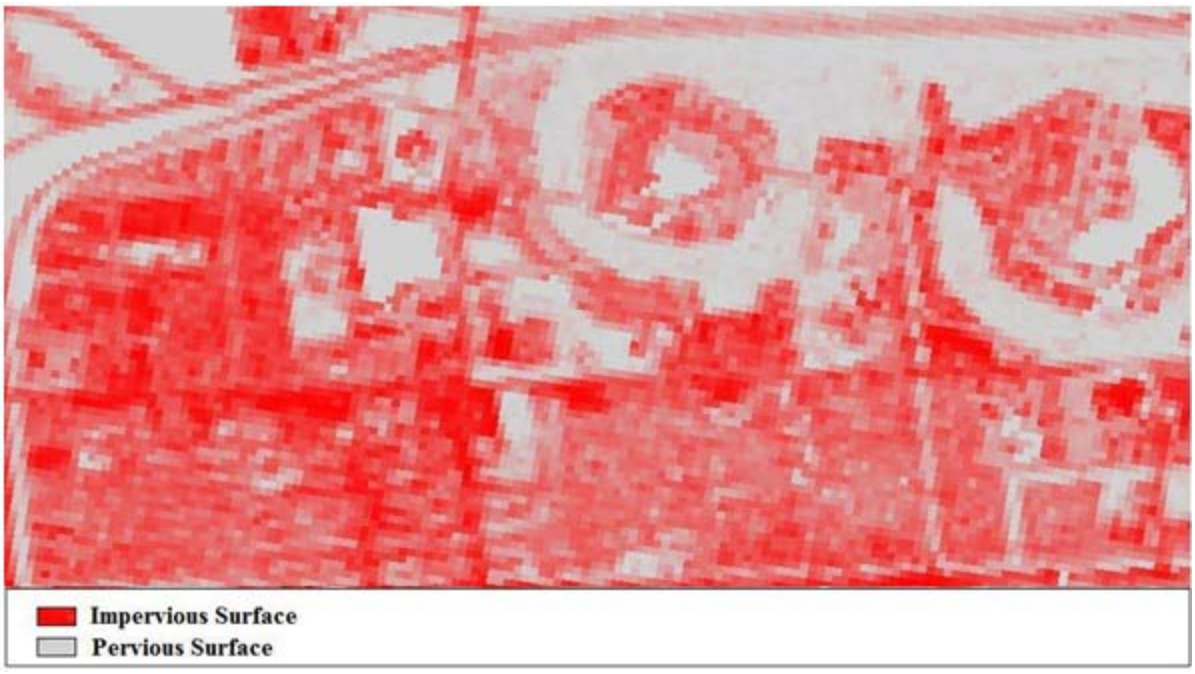

Source: The National Map Seamless Server U.S. Geological Survey (USGS).
Figure 115. Flash Flood Illustration. Impervious/Pervious areas for City of Sweetwater, 2001.

A 9922 node/19276 element mesh that extends for approximately 4 km x 2 km (see Figure 116) was generated for this model simulation. The total time of simulation was 52 hours. The initial condition was a completely dry bed bottom. Figure 116 shows the City of Sweetwater with extensive development in the neighborhood where the impervious areas cover almost the entire city.

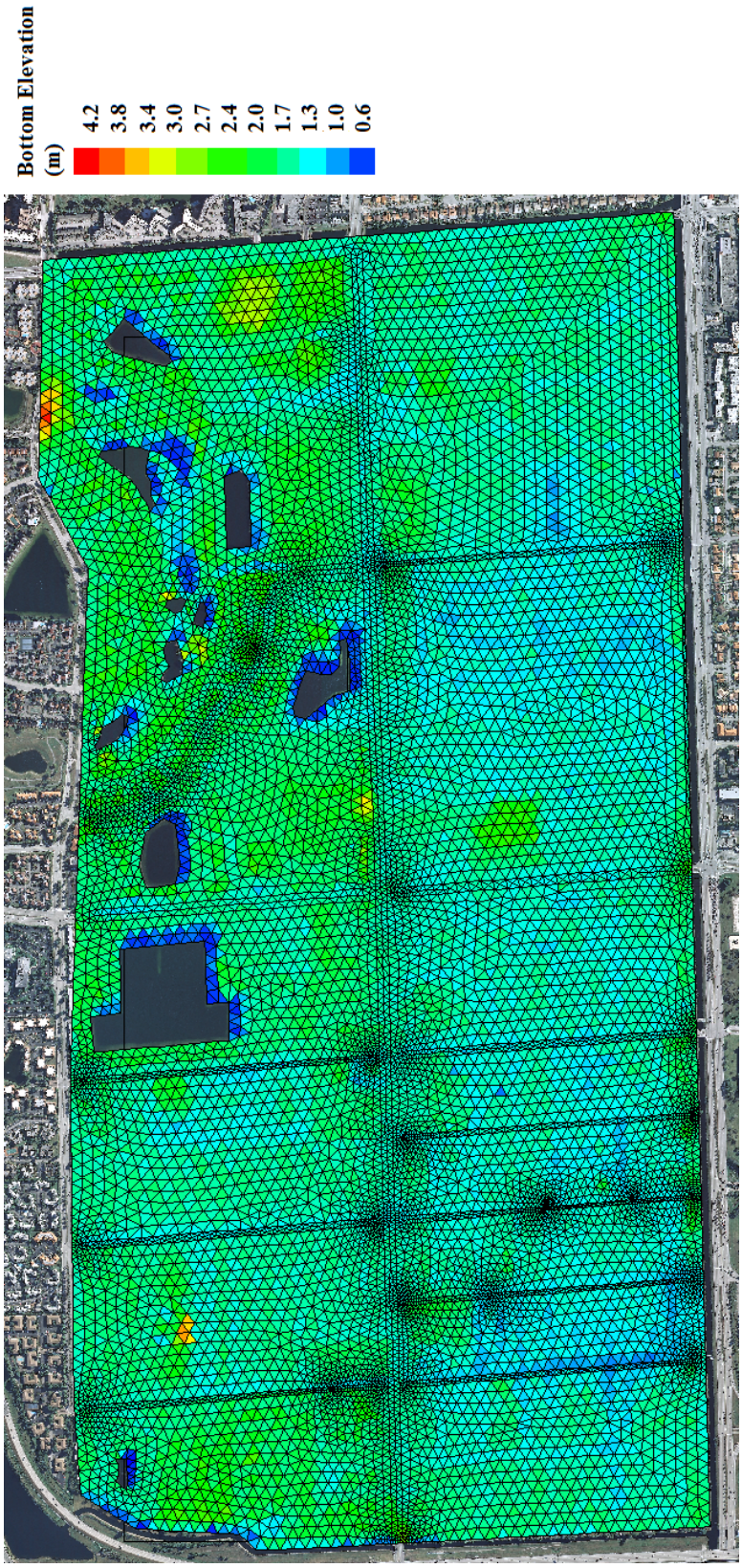

Figure 116. Flash Flood Illustration. Bed Elevations in the numerical mesh.

Numerical Model Results

Case 1: Convergence of the numerical mesh

Five simulations were conducted to get a mesh that satisfactorily balances accuracy and computing resources using the mesh convergence analysis.

Figure 117 to Figure 121 present the water depths for City of Sweetwater at the end of the simulation of 52 hrs (October 16, 1999 at 2 A.M.) for the five scenarios used for the mesh convergence (see Table 15). No differences can be seen between the RiverFLO-2D numerical water depths for RUN3 and RUN 4, respectively. As a result of this case, a Δx of 31m was selected as the mesh size that predicts an accurate solution with a mesh that is sufficiently dense to test RiverFLO-2D for Hurricane Irene flooding for cases 2 and 3.

Case 2: Evaluating the influence of streets in the flooding event

Case 2 presents a simulation including the main streets in the basin of Sweetwater City (see Table 16).

Figure 122 shows the water depths for City of Sweetwater at 52 hr including the streets in the analysis to evaluate their influence in the flooding of the Sweetwater City and how they can affect the flow path of the inundation.

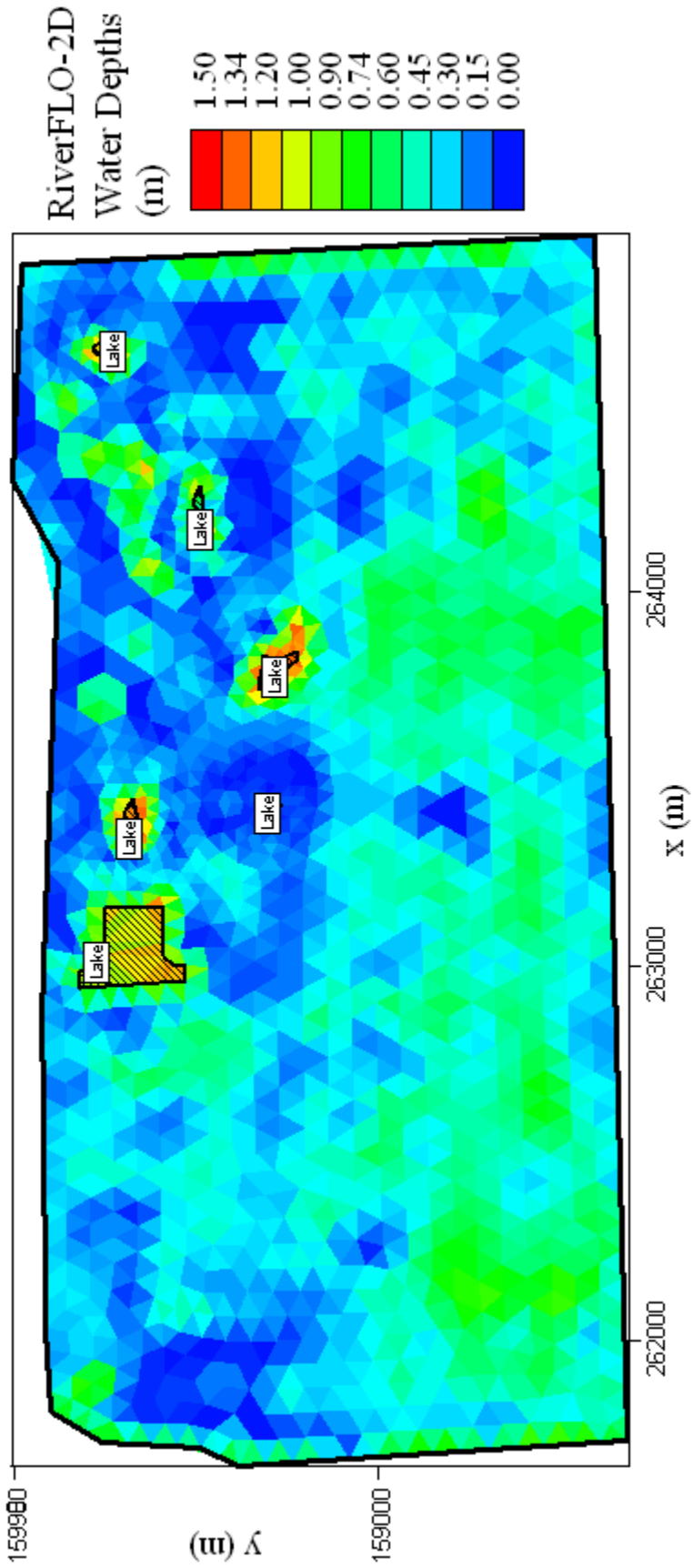

Figure 117. Flash Flood Illustration. Water depths for City of Sweetwater at 52 hr for RUN0.

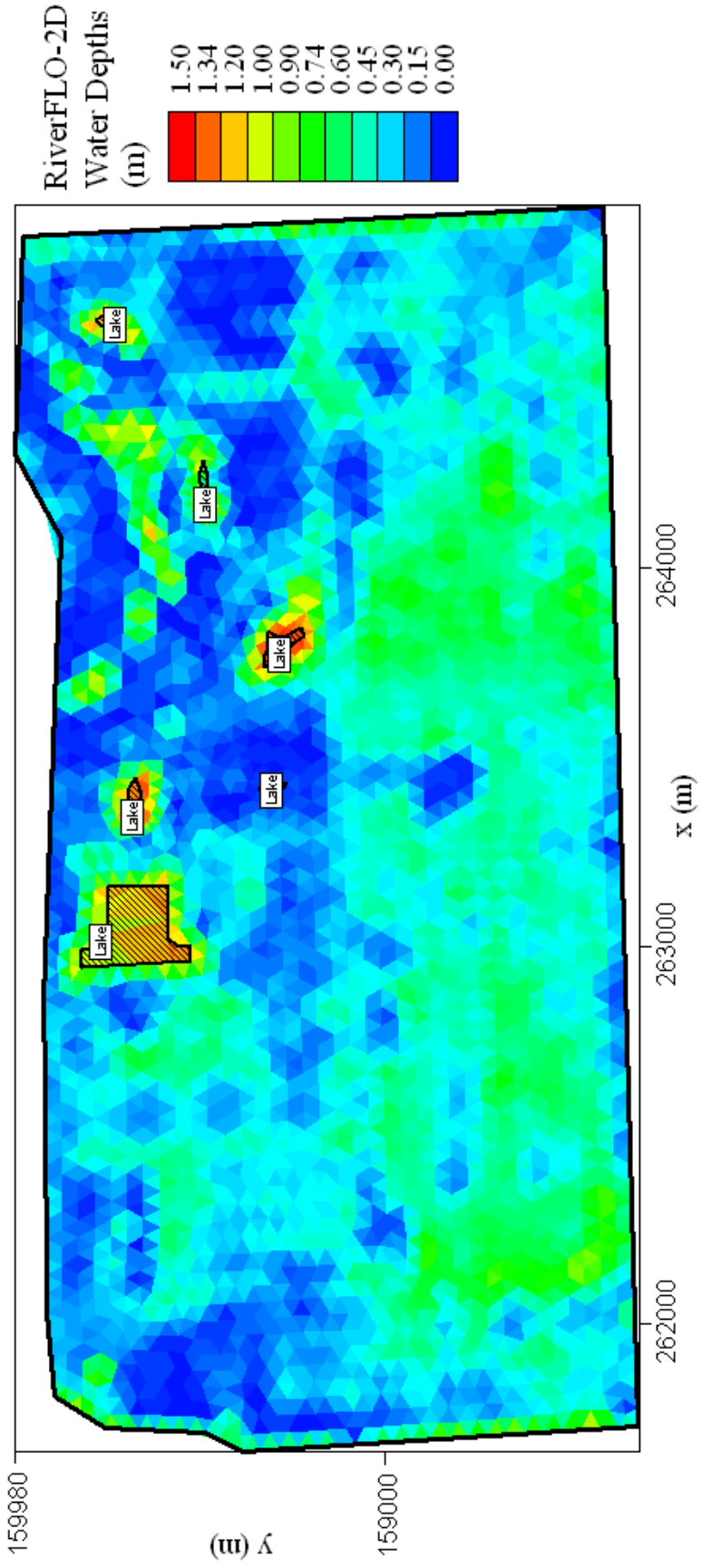

Figure 118. Flash Flood Illustration. Water depths for City of Sweetwater at 52 hr for RUN1.

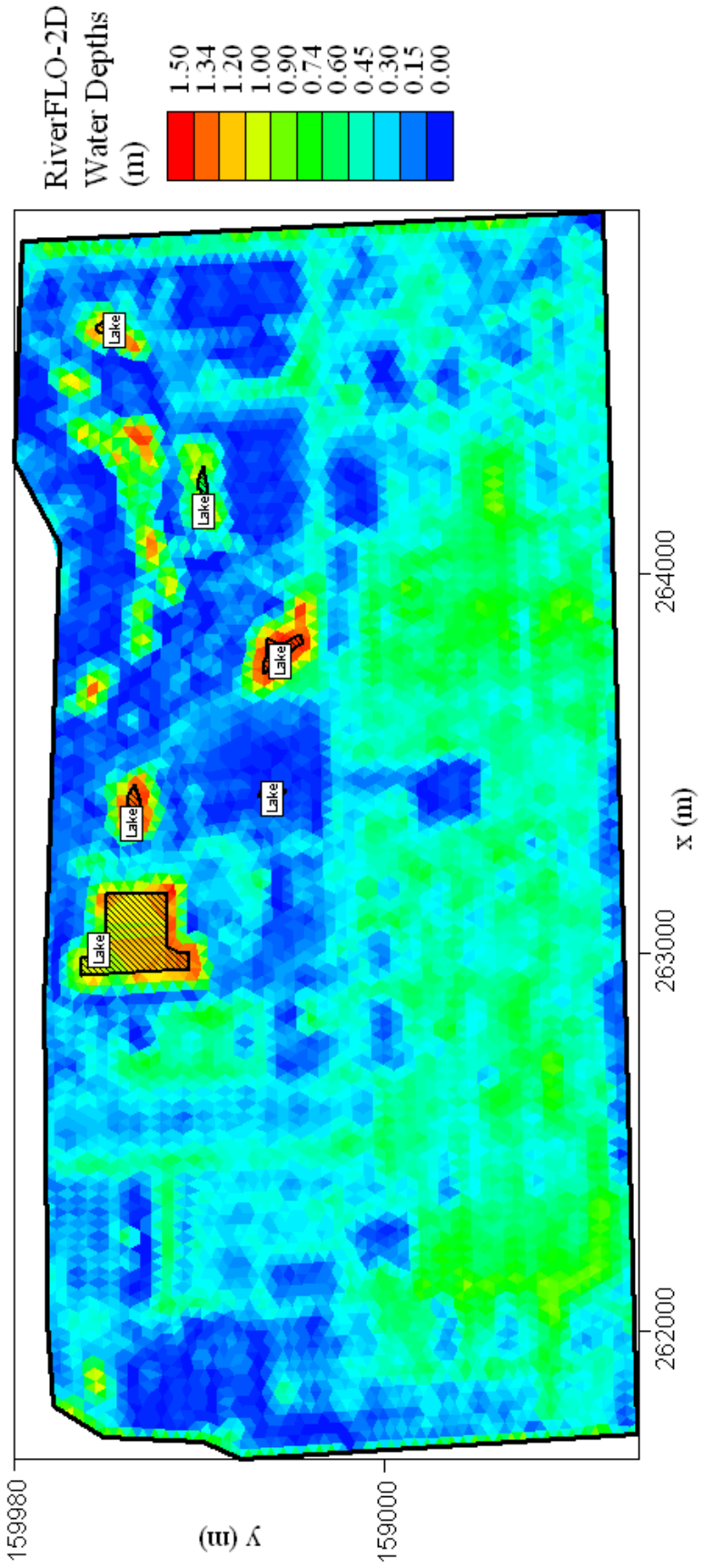

Figure 119. Flash Flood Illustration. Water depths for City of Sweetwater at 52 hr for RUN2.

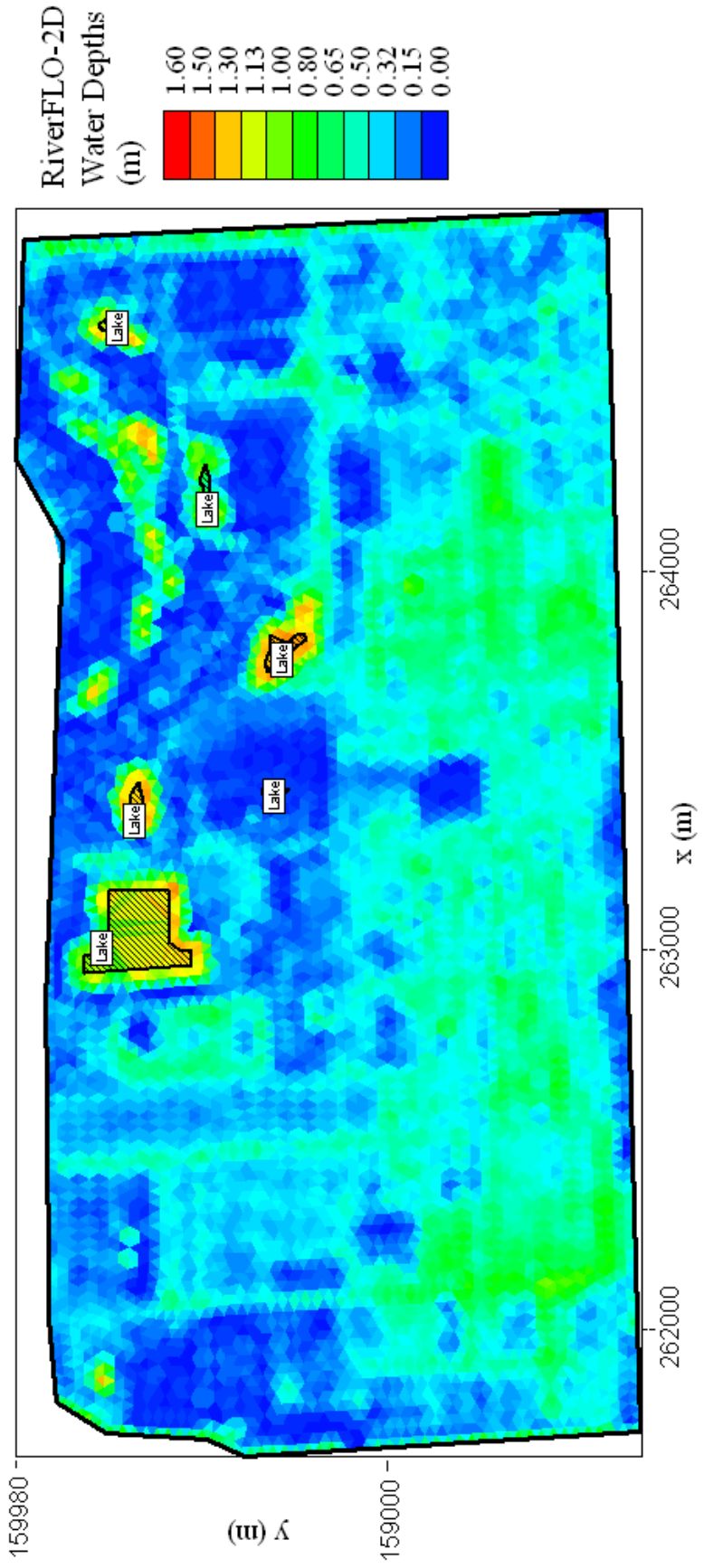

Figure 120. Flash Flood Illustration. Water depths for City of Sweetwater at 52 hr for RUN3.

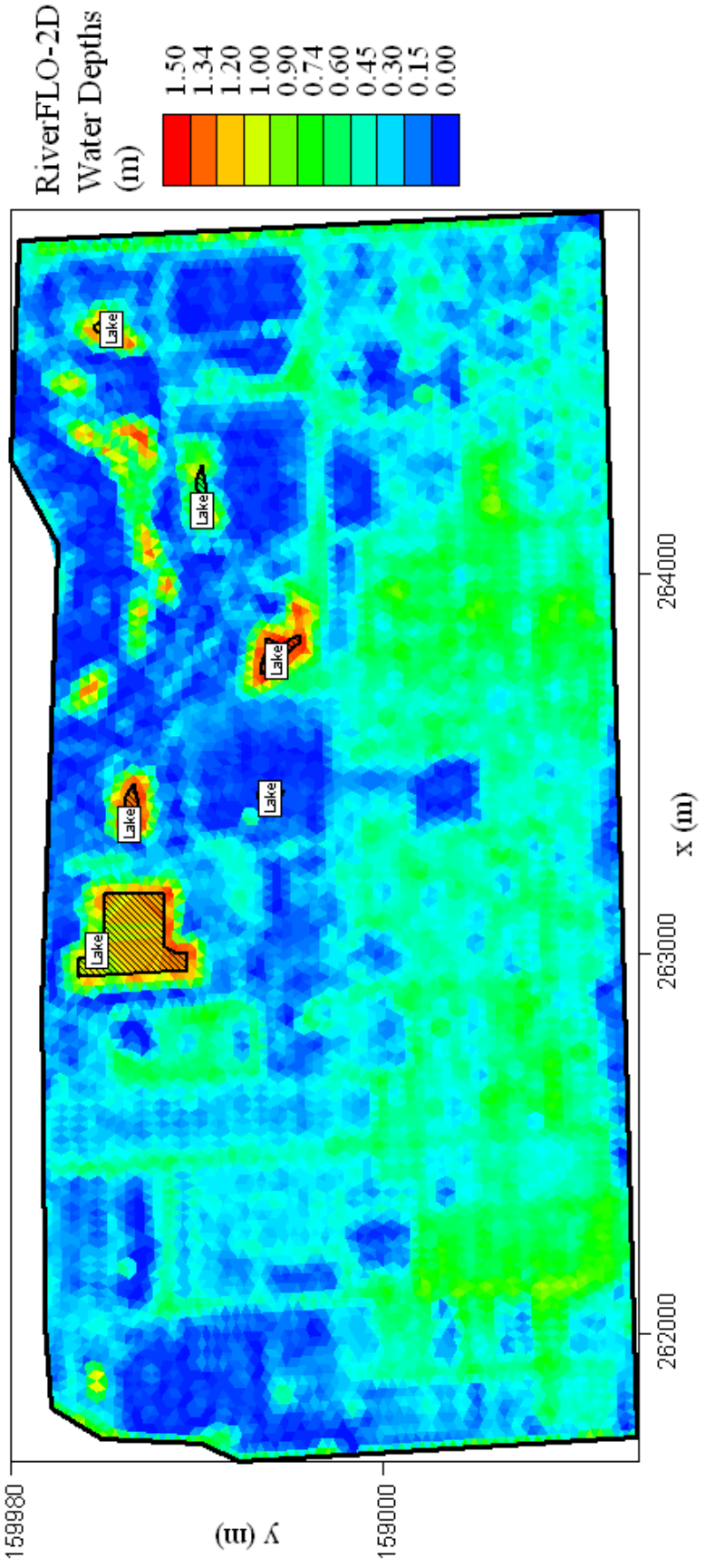

Figure 121. Flash Flood Illustration. Water depths for City of Sweetwater at 52 hr for RUN4.

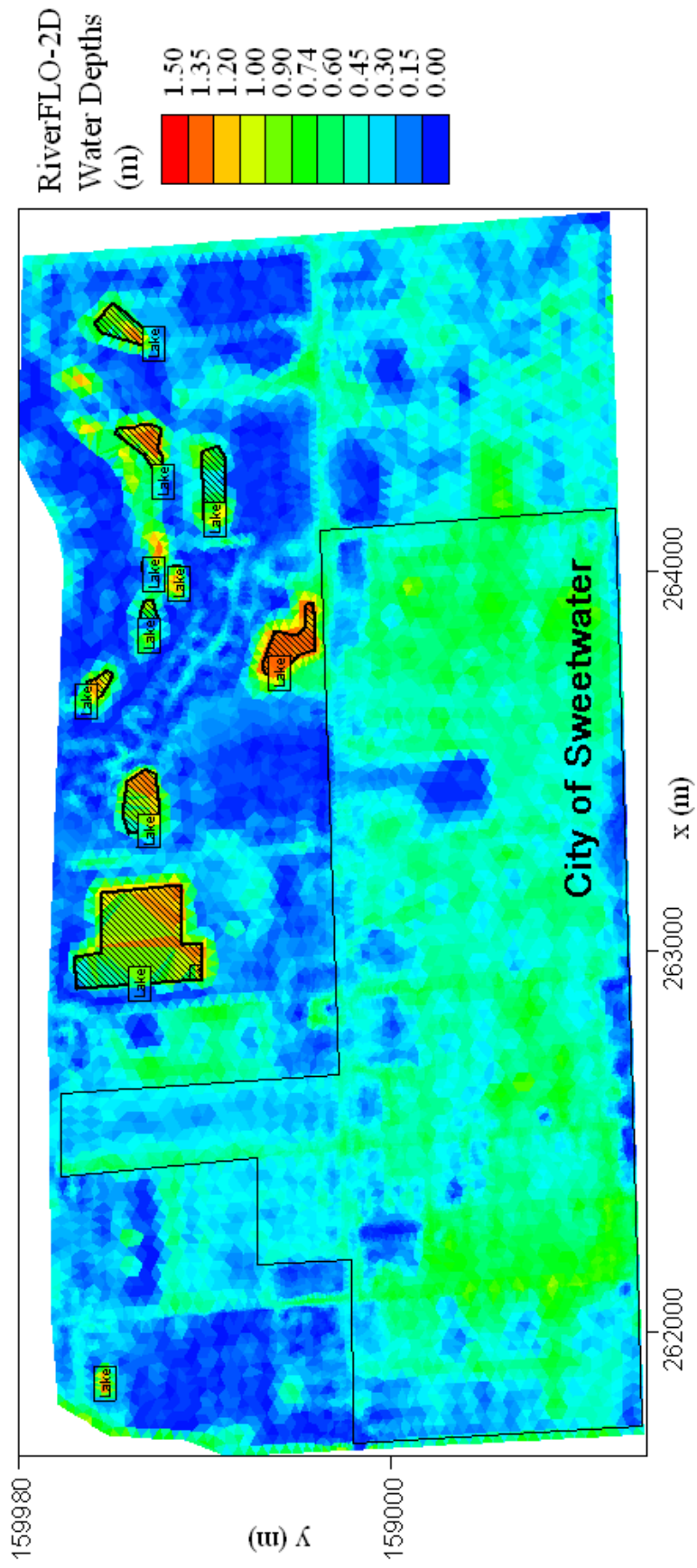

Figure 122. Flash Flood Illustration. Water depths for City of Sweetwater at 52 hr including the main 13 streets in the simulation and the original set of n of Manning (see Case 3).

Case 3: Evaluating the influence of the variability of the *n* of Manning in the flooding event.

Three different numerical simulations were conducted to determine the importance of the *n* of Manning uncertainty in the numerical analysis. The flooding of Sweetwater due to the flat topography and the characteristics of the basin was a flooding with very low velocities and large depths, ponding the City of Sweetwater for several days. Due to this reasons the inundation extension should not be largely affected by variations in the roughness of the bed basin.

Figure 122 present the water depths obtained for the case with the original set of Manning's *n* that were selected as 0.020 for streets, 0.040 for undeveloped areas, and 0.07-0.08 for medium and high developed areas. Figure 123 and Figure 124 shows the water depths for an increment of 100% and a reduction of 100% in Manning's *n*, respectively

Figure 123. Flash Flood Illustration. Water depths for City of Sweetwater at 52 hr with the increase set of n of Manning in 100%.

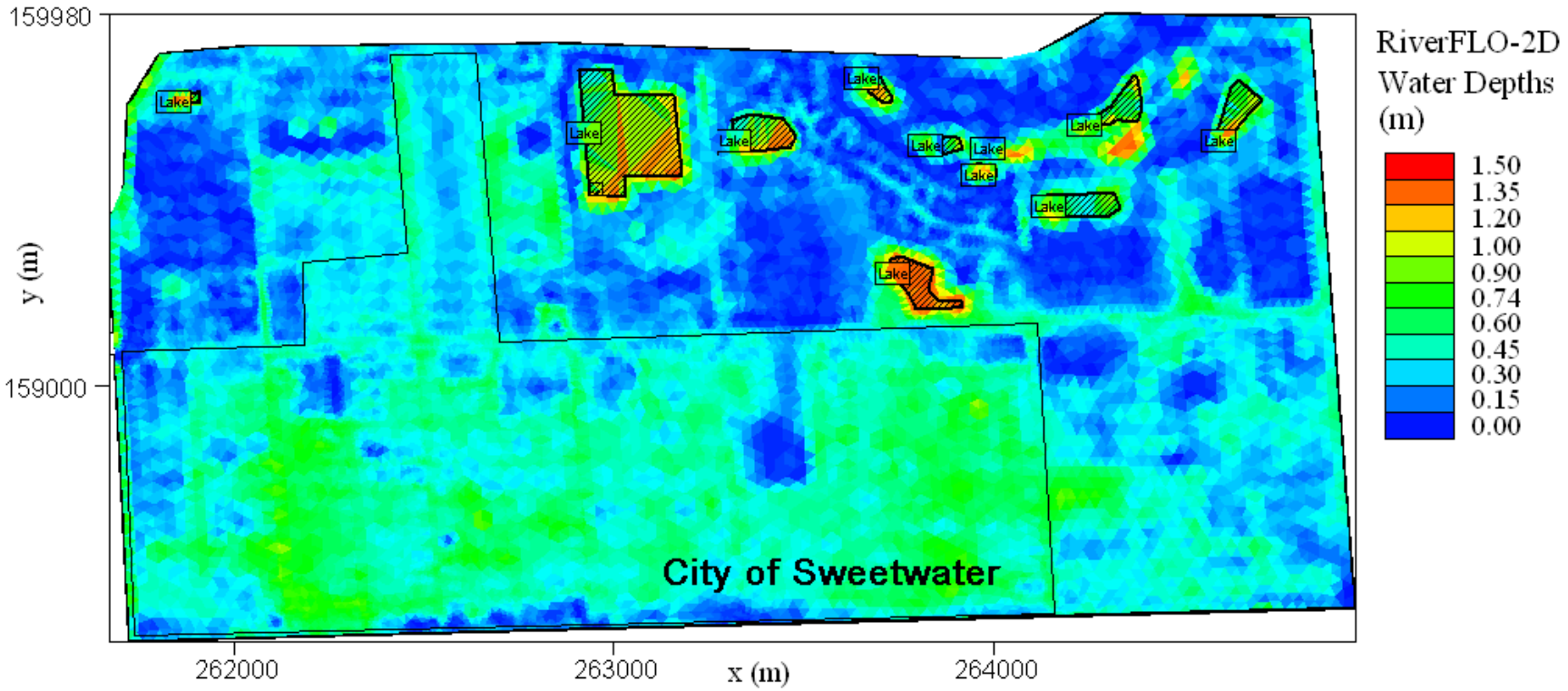

Figure 124. Flash Flood Illustration. Water depths for City of Sweetwater at 52 hr with the reduce set of n of Manning in 100%.

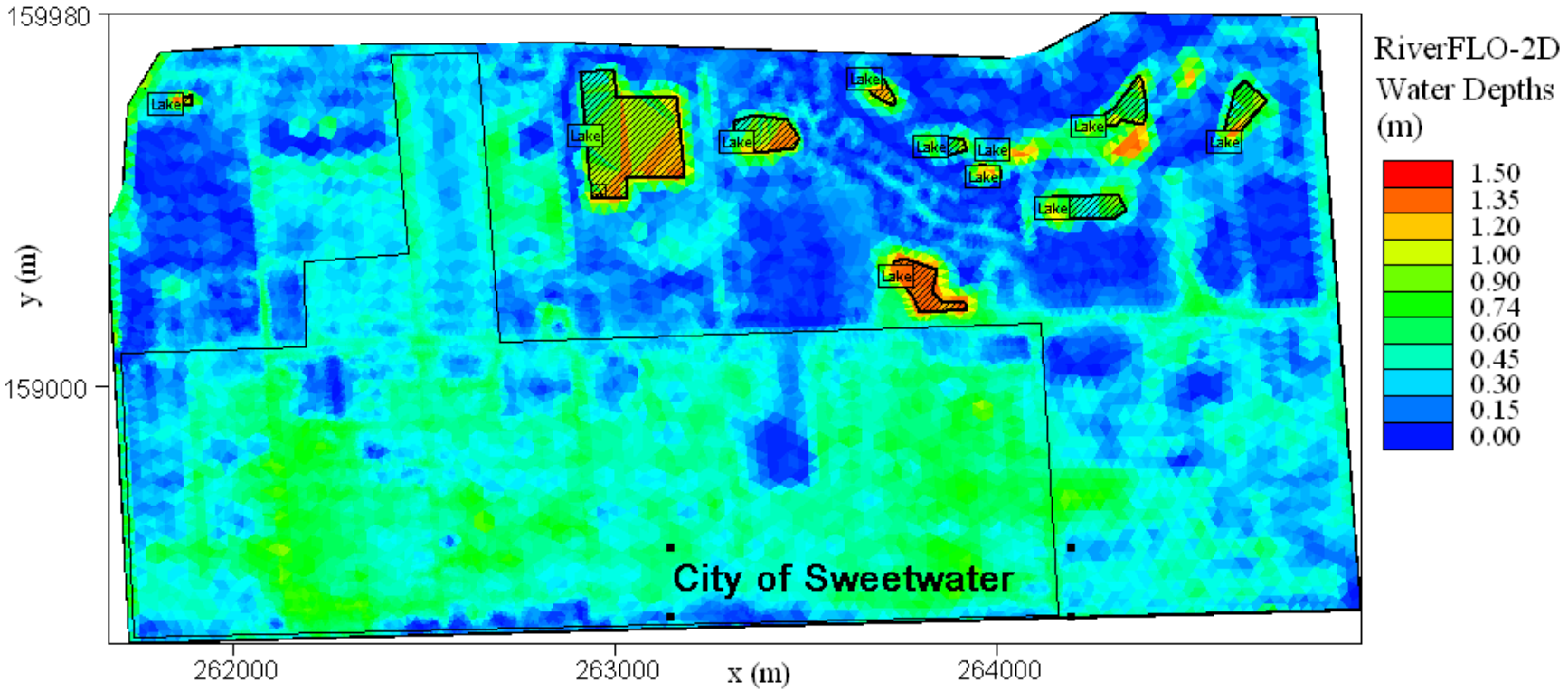

A comparison of depths and velocities element by element was completed for case 3 with average differences fifth decimal place, maximum differences in the second decimal place and minimum differences in the third decimal place. No differences can be notice between Figure 122, Figure 123 and Figure 124. The velocities for Sweetwater application are so low that roughness variability is a second order effect that has much less influence on results as other factors.

Table 17. Comparison of average differences on depths and velocities element by element between original, reduced and increased set of n of Manning for case 3.

Average Differences	Reduced n of Manning in 100%	Increased n of Manning in 100%
Depth (m)	0.000014	0.000044
Velocity (m/s)	0.000021	0.000062

Figure 120, Figure 121, Figure 122, Figure 123 and Figure 124 show the entire City of Sweetwater flooded with water depths between 0.15m and 0.90m. These results agree with those reported by Task Management Force and observers (see Figure 103, Figure 109 and Figure 110).

CHAPTER 5. CONCLUSIONS AND RECOMMENDATIONS

The enhanced RiverFLO-2D numerical modeling results demonstrate the developed model's capability to simulate the propagation of water waves in urban areas, including the temporal and spatial variability of the characteristics of the event involved, such as rainfall estimates, roughness, infiltration and urban features. Several cases were used to verify and validate the enhanced numerical model. Each case was set with a specific purpose with the general objective of making the model more suitable to predict the physics of flash flood movement over complex terrain. The prediction of flash floods in urban areas using distributed rainfall-runoff models is a complex problem and it was necessary to simplify the problem so that an adequate numerical solution was possible with the developed computational methods and data, in the timeframe of this PhD thesis. Thus, additional work may be focused in further exploring some of the limitations in the model formulation and its implementation (see limitations of the model below).

The following conclusions can be made:

1. The model performance was improved with the implementation of a wet and dry technique for a fixed finite element mesh, showing an acceptable performance for the verification and validation cases. The model is capable of predicting the dynamic characteristics of the flooding as well as the movement of the flow without numerical instabilities for cases that start the simulation with a bed entirely dry or for those that during the simulation present large dry

areas over the mesh, providing significantly stable solutions and conserving volume. Each time step, wet, partially dry and totally dry elements are identified by comparing the water depths in each node of the element with a water depth tolerance that could be zero. Then, the implemented technique modified the governing equations for the dry elements, eliminating them from the calculation. The velocity components for the partially dry elements are set equal to zero and full governing equations are solved.

2. The OpenMP Parallelization Technique was successfully implemented in the numerical model, presenting improvements in the computational time as much as 5 times faster on a 2 quad-core (8 processors) DELL PRECISION T7400 Intel Xeon CPU X5472 @3.00GHz 16GB of RAM
3. The enhanced numerical model was applied to benchmark cases, laboratory experiments and real flood events, showing that the model results present an agreement with existing data. In that sense, the enhanced numerical model was intensively verified and validated following the ASCE Task Committee on Model Verification and Validation process (Wang, Roche, Schmalz, Jia, & Smith, 2008).
4. Sensitivity analyses of the model were performed for different parameters such as Manning's roughness, lumping parameter and grid size using the verification and validation cases and the illustrative application, and improved the understanding of the relationships between model input and output.
5. The Sumacarcel flooding as well as the Sweetwater test cases showed that urban characteristics such as buildings and streets are very important features

to include in the prediction of urban flooding. The extension of the inundation as well as the water depths and velocities are affected by the urban features. The water wave moves through the streets passing between buildings and being accelerated in some segments and stagnated in others. The prediction of the flooding of Sumacarcel was possible with the inclusion of the urban structures in the set up of the simulation.

6. The illustration case for the City of Sweetwater flooding showed that all the techniques developed for the RiverFLO-2D model can be successfully applied to an extreme rainfall real case using NEXRAD rainfall estimates.
7. The illustrative applications should be seen as a proof of concept for the methodology and the numerical tool developed in this dissertation. Due to large uncertainty on the available data, the model simulations presented in this dissertation should not be viewed as detailed flooding predictions, but rather as an illustration of the integration of rainfall estimates with numerical modeling computations.

The model performance can be improved as new data becomes available for calibration of extreme flooding events in urban areas. An effort to collect post-flooding data specifically water depths, velocities and flooding extension should be developed for Federal Agencies to assure that detailed studies can go further for real flash flooding applications.

For further studies where detailed post-flooding data will be available, an analysis of the uncertainty in the interpolation of NEXRAD rainfall estimates and the influence this may have to the predicted flooding inundation areas should be included.

To successfully apply the numerical model, it is fundamental to understand that the modeling effort has been simplified having a number of limitations that come from different sources:

- The model does not take into the account the storm water drainage. An evaluation of the influence that the drainage system could have on the flooding should be included in further analysis. The analysis of the drainage system and its influence over the surface water depths and velocities should be evaluated for real cases in the first times of the simulation, before the drainage system capacity collapses due to infiltration of major volumes of water. In this dissertation, the drainage capacity system was assumed collapsed at the onset of the simulation and it was not included in the analysis.
- The model is based on the 2D shallow water-depth integrated approximation that does not account for large vertical accelerations that may occur near dam sites in the case of dam-break simulations.
- The numerical solution of the model is explicit. Therefore, time steps are limited by the CFL condition; this may be a limitation for long term regional simulations, and may limit the model use to short term localized applications.
- The model accounts for infiltration as losses but there is no interaction with groundwater. The ground-surface water interaction could be a decisive key in the dynamics of the flooding for highly saturated soils.
- The model is capable to include NEXRAD rainfall estimates as an input rainfall. However, a high uncertainty is present in the numerical results of the Sweetwater application due to the existence of an error in the spatial interpolation of the

NEXRAD rainfall from the original grid to the finite element grid that was not quantified in this dissertation. This uncertainty should be analyzed in further research; the accuracy in the calculation of the spatial variability of the rainfall is a key component in the improvement of the predictions of water depths, velocities and flooding extension.

REFERENCES

Ahrens, S., & Maidment, D. (1999). Flood forecasting for the Buffalo Bayou using CRWR-PrePro and HEC-HMS. CRWR Report 99-6. Austin, Texas.

Akanbi, A., & Katopodes, N. (1988). Model for flood propagation on initially dry land. Journal of Hydraulic Engineering , V.114, 689-706.

Alcrudo, F., & Mulet, J. (2007). Description of the Tous Dam break case study (Spain). Journal of Hydraulic Research , V.45, 45-57.

Alcrudo, F., & Mulet, J. (2003). Impact project flood propagation case study: the flooding of Sumacárcel after Tous dam break. EC Contract EVG1-CT-2001-00037 .

Anderson, M., Chen, Z., Kavvas, M., & Feldman, A. (2002). Coupling HEC-HMS with atmospheric models for prediction of watershed runoff. Journal of Hydrologic Engineering , V.7, No.4, 312-318.

Baeck, M., & Smith, J. (1998). Rainfall Estimation by the WSR-88D for heavy rainfall events. Weather and Forecasting , V.13, 416-436.

Bates, P. (2004). Remote sensing and flood inundation modelling. Hydrological Processes , V.18, 2593-2597.

Bates, P., & De Roo, A. (2000). A simple raster-based model for flood inundation simulation. Journal of Hydrology, V.236, 54-77.

Bates, P., & Hervouet, J. (1999). A new method for moving boundary hydrodynamic problems in shallow water. Proceedings of the Royal Society of London, 3107-3128.

Bedient, P. B., Hoblit, B. C., Gladwell, D. C., & Vieux, B. E. (2000). NEXRAD radar for flood prediction in Houston. Journal of Hydrologic Engineering , V., No.3, 269-277.

Bedient, P., Holder, A., Benavides, J., & Vieux, B. (2003). Radar-based flood warning system applied to tropical storm Allison. Journal of Hydrologic Engineering, V.8, No.6, 308-318.

Bedient, P., Huber, W., & Vieux, B. (2008). Hydrology an floodplain analysis. Prentice Hall. Fourth edition. Upper Saddle River.

Brufau, P., García-Navarro, P., & Vázquez-Cendón, M. (2004). Zero mass error using unsteady wetting/drying conditions in shallow flows over dry irregular topography. International Journal for Numerical Methods in Fluids, 1047-1082.

Brufau, P., Vázquez-Cedón, M., & García-Navarro, P. (2002). A numerical model for the flooding and drying of irregular domains. International Journal for Numerical Methods in Fluids, V.39, 247-275.

Carpenter, T., Sperfslage, J., Georgakakos, K., Sweeney, T., & Fread, D. (1999). National threshold runoff estimation utilizing GIS in support of operational flashflood warning systems. Journal of Hidrology, V.224, 21-44.

CEDEX. (1988). Estudio en modelo matemático de las inundaciones de octubre de 1982 en la plana del Júcar. Informe Técnico para la Dirección General de Carreteras.

CEDEX. (1984). Estudio hidrológico de la crecida ocurrida en los días 20 y 21 de Octubre de 1982 en la cuenca del Júcar. Informe técnico nº 2 para la Dirección General de Obras Hidráulicas.

CEDEX. (1989). Revisión del estudio hidrológico de la crecida ocurrida en los días 20 y 21 de Octubre de 1982 en la cuenca del Júcar. Informe Técnico para la Dirección General de Obras Hidráulicas.

CEDEX. (1998). Síntesis de las avenidas del río Júcar en su llanura de inundación. Análisis de la situación actual y líneas de actuación. Informe Técnico para la Dirección General de Obras Hidráulicas y Calidad de las Aguas.

Chandra, R., Dagum, L., Kohr, D., Maydan, D., MacDonald, J., & Menon, R. (2001). Parallel programing in OpenMP. Academic Press. San Diego, California.

Jucan River Basin Authority (CHJ). (1985). Plan general de defensa contra avenidas en la cuenca del Río Júcar (Valencia y otras). Confederación Hidrográfica del Júcar.

Jucan River Basin Authority (CHJ). (1999). Plan global frente a las inundaciones en la ribera del Júcar: líneas de actuación. Confederación Hidrográfica del Júcar.

Maidment, V.T., Maidment, D.R. and Mays, L.W. (1988), Applied Hydrology. McGraw-Hill. New York, 570.

Committee to Assess NEXRAD Flash Flood Forecasting Capabilities. (2004). Sulphur Mountain. National Academy of Sciences. California.

Courant, R., Friedrichs, K., & Lewy, H. (1967). On the partial difference equations of mathematical physics. IBM Journal, 215-234.

Crum, T., & Alberty, R. (1993). The WSR-88D and the WSR-88D operational support facility. Bulletin of the American Meteorological Society, V.27, No.9, 1669-1687.

Defina, A. (2000). Two-dimensional shallow flow equations for partially dry areas. Water Resources Research, V.11, 3251-3264.

Defina, A., D'Alpaos, L., & Matticchio, B. (1994). A new set of equations for very shallow water and partially dry areas suitable to 2D numerical models. In Proceedings of Modelling of Flood Propagation Over Initially Dry Areas, ASCE, 72-81.

Donnell, B.P., Letter, J.V., & McAnally, W.H. (2005). User guide for RMA2 version 4.5. US Army, Engineer Research and Development Center, 296.

Eggert, K. (1976). Modeling the unsteady infiltration process. Fort Collins: Colorado State University. Master Thesis.

Flood Management Task Force, M.D.C. (2000). Hurricane Irene. Miami-Dade County.

Frazao, S. (2003). Dam-break induced flows in complex topographies. Proceedings 3rd Project Workshop, Louvain-la-Neuve. Investigation of Extreme Flood Processes and Uncertainty Project . Louvain-la-Neuve, Belgium.

Fread, D., Shed, R., Smith, G., Farnsworth, R., Hoffeditz, C., Wenzel, L., et al. (1995). Modernization in the national weather service river and flood program. Weather and Forecasting , V.10, 477-484.

Froehlich, D. (1989). HW031 D-finite element surface-water modeling system: two-dimensional flow in a horizontal plane. User's manual. Federal Highway Administrative Report FHWA-RD-88-177.

Froehlich, D. (2003.). User Manual for FESWMSFST2DH: Two-dimensional depth-averaged flow and sediment transport model. Release 3. Report FHWA-RD-03-053.

Fulton, R., & Seo, D.-L. (2000). A prototype operational 0-1 hour radar-based flash flood potential algorithm. 15th Conference on Hydrology. Long Beach, California.

Garcia, F., & Kahawita, R. (1986). Numerical solution of the St. Venant equations with the MacCormack finite-difference scheme. International Journal for Numerical Methods in Fluids , V.6, No.5, 259-274.

Garcia, R., Espinoza, R., Valera, E., & Gonzalez, M. (2006). An explicit two-dimensional finite element model to simulate short and long term bed evolution in alluvial rivers. Journal of Hydraulic Research, V.44, 755–766.

García-Navarro, P., & Vázquez-Cendón, M. (2000). On numerical treatment of the source terms in the shallow water equations. Computers and Fluids , V.29, 951-979.

Gourley, J., Maddox, R., Howard, K., & Burgess, D. (2002). An exploratory multisensor technique for quantitative estimation of stratiform rainfall. Journal of Hydrometeorology, V.3, No.2.

Green, W., & Ampt, G. (1911). Studies on soil physics, part I, the flow of air and water through solids. Journal of Agricultural Science , V.4, No.1, 1-24.

Henderson, F. M., & Wooding, R. A. (1964). Overland flow and groundwater flow from a steady rainfall of finite duration. Journal of Geophysical Research, V.69, No.8, 1531-1540.

Heniche, M., Secretan, Y., Boudreau, P., & Leclerc, M. (2000). A two-dimensional finite element drying-wetting shallow. Advances in Water, V.23, 359-372.

Hervouet, J. (2007). Hydrodynamics of free surface flows modelling with the finite element method. John Wiley & Sons. England.

Hervouet, J. M. (1993). Validating the numerical simulation of dam-breaks and floods. Advances in Hydro-science and Engineering; Proceedings of the First International Conference on Hydro-Science and Engineering, Washington, D.C., 754-761.

Hervouet, J.-M., & Petitjean, A. (1999). Malpasset dam-break revisited with two-dimensional computations. Journal of Hydraulic Research, 777-787.

Horrit, M., & Bates, P. (2002). Evaluation of 1D and 2D numerical models for predicting river flood inundation. Journal of Hydrology, V.268, 87-99.

Hubbard, M., & García-Navarro, P. (2000). Flux difference splitting and the balancing of source terms and ux gradients. Journal of Computational Physics, V.165, 89-125.

Hudlow, M. (1988). Technological developments in real time operational hydrologic forecasting in the United States. Journal of Hydrology, V.102, 69-92.

Hyannis, M., Zhang, J., Howard, K., & Gourley, J. J. (2005). Constructing three-dimensional multiple-radar reflectivity mosaics: examples of convective storms and stratiform rain echoes. Journal of Atmospheric and Oceanic Technology, V.22, 30-41.

Iwagaki, Y. (1955). Fundamental studies on runoff analysis by characteristics. Disaster Prevention Research Institute, V.10, 1-25.

James, W., Robinson, C., & Bell, J. (1993). Radar assisted real-time flood forecasting. Journal of Water Resources , V.119, No.1, 32-34.

Johnson, L., & Dallman, J. (1987). Flood flow forecasting using microcomputer graphics and radar imagery. Microcomputers in Civil Engineering, V.2, 85-89.

Kawahara, M., & Umetsu, T. (1986). Finite element method for moving boundary problems in river flow. International Journal for Numerical Methods in Fluids, V.6, 365-386.

Kawahara, M., Hirano, H., & Tsubota, K. (1982). Selective lumping finite element method for shallow water flow. International Journal for Numerical Methods in Fluids, V.2, 89-112.

Kawahara, M., Takeuchi, N., & Yoshida, T. (1978). Two-step explicit finite element method for two-dimensional tsunami wave propagation analysis. International Journal for Numerical Methods in Engineering, V.12, No.2, 331-351.

Kazezyilmaz-Alhan, C., & Medina, M. (2007). Kinematic and diffusion waves: analytical and numerical solutions to overland and channel flow. Journal of Hydraulic Engineering, 217-228.

Knebl, M., Yang, Z.-L., Hutchison, K., & Maidment, D. (2005). Regional scale flood modeling using NEXRAD rainfall, GIS, and HEC-HMS/RAS: a case study for the San Antonio River Basin Summer 2002 storm event. Journal of Environmental Management, V.75, 325-336.

Larson, L., Ferral, R., Strem, E. T., Morin, A., Armstrong, B., Carrol, T., et al. (1995). Operational responsabilities of the national weather service river and flood program. Weather and Forecasting, V.10, 465-476.

Lee, J., & Froehlich, D. (1989). HW031.X Research Report. U.S. Federal Highway Administrative Report.

Li, R., Stevens, M., & Simmons, D. (1976). Solutions to Green-Ampt infiltration equations. Journal of the Irrigation and Drainage Division, 239-248.

Lynch, D. R., & Gray, W. G. (1980). Finite element simulation of flow in deforming regions. Journal of Computational Physics, V.36, 135-153.

Matsumoto, J., Khan, A., Wang, S., & Kawahara, M. (2002). Shallow water flow analysis with moving boundary technique using least-squares bubbke function. International Journal of Computational Fluid Dynamics, V.16, No.2, 129-134.

Meselhe, E., & Holly, F. J. (1993). Simulation of unsteady flow in irrigation canals with dry bed. Journal of Hydraulic Engineering, 119 (9), 1021-1039.

Mimikou, M., & Baltas, E. A. (1996). Flood forecasting based on radar rainfall measurements. Journal of Water Resources, V.122, No.3, 151-156.

Murillo, J., García-Navarro, P., Burguete, J., & Brufau, P. (2006). A conservative 2d model of inundation flow with solute transport over dry bed. International Journal for Numerical Methods in Fluids, V.52, 1059–1092.

Neary, V., Habib, E., & Fleming, M. (2004). Hydrologic modeling with NEXRAD precipitation in Middle Tennessee. Journal of Hydrologic Engineering, 339-349.

Norton, W., King, I., & Orlob, G. (1973). A finite element model for Lower Granite Reservoir, water quality report: Lower Granite Lock and Dam, Snake River, Washington-Idaho finite element hydrodynamic model. Water Resources Engineers, Inc., for U.S. Army Corps of Engineers District. Walla Walla, Washington.

Ogden, F. L., & Julien, P. Y. (1993). Runoff sensitivity to temporal and spatial rainfall variability at runoff plane and small basin scales. Water Resources Research, V.29, No.8, 2589–2597.

OpenMP: An API for multi-platform shared-memory parallel programming in C/C++ and Fortran. (2009). Retrieved from www.openmp.org

Pathak, C. S. (2008). South Florida environmental report. West Palm Beach: South Florida Water Management Disctrict (SFWMD).

Perry, C. A. (2000). Significant floods in the United States during the 20th century. USGS measures a century of floods. USGS Fact Sheet 024-00.

Rao, P. (2004). A parallel hydrodynamic model for shallow water equations. Applied Mathematics and Computation, V.150, 291-302.

Reed, S., Fulton, R., Zhang, Z., & Guan, S. (2007). Use of 4km, 1hr, precipitation forecasts to drive a distributed hydrologic model for flash flood prediction. National Weather Service, Advanced Hydrologic Prediction Service (AHPS).

Reed, S., Fulton, R., Zhang, Z., & Guan, S. (2006). 1 Hr precipitation forecasts to drive a distributed hydrologic model for flash flood prediction. 20th Conference on Hydrology.

Reed, S., Schaake, J., Koren, V., & Smith, M. (2004). A statistical-distributed modeling approach for flash flood prediction. Proceedings of the 18th Conference on Hydrology. American Meteorology Society. Seattle, Washington.

Sabol, G., Rumann, J., Khalili, D., & Waters, S. (1991). Drainage design manual for Maricopa County. Hydrology Division Flood Control District. Arizona.

Seo, D., Kondragunta, C. R., Kitzmiller, D., Howard, K., Zhang, J., & Vasiloff, S. (2005). The national mosaic and multisensor QPE (NMQ) project – status and plans for a community tested for high-resolution multisensor quantitative precipitation estimation (QPE) over the United Status. National Severe Storms Laboratory and Office of Hydrologic Development, NMQ Project. National Weather Service.

Smith, M., Seo, D., Koren, V., Reed, S., Zhang, Z., & Duan, Q. (2003). The distributed model intercomparison Project (DMIP): Motivation and Experiment Design. Journal of Hydrology, V.298, 4-26.

Stallings, E., & Wenzel, L. (1995). Organization of the river and flood program in the National Weather Service. Weather and Forecasting, V.10, 457-464.

Tchamen, G., & Kahawita, R. (1998). Modelling wetting and drying effects over complex topography. Hydrological Processes, V.12, No.8, 1151-1182.

Tchamen, G., & Kahawita, R. (1994). Numerical simulation of wetting and drying areas using Riemann solvers. Proceedings of the Specialty Conference on Modelling of Flood Propagation Over Initially Dry Areas, 127-136.

Topper, J., & Kawahara, T. (1978). Approximate equations for long nonlinear waves on a viscous film. Journal of Physical Society. Japan, V.44, No.2, 663-666.

Townsend, P., & Walsh, S. (1998). Modeling floodplain inundation using an integrated GIS with radar and optical remote sensing. Geomorphology, V.21, No.3-4, 295-312.

Umetsu, T., & Matsumoto, J. (1998). Sediment transport FEM analysis using moving boundary technique. International Symposium on River Sedimentation, V.7, 757-762.

Vieux, B.E. (2004). Distributed hydrologic modeling using GIS. Second Edition. Kluwer Academic Publishers. Water Science Technology Series. Norwell, Massachusets. 48.

Vieux, B., & Farajalla, N. (1996). Temporal and spatial aggregation of NEXRAD rainfall estimates on distributed storm runoff simulation. Proceeding, 3rd International Conference on GIS and Environment. National center for Geographic Information and Analysis. Santa Fe, New Mexico. 199-208.

Wang, S. S., Roche, P. J., Schmalz, R. A., Jia, Y., & Smith, P. E. (2008). 3D free-surface flow models. American Society of Civil Engineers. Reston.

Whiteaker, T., Maidment, D., & Robayo, O. (2006). From a NEXRAD rainfall map to a flood inundation map. Journal of Hydrologic Engineering , V.11, No.1.

Wooding, R. A. (1965). A hydraulic model for the catchment-stream problem. Journal of Hydrology, V.3, 254-267.

Xu, X., Howard, K., & Zhang, J. (2007). An automated radar technique for the identification of warm rain processes. Submitted to Journal of Hydrometeorology.

Zhang, J., Howard, K., & Wang, S. (2006). Single radar cartesian grid and adaptative radar mosaic system. 12th Conference on Aviation, Range, and Aerospace Meteorology. Atlanta, Georgia.

Zhang, J., Wang, S., & Clarke, B. (2004). WSR-88D reflectivity quality control using horizontal and vertical reflectivity structure. 11th Conference on Aviation, Range, and Aerospace Meteorology, 8.

Zhang, W., & Cundy, T. W. (1989). Modeling of two-dimensional overland flow. Water Resources Research , V.25, No.9, 2019-2035.